UNH-R69-7
N69-28532
NASA CR-101428

INVESTIGATION OF AURORAL PHENOMENA BY SOUNDING ROCKET

BY

WENTWORTH EDWARDS POTTER

CASE FILE
COPY

Space Science Center
Department of Physics
UNIVERSITY OF NEW HAMPSHIRE
Durham

INVESTIGATION OF AURORAL PHENOMENA BY SOUNDING ROCKET

by

WENTWORTH EDWARDS POTTER
B.S., Allegheny College, 1964
M.S., University of New Hampshire, 1967

A THESIS

Submitted to the University of New Hampshire
In Partial Fulfillment of
The Requirements for the Degree of
Doctor of Philosophy

Graduate School
Department of Physics
March, 1969

ACKNOWLEDGMENTS

The author wishes to express his sincere appreciation to Dr. Laurence J. Cahill, Jr. for his guidance during the course of this research.

Thanks is given to Dr. Roger Arnoldy and the members of the author's thesis committee for many meaningful discussions, and to Bob Swasey and Mrs. Jewel Chaudhary for their data reduction programming. The author is indebted to Mrs. Suzanne Rusay and Miss Patti Streff for patiently typing the manuscript, to Herb Scheibel and Bill Schaffner for their drafting assistance, and to his wife, Sue, for proofreading the paper. Machining work was done by Al Knight and Karl Flanders.

The author appreciates the assistance given to him by Larry Choy, Shadrack Ifedili, and the staff of the Magnetic Field Lab and Space Science Center at the University of New Hampshire. Steve Rearwin and Anil Davé at the Space Science Institute, University of California at San Diego provided assistance in the payload construction and testing.

Ground support at Churchill was given by the Ft. Churchill Research Range and the National Aeronautics and Space Administration.

The author would like to thank the National Aeronautics and Space Administration for awarding him a three year

predoctoral traineeship which made his graduate work possible.

This research was supported by National Aeronautics and Space Administration Contract NGR-30-002-028 and Grant ~~NsG-624~~. (NGR-30-002-010)

TABLE OF CONTENTS

LIST OF TABLES viii

LIST OF FIGURES ix

ABSTRACT xv

I. INTRODUCTION 1

II. THEORETICAL AND EXPERIMENTAL BACKGROUND

1. Auroral Morphology 8

2. Charged Particles and Auroral Excitation 11

3. Auroral Electrojet 14

4. Auroral Theories 18

5. Critical Measurements 23

6. Purpose of Auroral Sounding Rocket Program . . . 25

III. EXPERIMENTAL DESIGN AND TESTING OF ROCKET PAYLOAD

1. General Description of Payload 27

2. Electric Field Measurements

a. Measurement Techniques 31

b. Electric Field Booms 34

c. Electric Field Electronics 37

3. Magnetic Measurements

a. Experimental Techniques 41

b. Proton Precession Magnetometer 42

c. Axial Fluxgate Magnetometer 47

d. Transverse Fluxgate Magnetometer 48

4. Auroral Photometers. 49

5. Solid State Particle Detectors 52

6. Curved Plate Particle Detectors. 53

7. Payload Telemetry. 55

8. Payload Power. 57

9. Payload Testing. 57

IV. ANALYSIS OF DATA AND DISCUSSION OF ERRORS

1. Telemetry. 60

2. Proton Precession Magnetometer 60

3. Electric Field Meter 62

4. Axial Fluxgate Magnetometer. 66

5. Photometers. 66

6. Solid State Particle Detectors 67

V. EXPERIMENTAL RESULTS

1. Flight UNH 68-1. 68

2. Flight UNH 68-2. 70

3. Flight UNH 68-3. 76

4. Flight UNH 68-4. 82

5. Flight UNH 68-5. 83

VI. CONCLUSIONS

1. Discussion of Rocket Results 91

2. Recommendations for Future Experiments 97

BIBLIOGRAPHY 99

APPENDIX A 104

APPENDIX B. 109

TABLES. 111

FIGURES 123

LIST OF TABLES

1. Important Plasma Parameters 111

2. Rocket Trajectory Program 112

3. Theoretical Magnetic Field Program 116

4. Data Interpolation Program 121

LIST OF FIGURES

1. General Picture of Magnetosphere (Due to solar wind distortion of magnetosphere, the auroral ovals are at high latitudes on day side and low latitudes on night side of earth) 123

2. McIlwain's L Shells (Venkatesan, 1965) 124

3. Ionospheric Conductivities (After Fahleson, 1967) . . 125

4. Magnetosphere Plasma Convection Theories 126
   a. Closed Model (After Axford and Hines, 1961)
   b. Open Model (After Dungey, 1961)

5. Neutralizing Currents in Magnetosphere (After Fejer, 1963) 127

6. Lines of Equal Magnetic Field Intensity(In gauss) . . 128

7. Nike Tomahawk Rocket 129

8. Auroral Sounding Rocket Payload Construction 130

9. Auroral Sounding Rocket Payload with Ceramic Nosecone 131

10. Squib Circuits - Auroral Sounding Rocket Payload . . 132

11. External Control Box Wiring Diagram. 133

12. Auroral Sounding Rocket Payload Wiring Diagram . . . 134

13. The $\bar{v} \times \bar{B}$ Effect for Collinear Cylindrical Probes. . 135

14. Ejection Sequence - Unfurlable Electric Field Booms. 136

15. Electric Field Measuring Technique - Block Diagram . 137

16. Field Effect Voltage Follower Front End - Schematic. 138

17. Calibration Circuit with Operational Amplifier - Schematic. 139

18. Calibration Curve - 18.39 Electric Field Meter . . . 140

19. Photograph. 141
a. Top - Electric Field Boom Deck
b. Bottom - Electric Field Meter Electronics

20. Proton Magnetometer - Pre Amp (Maynard, 1966) . . . 142

21. Proton Magnetometer - Main Amp (Maynard, 1966). . . 143

22. Proton Precession Magnetometer - Block Diagram. . . 144

23. Photograph. 145
a. Top - Proton Magnetometer Pickup Coil
b. Bottom - Proton Magnetometer Signal (Large amplitude signal contains precession frequency; small amplitude signal is amplifier noise during polarize cycle)

24. Photograph. 146
a. Top - Proton Magnetometer Main Amp Electronics
b. Middle - Proton Magnetometer Pre Amp Electronics
c. Bottom - Fluxgate Magnetometer Deck - Axial and Transverse Sensors

25. Axial and Transverse Fluxgate Magnetometers - Block Diagram 147

26. Fluxgate Magnetometer - Operational Diagram 148

27. Axial Fluxgate Magnetometer - Bucking Coil Circuits- Astable and Monostable Multivibrator Schematic. . 149

28. Axial Fluxgate Magnetometer - Bucking Coil Circuits- Ring Counter and Switch Schematic 150

29. Axial Fluxgate Magnetometer - Bucking Coil Circuits- Constant Current Supply 151

30. Auroral Photometer - D.C. Log Amplifier Schematic . 152

31. Auroral Photometers, 5577Å and 6300Å - Block Diagram. 153

32. Photograph. 154
a. Top - Auroral Photometer Electronics
b. Bottom - Auroral Photometer - Photomultiplier Tube and D. C. - D. C. Converter Assembly

33. Solid State Electron Detector - Block Diagram. . . . 155

34. Photograph 156
a. Top - Solid State Particle Detector
b. Middle - HR 1.5 Silver Cell Battery Box for Experiments
c. Bottom - HR3 Silver Cell Battery Box for Telemetry and Proton Magnetometer

35. Simple D. C. Voltage Regulator - Schematic 157

36. Magnetic Signature - Electric Field Meter. 158

37. Proton Magnetometer - Data Reduction Technique . . . 159

38. Computed $\bar{v} \times \bar{B}$ Field - UNH 68-5, 3 May 1968. 160

39. Phase and Magnitude Differences of Electric and $\bar{v} \times \bar{B}$ Field - UNH 68-5, 3 May 1968 161

40. Rocket Trajectories - Churchill Research Range, Manitoba, Canada - Flights UNH 68-1, 68-2, 68-3, and 68-5 162

41. Computed Rocket Trajectory - Flight UNH 68-1 (NASA 18.38), 5 February 1968. 163

42. Ground Station Magnetometer and Riometer Record, Fort Churchill - UNH 68-1, 5 February 1968. 164

43. Total Magnetic Field - Proton Magnetometer; Jensen and Cain (1962) Theoretical Field - UNH 68-1, 5 February 1968. 165

44. Computed Rocket Trajectory - Flight UNH 68-2 (NASA 18.41), 23 April 1968. 166

45. Ground Station Magnetometer and Riometer Records, Fort Churchill - UNH 68-2, 23 April 1968 167

46. Auroral Photometer - 5577$\mathring{A}$ Maximums - UNH 68-2, 23 April 1968 168

47. Auroral Photometer - 5577$\mathring{A}$ Minimums - UNH 68-2, 23 April 1968 169

48. Auroral Photometer - 6300Å Maximums - UNH 68-2, 23 April 1968. 170

49. Auroral Photometer - 6300Å Minimums - UNH 68-2, 23 April 1968. 171

50. Total Magnetic Field - Proton Magnetometer - UNH 68-2, 23 April 1968 172

51. Difference Field - UNH 68-2, 23 April 1968. 173

52. Electric Field (Corrected for $\bar{v} \times \bar{B}$) - Upward Leg - UNH 68-2, 23 April 1968 174

53. Electric Field (Corrected for $\bar{v} \times \bar{B}$) - Downward Leg - UNH 68-2, 23 April 1968 175

54. Charged Particle Fluxes - UNH 68-2, 23 April 1968 . . 176

55. Axial Magnetic Field - Axial Fluxgate Magnetometer - UNH 68-2, 23 April 1968 177

56. Angle Between Spin Axis and Magnetic Field (ψ) - UNH 68-2, 23 April 1968; UNH 68-5, 3 May 1968 . . . 178

57. Computed Rocket Trajectory - Flight UNH 68-3 (NASA 18.42), 25 April 1968 179

58. Ground Station Magnetometer and Riometer Record, Fort Churchill - UNH 68-3, 25 April 1968. 180

59. Photograph - All Sky Camera - Fort Churchill - UNH 68-3, 25 April 1968 181
    a. Top - Rocket Position Among Auroral Forms at 100 Km on Upward Leg Shown by Black Dot
    b. Bottom - Rocket Position Among Auroral Forms at 100 Km on Downward Leg Shown by Black Dot

60. Auroral Photometer - 5577Å Maximums - UNH 68-3, 25 April 1968. 182

61. Auroral Photometer - 5577Å Minimums - UNH 68-3, 25 April 1968. 183

62. Auroral Photometer - 6300Å Maximums - UNH 68-3, 25 April 1968. 184

63. Auroral Photometer - 6300Å Minimums - UNH 68-3, 25 April 1968. 185

64. Total Magnetic Field - Proton Magnetometer - UNH 68-3, 25 April 1968 186

65. Difference Field - UNH 68-3, 25 April 1968. 187

66. Electric Field (Corrected for $\bar{v} \times \bar{B}$) - Upward Leg - UNH 68-3, 25 April 1968 188

67. Electric Field (Corrected for $\bar{v} \times \bar{B}$) - Downward Leg- UNH 68-3, 25 April 1968 189

68. Charged Particle Fluxes - UNH 68-3, 25 April 1968 . 190

69. Angle Between Spin Axis and Magnetic Field (ψ) - UNH 68-3, 25 April 1968 191

70. Computed Rocket Trajectory - Flight UNH 68-5 (NASA 18.39), 3 May 1968. 192

71. Ground Station Magnetometer and Riometer Record, Fort Churchill - UNH 68-5, 3 May 1968 193

72. Photograph - All Sky Camera - Fort Churchill - UNH 68-5, 3 May 1968. 194
   a. Top - Rocket Position Among Auroral Forms at 100 Km on Upward Leg Shown by Black Dot
   b. Bottom - Rocket Position Among Auroral Forms at 100 Km on Downward Leg Shown by Black Dot

73. Auroral Photometer - 5577Å Maximums - UNH 68-5, 3 May 1968. 195

74. Auroral Photometer - 5577Å Minimums - UNH 68-5, 3 May 1968. 196

75. Auroral Photometer - 6300Å Maximums - UNH 68-5, 3 May 1968. 197

76. Auroral Photometer - 6300Å Minimums - UNH 68-5, 3 May 1968. 198

77. Total Magnetic Field - Proton Magnetometer - UNH 68-5, 3 May 1968. 199

78. Difference Field - UNH 68-5, 3 May 1968. 200

79. Electric Field (Corrected for $\bar{v} \times \bar{B}$) - Upward Leg - UNH 68-5, 3 May 1968 201

80. Electric Field (Corrected for $\bar{v} \times \bar{B}$) - Downward Leg- UNH 68-5, 3 May 1968 202

81. Relative Directions of Electric and $\bar{v} \times \bar{B}$ Fields - UNH 68-5, 3 May 1968 203

82. Charged Particle Fluxes - UNH 68-5, 3 May 1968 . . . 204

83. Axial Magnetic Field - Axial Fluxgate Magnetometer - UNH 68-5, 3 May 1968 205

ABSTRACT

INVESTIGATION OF AURORAL PHENOMENA BY SOUNDING ROCKET

by

WENTWORTH EDWARDS POTTER

Auroral phenomena are discussed in light of previous experimental results and theoretical considerations. It is seen that visible aurora are only part of what is termed a magnetospheric substorm. The substorm phenomena include not only localized auroral zone events but also plasma convection and current systems far out into the magnetosphere. Auroral phenomena include charged particle precipitation down magnetic field lines into the ionosphere, magnetic disturbances due to electrojet currents, electric fields which drive the electrojet and the visible aurora.

Several theories of magnetospheric substorms are investigated. Some propose widespread circulation of the plasma in the magnetosphere with the resulting currents flowing down the field lines into the ionosphere. Here, due to enhanced conductivity, they "short" across the auroral zone and flow out along other field lines. Other theories assume current loops confined to the ionospheric shell are

formed from the tidal motion of the upper atmosphere.

The construction and testing of five Nike Tomahawk sounding rocket payloads are discussed. The experiments included vector and magnitude measurements of the magnetic field, measurements of the transverse electric field, measurement of charged particle fluxes, and an indication of the auroral light intensity at 6300Å and 5577Å. These measurements along with ground station magnetometer records, radar data, and all sky camera pictures were used to construct a model of the electrojet current system at the time of the flight.

The results from five rocket flights are presented. The rockets were launched during a variety of auroral and magnetic conditions although they all had similar trajectories. Magnetic disturbances measured during the flights indicated the existence of electrojet currents near 100 km flowing parallel to the visible auroral arcs. The presence of field aligned currents was indicated in the results of one flight.

Electric fields perpendicular to the magnetic field were measured. Fields of 25 to 70 mv/m were measured during all except one "quiet time" flight in which an upper limit of 20 mv/m was obtained for the electric field. The fields pointed southward and were consistent with a westward flowing

Hall current. There was no appreciable altitude dependence in the fields indicating, to first order, that the magnetic field lines were equipotentials.

Charged particle flux measurements showed particle precipitation existed during periods of visible auroral activity. A correlation between an increase in luminosity and an increase in flux was noticed. Particle precipitation was also indicated on ground based riometers.

SECTION I

INTRODUCTION

Across northern Canada and Alaska, on almost every clear night, thin luminous bands of color extend from eastern to western horizon. In the early evening, these auroral light displays form to the north in smooth, colorless arcs. As the light intensity gradually increases, a pale green hue is often noticed. These arcs of light move slowly southward and pass overhead and are followed by other arcs from farther north.

As midnight approaches, the arcs become convoluted forming complex, sheetlike draperies overhead; movement of these billowing curtains becomes more rapid, the color deepens, and great loops and folds are seen in the sheets. Red tinges appear at the lower edge of the sheets and the intensity of light varies from place to place across the sky. Rays of light stand out within the sheets apparently aligned with the near vertical earth's magnetic field. The light shimmers and flickers and sudden erratic movements of the draperies and loops are common. Great folds in the structure are seen to move rapidly across the observer's sky and folds within folds are often seen.

There is evidence that these nightly displays have

been observed for over 2,000 years and are among the earliest recorded geophysical phenomena. Due to the complex forms and erratic movement, it is difficult to describe auroral morphology although extensive systematic recording has taken place since the International Geophysical Year (1957-1958). Although auroral displays are mainly found at higher latitudes, they occasionally are seen in the United States and as far south as Mexico. In Canada, the line (isochasm) of 100 percent frequency of auroral displays (display every night) is near 60°N latitude.

The principal methods of observing auroral displays have been all sky cameras, visual observers, and spectrographs which record the composition of the light. Visual and camera observation is hindered by the large extent and complex rapidly moving forms of the aurora. This makes classification in record books very difficult. The polar location of the displays also complicates setting up auroral observation posts.

In many cases where visual auroral observation has taken place, there have also been measurements of changes in the earth's magnetic field. It has been noted that the aurora is closely linked to disturbances in the earth's field. As the field becomes more disturbed, the aurora becomes more intense and complex. The visible aurora is found in a "belt" at any given instant of time. This statistically appears as

an oval reaching high latitudes (~78°) on the dayside and low latitudes (~65°) on the nightside of the earth. An auroral oval also exists in the southern hemisphere where similar auroral activity is observed.

The earth's magnetic field lines, essentially dipolar, extend upward from the auroral displays and cross the equatorial plane at 5 to 9 earth radii. The auroral displays are but one evidence of large scale magnetohydrodynamic processes involving these outer shells of the earth's magnetosphere (that region of space around the earth dominated by the geomagnetic field). After a decade of investigation of the magnetosphere by satellite borne experiments, some features of these outer magnetospheric processes are becoming evident. We can observe this huge region by gaining only occasional glimpses of a few of the variables and we are still groping toward gaining an understanding of the processes. A speculative account of the processes is a convenient frame for describing the observed phenomena.

Solar wind plasma sweeps by and deforms the earth's magnetic field, compressing the field toward the sun and pulling the polar field lines into a big tail. This solar wind plasma may enter the tail region and at least sets in motion a convection of the magnetospheric plasma (near the boundary) towards the rear of the magnetosphere. The plasma

then returns up the center of the tail toward the earth. As the plasma enters the region of stronger magnetic field near the earth, the protons and electrons are separated by a $\nabla|\bar{B}|$ drift; protons drifting west and electrons east. This separation leads the protons into the evening quadrant where they inflate (weaken) the magnetic field. These particles engage in spiral motions characteristic of other particles trapped in the earth's magnetic field. Some of these penetrate into the ionosphere causing thermal ionization as well as the excitation of atmospheric molecules that lead to aurora light.

As new particles are injected from the tail, an electric field is established by charge separation and, since the conductivity along the field lines is very high, the same electric field is mapped along the field lines into the ionosphere. The drifting protons and electrons on the equator constitute an electrical current which may be completed by current flow up and down the magnetic field lines to the ionosphere. Current then flows horizontally in the highly conductive ionosphere associated with the auroral display.

In the past, the auroral displays and associated magnetic changes caused by the strong ionospheric electric currents were called auroral or polar substorms. The frequency and intensity of substorms is greatest at the onset of a world wide magnetic storm. This event involves the inner

magnetosphere and produces magnetic disturbances all over the earth's surface. Now realizing the scope of the processes extending throughout the magnetosphere we speak of a magnetospheric substorm. The substorms are usually one to three hours in duration.

Although many details of this account may prove to be in error, the observations must be accounted for in any correct explanation. The phenomena observable in the auroral ionosphere include the auroral light - its form, intensity and changes; the intense east - west electric currents (auroral electrojets); electric fields that drive these currents; and the energetic charged particles spiralling down field lines (usually electrons) that excite the auroras. Looking on the same field lines in the equatorial plane, pertinent observables are: plasma density and flow direction, energetic particle fluxes, electric fields and electrical currents producing magnetic field changes. Similar measurements on these field lines intersecting the southern ionosphere would also be valuable, but the region is less accessible.

Not all of these parameters have yet been observed. The active region is large on the equator (because of the divergence of field lines in the auroral zone, a few degrees extent in latitude, 50 to 100 miles north - south, expands to 2 earth radii, 8,000 miles, on the equator) and both

expensive and difficult to observe. Electric fields have not been observed there and technical difficulties preclude observation at present. The ionosphere is closer and less expensive to investigate and electric fields are easier to measure since the Debye length is smaller. The scale of the electric currents and particle fluxes is smaller and supporting measurements from the ground such as ionization density, all sky auroral photographs and magnetic observations are available.

The intent of the present rocket flights was to investigate several auroral phenomena simultaneously to help in determining the processes involved in magnetospheric substorms. One of the parameters selected for observation was the horizontal component of the electric field. Observation of the magnitude and direction of the field might allow selection between several plausible explanations of the magnetospheric substorm. Another vital observation was the extent, intensity, and structure of the auroral electrojet. Is the electrojet a current ribbon following the auroral loops; does it flow in a straight line only confined to the general latitude span of the auroral excitation? Is it thin or diffuse and are there currents flowing along the field lines? Vector measurements of the electrojet magnetic field were planned to assist in answering some of these questions. The third major experiment was an attempt to measure the charged particle fluxes

that are thought to excite the auroral displays. Are charged particle fluxes always coincident with auroral displays? Does the energetic charged particle flux constitute an electrical current? It was hoped that answers to these as well as other questions would be found.

The first five in a series of Nike-Tomahawk sounding rockets were flown during the first half of 1968 from Ft. Churchill, Manitoba. Four of the flights were made through visible auroral displays while the fifth was fired during a quiet period with no visible aurora or magnetic disturbances.

SECTION II

THEORETICAL AND EXPERIMENTAL BACKGROUND

1. Auroral Morphology

In order to understand better the processes involved in auroral zone phenomena, it is beneficial to define geographically what is meant when one discusses the auroral zone and auroral oval. Early study indicated the existence of auroral zones (bands about the poles where auroras are observed with equal frequency) about the boreal axis (northern geomagnetic pole) and austral axis (southern geomagnetic pole). The 100% isochasms (lines of equal occurrence) have an angular radius of about 23° about the pole. A belt of 2° on each side of this corresponds to a region in which the aurora is visible on nearly every clear night. These belts are known as the auroral zones, and they enclose the polar caps.

The auroral oval is the region where the magnetic field lines, which are near the outer edge of the trapping region, intersect with the earth's surface. The relative positions of the trapping region and auroral oval are seen in Figure 1.

A statistical study of the distribution of aurora

using records from many stations for each display shows that the distribution is in the shape of an oval reaching low latitudes (~65°N) on the night side and high latitudes (~78°N) on the day side of the earth (Akasofu, 1964). This in in contradiction to an earlier concept which proposed the existence of an "inner" and "outer" auroral belt at ~78°N and ~65°N latitude respectively.

Störmer (1955), Chamberlain (1961), and others have reviewed visible auroras and some guidelines and standards concerning visible auroras have been established. In North America, the line of 100 percent frequency of aurora is near 60°N latitude (Vestine, 1944). (Churchill Research Range is further north near the 90% isochasm). At this latitude there appear to be three stages of auroral displays as determined by visual observation, the study of all sky camera photographs, and the study of ground station magnetograms.

The three phases are:

i. Quiet arcs which rise slowly from the northern horizon and move southward are followed by other arcs from the north. These arcs may or may not cross the observer's zenith. This stage is usually in the pre-midnight period.

ii. The breakup period takes place near magnetic midnight. The arcs become thinner and better defined

thus becoming more like waving curtains or large enclosed loops.

iii. In the post-midnight period the curtains and loops disappear and leave luminous patches (up to ten minutes in duration) which often pulsate and drift eastward.

The visible auroral displays can also be separated into three basic types according to physical cause. There are aurora excited by electrons, those excited by protons, and those associated with magnetohydrodynamic waves and upper atmosphere heating. These three types can occur simultaneously.

The electron aurora is probably the most common of the three. The electrons are primarily of low energy (a few kev) with a widely varying energy spectrum. This type of aurora is most frequent on the ovals $\sim 23^{o}$ from the geomagnetic poles (Chamberlain, 1961).

Low energy proton auroras are not readily visible since they are usually formed from low intensity hydrogen emission. Proton energies greater than 5 kev have been seen in the auroral zone with precipitation zones bounded by the L = 5 and L = 10 (Figure 2) (McIlwain, 1961) shells (Evans et al.,1965). These displays are usually found at lower latitudes than the electron auroras.

Another type of aurora may be caused by magnetohydro-

dynamic waves entering the ionosphere. This is believed to cause red atomic oxygen emission near 200-300 km. This is a very diffuse form on which little experimental knowledge has been gained (Walt, 1965). The upper atmospheric heating, possibly due to these waves, seems to cause this emission which is also nearly always present during electron and proton injection.

2. Charged Particles and Auroral Excitation

A spectacular visible auroral display is usually accompanied by changes in other geophysical parameters. The exact relations between these are not immediately obvious and it is the purpose of auroral research to determine the physical causes of auroral displays and their relation to other physical phenomena. Some of the first investigations were of charged particle fluxes since it was believed they might be responsible for the ionization of molecules and atoms which produce the visible displays. Studies have been done in the auroral zone on the correlation of high electron fluxes to the position of high auroral luminosity. McIlwain (1960) and Davis et al. (1960) have shown such a correlation exists while also showing that the proton flux did not vary greatly over distances of approximately 40 km in regions of variable luminosity.

McIlwain (1960) found a nearly monoenergetic flux of

electrons near 6 kev of approximately 2 x 10^{11} electrons/ cm^2 - sec in an auroral arc. In a quiescent display, the flux was near 10^8 - 10^{10} electrons/cm^2 - sec. The energy fluxes were on the order of 10^{10} kev/cm^2 - sec for protons and 10^{12} kev/cm^2 - sec for electrons although this varied widely during the experiment. Evidence of aurora being caused by protons near 100 kev was also found by McIlwain (1960).

Evans (1968) has recently seen a monoenergetic 4 kev flux (isotropic) of electrons (4 x 10^8 electrons/cm^2 - sec - sterad) at auroral latitudes during a visible display. He also reported observing a 10 cps periodicity in the precipitation of auroral zone electrons from 1 to 120 kev (Evans, 1967). The source and acceleration mechanisms for auroral particles are still a matter of speculation.

A study of the hydrogen light in auroras gives further indication of some auroras being caused by protons. Mozer and Bruston (1966) saw an anticorrelation between electrons and protons along high latitude field lines indicating electric fields parallel to the magnetic field may be accelerating the particles. Evans (1968) agrees with this idea although he believes there is more than one acceleration mechanism involved. It is seen in the theory of trapped particles (Chapman, 1964) how particles with a small

enough pitch angle θ_e (when they cross the equator) can mirror at any latitude near 100 km. The collision with a molecule could then cause excitation and produce auroral light. In a dipole approximation, the equation for the field lines is $r = R_E \cos^2\phi$ where ϕ is the latitude and R_E is the distance from the earth's center at which the particle crosses the equatorial plane of the geomagnetic field. The distance from the center of the earth to the mirror point is $R_E \cos^2 \phi_m$ where ϕ_m is the mirror latitude.

From these observations, one naturally asks the question: Where do the particles come from? Basically, there appears to be three possible sources:

i. Magnetosphere tail

ii. Outer boundary of trapping region

iii. Trapping region

The trapping region seems to be an unlikely source since the energy spectra of electrons in aurora and the trapping region are quite different. The energy of the trapped radiation is not great enough to sustain an auroral display for an appreciable time (Chamberlain, 1961), and the total number of particles is not great enough. Another possibility is a mechanism in which particles are fed into the trapped particle region, held for a few bounces and then precipitated into the auroral zone. Even if this is the case, there has

to be a process where particles are brought into this region.

If particles enter into the tail through some form of solar wind interaction, they may proceed back up the tail lines. Evans (1968) has seen monoenergetic electron peaks in an auroral display and suggests that electric fields parallel to the magnetic field may facilitate the precipitation process by accelerating electrons to lower altitudes where they would produce auroral light. Since the conductivity along the magnetic field line is high, one does not expect electric fields parallel to $\bar{B}$ to be large compared to the expected transverse electric fields of 10-100 mv/m. Even if the parallel electric field is on the order of a few microvolts per meter, this may be large enough to accelerate the low energy electrons when distances of hundreds or thousands of kilometers are considered.

3. Auroral Electrojet

Quiet time observations of the geomagnetic field indicate the existence of variations (S_q) which are believed to be caused by the atmospheric dynamo motion or tidal motions (DeWitt and Akasofu, 1964). At auroral latitudes during magnetically disturbed times, a variable enhancement of the magnetic field is known to occur. This is the D_s variation, and the currents causing it are known

as the auroral electrojet (Fejer, 1963). Auroral displays are often accompanied by these local magnetic disturbances, and it is believed that the electrojet current is confined to or near the visible auroral structure. Assuming the current has the same limits as the visible aurora, it has been speculated that the electrojet often extends only a few kilometers in the north-south direction while its east-west extension may be on the order of several thousand kilometers.

The energy source which drives these ionospheric currents is unknown but several theories concerning its form have been proposed. An ionospheric source has been proposed by Swift (1963) in which the electrojet currents may be caused by winds in the upper atmosphere. The co-rotation of the atmospheric gas with the earth or the tidal winds implies a movement of plasma past the magnetospheric field if one considers the frozen field concept as valid (Alfvén, 1963). The plasma motion with a velocity vector $\bar{v}_n$ leads to an induction field $\bar{E}_i = \bar{v}_n \times \bar{B}$.

The shell between 80 to 140 km is thought to contain the ionospheric current since this is the area of largest auroral ionization. At 120 km during an auroral display, both the Pederson and Hall conductivities are near 10^{-3}/ohm-m while the conductivity parallel to the field lines is

~5/ohm-m (Fahleson et al., 1967) (Figure 3). The horizontal current density for a thin shell is given by (the x's indicate southward components while the y's indicate eastward components of $\bar{E}$ and $\bar{j}$).

$$\begin{pmatrix} j_x \\ j_y \end{pmatrix} = \begin{pmatrix} \sigma_{xx} & \sigma_{xy} \\ -\sigma_{xy} & \sigma_{yy} \end{pmatrix} \begin{pmatrix} E_x \\ E_y \end{pmatrix} \tag{1}$$

where

$$\sigma_{xx} \approx \frac{\sigma_1}{\sin^2 I} \tag{2}$$

$$\sigma_{yy} \approx \sigma_1 \tag{3}$$

$$\sigma_{xy} \approx \frac{\sigma_2}{\sin I} \tag{4}$$

I is the geomagnetic dip angle and σ_1 is the Pederson conductivity (where the current flow is in the direction of an electric field which is perpendicular to the magnetic field if one is present).

The Pederson conductivity is

$$\sigma_1 = e^2\left[\frac{N_e\ (\nu_e - i\omega)}{m_e\left[(\nu_e - i\omega)^2 + \omega_e^2\right]} + \frac{N_i\ (\nu_i - i\omega)}{m_i\left[(\nu_i - i\omega)^2 + \omega_i^2\right]}\right] \tag{5}$$

where $\omega_i = +B|e|/m_i$ is the ion cyclotron frequency and

$\omega_e = -B|e|/m_e$ is the electron cyclotron frequency. Other conductivities can also be defined for this region. The Hall conductivity (for computing currents which flow perpendicular to the $\bar{E}$ and $\bar{B}$ fields) is defined as

$$\sigma_2 = e^2 \left[\frac{N_e \omega_e}{m_e \left[(\nu_e - i\omega)^2 + \omega_e^2 \right]} - \frac{N_i \omega_i}{m_i \left[(\nu_i - i\omega)^2 + \omega_i^2 \right]} \right] \quad (6)$$

The Specific conductivity (determining current flow for an $\bar{E}$ field parallel to or in absence of a $\bar{B}$ field) is

$$\sigma_o = e^2 \left[\frac{N_e}{m_e (\nu_e - i\omega)} + \frac{N_i}{m_i (\nu_i - i\omega)} \right] \quad (7)$$

where N_i is the ion density (ions/cm^3), N_e is the electron density (electrons/cm^3), $e = 1.6 \times 10^{-20}$ emu, m_i is the ion mass (gm), m_e is the electron mass (gm), and ω is the driving frequency (collisions/sec). The electron collision frequency is ν_e and the ion collision frequency is ν_i.

If the velocity of the neutral gas v_n is included, the electric current density can be written $\bar{j} = \sigma_1 (\bar{E}_\perp + \bar{v}_n \times \bar{B}) + \sigma_2 \bar{B} \times (\bar{E}_\perp + \bar{v}_n \times \bar{B}) /B + \sigma_o \bar{E}_{11}$. In this expression $\perp$ and 11 are used to denote components of $\bar{E}$ perpendicular and parallel to the magnetic field $\bar{B}$.

According to calculations by Boström (1964), the wind associated with an auroral electrojet must have a speed of about 500 m/sec. Actual observations at auroral

altitudes (100-150 km) reveal wind speeds on the order of 100 m/sec. Even with using increased electron densities, it is hard to obtain values of electrojet current comparable to those measured which are $\sim 10^4 - 10^5$ amps (Davis, 1962). From these observations it appears that although a wind driven current may contribute to the auroral electrojet, it probably does not make up the total current. Another possible driving mechanism might be electric fields. Boström calculates these to be near 50 mv/m in the ionosphere if they are to produce the measured currents.

It was once believed that the electrojet was part of a current system with a loop structure totally confined to the ionospheric shell. The current system in the auroral regions was enhanced by the increased ionization and the return currents were over the pole and at lower latitudes. Recent ideas and measurements indicate a three dimensional current system in which currents, driven by magnetospheric electric fields in the equatorial plane flow down the magnetic field lines, "short" across the auroral zones and flow back out field lines.

4. Auroral Theories

There is evidence that convective motion of plasma exists throughout the magnetosphere. The cause of this convection may be due to solar wind interaction with the magnetosphere or possibly the co-rotation of part of the magnetosphere with the earth. The possibilities of convective motion in the tail region due to a viscous interaction between the solar wind and the magnetospheric plasma have been shown by Axford and Hines (1961).

They show inward convection of plasma from the tail into the main part of the magnetosphere nearer the earth can take place. There may exist turbulence at the outer boundary of the trapping region which enters the ionosphere in the auroral zone.

In Axford and Hines' theory, the interaction is assumed to be a momentum transfer through some form of viscous interaction between the solar wind and the magnetosphere. As the solar wind passes about the teardrop-shaped magnetospheric cavity, it carries plasma to the tail region with the return flow of ionized particles back up through the tail on the night side of the earth (Figure 4). With the convection of plasma past magnetic field lines, $\bar{v} \times \bar{B}$ electric fields will be induced. These can be mapped into the ionosphere assuming the magnetic field

lines are equipotential lines.

Dungey (1961) proposes a joining of the southward interplanetary field with the earth's field (Figure 4). The lines would be drawn through the plasma about the earth and disconnected in the tail thus causing plasma convection and induced electric fields.

Fejer (1963) describes the ionospheric dynamo field as that seen by an observer moving with the neutral particles in the absence of any polarization charges. A polarization field is an electric field due to the separation of oppositely charged particles. Assuming that low energy particles have a drift velocity perpendicular to $\bar{B}$ of $\bar{E} \times \bar{B}/B^2$, it is seen that these low energy particles take part in magnetospheric convection. Higher energy particles are more affected by the dipole field ($\nabla|B|$ drift) rather than the drift of ionospheric tidal origin. These particles have energies over 40 kev and behave almost independently of the tidal drift velocities. The dipole drift velocity is west to east for electrons and east to west for ions and is about twenty times greater than the drift velocity of tidal origin. The next assumption is that positive energetic particles are present in much larger numbers than particles of the other sign. The energetic particles have an east-west drift but no outward

or inward motion, thus we can assume they are on surfaces of constant number density. These assumptions have been verified in part by Explorer 12 results, (Davis and Williamson, 1962).

If one now considers outward convection of the magnetospheric plasma, the lower energy particles (following the convection) will drift out through the proton belt resulting in an effective negative charge on the outside and positive charge on the inside of the belt. Polarization fields are then set up which cause neutralization currents to flow down the field lines, short across the auroral zone and flow out into the magnetosphere again (Figure 5). The electric field can also cause a Hall current to flow east-west in the auroral zone ionosphere. A reversal in current can be attributed to an inward convection of the magnetosphere.

Fejer (1963) then considers co-rotation in which the neutral part of the atmosphere is taken to rotate with the earth at ionospheric heights. One can also assume that the force lines rotate with the earth since the ionospheric conductivity is high. Low energy plasma does not rotate at higher altitudes (5-10R_E), however, because of the distortion due to the magnetic-solar wind interaction. The solar wind interaction tends to compress the field more on

the day side than on the night side. Thus, the low energy plasma is nearer the earth on the day side than at night. Energetic trapped protons follow magnetic field lines of constant magnitude in the equatorial plane, and thus, unlike the low energy particles, are closer to the earth at night. This results in a drift of low energy particles through the trapping region. The drift is inward between midnight and noon and reverses for the remainder of the day (Fejer, 1961). Continued neutralization of the high energy protons results in a current system similar to Figure 5 with the corresponding Hall current (which flows eastward before midnight and then reverses direction) also being present.

Kern (1962) also proposes an electric field in the equatorial plane which is mapped down into the auroral zone. He suggests that a gradient in the magnetic field is somehow aligned parallel to the surfaces of constant number density which in turn causes a separation of the charged particles.

A common feature of theories in which the electric field is mapped down from the magnetosphere is that the fields in the ionosphere would be primarily in a north-south direction. Theories which propose electric fields due to low altitude interaction of the neutral atmosphere

with the magnetic field, however, can explain how east-west electric fields can be created.

5. Critical Measurements

There are several critical measurements essential to exploration of the auroral/magnetospheric substorm process. Electric fields are predicted to be a primary influence in auroral phenomena. At the present time, only exploratory electric field measurements have been made, and if a real knowledge of the auroral and magnetospheric processes is to be found, large scale electric field mapping must be accomplished. Earlier measurements by Mapleson and Whitlock (1955), Imyanitov and Shvarts (1963), and Kavadas (1965) have provided inconclusive data yet valuable information towards improving the electric field measuring techniques. Recent measurements by Mozer and Bruston (1967), Kelley et al. (1968), and Maynard (1968) indicate that measureable (10-100 mv/m) fields in the auroral zone exist although there are some discrepancies concerning their magnitude and direction. These recent measurements have been done using a potential difference measurement similar to that developed by Aggson and Heppner (1965), Fahleson (1966), and Potter (1966) and discussed elsewhere in this paper. Indirect measurements of the electric field can also be

done using ionized barium clouds as has been reported by Haerendel et al. (1967) and Föppl et al. (1967). There are still too few quantitative measurements to allow a complete description of the electric fields during auroral displays. Further information can best be obtained by measurements in both quiet and active arcs as well as in the quiet ionosphere.

Another vital series of measurements has been directed toward determination of the structure of the electrojet current. Some measurements have been made (Meredith et al., 1958; Cahill, 1959; Scrase, 1967) but more specific questions will help to choose between various theories and models. Are the currents aligned with the visible aurora? Is the electrojet an ionospheric loop or a three dimensional current in the magnetosphere? What is the thickness, vertical extent, and intensity of the electrojet? These and other questions relating the electrojet to the electric fields, the auroral displays and the magnetosphere have yet to be answered.

The third critical series of measurements concerns the acceleration and precipitation of charged particle fluxes during the magnetospheric substorm. Are low energy charged particles present in the tail or on auroral field lines at the equator? What is the accelerating mechanism?

Do electric fields cause the acceleration?

Starting with these questions an experimental program has been planned. Not all of the questions can be answered by ionospheric investigations, but there are several experiments that are best done by sounding rocket.

6. Purpose of Auroral Sounding Rocket Program

The purpose of sounding rocket auroral investigations is direct observation of the physical processes taking place in and near an auroral display. The auroral electrojet, charged particle precipitation and relatively strong electric fields are expected to accompany the display, as described in earlier sections. The instantaneous auroral oval, both north and south pole branches, are only the rims of the toroidal shaped shells of plasma filled magnetic field. The primary processes are probably taking place in these shells near the equator, but the auroral ovals should contain important clues.

An important, yet little measured, parameter is the electric field. It was assumed that the component perpendicular to the field lines was greater than the parallel component so one of our experiments was designed to measure the component (transverse).

A second feature of the substorm is the electrojet

current. Ground and satellite measurements show that the current exists. The structure of the current, its relation to the auroral display and to the electric field are not known. A measurement of the vector magnetic field produced by the current would assist in deducing the location, intensity, and structure of the current. The vector components of the field as well as its magnitude were to be measured by three independent magnetometers.

Finally measurement of the proton and electron fluxes with good time and energy resolution was planned. The role of these particles in producing the auroral display ionospheric disturbance and electrojet should be explained in greater detail. The energy spectra and pitch angle distributions of the particles can provide information about processes out in the magnetosphere such as particle source and electric field distribution.

Auroral photometers were included principally to help determine the location of the rocket with respect to the auroral displays.

SECTION III

EXPERIMENTAL DESIGN AND TESTING OF ROCKET PAYLOAD

1. General Description of Rocket Payload

A series of five NIKE-TOMAHAWK sounding rockets were constructed at the University of New Hampshire Space Science Center to measure auroral phenomena. The project was funded under NASA contract NGR 30-002-028 and Grant NsG-624. The University of California at San Diego contributed two charged particle experiments to detect low energy electrons and protons. The University of California packages were self-contained and internally powered. The only electrical connection was through the rocket telemetry system constructed by the University of New Hampshire. The total payload weight was 205 pounds and was 120" long and 9" in diameter.

Several prototype payloads were constructed before the first flight model which was fired in February, 1968. After successful completion of that flight, four similar payloads were constructed and fired in April and May of 1968. All shots were made from the National Research Council Range at Ft. Churchill, Manitoba; geographical coordinates, $58^{o}45'$N and $93^{o}59'$W.

The construction of the payload is seen in Figure 8. Twenty subcarrier oscillators converted the experimental output voltages into varying frequencies which were summed at the mixer amplifier and used to modulate the five watt FM transmitter. The ground station then recorded the transmitted signal on magnetic computer tape. Signal strengths of 20 to 50 microvolts/m were received during the flights.

The principal University of New Hampshire experiments were an electric field meter for measuring the transverse component of the field, a proton precession magnetometer for measuring the magnetic field magnitude, axial and transverse fluxgate magnetometers for obtaining the magnetic field components, two auroral photometers at 5577 $\mathring{A}$ and 6300 $\mathring{A}$ and a solid state particle detector for studying low energy electron fluxes.

Since several sensitive magnetometers were flown, care was taken to limit the amount of magnetic materials on the payload. Stainless steel and brass hardware were used wherever possible. The lower payload frame consisted of aluminum decks and vertical straps while the top 12" was a support structure of fiberglass to hold the proton coil away from the payload and aluminum shell. The nose cone, as seen in Figure 9, was made of ceramic to prevent

electrical current loops which would destroy the proton signal. Stray magnetic fields were reduced by using twisted wire pairs and non-magnetic plugs and batteries.

The payload magnetic field at the proton coil was measured at the University of New Hampshire's Magnetic Coil Facility and was found to be $2\gamma \pm 1\gamma$.

The payload construction was simplified by using a full length aluminum channel in which interconnecting wires ran to connectors at each deck (Figure 8). The experiment decks could be disconnected and easily replaced with other decks if necessary. An aluminum shell enclosed the basic framework with two rectangular doors for those experiments which needed direct access to the environment. The doors remained closed until about 80 km, at which point they were released simultaneously with pyrotechnic bolt cutters. The booms were then deployed. Figure 10 shows the firing circuit for both the booms and doors. Two altitude switches in parallel were used in the circuits to prevent accidental squib firing on the ground in case the timer was started. Diodes which could sustain a large current for a short time and then burn out were used as fuses to prevent discharge of the batteries in case the squibs shorted to ground after firing.

It was desirable to perform checks of the experimental

payload through the telemetry both on the launcher and in the lab. This was done with the external control box (Figure 11). Using the control box, one could turn on and off the payload experiments and telemetry as well as charge the silver cell batteries which powered the experiments and telemetry. The experiment performance could be determined by monitoring the telemetry signals. The external control box was attached to the rocket via an umbilical cable using a Deutsch pull away connector which pulled free at launch. The rocket wiring (Figure 12) incorporated latching relays to turn on and off the experiments. In the case a rocket was launched with the internal power off, parallel altitude switches which closed at 10,000 feet applied a voltage to the relays which would turn them on and hold them on for the remainder of the flight. A Raymond Timer (Model 1060 "g" weight) was used to open the doors, turn on UCSD high voltage and extend the UNH electric field booms. The timer was activated at launch by the acceleration of the rocket.

The rocket motor consisted of a solid fuel NIKE first stage and TOMAHAWK second stage. The initial spin rate was 7-8 rps. It was necessary to reduce this to .5 rps so that the booms would not break off. This was accomplished using a "yo-yo" symmetrical despin unit which was

extended at T + 43 seconds. This unit consisted of weights on the end of cables which, when released, unwound from just below the base section.

2. Electric Field Measurements

a. Measurement Techniques. Before an electric field meter could be constructed, it was necessary to review the various requirements for making electric field measurements. The measurements were made by measuring the potential difference between probe areas extended on two opposed booms with a known constant separation. Some of the requirements and problems are listed below.

i. Due to charged particle bombardment both probes may be floating at a negative or positive potential with respect to rocket ground. There would also be a potential difference between the two probes due to the ambient electrostatic and $\bar{v} \times \bar{B}$ electric fields. In order to measure the electric field, it was necessary to measure the potential difference between the probes with no response due to a common potential the probes may share. This could be done using a differential amplifier with a high "common mode" rejection ratio (Malmstadt et al., 1963).

ii. The current collected by the probes was on the order of 10^{-5} to 10^{-7} amps. With a current this low, it was necessary to use a circuit which drew only a small current relative to the current being collected. Since field effect transistors have a high input impedance and low leakage current, they were particularly suited for this application.

iii. Symmetrical probes and identical surfaces and connections should be used since contact potentials can result in inaccuracy in the electric field measurements. These potentials would be measured the same as external potentials. For those flights, the exposed probe areas were gold plated and precautions were taken to keep the surfaces and lengths of the booms as identical as possible. The booms should also be long enough to avoid an overlap of the plasma sheath which forms about metallic objects in space. This overlap can vary the boom potential. Longer booms also reduce the amount the rocket body shields the probes from the charged particle flux, thus resulting in more symmetrical current collection.

iv. The electric field meter (as well as the other experiments) should have a signal to noise ratio, size, weight, and power consumption which is acceptable for sounding rocket use.

Most of these requirements were met in the construction and design of the electronics and booms which are discussed later in this section. Another important consideration, however, was that the electric field measured in the moving reference frame of the rocket was not only the ambient electrostatic field but the $\bar{v} \times \bar{B}$ field due to the probe motion in the magnetic field. The resultant field measured was then

$$\bar{E}' = \bar{E}_o + \bar{v} \times \bar{B} \tag{8}$$

or in terms of the electric field meter output $\Delta\phi$ (Figure 13)

$$\Delta\phi = (\bar{E}_o + \bar{v} \times \bar{B}) \cdot \bar{d} \tag{9}$$

where $\bar{d}$ is the vector distance between the midpoints of the probes. In this case, the total instantaneous potential difference of the rocket is

$$\Delta\phi = \Delta\phi_o + \Delta\phi_1 \tag{10}$$

where

$$\Delta\phi_o = Ed \cos (\bar{d},\bar{E}) \tag{11}$$

$$\Delta\phi_1 = vBd \sin (\bar{v},\bar{B}) \cos (\bar{v} \times \bar{B}, \bar{d}) \tag{12}$$

The separation $|\bar{d}| = |l_1 - l_2|$ is known from the

physical layout of the booms. This remained constant during the flight. The measured electric field was then determined by

$$\left|\bar{E}_{\alpha}\right| = \frac{\Delta\phi}{\left|\bar{d}\right|} - \frac{(\bar{v} \times \bar{B}) \cdot \bar{d}}{\left|\bar{d}\right|} \qquad (13)$$

In the auroral zone (100-130 km) the electric fields were estimated to be 10 to 100 mv/m. If $\left|\bar{d}\right|$ is 2 meters, v is 1.5 km/sec and sin $(\bar{v},\bar{B})$ is 1/2 ($\theta = 30^{\circ}$), the maximum $\Delta\phi$, due to $\bar{v} \times \bar{B} \cdot \bar{d}$ for a magnetic field of .6 gauss, would be $\approx$90 mv. From this example it is easily seen that the $\bar{v} \times \bar{B}$ field can be the same order of magnitude or greater than the ambient electric field. Due to the changing angle between $\bar{v}$ and $\bar{B}$, when firing northward, the induced voltage would be less on the downward portion of the flight than on the upward leg. The accuracy of the electric field measurement in part depended upon the accuracy of determining the $\bar{v} \times \bar{B}$ field. Since the output depends on trigonometric functions, it was desirable to have the probe system rotating to obtain both maximum and minimum outputs as well as to partially eliminate problems due to amplifier drift and contact potential error. A discussion of the current balance equation applicable here is found in Appendix A.

b. Electric Field Booms. In order to make ac-

curate electric field measurements, it was necessary to make accurate potential difference measurements between two current collection areas separated by a known distance. The region of primary interest was approximately 100 to 130 km where the auroral displays were likely to occur. Calculations of the Debye length in this region show it is on the order of 10^{-2} meters. It was desirable to have the probe area extend beyond the rocket body by at least the Debye length. If the probes were closer to the rocket body than the Debye length (λD), there would be overlap between the rocket and probe sheath which could seriously affect the current collected by the probes. The current collecting probes were actually part of a cylindrical metallic boom which served as a conductor into the payload. The booms were 55" long with the inner 54" near the payload being insulated. There were two collinear booms mounted on each payload. The separation of the midpoints of the probe area was about 114". It is easily seen that short separation distances would not be applicable for use in satellites where it is calculated that at an altitude of 50,000 km the λ_D is ~40 m.

Previous measurements (Mozer and Bruston, 1967) indicated that problems exist in measuring the vertical electric field component (parallel to the magnetic field) since a

large probe separation is difficult to achieve along the vertical rocket spin axis. Also lack of a sinusoidal spin modulation makes contact potentials and other DC effects more serious problems. In addition, present theories (Kern, 1962) indicate only small electric fields on the order of microvolts/m may be expected parallel to the magnetic field because of the high specific conductivity along the magnetic field lines. The horizontal field, however, is expected to be on the order of 10-100 mv/m and thus would be more readily measured by a rotating probe system. In this developmental stage, it was decided to measure the transverse electric field (the field perpendicular to the spin axis was measured; this is a few degrees from being parallel to the earth's surface). The technique used was to mount the booms so that they were symmetrically opposed and perpendicular to the spin axis of the rocket payload. The booms were extended at T + 60 seconds at which time the rocket altitude was ~90.5 km and the velocity was ~1.76 km/sec. The probes had to be extended simultaneously to avoid inducing precession in the payload motion which could make the rocket unstable as well as causing problems in data reduction.

The large number of experiments on the payload meant a limited amount of space was available for the booms.

Instead of using mechanical fold-out booms, it was decided to use an unfurlable type which consisted of four layers of heat treated .002" thick beryllium copper tape initially wound on a drum, and when extended, had a cylindrical cross section. The design was such that pyrotechnic squibs, ignited by the "g weight" timer and experiment batteries, would release the drums simultaneously. As the drum went outward, the boom formed behind it until the end of the tape was reached, the spools continued travelling outward and fell away. The principle of operation was somewhat like a metal carpenter's rule (Figure 14). Since the boom itself was a conductor, it was used to connect the probe area to the payload. The inner portion (54") was insulated with GC acrylic while the outer current collecting area was gold plated to insure uniform, identical surfaces. The boom diameter was .512" and was formed from a 2" wide tape. The booms were insulated from the rocket body by a nylon base unit which was mounted on the deck plates. The booms extended through the doors which were opened at T + 55 seconds. DeHavilland Aircraft of Canada constructed the boom units and did the preflight testing and computer analysis of the spin reduction and resulting forces on the booms.

c. Electric Field Electronics. The electric field meter used on these rockets was similar to the one designed

earlier by the author (Potter, 1966). The basic principle of operation was one of making a potential difference measurement between two current collection areas separated by extending them on booms. Since the collection currents were relatively small ($\sim 10^{-5}$ - 10^{-7} amps), it was necessary to use a high input impedance device to measure the potential difference without, in effect, "shorting out" the field. The meter was to have had a high enough imput impedance ($\sim 10^{8}$ - 10^{10} ohms) to measure millivolt signals while drawing only a minimal current ($\sim 10^{-10}$ amps). The requirements relevant to space flight use (size, power, weight, ability to withstand vibration) were also taken into consideration.

A measurement of this type was best done using a differential amplifier which would measure only the difference potential between the inputs and not the DC voltage level that both probes might be sharing. This was necessary because it was expected that both probes might have a nearly identical negative potential with respect to the rocket ground since the electron flux hitting them would be greater than the proton flux due to the higher thermal velocity of the electron. Two high input impedance "voltage followers" (gain of one) were constructed which would each measure the potential of a respective probe with respect to

rocket ground. The outputs of these were then fed into a NEXUS SQ-10a differential amplifier which amplified the difference potential to a $\pm$ 2.5 volt level which modulated the telemetry subcarrier channel 7 operating at 1.7kHz $\pm$ 7.5% (Figure 15).

The most critical parts of the circuit are the two input voltage followers. The input impedance of such devices as NPN and PNP transistors was too low for application in this case so it was decided to use field effect transistors (FET) for the input stage. These devices acted as current gates and thus a voltage on the "gate" controlled the current flowing between the "drain" and the "source". The current collecting area (probes) was attached directly to this gate which drew only a very small current since it was the space charge about the gate which determined the current flow between the drain and the source by effectively narrowing or broadening the current channel.

The FET chosen (2N3955) were pairs with matched characteristics and were sealed in one case. One transistor of each pair was used in each voltage follower so that in each circuit the corresponding FET's would be matched pairs (Figure 16). Other transistors in the circuit were selected by matching gains since each voltage follower had to be as nearly identical as possible since a high common

mode rejection ratio was desired. A constant current supply was used in each circuit to insure stability of operation for different supply voltages and temperatures. The voltage followers had a unity gain. The outputs of the voltage followers went into a differential amplifier with zero DC offset. This had a gain determined by the feedback and summing resistors which was changed during flight by switching in different resistors using a calibration circuit shown in Figure 17.

The output range of the circuit was plus and minus 2.5 volts with respect to rocket ground. Trimming resistors were provided in the circuit to compensate for small differences in components. One percent precision resistors were used wherever needed to insure that the circuits would be as identical as possible.

Since this was a fairly new measuring technique, different types of in-flight calibration were used on the various flights. All flights had electric field meters with two linear ranges. In the first flight the electric field meter calibration consisted of shorting the probes to determine a zero level and applying a known voltage to the inputs to determine its proper operation. The switching was done using astable and monostable multivibrators. The need for a high input impedance eliminated the possibility

of electronic switching across the input and mechanical relays were used. Another type of calibration used on later flights consisted of putting 2×10^5 ohms between the probes for a period and then applying + 3.3 volts to the probes which biased them up from their expected negative floating potential. Regulators were used on the voltage supplies for the experiment.

The testing of the meter has been described more completely elsewhere (Potter, 1966) but essentially includes temperature, common mode, power supply variation, and repeatability tests. Also measured was the input impedance and frequency response of each unit. An input impedance of 5×10^8 ohms with a frequency response linear to 30 cycles was used on the Ft. Churchill flights.

3. Magnetic Measurements

a. Experimental Techniques. To determine the existence of ionospheric currents during the flight, it was necessary to obtain information of the magnetic field magnitude and direction. To find this information, three magnetometers were flown on each payload. They consisted of a proton precession magnetometer, a transverse magnetometer(perpendicular to payload spin axis) and an axial (parallel to payload spin axis) fluxgate magnetometer.

As with the other experiments, RF filters were placed in the input-output lines wherever necessary to block RF interference. The value of these filters was clearly seen when they were omitted and the package operated with the transmitter on. In many cases, the signal to noise ratio decreased to a point where the signal would have been unusable, or the circuit started oscillating due to its high gain.

b. Proton Precession Magnetometer. The proton magnetometer was similar to the one used by Maynard (1966) and was constructed in the lab. The design was an adaptation of those of Packard and Varian (1954), Waters (1955), and Cahill (1959). By applying a polarizing magnetic field much greater (at least two orders of magnitude) than the earth's field to a container of kerosene which was rich in hydrogen nuclei, the proton spin axes became aligned along the polarizing field. If the polarizing field was then removed, the protons would precess about the earth's field, and thus induce a small AC voltage at the precession frequency in a wire coil about the container of kerosene. The magnetic field is proportional to the precession frequency as seen in the Larmor equation

$$B = \frac{2\pi F_p}{\gamma_p} \qquad (14)$$

where γ_p is the gyromagnetic ratio of nucleus and F_p is the precession frequency. The accuracy of measurement is determined by γ_p (known to two parts in 10^5) and F_p. The polarizing coil, when disconnected from the polarizing supply, was connected to the high gain preamp and main amp and used as a pickup coil. To obtain complete alignment with the field, the polarize cycle must necessarily be longer than the relaxation time; thus, the polarize cycle lasted approximately 0.8 seconds. The kerosene relaxation time was about 0.7 seconds compared to a two second relaxation time for water. Water could be used; however, the rate of taking measurements would be decreased by a factor of 3.

The coil output has been written by Cahill and Van Allen (1956) as:

$$V = 4\pi\gamma_p \, KNAB_e \, XB_o . \sin^2\theta . e^{-t/T} \sin(\gamma_p B_e t) . 10^{-8} \text{ volts} \quad (15)$$

where

γ_p = gyromagnetic ratio of the proton
($2.67513 \pm .0002 \times 10^4$ radians/sec.-gauss, Driscoll and Bender, 1958)

X = paramagnetic susceptibility of the protons

K = geometric factor

A = cross section of sample

N = number of turns

B_o = polarizing field

t = time in seconds

T = transverse relaxation time

θ = angle between earth's field and coil axis

B_e = earth's field

Due to the $\sin^2\theta$ dependence, there was no signal when the coil axis was parallel to the magnetic field. For this reason the coil axis on the payload was placed perpendicular to the payload spin axis since the magnetic field at Ft. Churchill was expected to make only a small angle with the spin axis.

There were essentially three basic circuits comprising the magnetometer electronics. An astable multivibrator was used to switch the sensor coil to the polarizing batteries and alternately to the high gain preamp and main amp. Due to the high (4 amp) current used during the polarize cycle, relays which could withstand a maximum of 5 amps were chosen. During the polarize cycle, no data could be obtained since the amplifier was disconnected from the coil.

The preamp had a gain of about 3000 and amplified the signal to about 10 mv. It was a tuned amplifier with low noise RCA 2N220 germanium transistors. There were three basic stages, the first being a tuned, transformer

coupled amplifier. The second stage was an untuned voltage amplifier and the third was used for low output impedance and isolation of previous stages from possible loading effects (Figure 20).

The main amplifier consisted of four stages with a resulting ±2.5 volt clipped output signal (Figure 21) which modulated the 124 kHz subcarrier oscillator (Figure 22). The first two stages were voltage amplifiers, the second of which clipped the signal to decrease the effect of noise. The third stage was used for impedance matching into the fourth stage bandpass filter and another voltage follower. A detailed description of the circuit is found in the report by Maynard (1966). The magnetometers for the Ft. Churchill flights had a center frequency of 2460 Hertz with a bandpass filter width of ± 160 Hertz. The signal to noise ratio was better than 3:1. Each unit had to be tuned separately due to slight variations in the transistors and components. The tuning had to be done keeping in mind the locale at which the magnetometer was used and the magnetic fields expected there. The preamplifier and main amplifier were put into separate boxes to reduce the possibility of oscillation.

With the coil attached, the preamp was tuned by wrapping a single turn of wire about the sensor coil and

driving this with a variable frequency oscillator. Using this induced frequency, the filters were tuned by adjusting the proper components. The main amp was similarly tuned with a 10 mv audio oscillator signal on the input. When the units were connected together, further fine tuning was done by inducing a weak signal in the sensor coil.

In locations where the field results in a frequency outside the bandpass, the magnetometers could not be tested except in a coil system like that at the University of New Hampshire. At Ft. Churchill, the field was such that the signal could be seen on the ground provided that the sensor coil was taken away from all buildings and power lines. Correct operation was quickly determined by placing a steel wrench near the coil. If the unit operated correctly, the gradient from the wrench would destroy the signal. No in-flight calibration was needed since the frequency is determined only by the magnetic field and the γ_p nuclear constant.

The proton coil assembly consisted of 700 turns of #16 copper wire wrapped on a phenolic cylinder in which a polyethylene bottle containing kerosene was rigidly held. The coil was covered with a flexible printed circuit board with strips etched away. The strips were connected at one end and provided an electrostatic shield to reduce noise pickup without creating conductive loops which would destroy

any signal. The coil was put on its side and foamed into a larger phenolic cylinder which was then mounted so that the coil axis was perpendicular to the spin axis of the payload (Figure 23).

c. Axial Fluxgate Magnetometer. It was desirable to measure one component of the vector magnetic field since the other components could then be found using the information from the proton precession magnetometer and the transverse fluxgate magnetometer. A high sensitivity measurement was desired. This was difficult, however, since the field to be measured was a resultant vector field consisting of the earth's field of about 60,000γ and a smaller field due to the electrojet current (if present) on the order of 100 to 5000γ. The problem, then, was to measure accurately a field of 55,000γ to 64,000γ with an instrument with a range of $\pm$2500γ.

The problem was resolved by Mr. Shadrack Ifedili who mounted the axial sensor in a phenolic cylinder and wound a coil over it so that the sensor was inside the solenoid. Different currents were applied to the coil by means of a 7 stage ring counter triggered by an astable multivibrator (Figure 27). The ring counter (Figure 28) controlled a precision constant current supply which applied 7 different currents to the coil every second (Figure 29).

The changing currents resulted in changing magnetic fields of known levels at the sensor. These levels were determined by calibration at the UNH Magnetic Observatory Coil Facility.

When operating, the fluxgate would be in saturation on all but one or two of the steps. The applied bucking field on each current step was known to within $\pm 50\gamma$. The position on the staircase generated was determined by putting the programmed steps through a voltage divider and into the .56 kHz subcarrier oscillator. The programming circuits were put on printed circuit boards and mounted and foamed in a brass box. The currents needed to produce the required "bucking" fields were calculated first and fine adjustments were made during the calibration procedure.

d. Transverse Fluxgate Magnetometer. The magnetometer used in this case was a Schonstedt Model MND-5C-25 Magnetic Null Sensor which is a monaxial fluxgate with a range of $\pm 2500\gamma$. The sensor cylinder was mounted with its axis perpendicular to the rocket spin axis. In this configuration, it was used primarily to get an accurate phase angle of $B_\perp$ during the spin cycle and secondarily to obtain an accurate spin rate of the payload. A high sensitivity instrument was used since it would go into saturation and provide a fairly sharp square wave output from

which the spin rate and zero crossing could be precisely determined. The same model was used for the axial field measurement. It had a 0 to + 5 volt output determined from the equation

$$E = 2.50 - .001K\ H \cos \varphi \qquad (16)$$

where H is the ambient field in millioersteds, K is the sensitivity (100 millivolts per millioersted), φ is the angle between the field and the positive sensor axis, and E is the voltage output. From this equation we see that when $\varphi = 90^{o}$ or 270^{o}, the output will be 2.50 volts which corresponds to the center crossing of the square wave. With this information, we could determine when the magnetic field made a right angle with the sensor axis. The instrument was used as delivered from the supplier with no modifications made. The sensor cylinder was mounted parallel to a deck plate in a phenolic block with the electronics and the axial magnetometer on the same deck.

4. Auroral Photometers

Mr. Larry Choy constructed two auroral photometers which recorded the intensity of atomic oxygen lines 5577 $\mathring{A}$ and 6300 $\mathring{A}$. The data from these was used in conjunction with ground all sky cameras and photometers to locate the auroral displays with respect to the rocket location at any

particular time and to find their intensity. The expected light intensity range is from about 10R to 100 KR (Chamberlain, 1961).

The photomultiplier tubes used were RCA 8571 ruggedized 9 stage side window tubes which were mounted vertically below a Components Corporation Model 60-H DC-DC converter. The voltage distribution on the resistor chain was 0.1 HV (High Voltage) between dynode stages with the anode near ground and the photocathode at -HV which was -1000 volts. This was done to keep the signal near ground, thus requiring no HV decoupling and also reducing the HV noise and ripple pickup by the anode. To prevent the high voltage supply from interfering with the proton magnetometer, both the tube and supply were surrounded with a Mu metal and grounded copper shield. This also prevented disturbance of the photoelectrons in the tube from external magnetic or electric fields. The output current at the anode was proportional to the light intensity at the photocathode when the dynode voltages were held constant. To prevent arcing, the photomultiplier tube and high voltage supply were enclosed in a sealed container with a second order interference filter acting as a window. The two systems were identical except for the filters which had 90 $\mathring{A}$ bandwidths at 5577 $\mathring{A}$ and 6300 $\mathring{A}$. The "look" angle of the tubes was 7.35×10^{-2}

steradians. This was possible by using collimating tubes before the filters.

The telemetry input was restricted from 0 to 5 volts; thus, a logarithmic amplifier was chosen since the light intensity range covered over four decades. A linear amplifier would necessarily provide low resolution at low intensity levels and thus was not acceptable. Due to a restricted door length, only the photomultipliers were mounted looking out opposite doors. The electronics were located on another deck and connected via the wiring channel (Figure 8).

Since the photomultiplier had a high gain, it was not necessary to build a circuit with a high gain although it did have to have a logarithmic response for reasons mentioned earlier. These criteria along with those pertaining to small size and ability to withstand shock were met by feeding the output into the negative input of a NEXUS SQ-10a amplifier with a transconducting feedback element (Philbrick PPLIP) which resulted in a logarithmic output for a linear input. To match this output to the telemetry requirements, a linear NEXUS SQ-10a amplifier with a gain of 20 was added. The output voltage was proportional to the log of the input current. Allowance for a dark current offset voltage was made by summing a voltage into the final amplification stage (Figure 30). Resistor-capacitor networks

were added when needed to suppress oscillations at low currents.

The amplifiers were constructed on printed circuit boards and put into brass boxes. All inputs and outputs to the circuits had RF filters in series to prevent transmitter interference. These filters were placed in small boxes constructed inside the main packages and were constructed by wrapping three turns of #20 wire around 10μf ceramic capacitors. These were tuned to the transmitter frequency by using a "grid dip" meter and adjusting the spacing of the turns.

Calibration of the photometers was performed in a light tight box in which the sealed unit was placed. A General Electric certified standard candlepower lamp was obtained and used with neutral density filters to calibrate the instruments over the expected range of operation. Temperature tests were made and the electronics sealed in a foam before flight. Each unit had a small lamp in its window which was operated by an astable multivibrator and voltage regulator. The gaussian shaped light pulse provided relative in flight calibration and enabled one to quickly check for proper operation of the units. A block diagram of this measurement technique is shown in Figure 31.

5. Solid State Particle Detector

Dr. Roger Arnoldy from the University of New Hampshire flew a solid state charged particle detector on the 18.38-18.42 auroral flights described in this paper. The detector pointed 45^{o} upward with respect to the spin axis. Incoming particles were collimated using brass slits. The detector had a geometric factor of 10^{-2} steradians-cm^2 and was a 500 micron thick surface barrier solid state counter (Arnoldy, 1968). Since the detector was light sensitive, a 5000 $\mathring{A}$ nickel light shield was used over the counter to eliminate problems if the rocket flew beyond the shadow height and entered the sunlit region.

There were two integral energy thresholds for the experiment. The first was at 85 kev for electrons and 330 kev for protons. The second threshold was at 300 kev for electrons and 630 kev for protons. A block diagram (Figure 33) shows the electronic components used in the circuit. Counts from the detector were telemetered analog using a nonlinear rate meter. Using this output it was possible to read individual counts up to 100,000 counts per second. The continuous read out of data enables one to study time variations of particle fluxes limited only by the bandwidth of the subcarrier oscillator.

6. Curved Plate Particle Detectors

Two graduate students, Anil Davé and Steve Rearwin, working under Dr. C. E. McIlwain at UCSD in LaJolla, California, had two self-contained charged particle experiments on these flights. Their objective was to obtain a differential energy spectra of auroral electrons from 1-30 kev and protons from 10-40 kev, and also to record the various pitch angles. The primary requirements were:

i. Time resolution consistent with flux variations due to spatial, temporal and rotational effects.

ii. Sensitivity to low energy electrons and protons.

iii. Minimum of atmospheric contamination and pressure effects.

iv. Provision to obtain continuous differential energy spectra.

v. Acceptable size, weight and power requirements.

The electron experiment had two identical detectors, one pointed perpendicular and one pointed upward at 45^{o} to the spin axis. Each pair consisted of two 90^{o} cylindrical curved plate electrostatic analyzers. A complete differential energy spectra was obtained by applying a linear sweep voltage to 5 kev on each analyzer. Each analyzer had a channel electron multiplier for a detector (Channeltron). The pulses from the detectors were amplified by a charge sensitive amplifier. These were used to drive a multiscalar

which transformed the data into a form which could be telemetered.

The proton detector system was similar in that it also used curved plate analyzers and Channeltrons. The pulses were put into a charge sensitive preamp and scaled prior to pulse height encoding.

Lab calibrations were done with electron beams from an electron gun, proton beams from an accelerator, and a calibrated Ni^{63} beta source.

7. Payload Telemetry

Since 20 subcarrier oscillators were needed, it was decided to use the microminiature model (MMO-11), made by Vector, Division of United Aircraft Corporation. The "postage stamp" size allowed all 20 channels plus the mixer amplifier (MMA-11) to be mounted in the antenna section with the Vector 5-Watt TR-1125 crystal controlled FM transmitter. This was convenient since all telemetry inputs could be introduced into the antenna section via a 27 pin Cannon plug. This easily allowed the base section to be removed when necessary.

The mount for the subcarrier oscillators was made and wired at UNH and provided good service. The channels used were the standard $\pm$7.5% IRIG channels 1 through 20.

All channels had 0-5 volt inputs except for 6 and 20 which had ±2.5 volt inputs. The stability of the subcarrier oscillators was such that a change in supply voltage of ±10% would vary the center frequency less than ±0.5% of the designed bandwidth at temperatures from -20° to +80° C. The drift was less than ±0.25% of the design bandwidth.

The voltage output from each experiment was fed directly into a subcarrier oscillator. The outputs were then summed through 1/8 watt resistors in the mixer amplifier whose single output was applied to the transmitter. The transmitter was connected to the standard NIKE-TOMAHAWK antenna section which consisted of four tuned cavity antennas. The values of the summing resistors and the overall performance of the telemetry system were checked at the Beltsville Sounding Rocket Branch at Beltsville, Maryland. Final telemetry checks were performed at Ft. Churchill with the rocket on the launcher in horizontal and vertical positions.

The FM signal was received by the Ft. Churchill ground primary and backup telemetry stations and the video (subcarrier) signal recorded on magnetic tape along with the voice network, 100 kHz standard signal and 2 pps, 100pps timing signals. The ground station also provided "quick look" paper charts of the flight which showed the performance

of each channel during the 8 minute flight.

8. Payload Power

Due to the high current requirements of the proton magnetometer (4 amp) and the telemetry (1 amp) it was decided to have two battery packs. The package for the telemetry and proton magnetometer used Yardney HR3-NM non-magnetic silver cells (Figure 34). The other battery pack was used to power the remaining experiments and was made with HR 1.5-NM silver cells. During ground tests and preflight horizontal and vertical tests, it was occasionally desirable to be able to trickle charge the battery packs. This was accomplished using an external control box with built-in trickle chargers. An ammeter monitored the direction of current flow, and diodes were placed in the lines to prevent discharging the batteries through the control box.

On some experiments it was desirable to regulate the voltage to a certain DC level. On several of the experiments this was done using a simple, one transistor regulator shown in Figure 35.

9. Payload Testing

Several types of tests were performed on the total

payload and its individual packages. As previously mentioned, electrical operation tests on the packages were first performed on the bench to determine its performance. Such things as temperature testing, magnetic testing, and shock testing showed deficiencies in the circuits and packaging which had to be corrected. The next step was to place all of the packages in the payload frame which had previously been checked for correct wiring. In this configuration, the packages had to operate properly when the other packages and telemetry were turned on. Several integration meetings were held with UCSD to enable the experimenters to determine the operation of the packages through the telemetry. Further checks were conducted at Ft. Churchill while the final preparations were taking place and while the rocket was on the launcher.

Before the payloads were shipped to Ft. Churchill, they were taken to Beltsville Sounding Rocket Branch where a testing and evaluation period was held. The first payload (18.38) was put through complete vibration, shock, spin, moment of inertia, and electronic tests at Goddard Space Flight Center. The doors were tested during a simulated countdown where the timer was activated and the doors blown off.

It was also necessary to determine the magnetic

field of the payload itself since the proton magnetometer was very sensitive to any gradients across the sensor coil. The packages and complete payloads were tested at the UNH zero field lab where a Fanselau coil system cancelled out the earth's field and established a zero field to within one gamma. The payload was then placed on a cart which was drawn under a three-axis fluxgate magnetometer. The three components of the payload field were recorded with a light beam oscillograph (Figure 36). The amount of deflection indicated the magnetic properties of the package.

SECTION IV

ANALYSIS OF DATA AND DISCUSSION OF ERRORS

1. Telemetry

In an experimental package utilizing a telemetry system, it is necessary to consider errors in data transmission when discussing the experiments. One of the criteria in choosing a telemetry system was high accuracy and low drift rates. The system chosen (Vector) specified a frequency change of less than $\pm.05$ % of the center frequency for power supply variations of $\pm 10\%$ of the specified voltage and a temperature range of $-20^{o}C$ to $+80^{o}C$. The maximun expected drift was less than $\pm.25\%$ of the design bandwidth.

2. Proton Precession Magnetometer

The field magnitude obtained from the proton precession magnetometer contains several possible errors: the payload magnetic field, a contribution to the measured precession frequency due to the rocket spin, and errors in the measurement of the frequency ($f = B\gamma_p/2\pi$).

The payload field at the sensor location was measured before flight and was less than 3γ; $\sim 2\gamma$ along the

spin axis and $\sim 1\gamma$ perpendicular to the spin axis. The perpendicular component would contribute negligibly ($< 1\ \gamma$) to the magnitude of a 55,000γ vertical field. The axial component contributed a relatively steady addition of $\sim +\ 2\gamma$ to the magnitude. The rocket spin (UNH 68-5) was .64 rps and was equivalent to $\sim 15\gamma$, again a steady contribution throughout the flight. Since one was interested in relative changes in the field magnitude these first two contributions, provided they are constant throughout the flight, need not be considered further.

Errors in each individual frequency measurement are equivalent to errors in the field magnitude measurement (1 Hz $\approx 23\gamma$). To achieve measurement accuracy approaching $\pm\ 1\gamma$, frequency determinations to better than $\pm$0.1 Hz are necessary (.004% of 2,500Hz). The frequency was determined by measuring the number of cycles of a 100 kHz reference signal in a fixed number of precession signal cycles (Figure 37). The standard was stable to 1 part in 10^6 (.0001%) and an individual period measurement was precise to $\pm$1 cycle of the reference signal. Since 50,000 cycles of the reference signal were typically counted in each period measurement, individual measurements could be expected to show fluctuations of $\pm$.002% (1/50000) or $\pm\ 1\ \gamma$. The determination of the frequency of each proton signal was done 10 times

with a typical standard deviation (measured) of 12γ.

The relative error in individual field magnitude ($|\bar{B}| = 2\pi f/\gamma_p$) may be summarized:

$$\delta|B|_{MAX} = \frac{\partial|\bar{B}|}{\partial\gamma_p}\delta\gamma_p + \frac{\partial|\bar{B}|}{\partial f}\delta f$$

$$= \frac{2\pi f}{\gamma_p^2}\delta\gamma_p + \frac{2\pi}{\gamma_p}\delta f$$

$$= \frac{(1.5 \times 10^4)(2 \times 10^{-4})}{6.7 \times 10^8} + (2.3 \times 10^{-4})(.1)$$

$$= 4.4 \times 10^{-4}\gamma + 2.3\gamma \approx 2.3\gamma \qquad (17)$$

The error is reduced (if random) by averaging 10 times:

$$\delta|\bar{B}| = \frac{\delta|\bar{B}|_{MAX}}{\sqrt{10}} = .75\gamma \qquad (18)$$

Of course this calculation is for ideal conditions. Factors such as poor signal to noise ratios and faulty operation of the period measuring equipment raise the error of some measurements.

3. Electric Field Meter

The reduction of the electric field data involved many steps. The electric field measured was the component transverse to the rocket spin axis and although the rocket was nearly vertical at launch, the horizontal component will

be slightly different ($E \cos 15^{\circ} = E\ (.97)$). To obtain the transverse electric field, the output voltage (a sinusoidal variation) of the electric field meter $\Delta\varphi$ ($E_T = \Delta\varphi/d = (\bar{E} + \bar{v} \times \bar{B}) \cdot \bar{d}/|\bar{d}|$) was divided by the distance between the midpoints of the probes (d). This was transcribed to a computer magnetic tape along with the computed trajectory, magnetic field (using Jensen and Cain, 1962 field), azimuth (angle between spin axis and magnetic field) and aspect (angle between axis of transverse magnetometer and projection of magnetic field in plane perpendicular to rocket spin axis). The information on the angles was obtained from the transverse magnetometer, axial magnetometer, and information supplied by the Ft. Churchill Research Range.

Using these data, the computer was used to calculate $\bar{v} \times \bar{B} \cdot \bar{d}/|\bar{d}|$ which was subtracted from the total electric field ($\Delta\varphi/d$). The $\bar{v} \times \bar{B}$ field was subtracted since it was induced by the rocket motion in a magnetic field and was not part of the ambient field we wanted to measure. The period of rotation (UNH 68-5) was 1.56 seconds, thus a measurement of the transverse field was made every .78 seconds (for each maximum and minimum of the sinusoid). Data was read off the telemetry chart 32 times per second of flight time.

The final value of the electric field was dependent

on the accuracy of the original data ($\Delta\varphi/d$) and also on the accuracy of the calculated induced $\bar{v} \times \bar{B}$ field which must be subtracted from the original data. Errors in the total field were estimated to include $\pm$ .5 mv from chart reading errors, $\pm$ 4 mv from data transmission errors (sub-carrier drift, noise) and $\pm$ 1 mv due to calibration errors. These errors total 5.5 mv while the error in measuring d was estimated at $\pm$ .01 m. The resultant error in the total field (E) was:

$$\delta|E|_{MAX} = \frac{\partial E}{\partial \Delta\varphi}\,\delta\Delta\varphi + \frac{\partial E}{\partial d}\,\delta d$$

$$= \frac{\delta\Delta\varphi}{d} + \frac{\Delta\varphi}{d^2}\,\delta d$$

$$= 1.9 \text{ mv/m} + .1 \text{ mv/m}$$

$$= 2 \text{ mv/m} \qquad (19)$$

The errors in the $\bar{v} \times \bar{B}$ field were variable depending on the time during the flight. Comparing the digital record of rocket velocity derived from radar data with that calculated by computer, it was seen that the maximum error in velocity may occur near apogee. The error (in the magnitude of the velocity) was calculated to be less than $\pm$ 3% of the

velocity at that point. Near the start and finish of the flight, the error was less than $\pm$ .6%.

The magnetic field magnitude used in the calculation of $\bar{v} \times \bar{B}$ was from a spherical harmonic analysis of the earth's magnetic field done by Jensen and Cain (1962). The difference between the measured and calculated field amounted to .5% of the calculated magnetic field on the upward leg and 1.8% on the downward leg.

Several angles have been used in computing the induced field. The aspect angle was known to within $\pm 3^{o}$ while the maximum error expected in the azimuth angle as determined by the axial fluxgate was $\pm 5^{o}$. Figure 38 shows that the magnitude of $\bar{v} \times \bar{B}$ was nearly as large as the ambient field near the start and finish of the flight while Figure 39 shows the difference in phase and magnitude between the total electric field and the induced field. The resultant field was calculated in a geographic reference frame based on geographic North, East and the vertical (positive downwards) at the launch site. The induced field errors are summarized (using typical parameter values):

$$E_i = |v| \, |B| \sin\theta \cos\alpha$$

$$\delta \left| E_i \right|_{MAX} = \frac{\partial E}{\partial v} \delta v + \frac{\partial E}{\partial B} \delta B + \frac{\partial E}{\partial \theta} \delta\theta + \frac{\partial E}{\partial \alpha} \delta\alpha$$

$$= B \sin\theta \cos\alpha \, \delta v + v \sin\theta \cos\alpha \, \delta B + vB \cos\theta \cos\alpha \, \delta\theta + vB \sin\theta \sin\alpha \, \delta\alpha$$

(Note: $\sin\theta$, $\cos\theta$, $\sin\alpha$, $\cos\alpha \leq 1$; $|\sin\theta \cos\alpha|_{avg} \approx .5$)

Using $B = 55{,}000\ \gamma$ and $v = 1$ km/sec we find

$$\delta |E_i|_{MAX} = 1.0 \text{ mv/m} + .5 \text{ mv/m} + 2.2 \text{ mv/m} + 1.3 \text{ mv/m}$$

$$= 5 \text{ mv/m} \qquad (20)$$

When this error is added to the total field error, we find the maximum error was 7 mv/m. For a typical field of 55 mv/m this represented an error of ~ 13%.

4. Axial Fluxgate Magnetometer

The errors in the axial fluxgate magnetometer measurements were estimated to include a $\pm$ 50 γ uncertainty in the calibration of the bucking steps, $\pm$ 15 γ from data transmission errors, $\pm$ 15 γ from reading values off the telemetry record and $\pm$ 25 γ due to the magnetic field of the payload. The maximum error would be the sum of these or $\pm$ 105 γ while the most probable error is $\pm$ 60 γ. This is equivalent to an error of $\pm$ .12% of the axial field.

5. Photometers

The photometer experiment was prepared with the

intention of relating the rocket position to the visible aurora with less emphasis placed on absolute intensity measurements. The error bars shown on the photometer data are indications of the possible DC shift on the index scale because of the uncertainty in calibration (these errors were larger than others). Due to the logarithmic response of the circuit and the uncertainty in the calibration procedures, the estimate of error in the data on the Rayleigh scale is $\pm$ 20%. The error on the KiloRayleigh scale is near $\pm$ 10% (The scales referred to are the "index" scales shown in the figures).

6. Solid State Particle Detectors

One second averages were taken when reducing the solid state charged particle detector data. It is estimated that telemetry noise, which could be misinterpreted as counts, contributed the largest error ($\pm$ 100 particles/cm^2- sec-steradian). Since counts from the detector were telemetered analog using a nonlinear rate meter, it was possible to read individual counts up to 100,000 counts per second. The use of a 5000 Å nickel light shield over the detector eliminated the possibility of spurious counts caused by sunlight if the rocket flew beyond the earth's shadow.

SECTION V

EXPERIMENTAL RESULTS

1. Flight UNH 68-1

The first of five rockets (NASA flight number 18.38) was launched February 5, 1968 at 0506:58 UT (53 minutes before local midnight) from Ft. Churchill Research Range, Manitoba, Canada. The flight azimuth was 49° east of north (Figure 40) and the launch elevation was 85.7°. Peak altitude was at 256.5 km (estimated values, no radar data available) and the total time of flight was 487 seconds (observed from telemetry) (Figure 41). The rocket had a 29 second spin period after despin.

The rocket was fired during a magnetically quiet period when no measurable activity was recorded by the Ft. Churchill ground station fluxgate magnetometers (Figure 42). The 30 mHz riometer showed almost no change in the absorption of cosmic noise and no visible auroral displays were recorded by the ground based "all sky" cameras. Magnetograms from other nearby stations also showed little magnetic activity. This rocket was fired during a quiet time period in order to check the operation of the experiments and also to provide reference measurements which could be compared

with results obtained from later flights launched during periods of auroral activity.

The total scalar magnetic field was measured with the proton precession magnetometer and is shown in Figure 43. The lack of variations in the field indicate that no auroral electrojet current was present. The Jensen and Cain (1962) spherical harmonic analysis of the earth's field (calculated along the trajectory) has also been plotted on this graph and shows reasonable agreement (exact agreement would indicate that the Jensen and Cain field was a precise representation of the field along the trajectory). The magnetic field obtained on the upward leg of the flight is considered to be the quiet time reference field for this series. The downward leg results are less reliable since no radar trajectory was available.

The calibration sequence of an electric field meter flown on this rocket indicated that the instrument was working properly. The output showed a 29 second modulation due to the induced $\bar{v} \times \bar{B}$ field caused by the rocket motion. The results of this experiment, after subtracting $\bar{v} \times \bar{B}$, indicate a quiet time electric field of up to 20 mv/m may have existed during the flight. The field direction has not been determined at this time. The $\bar{v} \times \bar{B}$ field was approximately the same as that shown in Figure 38. Noise of an unexplained origin was seen as spikes on the telemetry record throughout

the flight. This noise was not present during the other flights.

One photometer responsive to 5577Å was flown on UNH 68-1. The light intensity recorded was below 5 Rayleighs thus confirming the lack of auroral activity seen on the all-sky photographs.

The axial fluxgate output indicated the instrument was in saturation throughout the flight, thus, no usable data was obtained. There was no solid state charged particle detector on this first payload.

2. Flight UNH 68-2

This rocket (NASA 18.41) was launched on April 23, 1968. The time of launch was 0452:38 UT, 68 minutes before local midnight. The flight azimuth was 20° east of north with an initial elevation of 86° (Figure 40). The total time of flight was 500 seconds with a 258 km apogee at 255 seconds. (Figure 44). The spin period, after despin, was 1.37 seconds.

The Churchill ground station magnetograms showed a negative magnetic disturbance which followed a larger negative bay that occurred approximately one hour before launch (Figure 45). The X (north) component was -170γ and the Y (east) component -280γ. The Z (vertical component) at

launch was -73γ but became positive about one minute after launch. This suggests that the associated electrojet current moved overhead to the south at this time. The vertical disturbance near the end of the flight was fairly constant near +60γ. Ground station magnetograms from six neighboring stations confirmed a westward flowing current system. The 30 mHz riometer measured ~1 db absorption at the time of launch and this remained fairly constant throughout the flight. This gave some indication that a steady precipitation of charged particles into the ionosphere was taking place.

The two photometers on the payload were mounted perpendicular to the spin axis and were responsive to 5577Å and 6300Å light. The photometer records 5577Å and 6300Å are plotted in Figures 46, 47, 48, and 49. The I_R and I_{KR} indices were proportional (nearly one to one) to the light intensity in Rayleighs and KiloRayleighs respectively. Both the maximum and minimum signals for each rotation have been plotted. Equal signals on the maximum and minimum traces indicate that the payload was immersed in the visible aurora.

An increase in the minimum intensity of 6300Å and 5577Å near 100 km is not accompanied by an increase on the plots of maximum light intensity. This indicates that the

rocket was not immersed in a visual auroral display but rather went to one side of it. The fact that the intensity of 5577Å (minimum) was nearly the same on both the upward and downward legs is an indication that the aurora was stable in the flight interval as confirmed by visual observation from the ground. The increase near apogee shown in Figures 46, 48 may be due to the sunlight as the rocket passed above the shadow of the earth. No explanation has been found at this time for the spikes seen in Figure 49. The ground station all sky camera was not adjusted properly and the resulting photographs of the visible aurora were out of focus and were not reproduced here. At the time of launch a bright band was visible overhead. It extended in the northwest-southeast direction and remained stable during the first half of the flight. This band gradually faded near the time of rocket apogee and was replaced by a diffuse aurora which covered much of the sky for the remainder of the flight.

In summary, the rocket UNH 68-2 was fired during a stable visible auroral display. The photometers on the rocket indicated the rocket flew to the northeast side of the display on both the upward and downward legs of the flight. A negative magnetic bay of -327γ existed at the time of flight with a negative vertical component. About

1 db absorption was measured on the 30 mHz riometer during the flight. Ground based magnetometers at six nearby stations recorded magnetic disturbances which indicated a westward flowing electrojet current may have caused the disturbances.

The scalar magnetic field measured by the UNH 68-2 proton precession magnetometer is shown in Figure 50. Although it was a period of moderate magnetic activity the field record shown no unusual disturbance other than a slight positive bulge of ~90γ on the upward leg near 140 km. This bulge is seen in detail on the difference field plot shown in Figure 51. If the bulge is assumed to be a spatial variation due to an electrojet, one can calculate the magnitude of a current which could cause this disturbance. Rough calculations indicate a current of $\sim 10^4$ amps at a distance of 22 km to the southwest of the rocket and flowing towards the northwest could have caused this bump. The altitude of the current would have to be near 140 km. There is a possibility that this current was aligned with the visible auroral band described earlier.

The fact that the difference field at the beginning of the upward leg is slightly negative may have been caused by the rocket flying over a line current north of Churchill.

In addition to the negative difference, there is a

broad peak at 150 km. This could result from passing over the current as the rocket moved northeast. The magnitude of the difference at 100 km (~ -200 gammas) is consistent with a line current 50 km northeast of the rocket at that time and also in approximate agreement with the ground level field (-100γ). Although this discussion provides a simple model to explain the measurements, it is not unique. The discussion of flight UNH 68-5 includes some possible errors which may have affected the difference field calculations for these flights.

The maximum electric field transverse to the rocket spin axis is plotted as a function of altitude in Figures 52, 53. Figure 52 shows the field measured on the upward leg of the flight after the induced $\bar{v} \times \bar{B}$ field has been subtracted. The average field value was near 40 mv/m although near 100 km it reached a maximum value of 70 mv/m. At higher altitudes the field magnitude decreased to a minimum near 150 km (nearly the same height as the proposed electrojet). The field then increased to 40 mv/m although it dropped to 25-30 mv/m at 200, 215, 225, and 232 km on the upward leg. In general there appears to be little significant altitude variation in the electric field.

The electric field measured on the downward leg was slightly higher and averaged 45-50 mv/m. Slight increases

in the field occurred near 240 and 210 km. The last increase was preceded by a decrease in the field to 30 mv/m at 220 km. A broader maximum occurred at 150 km (66 mv/m) on the downward leg. This variation occurs in the same altitude region as the visible aurora and the proposed electrojet currents. From the data obtained it is difficult to determine if the variations were primarily spatial or temporal. The field direction pointed towards the southwest quadrant throughout the flight except for a brief period near apogee when it pointed towards the southeast quadrant.

The particle fluxes during flight UNH 68-2 are plotted in Figure 54 as a function of altitude and flight time. The particle fluxes (electrons > 97 kev, protons > 272 kev) were quite steady (near 1500 particles/cm^2-sec-sterad) with the exception of the large flux seen just after apogee. No significant changes on the ground based magnetometers or riometer were seen at this time. The riometer remained steady showing ~1 db absorption indicating a steady precipitation of charged particles into the ionosphere was taking place. This is in agreement with the particle data shown here. The particle flux was slightly less on the downward leg of the flight when the magnetic disturbance was also decreasing and when the visible aurora was fading and becoming more diffuse.

The axial fluxgate magnetometer results for flight 18.41 are shown in Figure 55 . A portion of the data was missing where the axial field magnitude is thought to have gone below the range of the instrument. This field was used with the measured total scalar field to calculate ψ, the angle between the rocket spin axis and the magnetic field vector (Figure 56). The variations in ψ are very similar to those of UNH 68-5 (NASA 18.39) with the maximum and minimum falling at approximately the same times. No explanation for a change of this magnitude is evident although we did obtain upper and lower limits for ψ from this data. Considering the similarity of starting values of ψ and the subsequent variations we concluded that this was not due to rocket precession. It is interesting to note that ψ, obtained by an independent method on UNH 68-3 (NASA 18.42), varied in a similar manner.

3. Flight UNH 68-3

Rocket UNH 68-3 (NASA 18.42) was launched on April 25, 1968 at 0623:57 UT (23 minutes past local midnight). The flight azimuth was 39.5^{o} east of north (Figure 40). The initial elevation was 86.2^{o} and apogee was at 267 km. The time of apogee was 261 seconds and the total flight time was 511 seconds (Figure 57). The final spin period was 1.22 seconds.

The magnetic conditions at the time of launch are shown on the Ft. Churchill magnetograms in Figure 58 . The X (north) component shows a -195γ depression while the Y (east) component shows -268γ. The Z (vertical) component was initially near zero and then dropped to -110γ. The total horizontal disturbance was -332γ. A negative bay began ~43 minutes before launch and returned to normal 16 minutes before launch. Another negative bay began 3 minutes before launch and returned to normal 28 minutes after launch. Magnetograms from other nearby stations indicated a westward flowing current system existed although it was much more localized to the Churchill area than the current system during flight UNH 68-2. The 30 mHz riometer at Churchill recorded the greatest absorption of cosmic noise (~1 db) after the rocket had reached its peak altitude.

All sky cameras were used to record the visual aurora on photographs taken during the flight. The rocket position at 100 km altitude is shown by the dot on the upper photo in Figure 59 . This was taken during the upward leg. The lower photo and dot indicate the rocket position at 100 km on the downward leg of the flight.

A bright aurora was visible overhead during the first part of the flight. Many quickly moving rays projected down from the zenith indicating we were "looking up" the magnetic

field line upon which charged particles were spiralling into the ionosphere. This activity continued until the rocket approached ~175 km on the downward leg. By that time much of the visible aurora had faded with the exception of some diffuse patches at scattered spots. A series of photos taken during the flight is shown above the particle data (Figure 68).

The 5577Å and 6300Å photometer data is plotted in Figures 60, 61, 62, and 63. The auroral forms were changing rapidly during the flight and were interpreted in general terms. One feature is the wide increase centered near a point equal to half the apogee altitude. This indicates that the visible aurora was occurring at higher altitudes and was spread out over a wider altitude range since the peaks are broad. It is not known whether the rocket actually penetrated the aurora or went through a "hole" in it as seems to be the case when one studies the upper photograph in Figure 59.

From this data we conclude that the rocket was fired during a period of moderate magnetic activity accompanied by a very active aurora which was present during most of the flight. Nearby ground station magnetograms indicated the westward flowing current system was much more localized than on previous occasions. The rocket photometers results

indicated the rocket passed through or near the aurora on the upward leg and were in general agreement with the all sky camera photographs.

The results of the proton magnetometer experiment are shown in Figure 64. The total scalar magnetic field is plotted versus payload altitude. A bulge on the upward leg near 100 km indicates the existence of an electrojet current south of the rocket. This becomes more pronounced when the difference field is calculated by subtracting the 18.38 reference field (Figure 65). The bump was centered at 105 km and had a magnitude of ~300γ. If we assume that this was a spatial variation due to the rocket passing by a line electrojet we can calculate the current required to produce this disturbance. Simple calculations (not including induced currents in the earth) show this bump could be produced if the rocket flew within 30 km of a 4.5×10^4 amp line current located to the southwest of the rocket and flowing towards the northwest.

It is noted that the average difference field is negative during the upward leg of the flight. This may be due to another line current or currents located to the northeast of Churchill and flowing towards the northwest. The increase in the difference field which was seen on the downward leg was most likely a time variation in the field or due to errors

in the trajectory calculation for UNH 68-1 (used as the reference field). The downward leg increase (not plotted here) is believed erroneous, however, since the error in the trajectory of UNH 68-1 was progressively getting larger on the downward leg. It is noted that it is unlikely that any one current or group of currents represents the only model which will satisfy the existing conditions and that several groups of currents may produce the same effect depending on the intensity and location.

The horizontal electric field measured during this flight is plotted in Figures 66 and 67. The field in general was smaller than that measured on flight UNH 68-2 although variations occurred almost as frequently. The field measured on the upward leg is plotted in Figure 66. Variations on the order of 10-15 mv/m were seen up to an altitude of 220 km and again above 240 km. The field averaged near 20 mv/m.

The field decreased just past apogee (Figure 67) to 15 mv/m and then increased again to a maximum near 170 km. Another smaller maximum occurred near 140 km. The field plotted here is the resultant electric field after the induced $\bar{v} \times \bar{B}$ field has been subtracted.

It is difficult to determine whether these field variations are temporal or spatial. The visible aurora at this

time was changing in form rapidly, thus it is likely that both spatial and temporal variations of the electric field existed. The horizontal electric field pointed southward during the flight.

The particle flux has been plotted (by Dr. R. Arnoldy) as a function of time and altitude in Figure 68. Also included are all-sky photographs labeled with the time after launch in seconds. The flux recorded here was of electrons with energy greater than 85 kev and protons with energy greater than 255 kev. The rocket position was shown on the photos by the dots.

An interesting comparison can be made between the rapidly changing auroral forms and the particle fluxes during this time period. It is seen that the particle fluxes were highest during times of the greatest auroral activity. In general the flux is higher on the downward leg with the maximum flux occurring at apogee. The flux dropped off very rapidly near 440 seconds when the visible aurora was fading quickly. As noted earlier, the riometer measured the greatest absorption of cosmic noise just past apogee when the charged particle fluxes were greatest.

The axial fluxgate magnetometer used to measure the axial component of the magnetic field did not work properly on flight UNH 68-3. A new method was used to obtain ψ,

the angle between the rocket spin axis and the vector magnetic field. It was found by a method which involved finding the slope of the transverse magnetometer output trace when it crossed zero. The results of this calculation are shown in Figure 69. It is interesting to note that although ψ was obtained by an independent method it resembles closely the results of 18.39 and 18.41 shown in Figure 56. Although, in general, the angles are somewhat smaller it is important to note the shapes of the curves are very similar. It seems unlikely that a curve like this, if due to precession, would reach a maximum and minimum at near the same times for three separate flights. This curve provides upper and lower limits for the angle ψ.

4. Flight UNH 68-4

Another rocket (NASA 18.40) was launched at 0748:58 UT (168 minutes past local midnight) on April 30, 1968 from Ft. Churchill. The telemetry ground station reported loss of modulation on all subcarrier oscillators at 19 seconds after launch. Radar confirmed vehicle malfunction when it tracked multiple objects. Further investigation revealed that the payload probably broke off just above the telemetry section during the last second of the Tomahawk burn. This was apparently caused by an initial rocket spin rate which

was too low. No useful data was acquired from this flight.

5. Flight UNH 68-5

This rocket (NASA 18.39) was launched on May 3, 1968 at 0510:38 UT (10 minutes after local midnight). Launch azimuth was 76° with an initial elevation of 85° (Figure 40). Apogee was at 260 km and the flight lasted 502 seconds (Figure 70). The spin period, after despin, was 1.56 seconds and little precession was observed. The Ft. Churchill telemetry ground station received a clean telemetry signal of 15-20 μv/m throughout the entire flight.

At the time of launch, the ground station magnetometers at Churchill measured a disturbance of -462γ in the X (north) component, -375γ in the Y (east) component, and +350γ in the Z (vertical) component of the magnetic field (Figure 71). The negative bay began about one half hour before launch and lasted approximately one hour. Magnetograms from other nearby stations confirmed a westward flowing current system. The 30 mHz riometer measured ~2 1/2 db absorption of cosmic noise indicating enhanced ionization caused by precipitating particles.

Ground based all-sky cameras at Churchill showed a diffuse aurora overhead at the time of launch. Near the time of apogee a bright arc formed in the northeast. This

had begun to fade by the time the rocket reached 100 km on the downward leg. The dot on the upper photograph in Figure 72 indicates the rocket position at 100 km on the upward leg. The dot on the lower photograph shows the rocket position at 100 km on the downward leg. The intensity of 5577Å measured on the ground was greater than 10 KR.

The photometer records for this flight are plotted in Figures 73, 74, 75, and 76. Since the rocket was flown in late spring, it flew above the shadow created by the earth and entered into sunlight. The shadow height was approximately 230 km. This accounts for the increase in intensity of the photometer outputs above 220 km. A comparison of the 6300Å (upward leg) maximums and minimums (Figures 75, 76) shows penetration of the diffuse aurora overhead at approximately 110 km. Consideration of the 5577Å data (Figures 73, 74) indicates penetration also. One would estimate the vertical thickness of the aurora to be 15 or 20 km with a higher intensity at 6300Å than at 5577Å. These findings agree with the ground based all sky camera photographs.

The downward leg results show a difference between the maximum and minimum plots indicating penetration to the center of the display didn't take place. The reason for the rapidly varying 6300Å minimum trace is unexplained except for the possibility that it was caused by the distant diffuse

aurora above Ft. Churchill. The arc in the northeast had partially faded by the time the rocket reached 100 km.

Summarizing, the UNH 68-5 payload was fired during a negative bay with a horizontal magnetic disturbance of -595γ and a vertical component of +350γ. This indicates that an electrojet current flowing from the south to the west might have caused the disturbance. The visible aurora and the riometer absorption indicate the existence of charged particle precipitation in the ionosphere. The ground photographs of the aurora show that the rocket passed through a diffuse aurora on the upward leg and came near an arc on the downward leg.

The total (scalar) magnetic field measured with the proton precession magnetometer is shown in Figure 77. A $1/R^3$ field normalized to apogee has been plotted on this graph and falls along the upward leg. The difference field is plotted in Figure 78. The trajectory of this flight was approximately the same as that of UNH 68-1. The most prominent feature is the rapid field increase seen as a spike near 96 km on the upward leg. An offset in the field strength is also noticed on each side of the spike. At the same altitude the spike occurred, the rocket was passing through the diffuse aurora overhead. This peak, if assumed to be due to a spatial variation, could be reproduced by a

line current of $\sim 10^4$ amps at a distance of 5 km from the rocket. This current was flowing towards the northwest and was located to the southwest of the rocket.

A gradual increase in the difference field was seen during the downward leg of the flight. The UNH 68-1 reference field was used in calculating the difference field, thus errors in the UNH 68-1 trajectory will be inherent in the difference field. Time variations on the ground magnetograms indicate the increase on the down leg may have been partly due to an increase in the current intensity that occurred when the rocket reached apogee. This increase might be related to the formation of a bright arc in the northeast as the rocket approached apogee.

It has been noted in part 1 of this section that no radar data was available for flight UNH 68-1. The trajectory used in plotting the reference magnetic field was obtained using estimates of the time and altitude based on the averages of the other flights. The total time of flight and the flight azimuth were obtained from the telemetry ground station and were based on the "loss of signal" time and direction of maximum signal respectively. The minimum magnetic field was measured at apogee and provided another method of determining the time of maximum altitude.

There is a possibility that an error in computing the

trajectory of UNH 68-1 could have caused the increase in the difference field seen in flights UNH 68-2, UNH 68-3, and UNH 68-5. If the trajectory was in error, the primary change would be in the slopes of the difference field while the magnetic disturbances due to currents would still be fairly well represented.

Several features indicate these downward leg increases may have partially been due to time variations in the field. In all three cases, the time variations of the field shown on the ground magnetogram just past apogee can be used to explain the variations seen on the difference field plots. Another indication that the trajectory may be partially valid was that the quiet time total field agrees qualitatively with a quiet time field measured by Conley (1960). In the quiet time flights a larger field was measured on the upward leg while during the disturbed condition flights, the largest field was measured on the downward leg. The azimuths of both quiet time flights were similar.

The electric field perpendicular to the rocket spin axis is plotted as a function of altitude for the upward leg in Figure 79. The field for each revolution has been plotted and the induced $\bar{v} \times \bar{B}$ field due to the rocket motion has been subtracted. The field pointed towards the southwest quadrant throughout the entire flight and was in

agreement with the observed drift of the auroral forms in the $\bar{E} \times \bar{B}$ direction (Figure 81). The field was generally higher in the vicinity of the visible aurora; however, at 195 km and near apogee the field dropped briefly to lower values. The large spike at 105 km occurred just after the large spike appeared on the magnetic field record. The field magnitude was primarily in the 30 to 40 mv/m range.

The electric field on the downward leg is shown in Figure 80. The field increased just past apogee to 50 mv/m and then decreased to zero near 127 km. It then increased to a maximum near 100 km. The increase near 100 km occurred when the rocket was near the arc in the northeast.

The results of Dr. Roger Arnoldy's solid state charged particle detector experiment are given in Figure 82 where one second averages of the data were taken. This shows a maximum flux was measured near 220 km. This decreased to a low value near apogee and then increased to a smaller maximum near 170 km on the downward leg. These fluxes were in general agreement with the riometer record which also showed a dip near the time of apogee. There appears to be some correlation between the maximum fluxes and the visible aurora since on the upward leg the largest flux occurred approximately 100 km above the diffuse aurora

while another flux increase occurred on the downward leg above the rayed arc.

The results of the axial fluxgate magnetometer experiment are plotted in Figure 83. This measured the component of the magnetic field along the spin axis of the rocket (nearly vertical for this flight). Part of the data on the upward leg is missing because the field value went below the range of the instrument (Figure 83). The variation in the angle ψ between the rocket spin axis and the total magnetic field vector is shown in Figure 56. The angle ψ was found using the measured axial field and the measured total field magnitude. The spin axis initially made a 7.5° angle with the magnetic field. This angle is predicted to increase about 1° until apogee using the rocket trajectory, assumed rocket spin direction and the Jensen and Cain (1962) field. After apogee the angle should start to become smaller. A 1000γ disturbance field due to an electrojet at right angles to the earth's field of 55,000γ would only change the direction by $\sim 1^{\circ}$. The variation observed was nearer 12° and thus was probably not due to ionospheric currents. It was unlikely that this was caused by a very slow precession since flights UNH 68-2 and UNH 68-3 showed very similar angular changes (Figures 56, 69). Another possibility was that the variation was due to an

anomaly in the earth's field not accounted for by the Jensen and Cain (1962) field. It did give an upper and lower limit for the change in ψ during the flight and was used for estimating possible error in ψ when calculating $\bar{v} \times \bar{B}$ for the electric field measurements.

SECTION VI

CONCLUSIONS

1. Discussion of Rocket Results

The rockets of this series (UNH 68-1 to UNH 68-5) were launched during a variety of auroral and magnetic conditions. The first, UNH 68-1, was launched during a quiet period with little auroral or magnetic activity. This flight provided not only a test of the new experiments but also a relatively undisturbed "reference" magnetic field. The reference field, at least the upward leg of the first flight, was used to calculate the field due to ionospheric currents for the three other successful flights. An upper limit for quiet time D. C. electric fields of 20 mv/m was obtained. Unfortunately the trajectory for this flight was not well known due to the failure of the radar system to "lock on" the target.

The flights were similar in that the trajectories did not vary greatly in azimuth, altitude, and elevation; all flights were in the northeast quadrant. The time of the launches was near local midnight in each case and they were all fired from Ft. Churchill. The experimental payload remained the same for each flight.

Flights UNH 68-2, UNH 68-3, and UNH 68-5 were

launched during negative magnetic bays. The ground level components of the disturbance field indicated the bay could have been caused by an "equivalent" ionospheric line current flowing towards the northwest. An equivalent current is a model of a current that would produce the ground disturbance but is restricted to the ionospheric "shell". A current similar to the equivalent current may have created the disturbance but there is the possibility of additional current flow to and from the magnetosphere (field aligned currents).

The rocket measurements revealed that the greatest field distortion on several flights was between 90 and 150 km. These measurements are consistent with a localized ionospheric current flowing southeast to northwest. Field aligned currents may have been present but a field aligned current must produce a field of ~5000γ in order to make a change of ~200γ in the measured field magnitude. This is because the field aligned current produces a disturbance field which is at right angles to the earth's field. The total field magnitude is then the square root of the sum of the squares of the disturbance field and the relatively large earth's field (55,000γ). Magnetic fields due to field aligned currents can change the direction of the vector magnetic field but since the earth's field is greater than 50,000γ a disturbance field of 5000γ would result in a change

of direction of the vector field of only 5^{o}.

The westward flowing electrojet measured during these flights is consistent with a current system suggested by Akasofu and Meng (1969). They suggest a current flowing down field lines in the morning sector, flowing westward across the auroral zone along the auroral oval and flowing out field lines in the evening sector. It is also consistent with a current system flowing only in the ionosphere.

One can say that the currents that produced the very narrow peak on the UNH 68-5 record were very localized. The dimension of the cross section of the current must be less than 5 km. The current might have been a band with a thickness of several kilometers perpendicular to the field and a height of 10 to 30 kilometers along the field. Using these figures, one can estimate a current density in the range of 1×10^{-5} amp/m^2 to 3×10^{-5} amp/m^2 which agrees with the prediction of Boström (1964).

Field aligned currents may have existed during flight UNH 68-3. The visible auroral forms during much of this flight consisted of auroral rays extending down from the zenith. This indicates we were looking up field lines upon which charged particles were spiralling into the ionosphere. The particle flux measured during the flight reached a maximum near apogee of $\sim 10^6$ particles/cm^2-steradian. A rough calculation of the

current density ($J \sim 10^6/cm^2$ sec x 1.6 x 10^{-19} coul $\sim 1.6 \times 10^{-9}$ amp/m^2) indicates a field aligned current due to the measured particles is too small to produce the measured magnetic disturbances, thus our measurements alone cannot confirm field aligned currents.

A 5^o change in azimuth angle (between spin direction and magnetic field) was measured on UNH 68-3. Considering this as due to a field aligned current, it would indicate a disturbance field of $\sim 5000\gamma$ or a change of $\sim 200_\gamma$ in the total field (which was measured). Assuming the rocket flew within 10 km of the current, we can calculate an upper limit for the field aligned current of 2.5×10^5 amp.

It is noticed that the transverse electric field on UNH 68-3 was on the average two to three times smaller than on UNH 68-2 which was fired during a period of widespread moderate magnetic activity. Since the ionosphere is a highly conducting "shell" a field aligned current, upon entering the ionosphere, could spread out into several less intense currents. These currents would produce a more localized ground magnetic disturbance as was measured during UNH 68-3 and would require smaller horizontal electric fields to drive them while the field aligned current might be driven by a stronger parallel electric field. Another possible cause of the lower electric fields measured in UNH 68-3 is that the payload was in the aurora during much

of the flight. Previous experiments indicate the fields tend to be lower inside regions of auroral activity. Photometer results on this flight indicate visible aurora over a large altitude span.

A widespread electrojet system was present during flight UNH 68-2 as mentioned earlier. The larger westward flowing currents ($\sim 10^4$ amp) coupled with the predicted Hall conductivity ($\sim 10^{-3}$ mho/m) could result from southward directed electric fields of the same order that were measured (30-60 mv/m). Similar remarks can be made about flight UNH 68-5.

The direction of the model electrojet currents (based on experimental results) were compared with the direction of the visible aurora. In UNH 68-2 and UNH 68-5, the current was flowing approximately parallel to arcs or bands at several times. A comparison of this type was not attempted for UNH 68-3 due to the unique forms and rapid changes. The parallel flow of current reveals regions of higher conductivity parallel to and probably caused by the ionization present in or near an auroral form. The southward electric fields measured were approximately perpendicular to the electrojets and indicates the electrojet is primarily a Hall current. The direction and magnitude of the fields was similar to those predicted by Fahleson et al. (1967).

A comparison of the electric field with the rocket photometer and all sky camera results indicated in several cases that the electric field tended to be lower inside the auroral form than in regions outside of it. A similar observation was also made by Maynard (1968).

In flight UNH 68-5, the auroral forms were observed to drift in the $\bar{E} \times \bar{B}$ vector direction (for a measured southward E field). If one assumes (as indicated by lack of variation of E with altitude) that the electric fields were mapped along the magnetic field lines (assumed to be equipotential), then the electric fields pointed radially inward in the equatorial plane on the night side of the earth at distances of several earth radii. According to Fejer (1963) this would indicate an inward drift of low energy electrons was taking place at 3 to 6 R_E (relative to higher energy protons). This is in general agreement with the concept of plasma coming up the magnetospheric tail towards the night side of the earth. The $\nabla|B|$ drift leads protons to the evening quadrant where they inflate (weaken) the magnetic field. The electric field caused by the charge separation can then cause currents to flow along the auroral oval.

Fluxes of charged particles are closely tied in with auroral phenomena. Previous experiments have shown the visible aurora is associated primarily with low energy (kev)

electrons (McIlwain, 1960). The results of the present flights show a correlation between the cosmic noise absorption measured by the riometer and the particle fluxes. This indicates the particles were causing increased ionization at auroral altitudes. This was further seen in several cases when the auroral intensity increased at the same time the particle fluxes were increasing.

The data on the axial magnetic field from flights UNH 68-2 and UNH 68-5 shows a normal decrease in the field on the upward legs. The downward leg records show a flattening of the data at a lower than expected field magnitude. Since the downward axial field was low and the total field was normal (or slightly higher), the angle between the spin axis and the field changed. This could be a combination of a change in the spin axis direction and the changing magnetic field direction due to the curvature of the field lines and the horizontal movement of the rocket.

2. Recommendations for Future Experiments

It is the opinion of the author that a necessary and logical next step in investigating auroral phenomena would be to determine the processes involved in a magnetospheric substorm. With a knowledge of this, one could not

only gain insight into auroral physics but also magnetospheric and planetary physics.

One of the least studied auroral parameters at this time is the electric field. It is not only closely connected with the magnetic field but also with the conductivity, current systems and plasma properties of this region. An increased understanding of the electric field would greatly help to determine more about the magnetospheric substorm.

The measurements discussed in this paper give some insight into the substorm process. They were, by necessity, limited to short periods of time at near the same altitude and location although they were done during several types of auroral conditions. The next measurement should be measurements of the electric field and could be done with several sets of probes and booms. In conjunction with this, there should be more accurate measurements of the vector magnetic field to help in locating the small direction and magnitude changes of the field created by field aligned currents.

BIBLIOGRAPHY

Aggson, T. L. and J. P. Heppner, Proposal for electric field measurements on POGO satellites (OGO-D and OGO-F), NASA-GSFC, October, 1965.

Akasofu, S. -I., Latitudinal shift of the auroral belt, J. Atmos. and Terres. Phys., 26, 1167-1174, 1964.

Akasofu, S. -I., and C. -I. Meng, A study of polar magnetic substorms, J. Geophys. Res., 74, 293-313, 1969.

Alfvén, H., and G. -G. Fälthammar, Cosmical Electrodynamics, Oxford University Press, London, 1963.

Arnoldy, R. L., Private Communication, 1968.

Axford, W. I., and C. O. Hines, A unifying theory of high-latitude geophysical phenomena and geomagnetic storms, Canadian Journal of Physics, 39, 1433-1464, 1961.

Boström, R., A model of the auroral electrojets, J. Geophys. Res., 69, 4983-4999, 1964.

Bourdeau, R. E., J. L. Donley, G. P. Serbu, and E. C. Whipple, Jr., Measurements of sheath currents and equilibrium potential on the Explorer VIII satellite, J. Astron. Sci., 8, 65-73, 1961.

Cahill, L. J., Jr., Detection of an electrical current in the ionosphere above Greenland, J. Geophys. Res., 64, 1377-1380, 1959.

Cahill, L. J., Jr., and J. A. Van Allen, High altitude measurements of the earth's magnetic field with a proton precession magnetometer, J. Geophys. Res., 61, 547-558, 1956.

Chamberlain, J. W., Physics of the Aurora and Airglow, Academic Press, New York, 1961.

Chapman, S., Aurora and geomagnetic storms, in Space Physics edited by D. P. LeGalley, and A. Rosen, Chap. 7, John Wiley and Sons, Inc., New York, 1964.

Conley, J. M., Earth's main magnetic field to 152 kilometers above Ft. Churchill, J. Geophys. Res., 65, 1074-1075, 1960.

Davis, L. R., O. E. Berg, and L. H. Meredith, Direct measurements of particle fluxes in and near auroras, in Space Research I, edited by H. Kallman-Bijl, pp. 721-735, North Holland Publishing Co., Amsterdam, 1960.

Davis, L. R., and J. M. Williamson, Low energy trapped protons, in Proc. Intern. Space Sci. Symp., 3rd, Washington, 1962.

Davis, T. N., Horizontal auroral motions and magnetic disturbance at the auroral zone, J. Phys. Soc. Japan, 17, Suppl. A-1, Kyoto Conf., 216-218, 1962.

Dewitt, R. N., and S. -I. Akasofu, Dynamo action in the ionosphere and motions of the magnetospheric plasma, Planetary Space Sci., 12, 1147-1156, 1964.

Driscoll, R. L., and P. L. Bender, Gyromagnetic ratio of proton redetermined, N. B. S. Tech. News Bull., 42, 217-219, 1958.

Dungey, J. W., Interplanetary magnetic field and the auroral zones, Phys. Rev. Letters, 6, 47-48, 1961.

Evans, D. S., A 10-cps periodicity in the precipitation of auroral zone electrons, J. Geophys. Res., 72, 4281-4291, 1967.

Evans, D. S., The observations of a near monoenergetic flux of auroral electrons, J. Geophys. Res., 73, 2315-2323,1968.

Evans, J. E., E. G. Joki, R. G. Johnson, and R. D. Sharp, Austral and boreal zone precipitation patterns for low-energy protons, in Space Research VI, edited by R. L. Smith-Rose, 773-788, 1965.

Fahleson, U., Theory for electric field measurements in the magnetosphere with electric probes, Royal Institute of Technology Technical Report, 66-02, Stockholm Sweden, 1966.

Fahleson, U., R. Boström, and C. -G. Fälthammar, Problems of rocket-borne electric field measurements in the ionosphere, Royal Institute of Technology Report, 67-24, Stockholm, Sweden, 1967.

Fejer, J. A., The effects of energetic trapped particles on magnetosphere motions and ionospheric current, Can. J. Phys., 39, 1409-1417, 1961.

Fejer, J. A., Theory of auroral electrojets, J. Geophys. Res., 68, 2147-2157, 1963.

Föppl, H., G. Haerendel, L. Haser, J. Loidl, P. Lütjens, R. Lüst, F. Melzner, B. Meyer, H. Neuss, and E. Rieger, Artificial strontium and barium clouds in the upper atmosphere, Planetary Space Sci., 15, 357-372, 1967.

Haerendel, G., R. Lüst, and E. Rieger, Motion of artificial ion clouds in the upper atmosphere, Planetary Space Sci., 15, 1-18, 1967.

Hinteregger, H. E., K. R. Damon, and L. A. Hall, Analysis of photoelectrons from solar extreme ultraviolet, J. Geophys. Res., 64, 961-969, 1959.

Jensen, D. C., and J. C. Cain, An interim geomagnetic field, J. Geophys. Res., 67, 3568-3569, 1962.

Imyanitov, I. and Ya. M. Shvarts, Pair of sensitive field mills on Sputnik III, Iskusstvennyye Sputniki Zemli, 17, 59-65, 1963.

Kavadas, A., Electric fields in the upper atmosphere, Research Report, Institute of Upper Atmospheric Physics, University of Saskatchewan, 1965.

Kelley, M. C., F. S. Mozer, and U. V. Fahleson, Auroral zone electric field measurements on a sounding rocket, Fall Meeting, American Geophysical Union, San Francisco, Calif., December 1968.

Kern, J. W., A charge separation mechanism for the production of polar auroras and electrojets, J. Geophys. Res., 67, 2649-2665, 1962.

Malmstadt, H. V., C. G. Enke, and E. C. Toren, Jr., Electronics for Scientists, W. A. Benjamin, Inc., New York, 1963.

Mapleson, W. W., and W. S. Whitlock, Apparatus for the accurate and continuous measurement of the earth's electric field, J. Atmos. and Terres. Phys., 7, 61-72, 1955.

Maynard, N. C., Measurements of ionospheric currents, University of New Hampshire Report, 66-2, 1966.

Maynard, N. C. Private communication, 1968.

McIlwain, C. E., Direct measurement of particles producing visible auroras, J. Geophys. Res., 65, 2727-2747, 1960.

McIlwain, C. E., Coordinates for mapping the distribution of magnetically trapped particles, J. Geophys. Res., 66, 3681-3691, 1961.

Meredith, L. H., L. R. Davis, J. P. Heppner, and O. E. Berg, Rocket auroral investigations, IGY Rocket Report Series, 1, 169-178, 30 July 1958.

Mozer, F. S., and P. Bruston, Auroral-zone proton-electron anticorrelations, proton angular distributions, and electric fields, J. Geophys. Res., 71, 4461-4467, 1966.

Mozer, F. S. and P. Bruston, Electric field measurements in the auroral ionosphere, J. Geophys. Res., 72, 1109-1114, 1967.

Packard, M., and R. Varian, Free nuclear induction in the earth's magnetic field, Phys. Rev., 93, 941, 1954.

Potter, W. E., An electric field meter for rocket and satellite use, Masters Thesis, University of New Hampshire, 1966.

Reitz, J. R., and F. J. Milford, Plasma Physics, Foundations of Electromagnetic Theory, Chap. 14, Addison-Wesley, Reading, Massachusetts, 1962.

Scrase, F. J., The electric current associated with polar magnetic sub-storms, J. Atmos. and Terres. Phys., 29, 567-579, 1967.

Störmer, C., The Polar Aurora, Clarendon, Oxford, 1955.

Swift, D. W., The generation and effect of electrostatic fields during an auroral disturbance, J. Geophys. Res., 68, 2131-2140, 1963.

Venkatesan, B., Isocontours of magnetic shell parameters B and L, J. Geophys. Res., 70, 3771-3780, 1965.

Vestine, E. H., The geographic incidence of aurora and magnetic disturbance, northern hemisphere, Terres. Magn., 49, 77-102, 1944.

Walt, M., (ed.), Auroral Phenomena, Stanford University Press, Calif., 1965.

Waters, G. S., A measurement of the earth's magnetic field by nuclear induction, Nature, 176, 691, 1955.

APPENDIX A

CURRENT COLLECTION BY METALLIC PROBES

When an uncharged metallic body is placed in the ionosphere it is likely to become negatively charged since more electrons collide with it than ions due to the higher electron thermal velocities. In this discussion, it is assumed the body is negatively charged. When a charged metallic object is immersed in a plasma, a sheath of the opposite charge will be formed about it to a thickness beyond which the plasma appears electrically neutral. In the case of electric field measurements, it is necessary to avoid overlap of the probe and rocket body sheaths wherever possible since this may cause variations of the potential between the probes, thus affecting the measurement. The equation for the Debye Length is (Reitz and Milford, 1962)

$$\lambda_D = \sqrt{\frac{\epsilon_o kT}{2N_o e^2}} \qquad \text{(A1)}$$

The Debye Length is ~2 x 10^{-3} m in the 100-200 km region. Thus at lower altitudes, sheath overlap is not a serious problem since it is short.

It has also been noticed by Bourdeau et al. (1961) that for higher rocket and satellite velocities the spacecraft "rams" the ions since it has a velocity greater than the ion velocity. Also, it is noticed that a negative wake exists

on the anti-velocity vector side since the ions cannot overtake the spacecraft due to their lower velocity. This results in a higher ion current on the front side of the probes (velocity vector side) as seen in Figure 15 . This is taken into account by adding the relative ion and spacecraft velocity to the current density equation for an assumed Maxwell-Boltzman distribution.

$$J_+ = \frac{N_+ e v'_+}{4} \exp\left(\frac{e\phi}{kT_+}\right) \tag{A2}$$

where N_+ is the ion density (ions/m^3) and v'_+ is the mean ion velocity plus the spacecraft velocity relative to the plasma.

$$v'_+ = \sqrt{\frac{8kT_+}{\pi m_+} + v^2} \tag{A3}$$

where k is Boltzman's constant (Joule/K°), T is ambient ion temperature (°K), and m_+ is the ion mass (Kgm). The electron current density is likewise given as

$$J_e = -\frac{N_e e v_e}{4} \exp\left(\frac{e\phi}{kT_e}\right) \tag{A4}$$

where ϕ is the potential of the probe, N_e is the electron density (electrons/m^3), T_e is ambient electron temperature (°K), and v_e is the mean thermal electron velocity (m/sec). In the case of daylight flights, one must also consider a photoelectric emission current density J_{ph}. Hinteregger (1959) has evaluated this as

$$J_{ph} \sim .5 \times 10^{-5} \text{ amps/m}^2 \tag{A5}$$

For equilibrium conditions the net current flow to the sphere is zero, and one can write a current balance equation

$$\int J_e ds + \int J_+ ds + \int J_{ph} ds = 0 \tag{A6}$$

For a moving probe, the electron current density in terms of a total potential including $\bar{E} \cdot \bar{r}$ and $\bar{v} \times \bar{B} \cdot \bar{r}$ is

$$J_e = -j_e \exp\left[\frac{e(\phi + [\bar{E} + \bar{v} \times \bar{B}]\cdot\bar{r})}{kT_e}\right] \tag{A7}$$

We can solve for the potential for a probe of radius a. The potential ϕ_+ of the righthand boom in Figure 13 (after Aggson and Heppner, 1965) is

$$2\pi a j_e \int_{\bar{d}_1}^{\bar{d}_2} \exp\left[\frac{e(\phi_+ + [\bar{E} + \bar{v} \times \bar{B}] \cdot \bar{r})}{kT_e}\right] dr = \int J_+ ds + \int J_{ph} ds$$

$$2\pi a j_e \left[\frac{kT_e}{e(\bar{E}+\bar{v}\times\bar{B})}\right]\left[\exp\left(\frac{e(\bar{E}+\bar{v}\times\bar{B})\cdot\bar{d}_2}{kT_e}\right) - \exp\left(\frac{e(\bar{E}+\bar{v}\times\bar{B})\cdot\bar{d}_1}{kT_e}\right)\right]\exp\left(\frac{e\phi_+}{kT_e}\right) =$$

$$\int J_+ ds + \int J_{ph} ds \tag{A8}$$

This expression can be solved for ϕ_+

$$\phi_+ = \frac{-kT_e}{e} \; Ln\left[\left(\frac{2\pi a j_e\left\{\dfrac{kT_e}{e(\bar{E}+\bar{v}x\bar{B})}\right\}}{\int J_+ ds \; + \; \int J_{ph} ds}\right) \cdot \right.$$

$$\left.\left(\exp\left[\frac{e(\bar{E}+\bar{v}x\bar{B})\cdot\bar{d}_2}{kT_e}\right] - \exp\left[\frac{e(\bar{E}+\bar{v}x\bar{B})\cdot\bar{d}_1}{kT_e}\right]\right)\right] \quad (A9)$$

The potential ϕ_- for the other probe is found in the same way.

$$\phi_- = \frac{-kT_e}{e} \; Ln\left[\left(\frac{2\pi a j_e\left\{\dfrac{kT_e}{e(\bar{E}+\bar{v}x\bar{B})}\right\}}{\int J_+ ds \; + \; \int J_{ph} ds}\right) \cdot \right.$$

$$\left.\left(\exp\left[\frac{-e(\bar{E}+\bar{v}x\bar{B})\cdot\bar{d}_1}{kT_e}\right] - \exp\left[\frac{-e(\bar{E}+\bar{v}x\bar{B})\cdot\bar{d}_2}{kT_e}\right]\right)\right] \quad (A10)$$

The potential difference between the probes is found by subtracting $(\phi+)$ from $(\phi-)$.

$$\Delta\phi = \phi_- - \phi_+ = \frac{-kT_e}{e} \; Ln\left[\frac{\exp\left(\dfrac{-e(\bar{E}+\bar{v}x\bar{B})\cdot\bar{d}_1}{kT_e}\right) - \exp\left(\dfrac{-e(\bar{E}+\bar{v}x\bar{B})\cdot\bar{d}_2}{kT_e}\right)}{\exp\left(\dfrac{e(\bar{E}+\bar{v}x\bar{B})\cdot\bar{d}_2}{kT_e}\right) - \exp\left(\dfrac{e(\bar{E}+\bar{v}x\bar{B})\cdot\bar{d}_1}{kT_e}\right)}\right] \quad (A11)$$

This is reduced to

$$\Delta\phi = (\bar{E} + \bar{v} \times \bar{B}) \cdot (\bar{d}_1 + \bar{d}_2) \qquad \text{(A12)}$$

The separation $\bar{d}$ between the centers of the current collecting probes is just $\bar{d}_1 + \bar{d}_2$.

$$\bar{d} = \left(\frac{\bar{d}_1 + \bar{d}_2}{2}\right) - \left(\frac{-\bar{d}_1 - \bar{d}_2}{2}\right) = \bar{d}_1 + \bar{d}_2 \qquad \text{(A13)}$$

APPENDIX B

The data analysis for the rocket series was accomplished with the aid of several computer programs written in Fortran IV for the IBM 360 and 1620. One of the first problems involved calculating the trajectory of the rocket using the radar plotboard data received from Ft. Churchill. In every case this data was incomplete and covered only portions of the trajectory. To compute the trajectory, a variable g, free fall trajectory program was written which assumed a constant horizontal velocity and could be used above ~40 km. The input for each trajectory to be computed was the time at apogee, altitude at apogee and range at apogee. The output consisted of a plot of the computed trajectory, a deck of cards with the altitude, time, range, and velocity for a given altitude, and a listing of the data that is punched on the cards.

On several flights, the apogee information was not available since radar lost track early in the flight. In these cases a least squares fit program allowed using what radar data was available. All flights had some radar data except 18.38. Predicted vehicle performance data was used to compute the trajectory for that flight.

The output of the trajectory program was then used as the input to a program which changed the velocity and range to spherical coordinates and calculated the latitude and longitude of the rocket as a function of time. The output consisted of

a deck of cards on which were the altitude, time, components of velocity, latitude and the longitude. The next program interpolated these quantities to 32 times a second and also calculated the aspect angle β in the plane perpendicular to the spin axis. These values were stored on a magnetic tape.

The theoretical magnetic field of the earth was also calculated using Jensen and Cain coefficients in a spherical harmonic analysis program. The results of the preceding programs plus data on the angle between the spin axis and the magnetic field (ψ) and the incremental values of the $\bar{v} \times \bar{B}$ electric field were then put on a master rocket tape. Once the master tape was made it was easier to write smaller programs for the individual experiments which could call on the tape for needed information. An example of a program of this type was one which subtracted the induced electric field from the total measured electric field. Programs for the trajectory, magnetic field and interpolation are included for reference.

TABLE 1

PLASMA PARAMETERS

Altitude km	Conditions	Ion Density m^{-3}	Ion Temp. °K	Electron Temp. °K	Magnetic Field gauss	Electron Debye Length m	Ion Gyro Radius m	Electron Gyro Radius m	Mean Free Path m
80	night	3×10^{3}	200	200	0.5	6×10^{-2}	2	10^{-2}	10^{-2}
80	day	10^{9}	200	200	0.5	3×10^{-2}	2	10^{-2}	10^{-2}
120	night	10^{9}	300	300	0.5	4×10^{-2}	2	10^{-2}	1
120	aurora	10^{12}	400	500 ?	0.5	2×10^{-3}	3	10^{-2}	1
120	day	10^{11}	400	400	0.5	4×10^{-3}	3	10^{-2}	1
300	night	3×10^{11}	700	10^{3}	0.45	4×10^{-3}	3	2×10^{-2}	10^{3}
300	day	10^{12}	1800	2×10^{3}	0.45	3×10^{-3}	5	3×10^{-2}	10^{3}
3000	day	5×10^{9}	3×10^{3}	3×10^{3}	0.16	5×10^{-2}	9	10^{-1}	10^{5}
30000	day	3×10^{8}	3×10^{4} ?	3×10^{4} ?	7×10^{-3}	0.7	300	8	10^{6}
50000	day	10^{6}	3×10^{5} ?	3×10^{5} ?	7×10^{-4}	40	10^{4}	200	10^{8}

(Fahleson, 1966)

TABLE 2

```
                C     TRAJECTORY PROGRAM
0001                  DIMENSION  SAVEX(1000), SAVEY(1000),HEADER(10)
0002                  HK1=795866.
0003                  C2=6378.388
                C
                C
                C         TA = TIME IN SECONDS TO REACH APOGEE
                C         YA = VERTICLE DISTANCE IN FEET TO APOGEE
                C         XA = HORIZONTAL DISTANCE IN YARDS TO APOGEE
                C         ZINC = INCREMENT IN KILOMETERS AT WHICH YOU WANT CARDS PUNCHED
                C             OUT FOR MAGNETIC FIELD PROGRAM (USUALLY 1.0 KM)
                C         YINC = INCREMENT IN KILOMETERS AT WHICH POINTS WILL BE PLOTTED
                C            ON GRAPH     (NOT LESS THAN 5.0KM. AND USUALLY 5.0 KM.)
                C
                C
0004              18  READ (1,900,END=999) TA, YA,XA,ZINC,YINC
0005             900  FORMAT (5F10.1)
0006                  READ 910, (HEADER(I),I=1,10)
0007             910  FORMAT(10A4)
0008                  IT=TA
0009                  XMAX=(2*IT)/50*50+50
0010                  XLEN=XMAX/50
0011                  CALL PLOT(1,0.0,XMAX,XLEN,50.,0.0,360.0,9.0,40.0)
0012                  NUM=100
0013                  X=85.0
0014                  ITICK=XLEN/2.0
0015                  DO 1 I=1,ITICK
0016                  CALL PLOT(91,X,-12.)
0017                  WRITE(4,1000)NUM
0018                  CALL CHAR(.2,0)
0019            1000  FORMAT(13,100X)
0020                  X=X+100.
0021                1 NUM=NUM+100
```

```
0022              X=XMAX/2.0-70.
0023              CALL PLOT(91,X,-30.)
0024              WRITE(4,1001)
0025              CALL CHAR(.2,0)
0026         1001 FORMAT(14HTIME (SECONDS),100X)
0027              NUM=0
0028              Y=-12.0
0029              DO 2 I=1,5
0030              CALL PLOT(91,-5.0,Y)
0031              WRITE(4,1002)NUM
0032              CALL CHAR(.2,1)
0033         1002 FORMAT(13,100X)
0034              Y=Y+80.
0035            2 NUM=NUM+80
0036              CALL PLOT(91,-30.,128.)
0037              WRITE(4,1003)
0038              CALL CHAR(.2,1)
0039         1003 FORMAT(13HALTITUDE (KM),100X)
0040              X=XMAX/2.0-95.
0041              CALL PLOT(91,X,355.)
0042              WRITE(r,5000)
0043              CALL CHAR(.2,0)
0044         5000 FORMAT(19HCOMPUTED TRAJECTORY, 100X)
0045              X=XMAX/2.0-200.
0046              CALL PLOT(91,X,335.)
0047              WRITE(4,5001) (HEADER(I),I=1,10)
0048              CALL CHAR(.2,0)
0049         5001 FORMAT(10A4,100X)
0050              ITH=2./3.
0051              HTT=3./2.
0052              YA=YA*.0003048006
0053              VT=(XA*3.0*.003048006)/TA
0054              HK3=HK1/(YA+C2)
0055              HK4=(SQRT(HK1)*TA)/((YA+C2)**HTT)
0056              W=HK3/HK1
0057              U=HK1/(HK3*SQRT(HK3))
```

```
0058            PRINT 901,YA,TA,HK3,HK4
0059          901 FORMAT (8H1APOGEE=,F10.3,12H KM,  TIME=,F10.2,
                 111H SEC,  K3=,F10.5,8H   K4=,F15.5//60H          T UP
                 1T DOWN      ALTITUDE     VELOCITY,34H   RANGE UP         RA
                 1NGE DOWN/)
0060             15 Z=0
0061               ZZ=40.0
0062               KOUNT=0
0063             14 Z=Z+ZINC
0064               R=W*(Z+C2)
0065               IF (R-1.) 5,5,16
0066              5 X=SQRT(R-(R*R))
0067               Y=SQRT(1.-R)
0068               Y=SIN(Y)
0069               S=ATAN(Y/SQRT(1.-Y*Y))
0070               T=(X+S-HK4)*U
0071               TT=(-X-S-HK4)*U
0072               R1=T*VT
0073               R2=TT*VT
0074               VEL=SQRT((HK1/(Z+C2))-HK3)
0075               IF(Z.LT.ZZ)   GO TO3
0076               ZZ=ZZ+YINC
0077               KOUNT=KOUNT+1
0078               SAVEY(KOUNT)=Z
0079               SAVEX(KOUNT)=TT
0080               CALL PLOT(88,T,Z,0,3)
0081              3 PRINT 902,T,TT,Z,VEL,R1,R2
0082          902 FORMAT (6F15.3)
0083               PUNCH 905,T,TT,Z,VEL,R1,R2
0084          905 FORMAT(6F10.3)
0085               GO TO 14
0086             16 CALL PLOT(88,TA,YA,0,3)
0087               IND=KOUNT
0088               DO 17 I=1,KOUNT
0089               X=SAVEX(IND)
0090               Y=SAVEY(IND)
```

```
0091              IND=IND-1
0092           17 CALL PLOT(88,X,Y,0,3)
0093              CALL PLOT(99)
0094              CALL PLOT(7)
0095              GO TO 18
0096          999 CALL PLOT(100)
0097              CALL EXIT
0098              END
```

TABLE 3

```
C     PROGRAM TO CALCULATE THEORETICAL MAGNETIC FIELD OF EARTH
C     SEE MARILYN WINGERSKY, TRANSFORMATION OF VECTORS BETWEEN VARIOUS
C     COORDINATE SYSTEMS, UNH-64-3, PAGES 14,34-39, AND CAIN, JOUR.
C     OF GEOPHYS. RES., 70, (1965), 3656.
C     READ COEFFICIENTS.
0001        DIMENSION G(6,7),H(6,7),P(6,7),DP(6,7)
0002        DO 10 M = 1,7
0003   10   READ 500,G(1,M),G(2,M),G(3,M),G(4,M),G(5,M),G(6,M)
0004        DO 11 M = 1,7
0005   11   READ 500, H(1,M),H(2,M),H(3,M),H(4,M),H(5,M),H(6,M)
0006  500   FORMAT (7F10.4)
0007        PRINT 504
0008  504   FORMAT (                  120H1          SEC      AL
           1TITUDE           X          Y          Z        TH. B
           1           EX. B         DIF/)
0009        ERAD = 6371.
0010        SR70=8.3666003
0011        SR3=1.7320508
0012        SR35=5.9160798
0013        SR15=3.8729833
0014        SR10=3.1622777
0015        SR462=21.494185
0016        SR154=12.409674
0017        SR14=3.7416574
0018        EXF=0
0019        W=1./57.29578
0020   60   READ(1,503,END=999) ALT,TSECS,GCLAT,GDLON
0021  503   FORMAT(2F10.3,30X,2F10.5)
0022        THETA=(90.-GCLAT)*W
0023        IF(GDLON)1,2,2
0024   1    GDLON=360.+GDLON
0025   2    PHI=GDLON*W
0026        DIST=ERAD/(ALT+6371.)
C     USING FIRST DEGREE POLYNOMIALS
```

```
0027                ST = SIN(THETA)
0028                CT = COS(THETA)
0029                P(1,1) = CT
0030                DP(1,1) = -ST
0031                P(1,2) = ST
0032                DP(1,2) = CT
              C     USING SECOND DEGREE POLYNOMIALS
0033                SSQT = ST*ST
0034               A2=2.*THETA
0035                STT = SIN(A2)
0036                CTT = COS(A2)
0037               P(2,1)=.75*CTT+.25
0038               DP(2,1)=-1.5*STT
0039               P(2,2)=SR3*ST*CT
0040               DP(2,2)=SR3*CTT
0041               P(2,3)=SR3*SSQT*.5
0042                DP(2,3) = P(2,2)
0043               SCUT=SSQT*ST
0044               A3=3.*THETA
0045               STHT=SIN(A3)
0046               CTHT=COS(A3)
0047                P(3,1) = (5.*CTHT+3.*CI)*.125
0048                DP(3,1) = (-15.*STHT-3.*ST)*.125
0049               PTO=.30618621
0050                PTT = 5.*CTT+3.
0051                P(3,2) = PTO*ST*PTT
0052                DP(3,2) = PTO*(ST*(-10.*STT)+PTT*CT)
0053               P(3,3)=SR15*ST*STT*.25
0054                DP(3,3)=SR15*(ST*2.*CTT+STT*CT)*.25
0055               P(3,4)=SR10*SCUT*.25
0056               DP(3,4)=SR10*SSQT*CT*.75
0057               DP(3,4)=SR10*3.*SSQT*CT*.25
0058               SFPT=SCUT*ST
0059                CSQT = CT*CT
0060               CCUT=CSQT*CT
0061                 A4=4.*THETA
0062               SFT=SIN(A4)
```

```
0063              CFT=COS(A4)
0064              P(4,1)=(35.*CFT+20.*CTT+9.)*.015625
0065              DP(4,1)=(-140.*SFT-40.*STT)*.015625
0066              PTO=SR10*.25
0067               PTT = 7.*CCUT-3.*CT
0068               P(4,2) = PTO*ST*PTT
0069               DP(4,2) = PTO*(ST*(-21.*CSQT*ST+3.*ST)+PTT*CT)
0070              PTO=.55901700
0071               PTT = 7.*CSQT-1.
0072               P(4,3) = PTO*SSQT*PTT
0073               DP(4,3) = PTO*(SSQT*(-14.*CT*ST)+PTT*2.*ST*CT)
0074              PTO=SR70*SCUT*.25
0075               P(4,4) = PTO*CT
0076               DP(4,4)=SR70*(-SCUT*ST+3.*CSQT*SSQT)*.25
0077              P(4,5)=SR35*SFPT*.125
0078              DP(4,5)=SR35*SCUT*CT*.5
0079              CFPT=CCUT*CT
0080              A5=5.*THETA
0081              SFVPT=SFPT*ST
0082              SFVT=SIN(A5)
0083              CFVT=COS(A5)
0084              P(5,1)=(63.*CFVT+35.*CTHT+30.*CT)*.0078125
0085              DP(5,1)=(-315.*SFVT-105.*STHT-30.*ST)*.0078125
0086              PTO=SR15*.125
0087               PTT = 21.*CFPT-14.*CSQT+1.
0088               P(5,2) = PTO*ST*PTT
0089               DP(5,2) = PTO*(ST*(-84.*CCUT*ST+28.*CT*ST)+PTT*CT)
0090               PTO=10.246951*.25
0091               PTT = 3.*CCUT-CT
0092               P(5,3) = PTO*SSQT*PTT
0093               DP(5,3) = PTO*SCUT*(-9.*CSQT+1.)+PTT*2.*ST*CT)
0094              PTO=SR70*.0625
0095               PTT = 9.*CSQT-1.
0096               P(5,4) = PTO*SCUT*PTT
0097               DP(5,4) = PTO*(SCUT*(-18.*CT*ST)+PTT*3.*SSQT*CT)
```

```
0098              P(5,5)=SR35*SFPT*CT*.375
0099              DP(5,5)=SCUT*SR35*(4.*CSQT-SSQT)*.375
0100              P(5,6)=SR14*SFVPT*.1875
0101              DP(5,6)=SR14*SFPT*CT*.9375
0102              CFVPT=CFPT*CT
0103              SSPT=SFVPT*ST
0104              A6=6.*THETA
0105              SST=SIN(A6)
0106              CST=CPS(A6)
0107               P(6,1) = (231.*CST+126.*CFT+105.*CTT+50.)/512.
0108               DP(6,1) = (-1386.*SST-504.*SFT-210.*STT)/512.
0109              PTO=.57282196
0110               PTT = (33.*CFVPT-30.*CCUT+5.*CT)
0111               P(6,2) = PTO*ST*PTT
0112               DP(6,2) = PTO*(SSQT*(-165.*CFPT+90.*CSQT-5.)+PTT*CT)
0113              PTO=.4528553
0114               PTT = 33.*CFPT-18.*CSQT+1.
0115               P(6,3) = PTO*SSQT*PTT
0116               DP(6,3) = PTO*(SSQT*(-132.*CCUT*ST+36.*CT*ST)+PTT*2.*ST*CT)
0117              PTO = 2.*PTO
0118               PTT = 11.*CCUT-3.*CT
0119               P(6,4) = PTO*SCUT*PTT
0120               DP(6,4) = PTO*(SCUT*(-33.*CSQT*ST+3.*ST)+PTT*3.*SSQT*CT)
0121              PTO=.49607837
0122               PTT = 11.*CSQT-1.
0123               P(6,5) = PTO*SFPT*PTT
0124               DP(6,5) = PTO*(SFPT*(-22.*CT*ST)+PTT*4.*SCUT*CT)
0125              P(6,6)=SR154*SFVPT*CT*.1875
0126              DP(6,6)=SR154*(-SSPT+5.*CSQT*SFPT)*.1875
0127              P(6,7)=SR462*SSPT*.03125
0128              DP(6,7)=SR462*SFVPT*CT*.1875
0129          50    X = 0.0
0130                Y = 0.0
0131                Z = 0.0
0132              DO 51 N=1,6
0133               NPO = N+1
0134               NN=N+2
```

```
0135                TA=DIST**NN
0136                DNO=N+1
0137                DO 51 M=1,NPO
0138                DM=M-1
0139               TC=COS(DM*PHI)
0140               TS=SIN(DM*PHI)
0141               X=X+DP(N,M)*TA*((G(N,M)*TC)+(H(N,M)*TS))
0142                IF (ST) 53,52,53
0143             52  Y = 0.0
0144                 GO TO 54
0145             53 YA=P(N,M)*DM*TA*((-G(N,M)*TS)+(H(N,M)*TC))
0146                Y=Y-YA/ST
0147             54 Z=Z+P(N,M)*DNO*TA*((-G(N,M)*TC)-(H(N,M)*TS))
0148                BG=X*100000.
0149                GB=Y*100000.
0150             51  CONTINUE
                C     DETERMINE THE FIELD IN GAMMA
0151                F=SQRT((X*X)+(Y*Y)+(Z*Z))
0152                 F = F*100000.
0153                Z=Z*100000.
0154                Y=Y*100000.
0155                X=X*100000.
0156                DIF=EXF-F
0157                PRINT 501,TSECS,ALT,X,Y,Z,F,EXF,DIF
0158              501 FORMAT(10X,2F10.3,6F15.7)
0159                 GO TO 60
0160              999 CALL EXIT
0161                END
```

TABLE 4

```
                C     INTERPOLATION PROGRAM
0001                  DIMENSION A(2),T(2),VR(2,VT(2)VP(2),XLAT(2),XLONG(2),TO(150)
0002                  TINC=1./32.
0003                  READ 100, SEC,PERIOD
0004                100 FORMAT(2F10.3)
0005                  I=1
                C
                C         SEC  IS THE STARTING TIME AT WHICH YOU WANT TO START THE
                C                              INTERPOLATION.
                C         PERIOD  SPIN PERIOD (IN SECONDS)
                C         TO  REFERENCE TIME WHEN BETA IS 0 DEGREES
                C
0006                  1 READ 102, TO(I)
0007                102 FORMAT (F10.2)
0008                  IF(TO(I).EQ.0.)  GO TO 6
0009                  I=I+I
0010                  GO TO 1
0011                6 J=1
0012                7 TBASE=TO(J)-.39
0013                4 TBASE=TBASE-PERIOD
0014                  IF(TBASE.GT.SEC)    GO TO4
0015                  READ 101,A(1),T(1),VR(1),VT(1),VP(1),XLAT(1),XLONG(1)
0016                101 FORMAT(2F10.3,5F10.5)
0017                  2 READ(1,101,END=99) A(2),T(2),VR(2),VT(2),VP(2),XLAT(2),XLONG(2)
0018                  3 IF(SEC.GT.T(2))    GO TO 5
0019                  FACTOR = (SEC-T(1))/(T(2)-T(1))
0020                  AT = FACTOR*(A(2)-A(1))+A(1)
0021                  VR1 = FACTOR*(VR(2)-VR(1))+VR(1)
0022                  VT1 = FACTOR*(VT(2)-VT(1))+VT(1)
0023                  VP1 = FACTOR*(VP(1))+VP(1)
0024                  YLAT = FACTOR*(XLAT(1)-XLAT(1))+XLAT(1)
0025                  YLONG = FACTOR*(XLONG(2)-XLONG(1))+XLONG(1)
0026                  IPER=(SEC-TBASE)/PERIOD
```

```
0027              PER=IPER
0028              BETA=360./PERIOD*(SEC-TBASE-PERIOD*PER)
                C     WRITE(10,1000) SEC,AT,VR1,VT1,VP1,YLAT,YLONG,BETA
0029                  WRITE( 3,1000) SEC,AT,VR1,VT1,VP1,YLAT,YLONG,BETA
0030              1000 FORMAT(2F10.3,6F10.5)
0031                  SEC=SEC+TINC
0032                  IF(J.EQ.I)   GO TO 3
0033                  IF(SEC.LT.TO(J+1))  GO TO 3
0034                  J=J+1
0035                  GO TO 7
0036                5 A(1)=A(2)
0037                  T(1)=T(2)
0038                  VR(1)=VR(2)
0039                  VT(1)=VT(2)
0040                  VP(1)=VP(2)
0041                  XLAT(1)=XLAT(2)
0042                  XLONG(1)=XLONG(2)
0043                  GO TO 2
0044               99 CALL EXIT
0045                  END
```

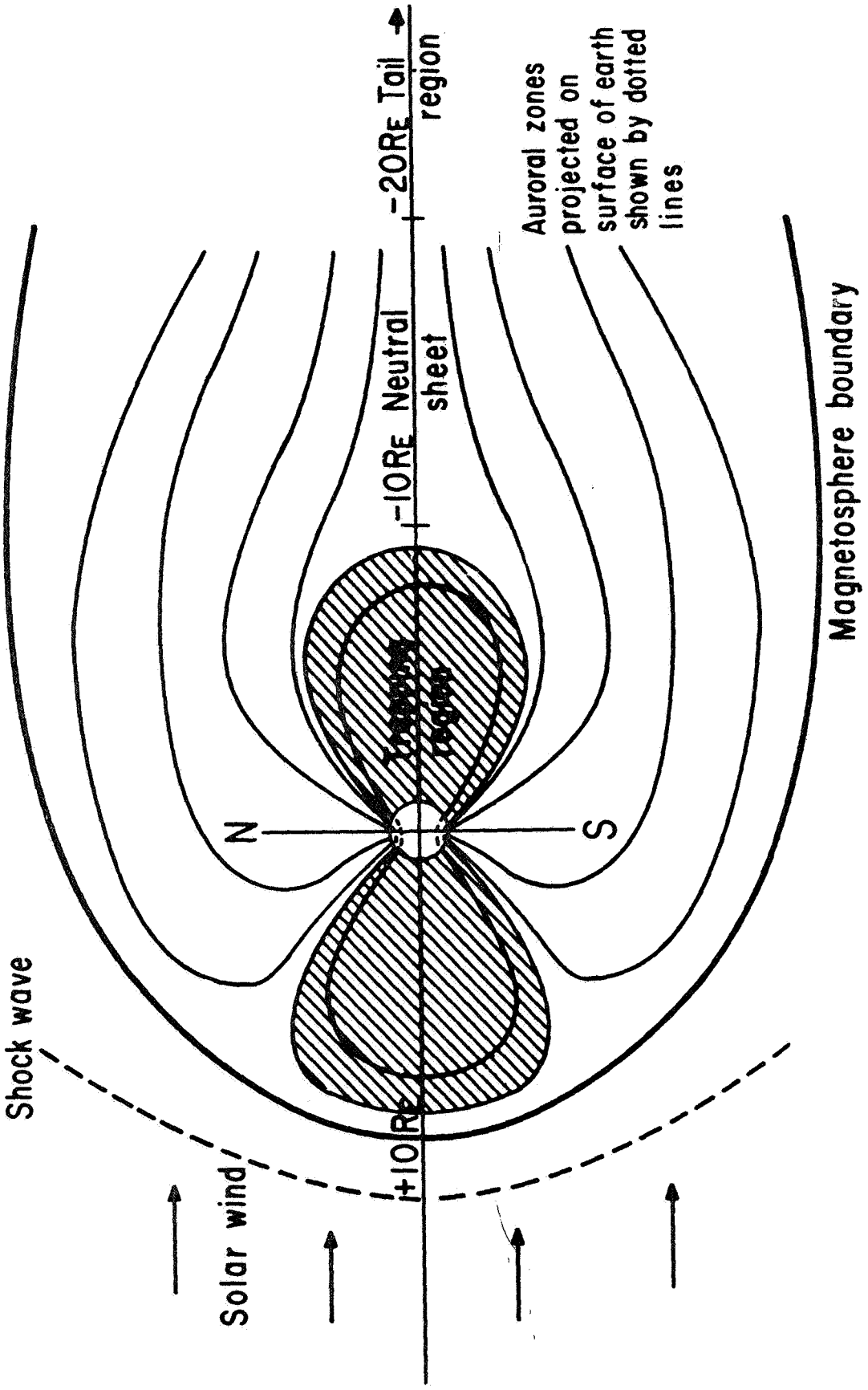

General picture of magnetosphere

Figure 1

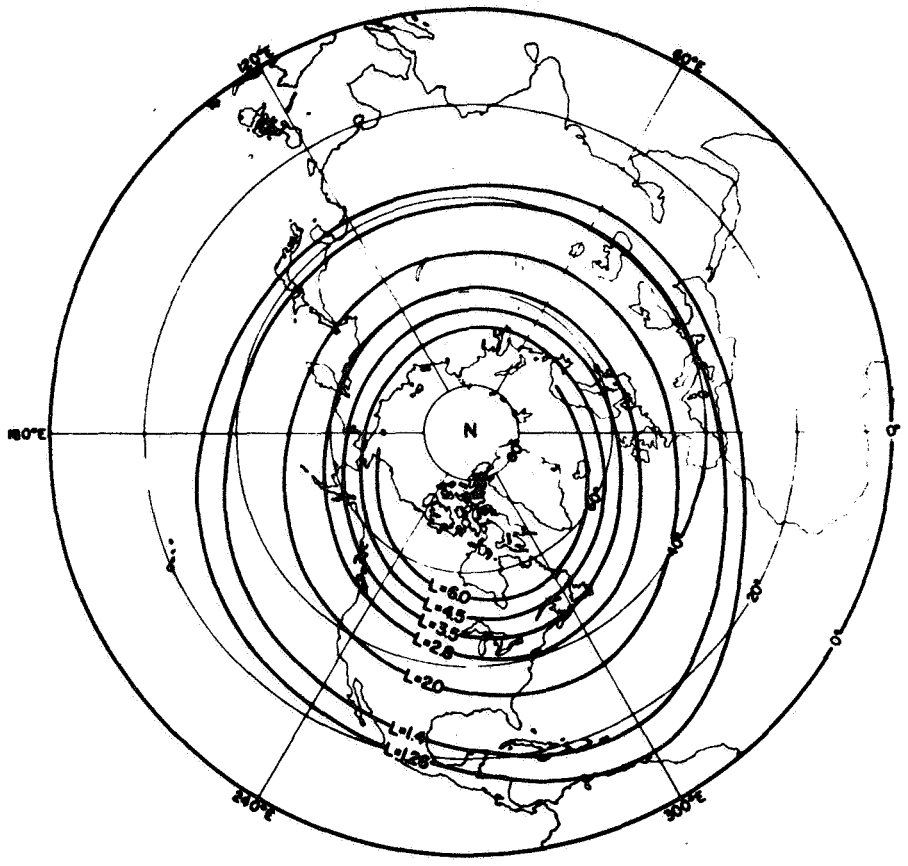

McIlwain's L shells (Venkatesan, 1965)

Figure 2

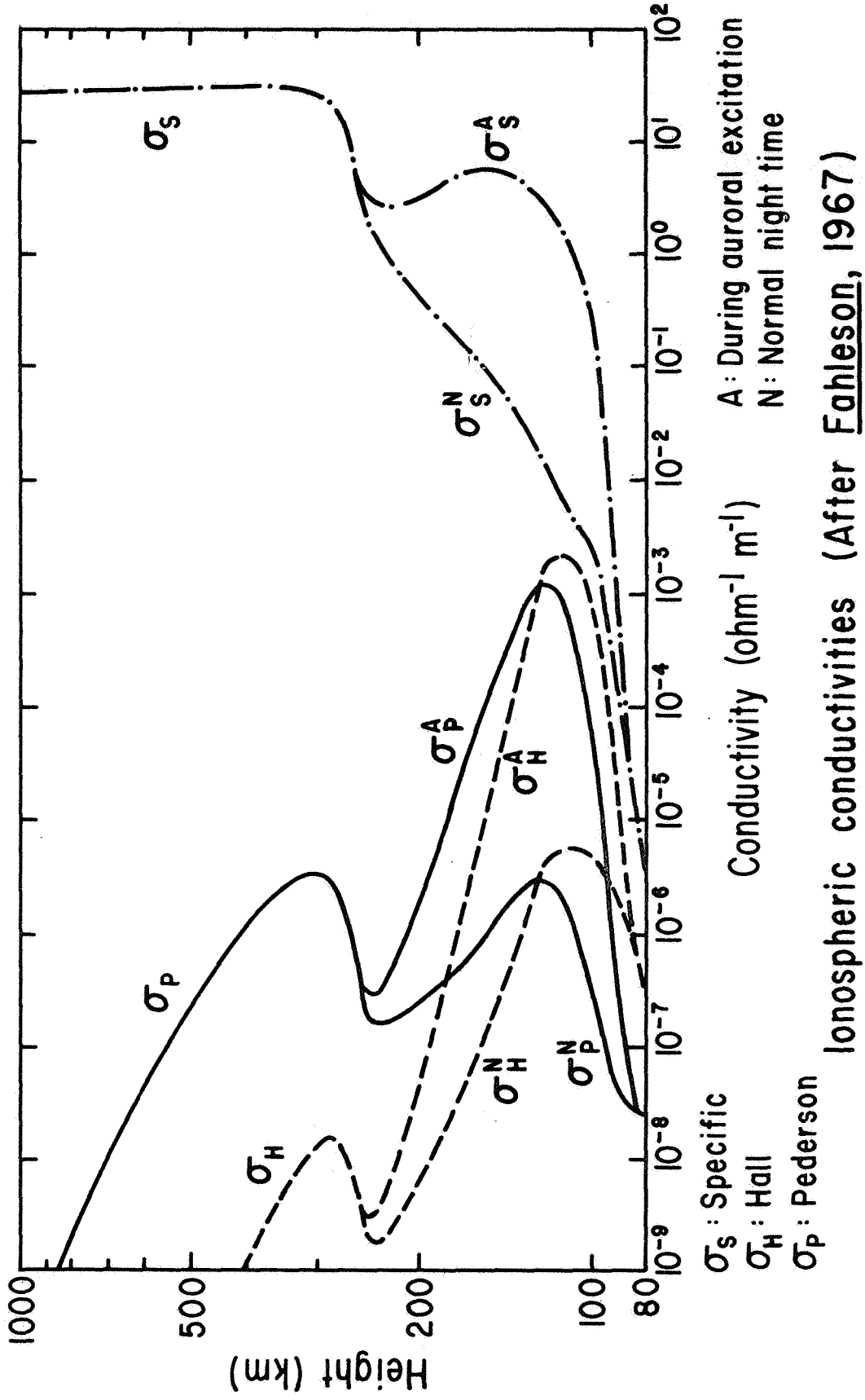
Ionospheric conductivities (After Fahleson, 1967)
Height (km)
1000
500
200
100
80
Conductivity (ohm⁻¹ m⁻¹)
10⁻⁹
10⁻⁸
10⁻⁷
10⁻⁶
10⁻⁵
10⁻⁴
10⁻³
10⁻²
10⁻¹
10⁰
10¹
10²
σS : Specific
σH : Hall
σP : Pederson
A: During auroral excitation
N: Normal night time
σS
σP
σH
σSA
σSN
σPA
σHA
σPN
σHN

Figure 3

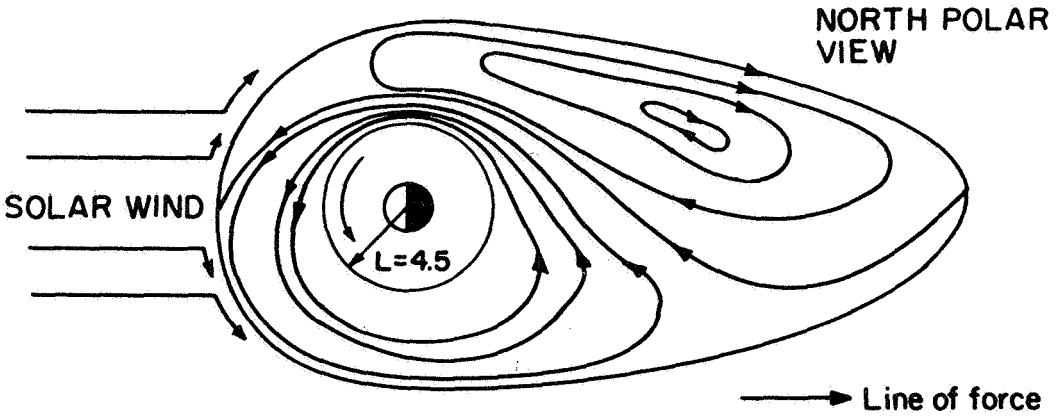

CLOSED MODEL

(a)

After AXFORD and HINES, 1961

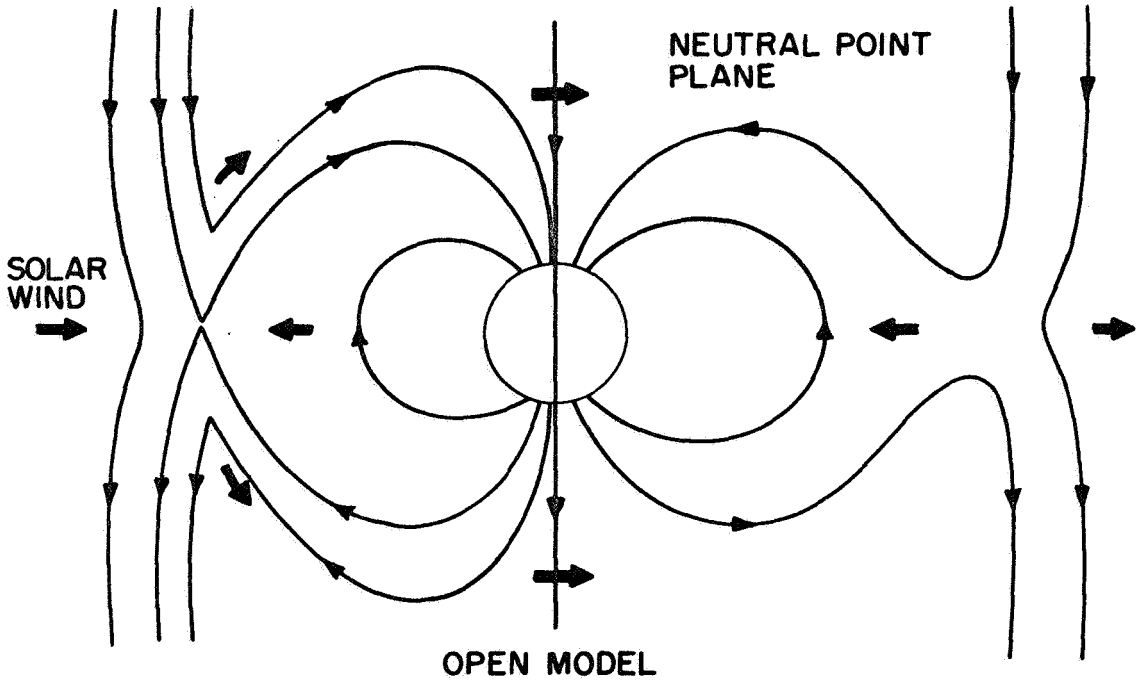

OPEN MODEL

After DUNGEY, 1961

(b)

Flow direction

Line of force

Magnetosphere plasma convection theories

Figure 4

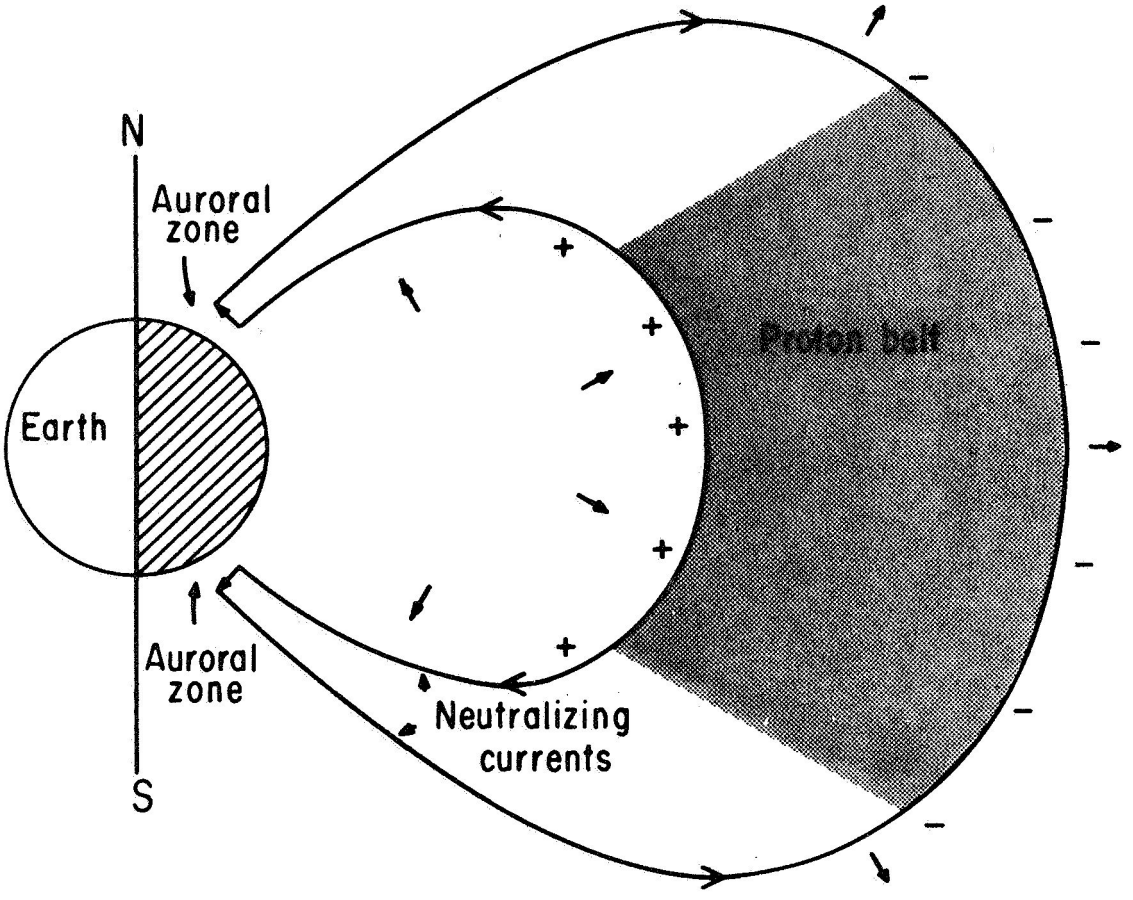

Neutralizing currents in magnetosphere

(After Fejer, 1963)

Figure 5

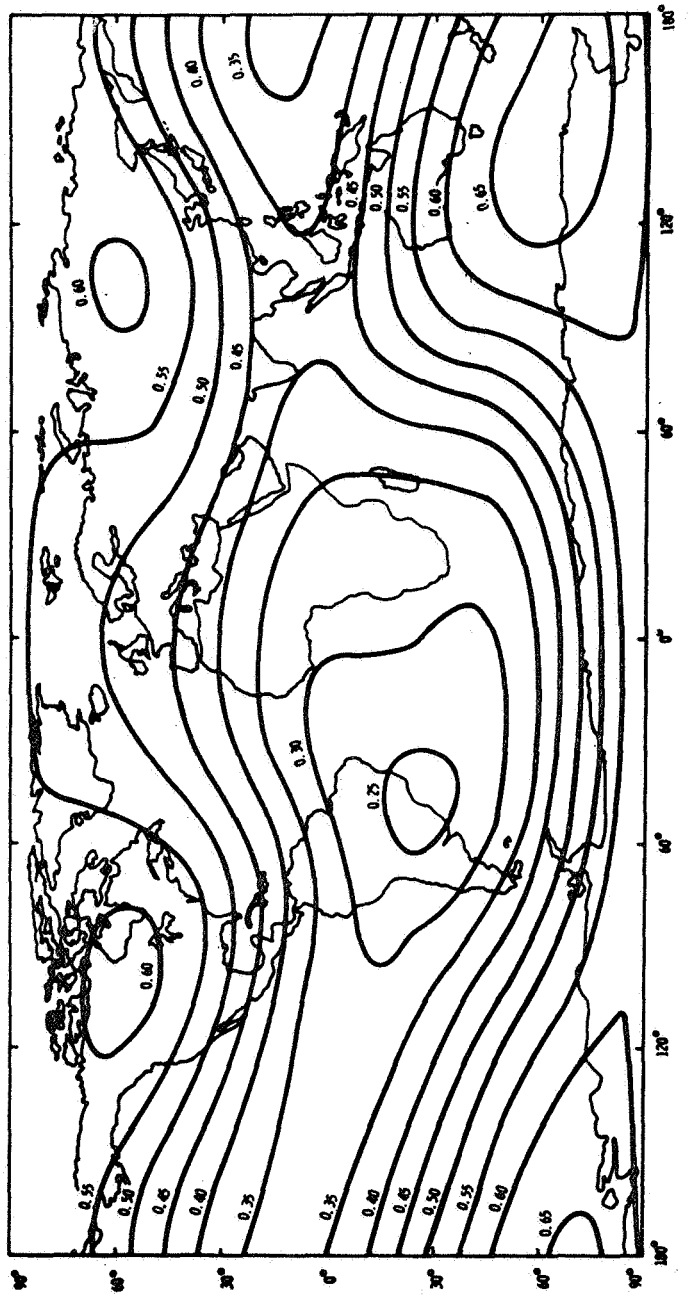

Figure 6

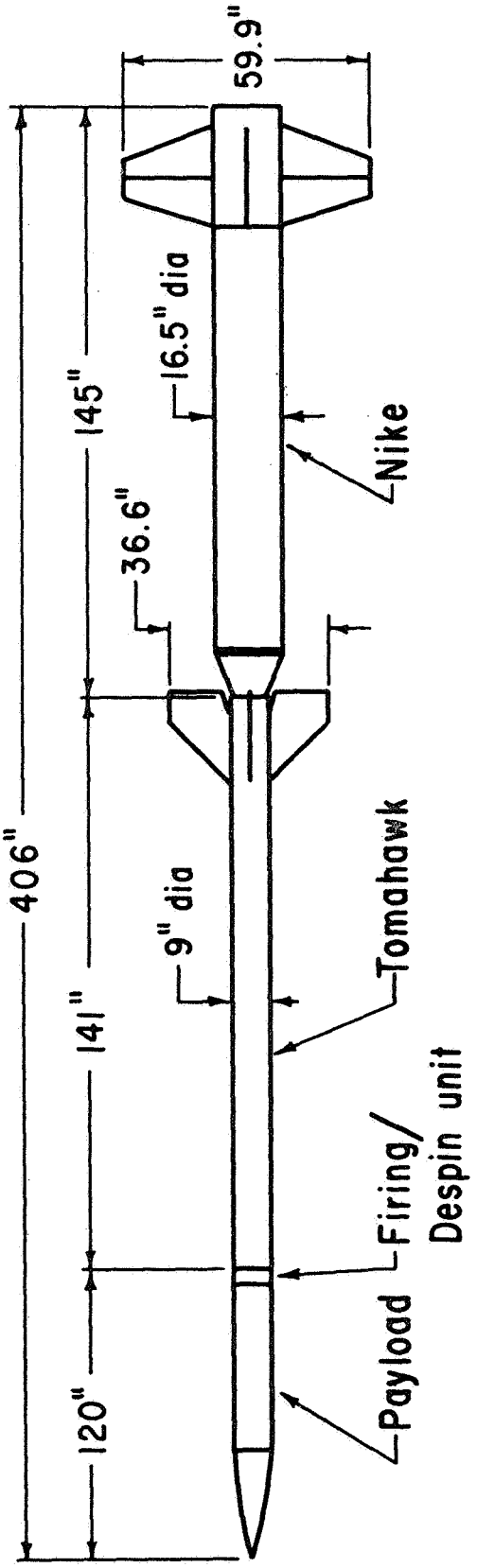

Nike Tomahawk

Figure 7

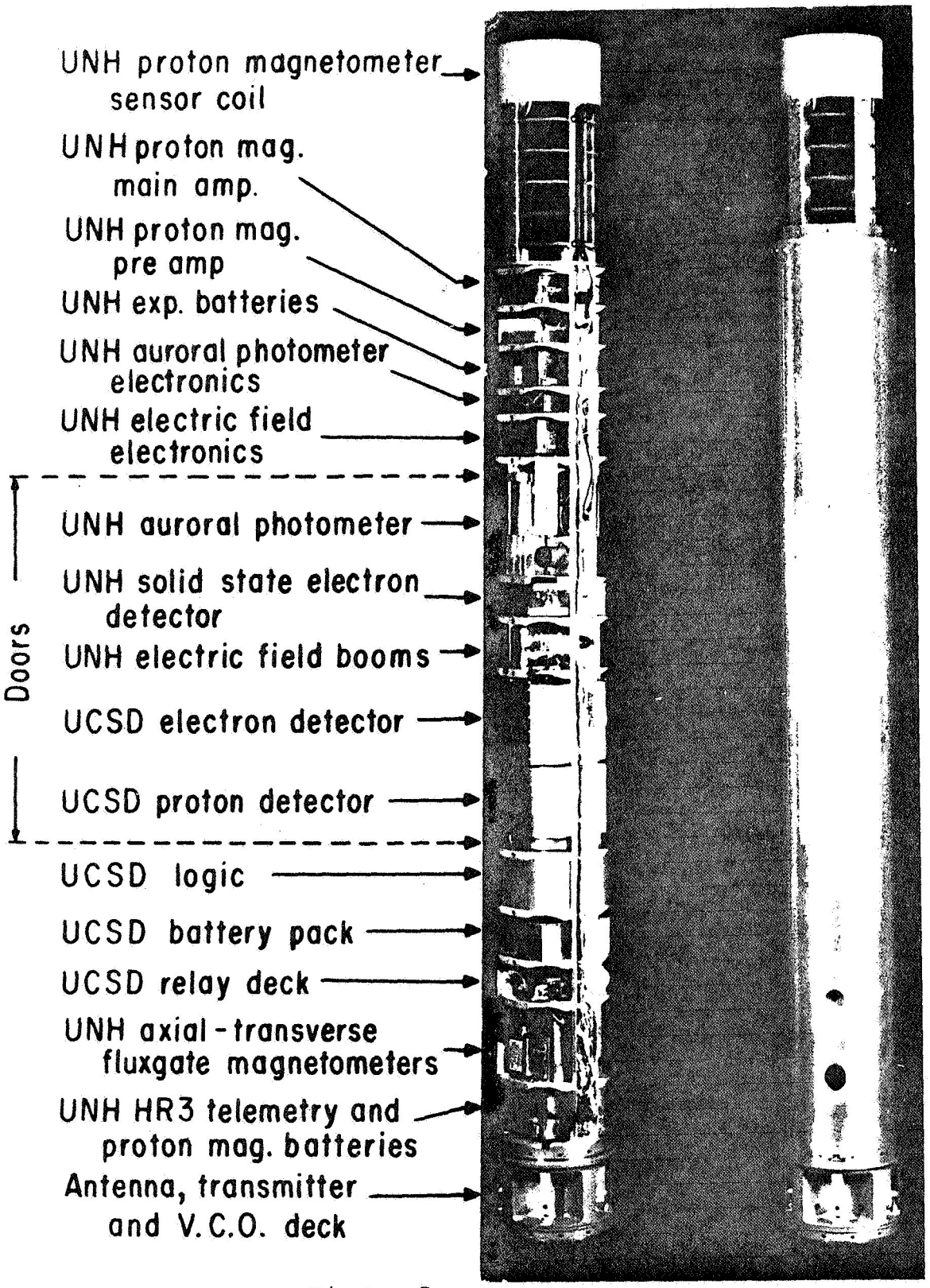
UNH proton magnetometer sensor coil
UNH proton mag. main amp.
UNH proton mag. pre amp
UNH exp. batteries
UNH auroral photometer electronics
UNH electric field electronics
UNH auroral photometer
UNH solid state electron detector
UNH electric field booms
UCSD electron detector
UCSD proton detector
Doors
UCSD logic
UCSD battery pack
UCSD relay deck
UNH axial-transverse fluxgate magnetometers
UNH HR3 telemetry and proton mag. batteries
Antenna, transmitter and V.C.O. deck

Figure 8

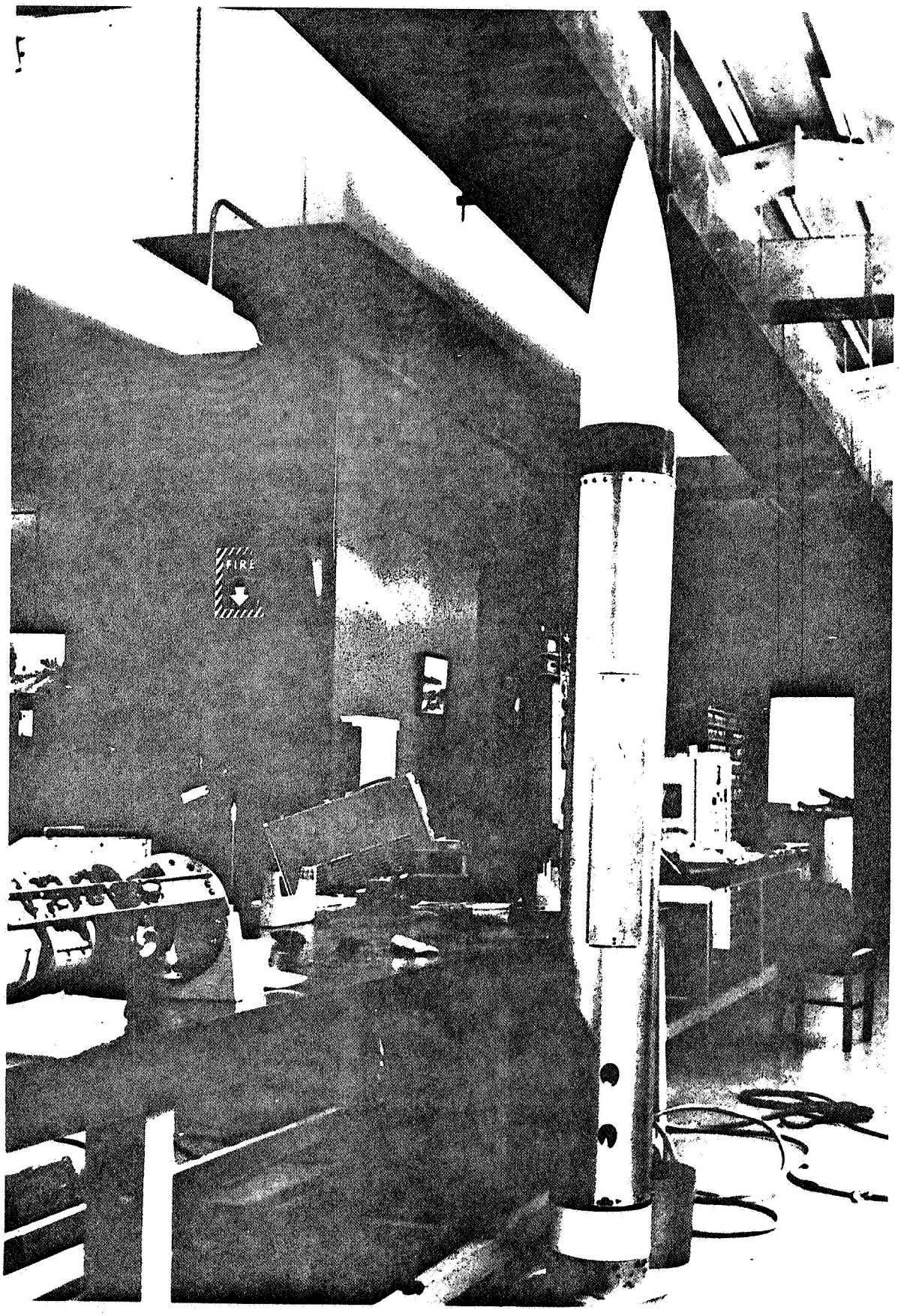

Figure 9

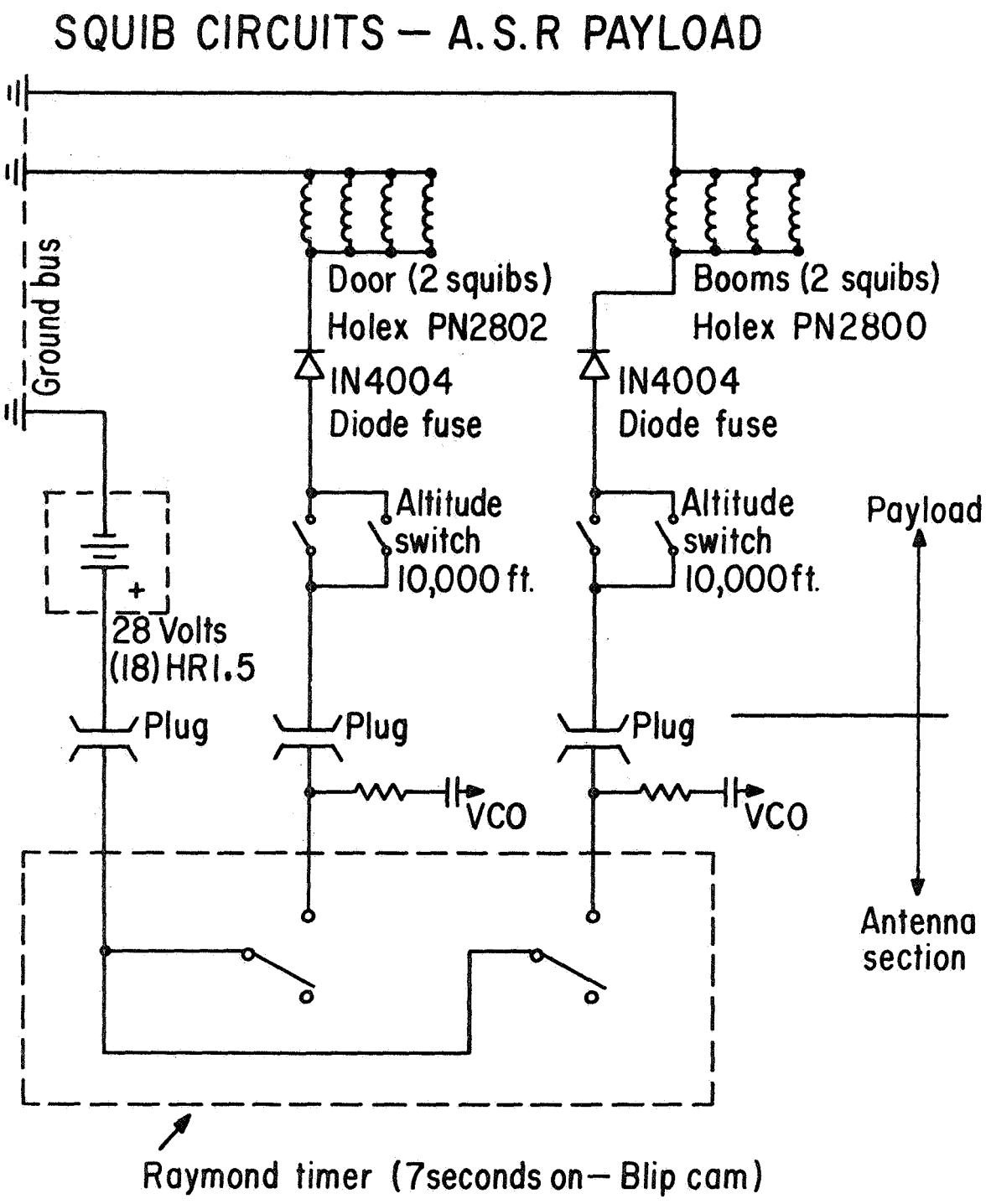

Bridge resistance ~.66 Ω each (4 bridges in parallel ~.16 Ω)

100% fire current 1.5 amps. min.

Use # 18 or # 20 *copper stranded wire*

Figure 10

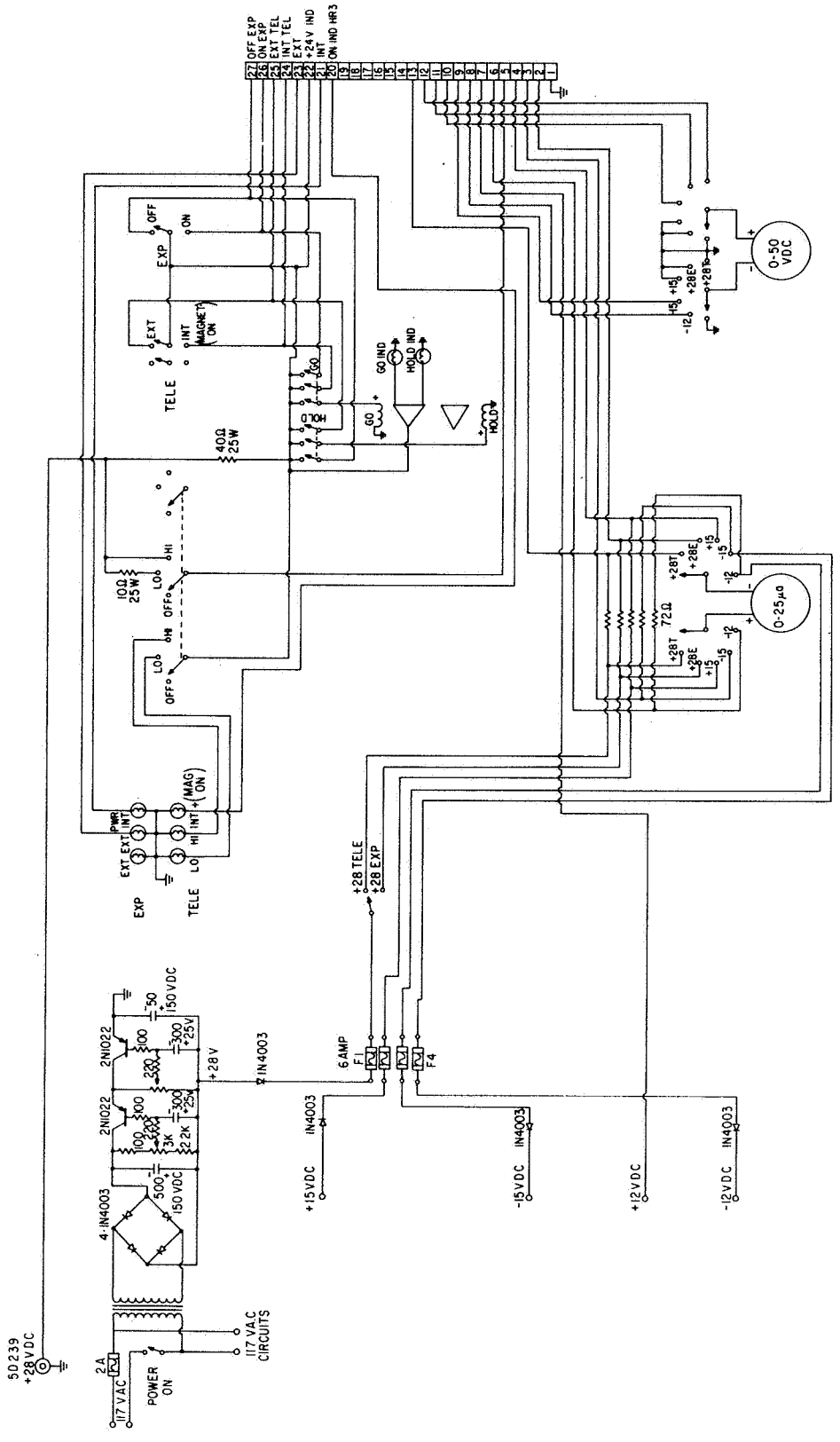
AURORAL SOUNDING ROCKET, CONTROL BOX, SERIES 18.38 - 18.42
50239
+28 VDC
2A
117 VAC
POWER ON
117 VAC CIRCUITS
4-IN4003
2N1022
2N1022
150 VDC
+28 V
IN4003
6 AMP
F1
F4
+28 TELE
+28 EXP
+15VDC
-15VDC
+12VDC
-12VDC
EXP
TELE
EXT
INT
PWR
HI
LO
(MAG) ON
TELE
EXP
OFF
ON
EXT
INT (MAGNET ON)
GO
GO IND
HOLD IND
HOLD
40Ω 25W
10Ω 25W
72Ω
0-50 VDC
0-25μa
OFF EXP
ON EXP
EXT TEL
INT TEL
EXT +24V IND
INT
ON IND HR3

Figure 11

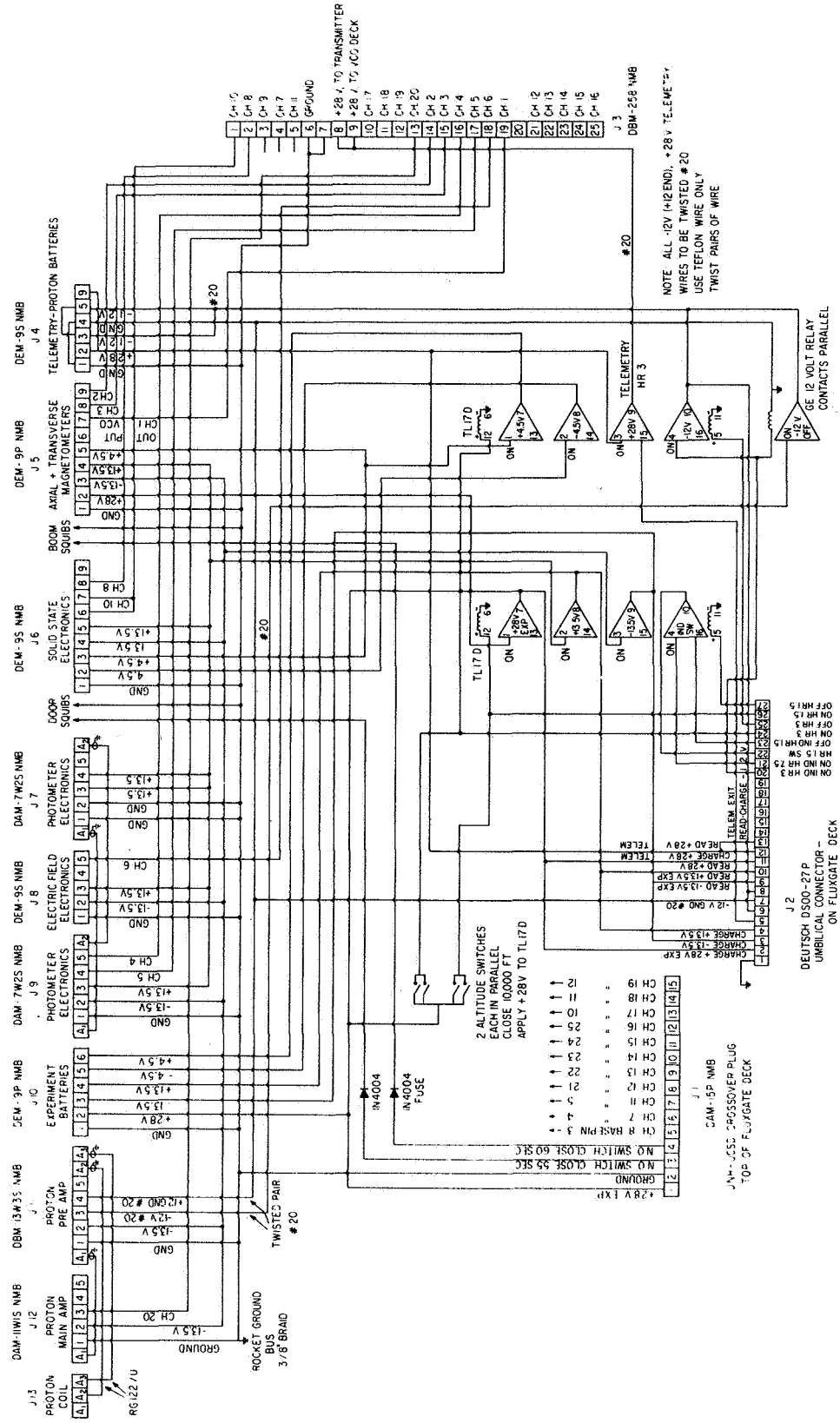
RACEWAY WIRING, UNH AURORAL SOUNDING ROCKET, SERIES 18.38-18.42 NIKE TOMAHAWK
NOTE ALL -12V (+12 END), +28 V TELEMETRY WIRES TO BE TWISTED #20
USE TEFLON WIRE ONLY
TWIST PAIRS OF WIRE
2 ALTITUDE SWITCHES EACH IN PARALLEL CLOSE 100,000 FT APPLY +28V TO TL17D
IN4004 FUSE
IN4004
TWISTED PAIR #20
ROCKET GROUND BUS 3/8" BRAID
RG122/U
DEUTSCH DSOO-27P UMBILICAL CONNECTOR - ON FLUXGATE DECK
TELEMETRY HR 3
GE 12 VOLT RELAY CONTACTS PARALLEL
TL17D
DBM-25B NMB
DAM-15P NMB
DAM-11W1S NMB
DBM-13W3S NMB
DEM-9P NMB
DAM-7W2S NMB
DEM-9S NMB
DEM-9P NMB
DEM-9P NMB
DEM-9S NMB
DAM-7W2S NMB
DEM-9S NMB
DEM-9P NMB
DEM-9S NMB
PROTON COIL
PROTON MAIN AMP
PROTON PRE AMP
EXPERIMENT BATTERIES
PHOTOMETER ELECTRONICS
ELECTRIC FIELD ELECTRONICS
PHOTOMETER ELECTRONICS
SOLID STATE ELECTRONICS
BOOM SQUIBS
AXIAL + TRANSVERSE MAGNETOMETERS
TELEMETRY-PROTON BATTERIES
+28 V TO TRANSMITTER
+28 V TO ACS DECK
GROUND
NO SWITCH CLOSE 55 SEC
NO SWITCH CLOSE 60 SEC
+28V EXP
TELEM EXIT
READ-CHARGE

Figure 12

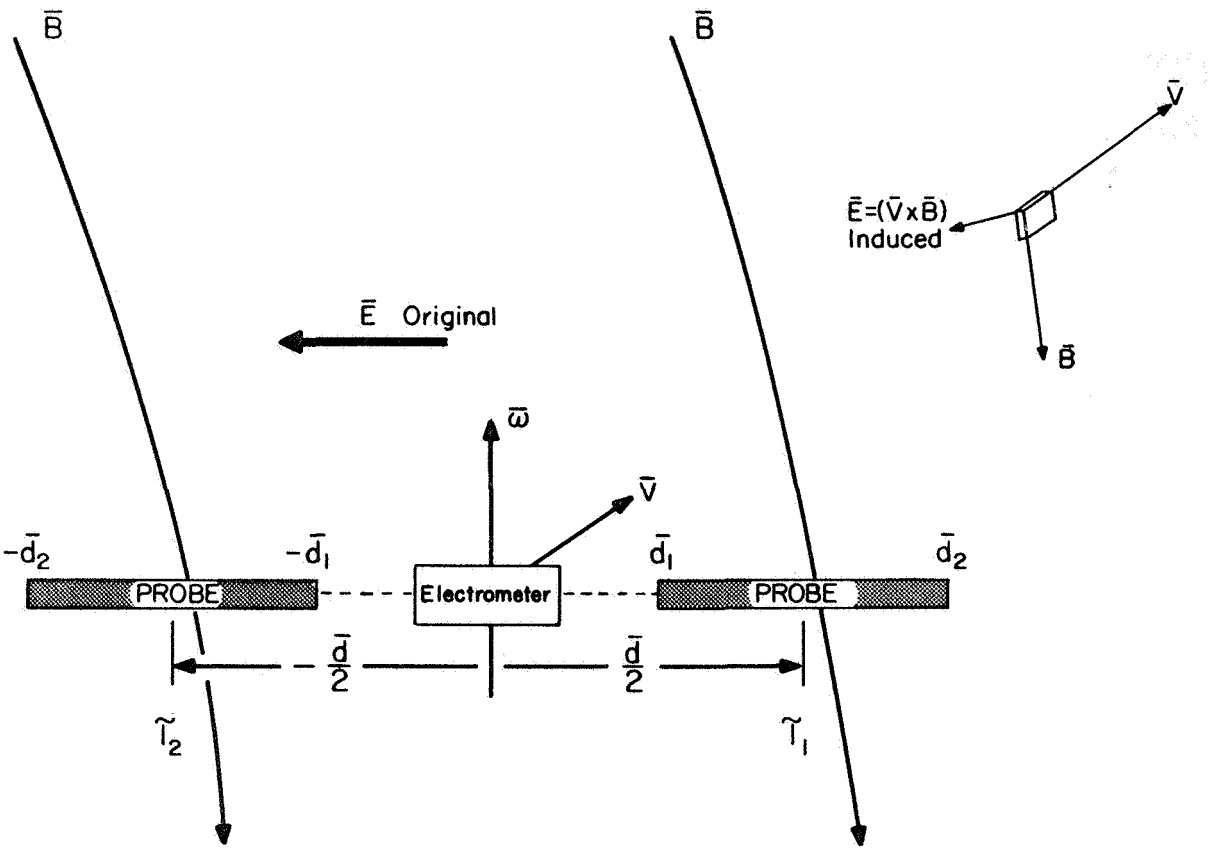

$\Delta\phi = \Delta\phi_o + \Delta\phi_1$ Potential difference between $\tilde{l}_1$ and $\tilde{l}_2$

$\Delta\phi_o = E\,d\,\cos(\tilde{d},\tilde{E})$

$\Delta\phi_1 = vBd\,\sin(\bar{v},\bar{B})\,\cos(\bar{v}\times\bar{B},\bar{d})$

The $\tilde{V}\times\tilde{B}$ effect for collinear cylindrical probes (After Potter, 1966)

Figure 13

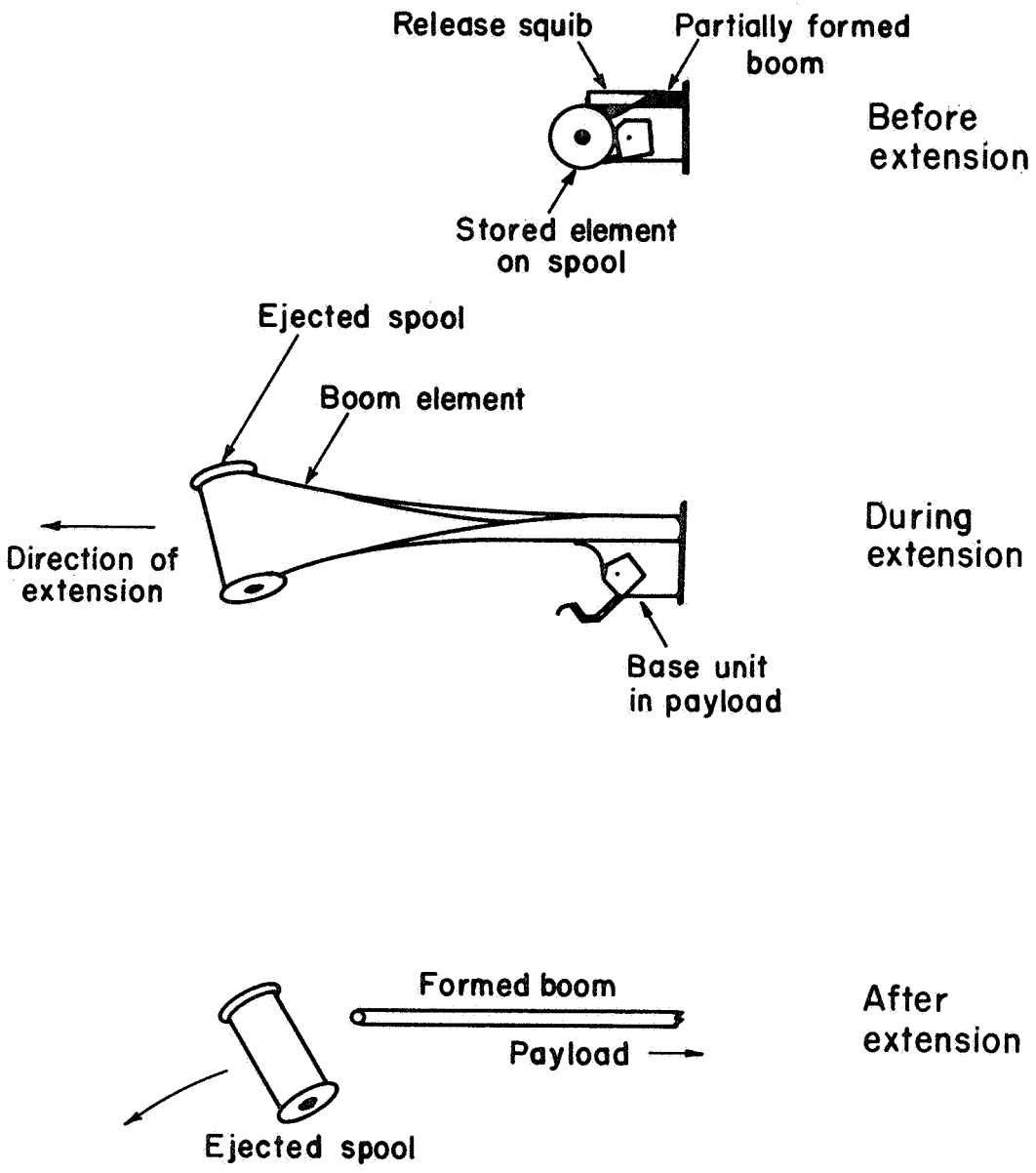

Ejection sequence
Unfurlable electric field booms

Figure 14

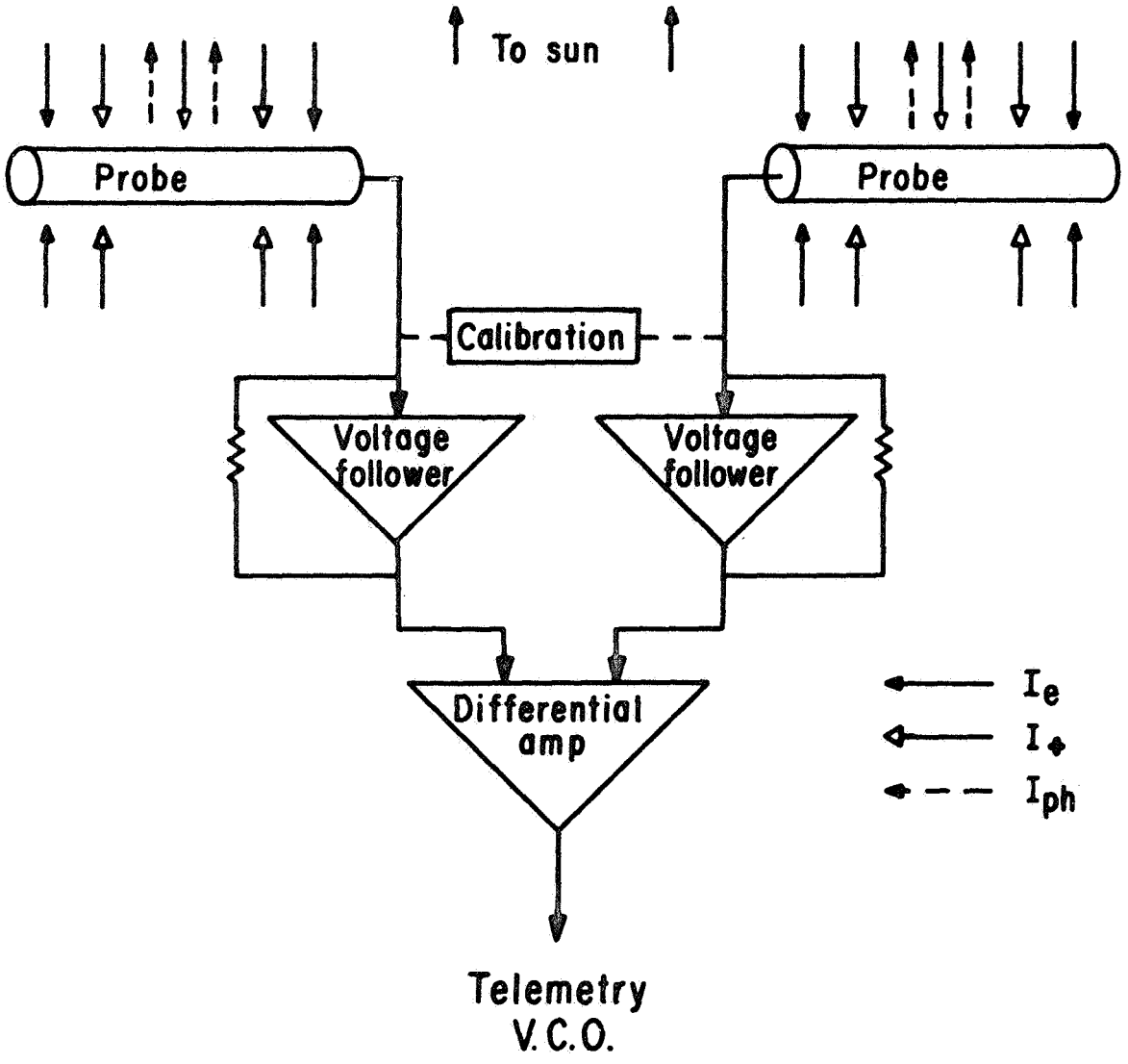

Electric field measuring technique

Figure 15

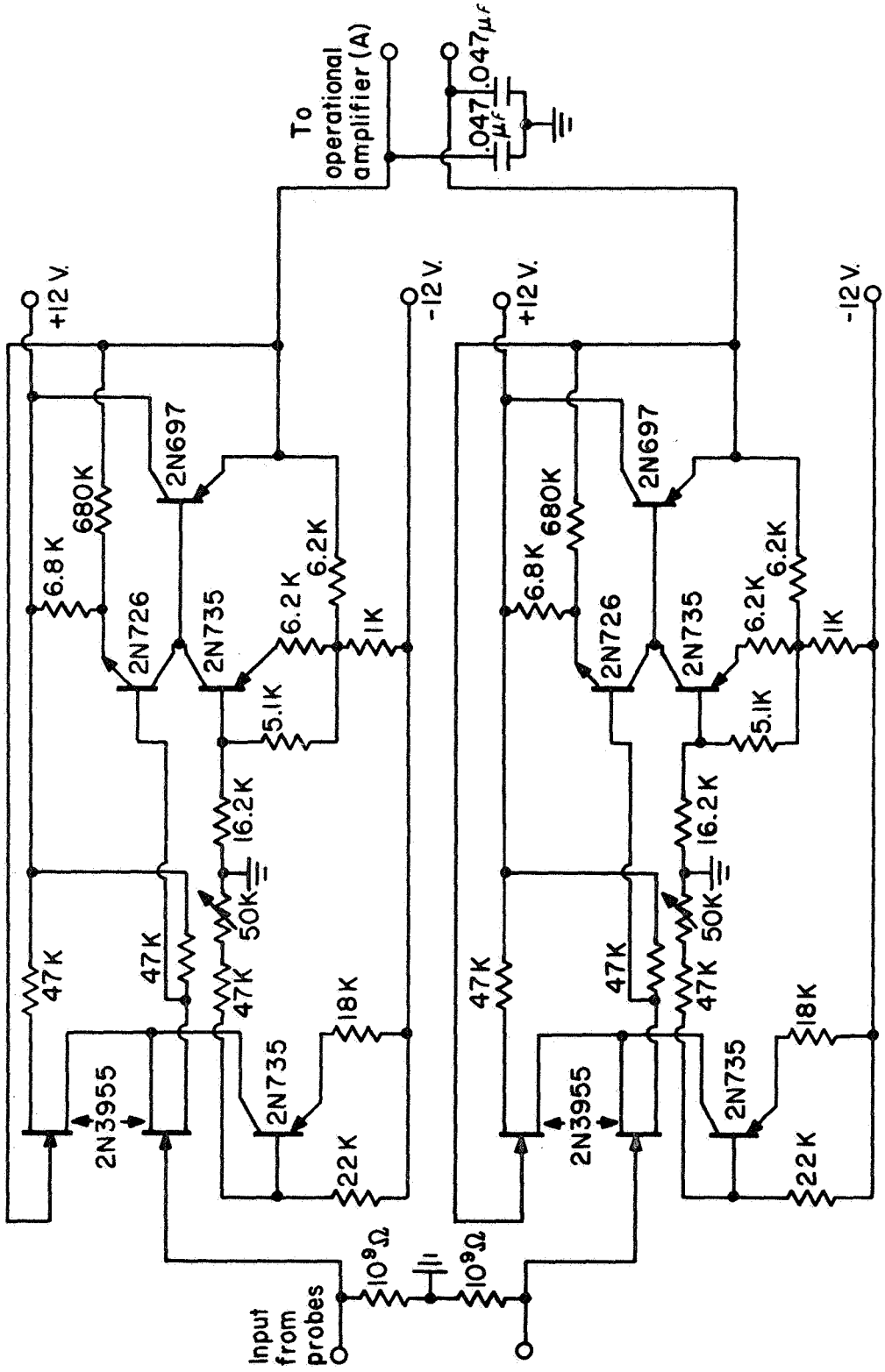
Field effect voltage follower front end
To operational amplifier (A)
.047 μf
.047 μf
+12 V.
-12 V.
+12 V.
-12 V.
2N697
2N726
2N735
2N3955
680K
6.8 K
6.2K
1K
5.1K
16.2K
50K
47K
18K
22K
Input from probes
10⁹Ω
10⁹Ω

Figure 16

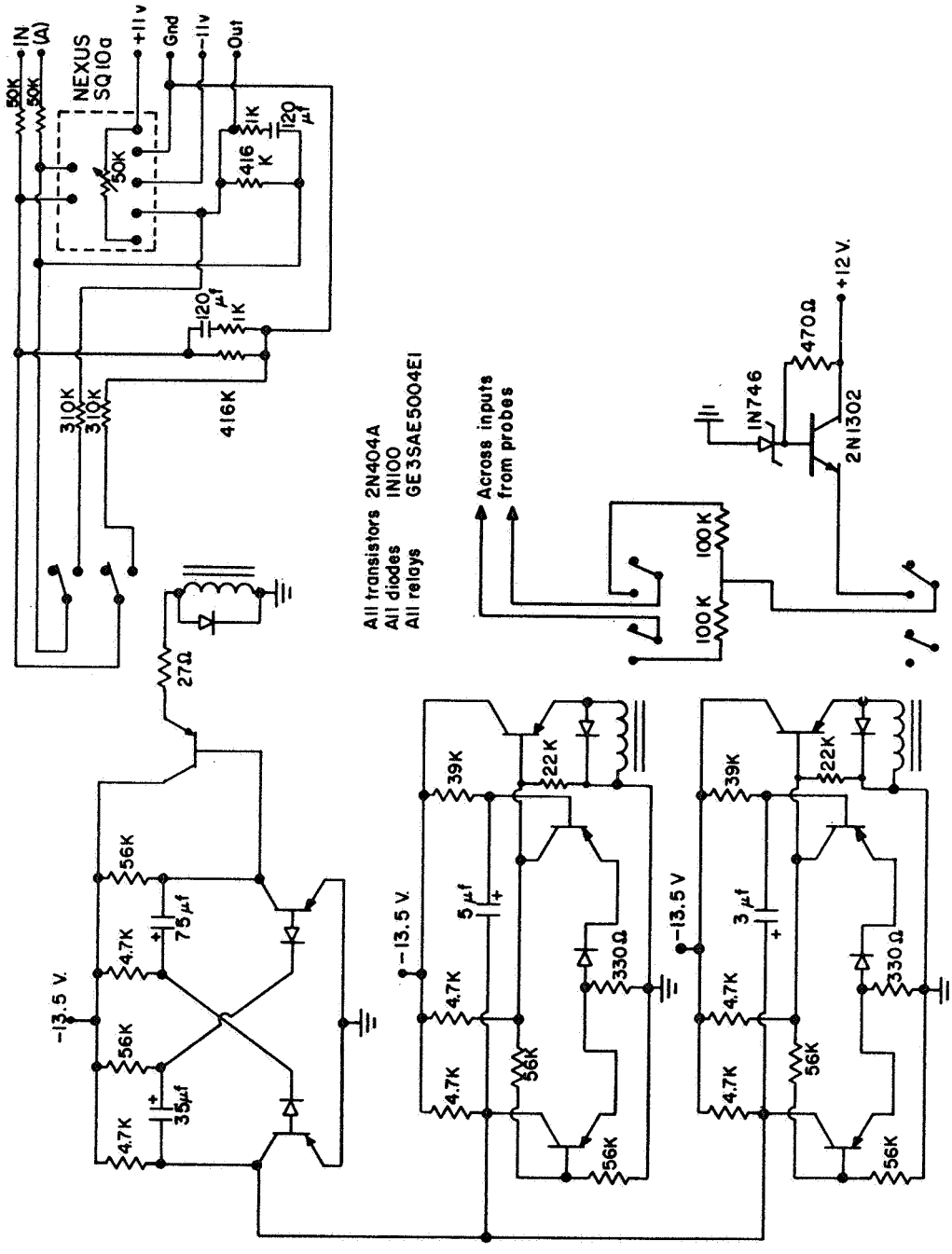

Calibration circuit with operational amplifier

Figure 17

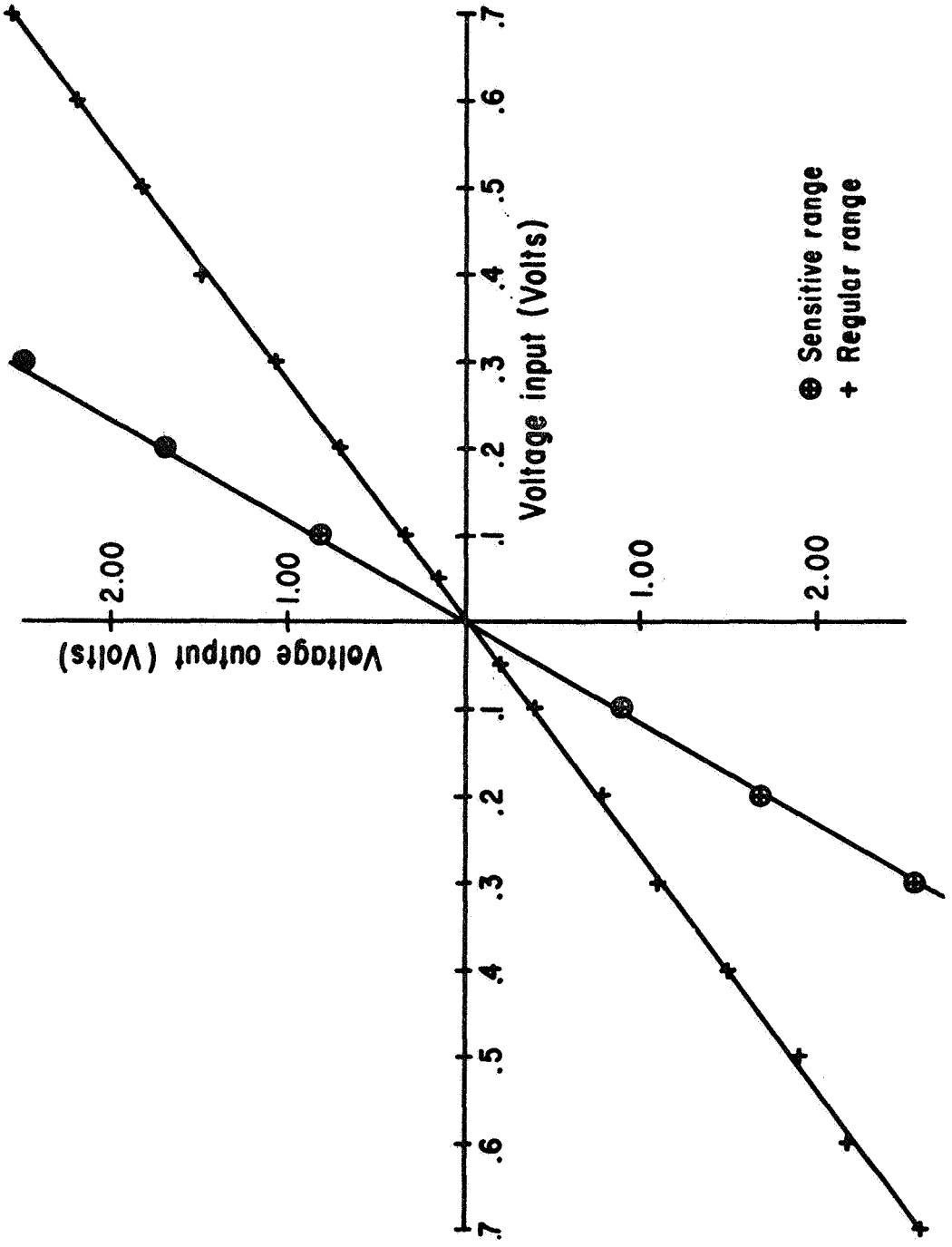

Calibration curve 18.39 electric field meter

Figure 18

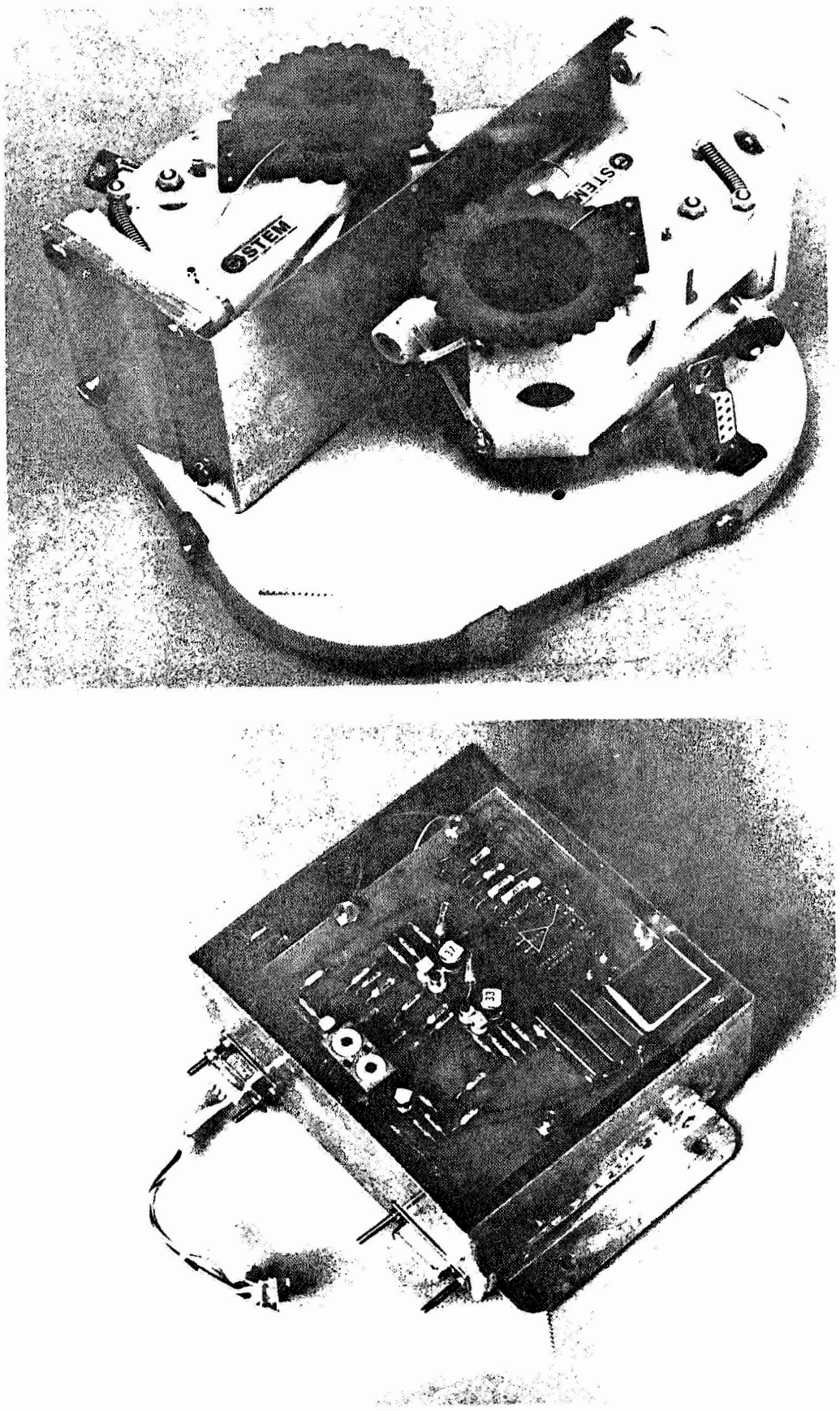

Figure 19

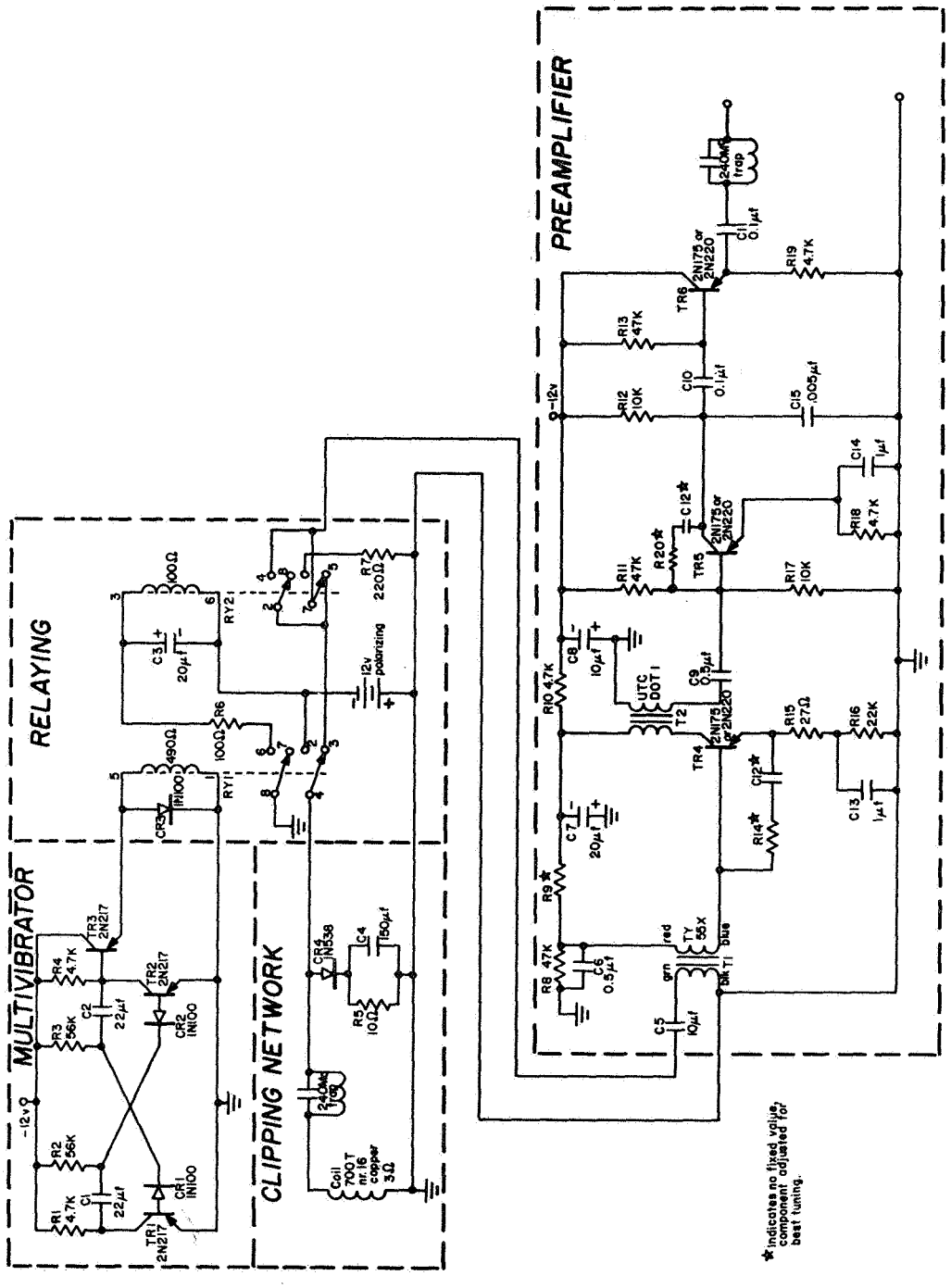

Proton magnetometer (Maynard, 1966)

Figure 20

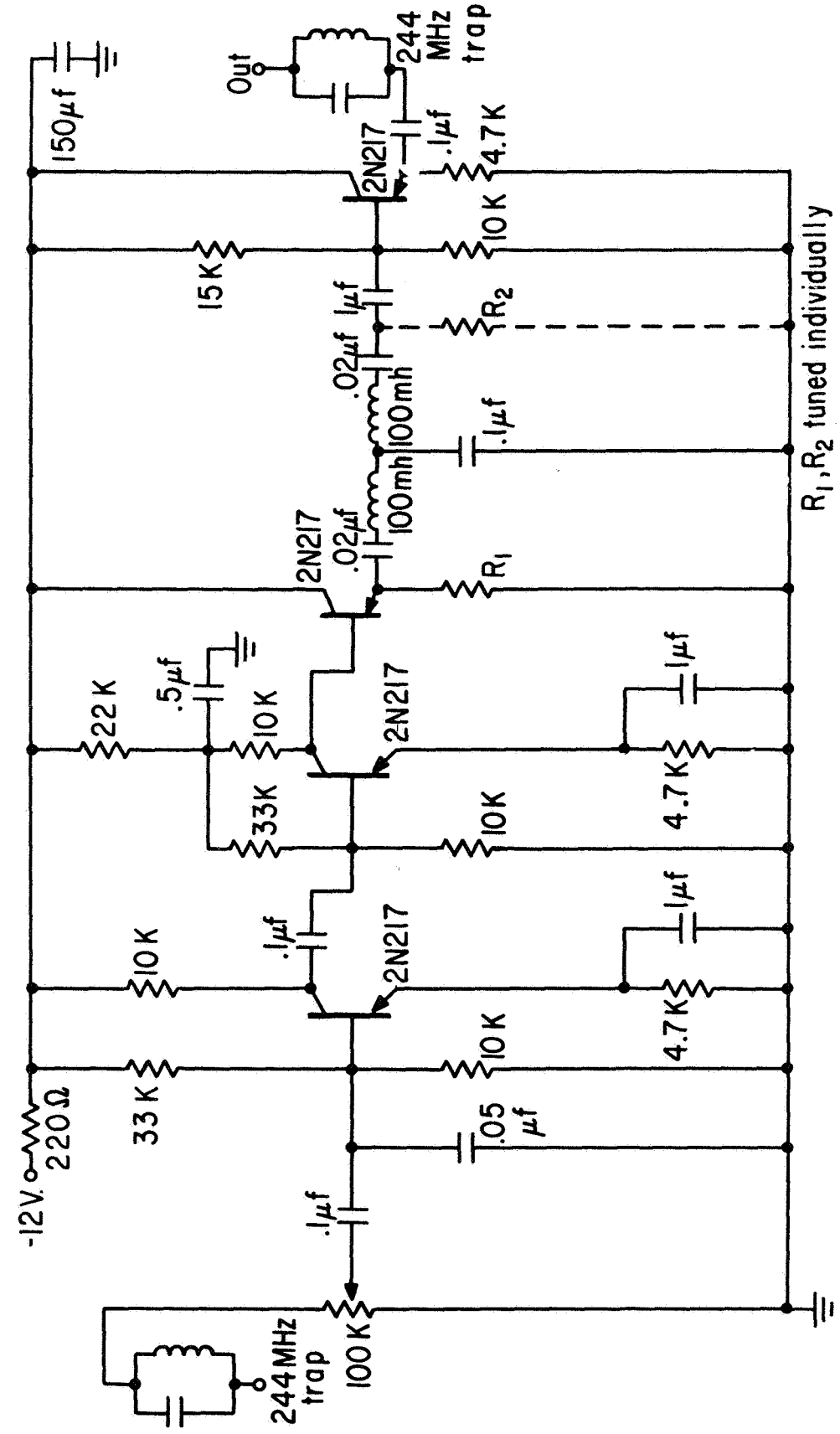

Proton magnetometer main amp (Maynard, 1966)

Figure 21

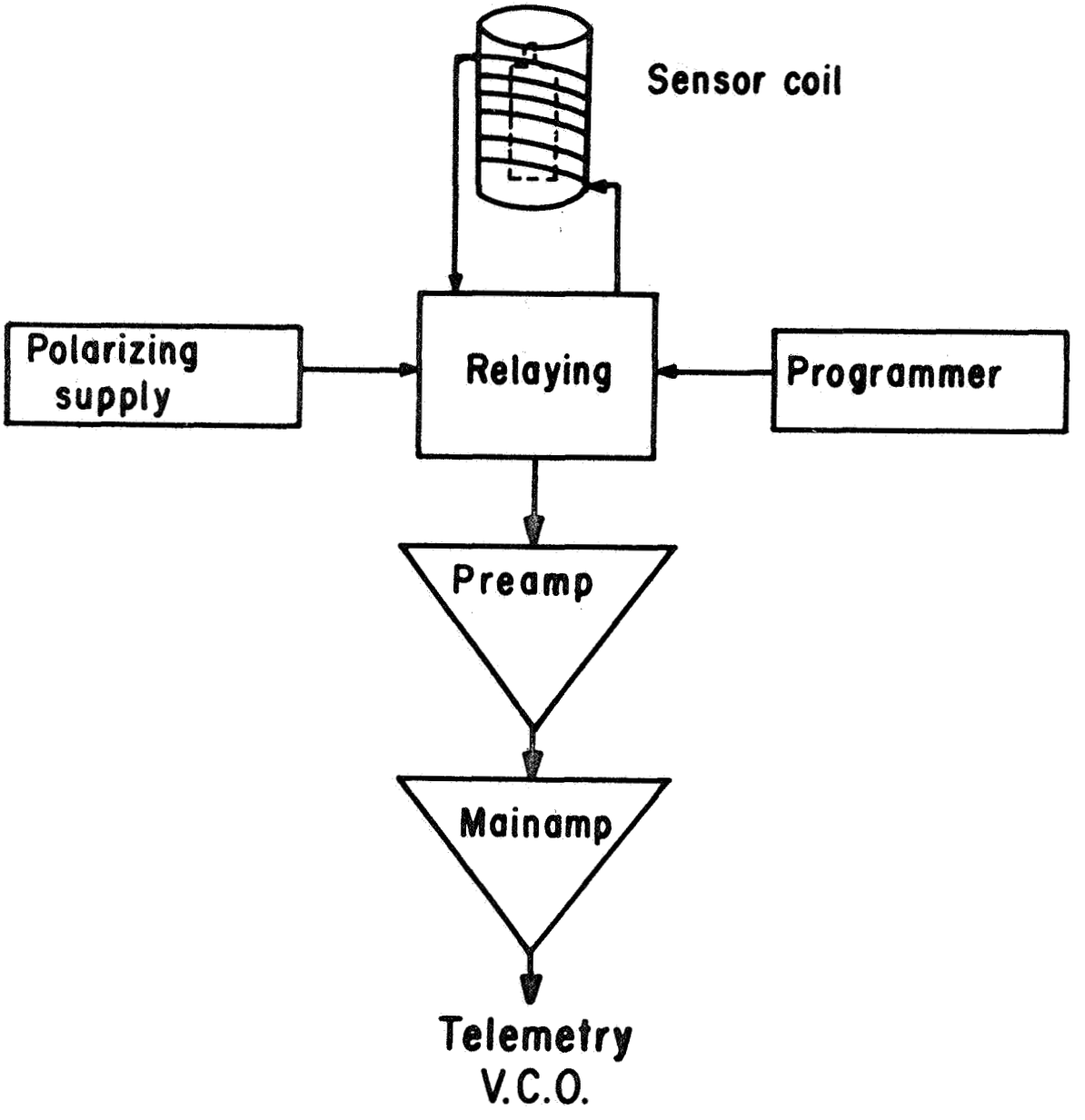

Proton precession magnetometer

Figure 22

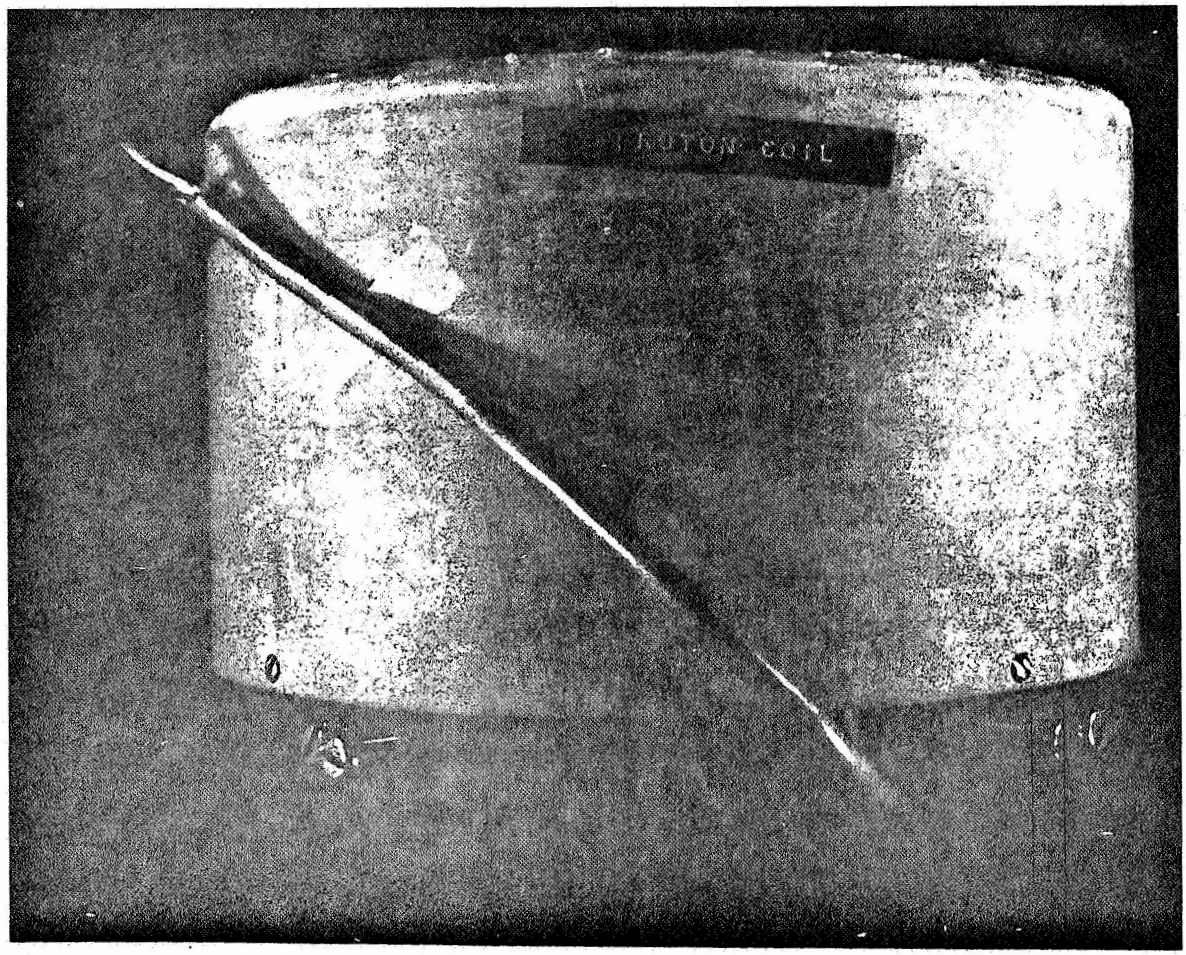

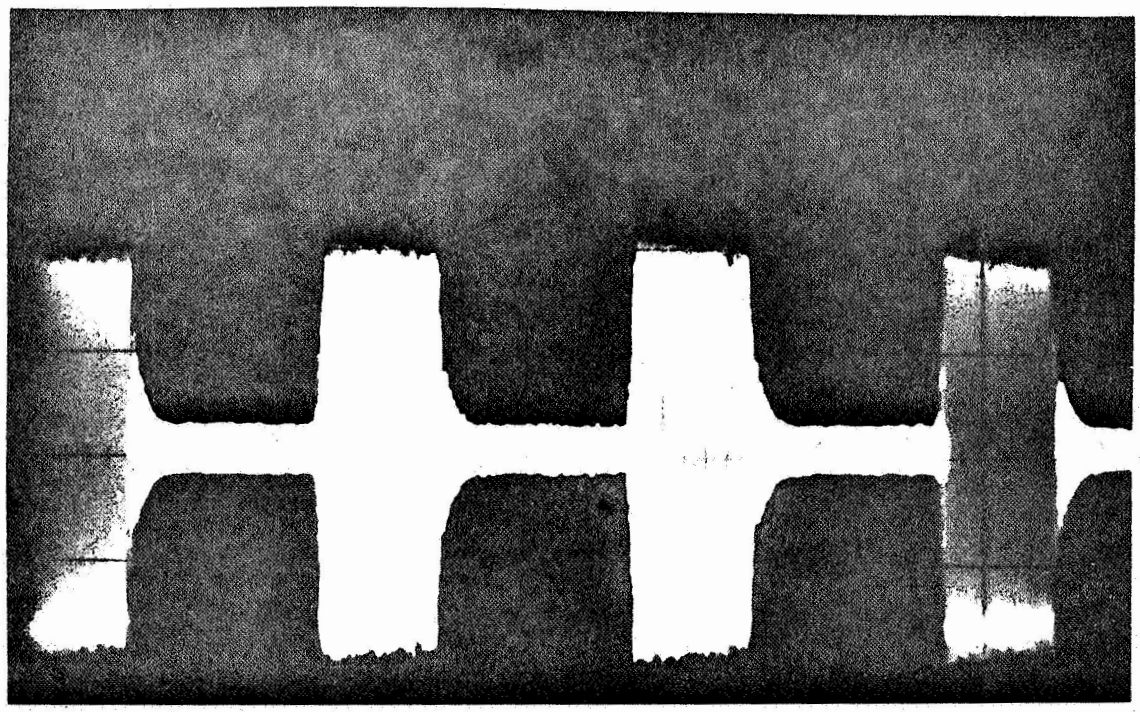

Figure 23

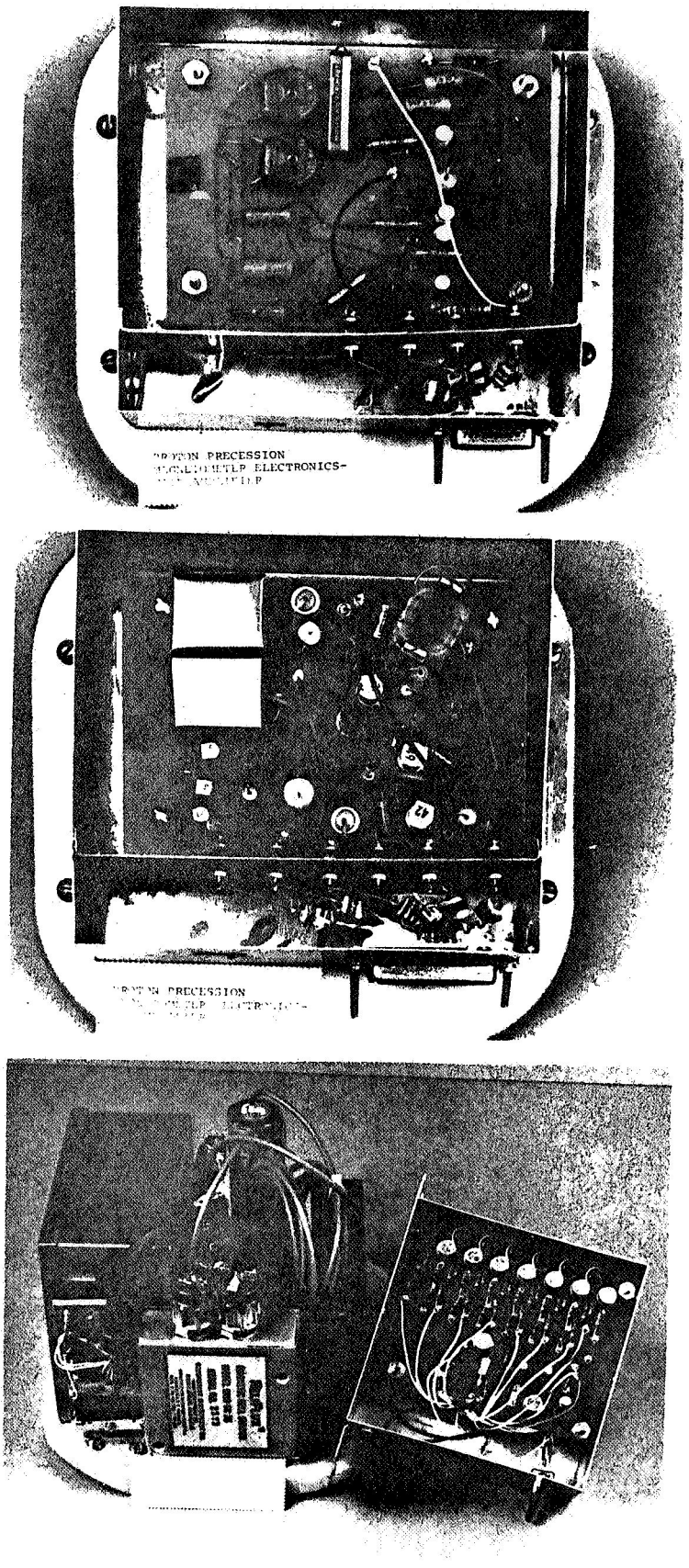

Figure 24

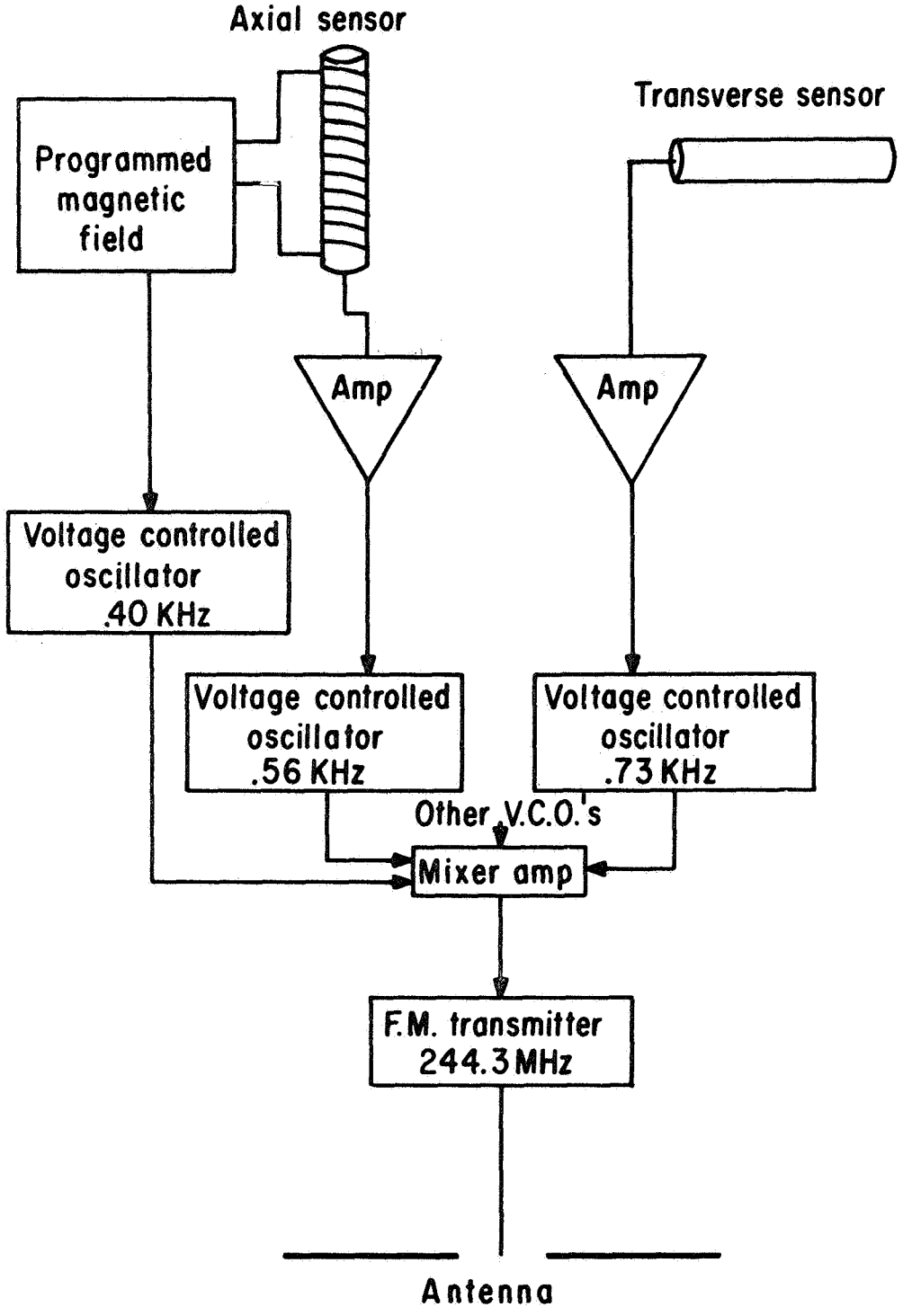

Axial and transverse fluxgate magnetometers

Figure 25

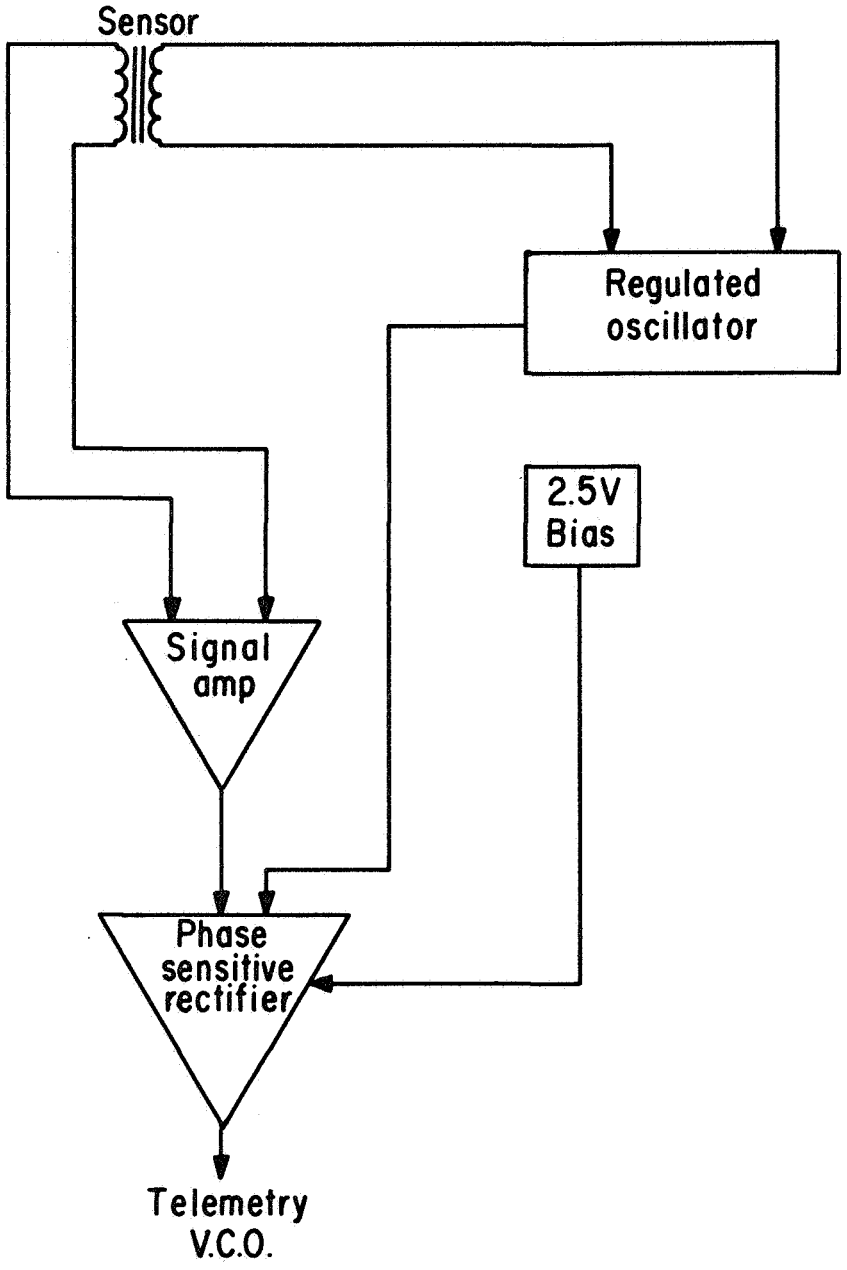

Fluxgate magnetometer diagram

Figure 26

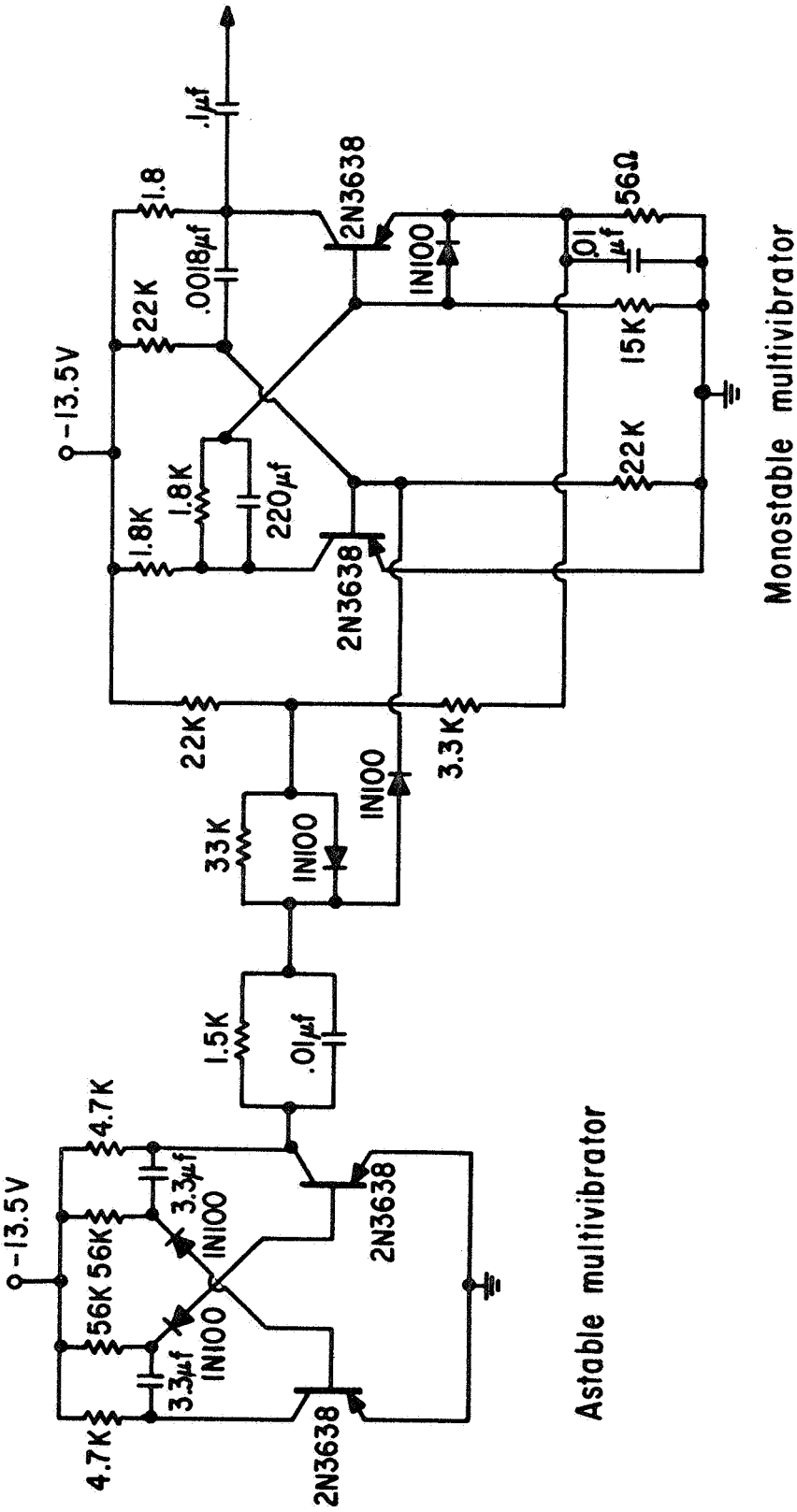

Axial fluxgate magnetometer- Bucking coil circuits

Figure 27

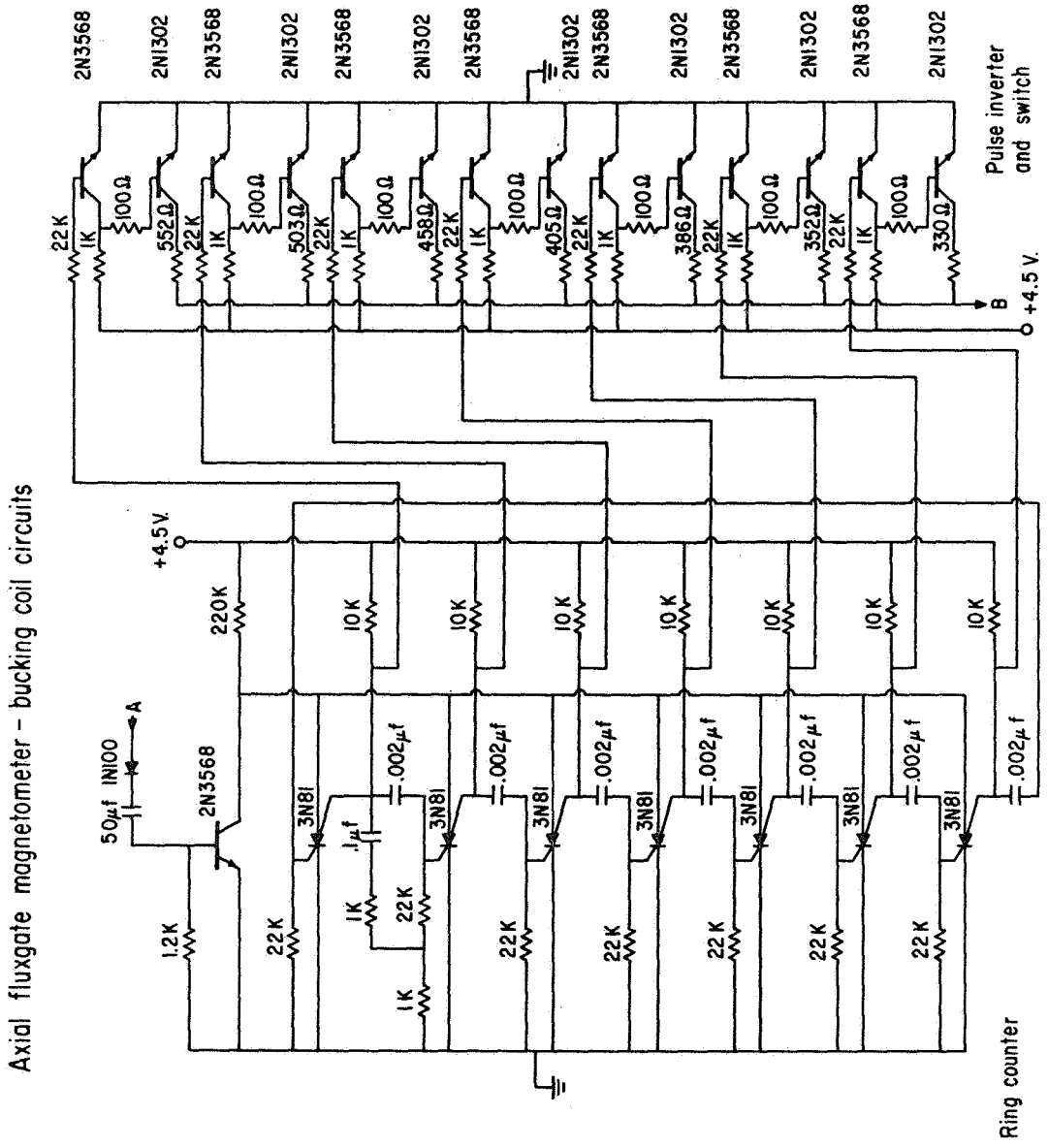
Axial fluxgate magnetometer - bucking coil circuits
Pulse inverter and switch
Ring counter
+4.5 V.
+4.5 V.
B
A
2N3568
2N1302
50μf
IN100
1.2K
220K
10K
22K
1K
.002μf
.1μf
3N81
100Ω
552Ω
503Ω
458Ω
405Ω
386Ω
352Ω
330Ω

Figure 28

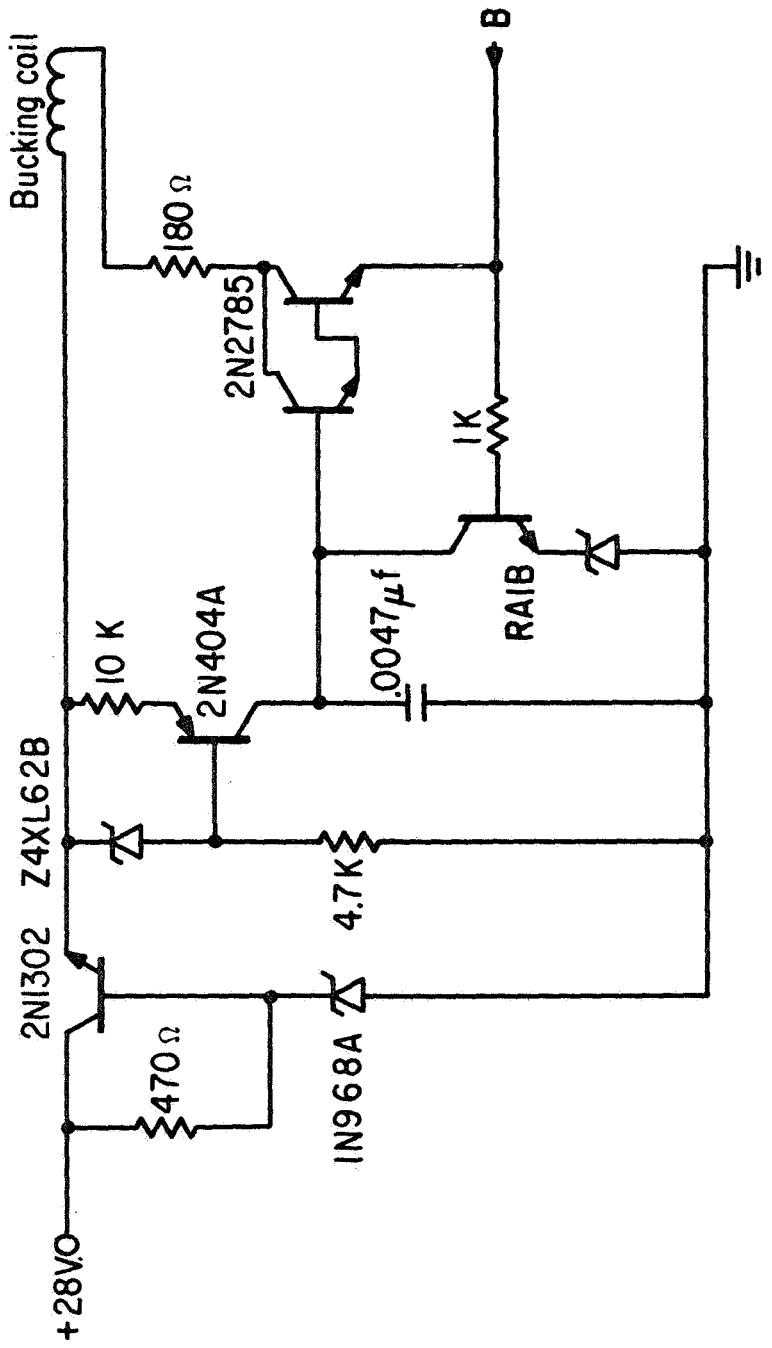

Constant current supply
Axial fluxgate magnetometer - Bucking coil circuits

Figure 29

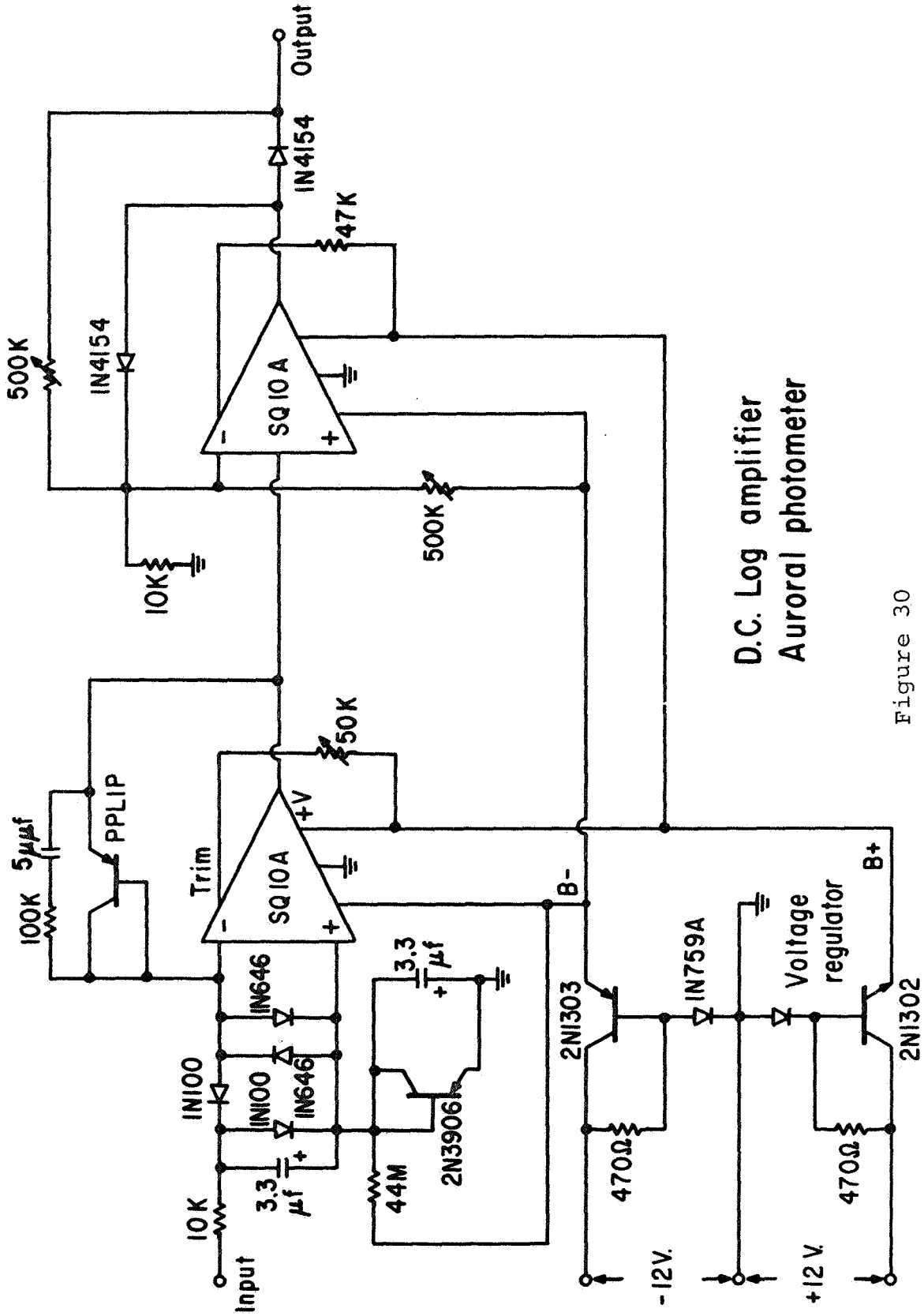
D.C. Log amplifier
Auroral photometer
Output
IN4154
47K
500K
IN4154
SQ 10 A
500K
10K
50K
+V
Trim
SQ 10A
PPLIP
100K
5μμf
IN646
IN100
IN100
IN646
3.3 μf
3.3 μf
2N3906
44M
10K
Input
B-
2N1303
IN759A
Voltage regulator
B+
2N1302
470Ω
470Ω
-12V.
+12 V.

Figure 30

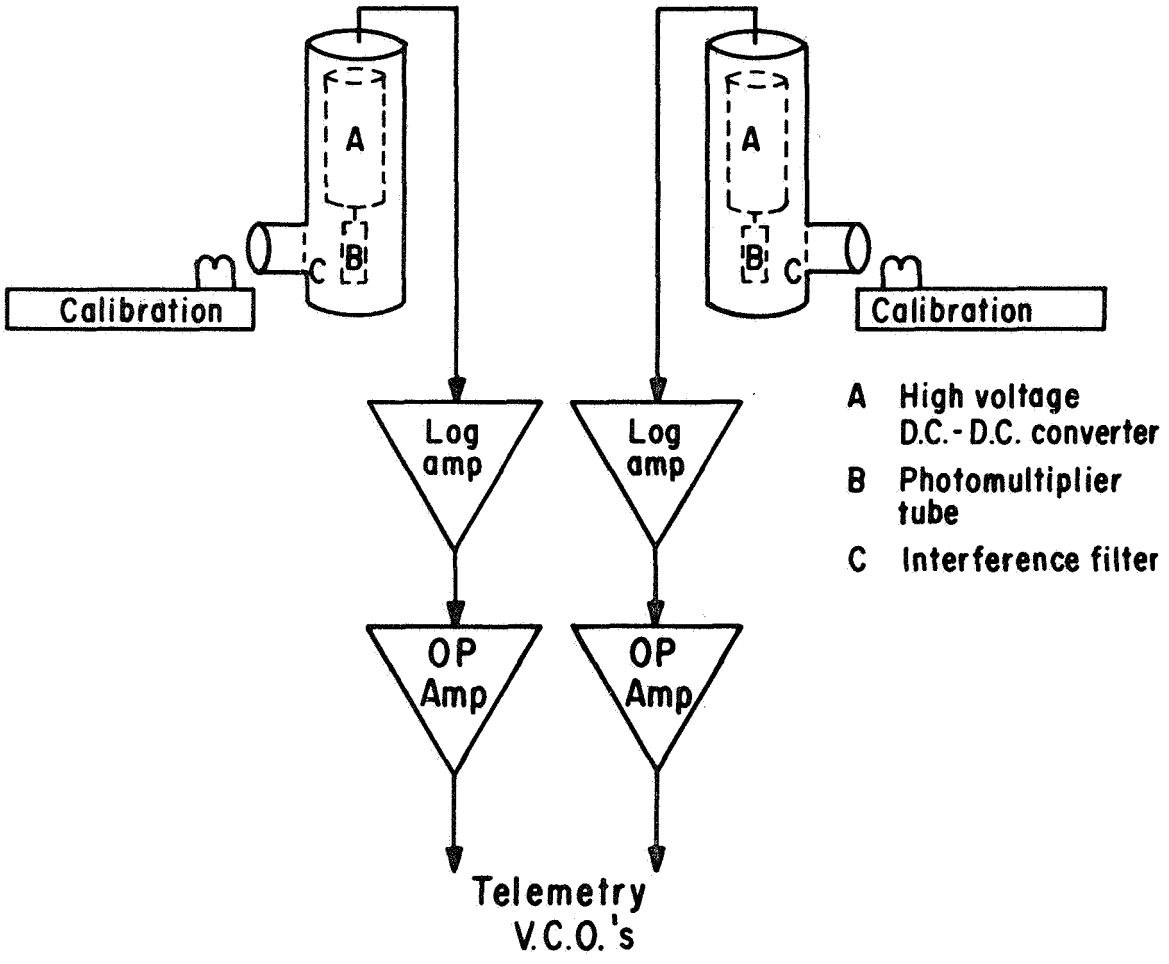

Auroral photometers 5577 Å, 6300 Å

Figure 31

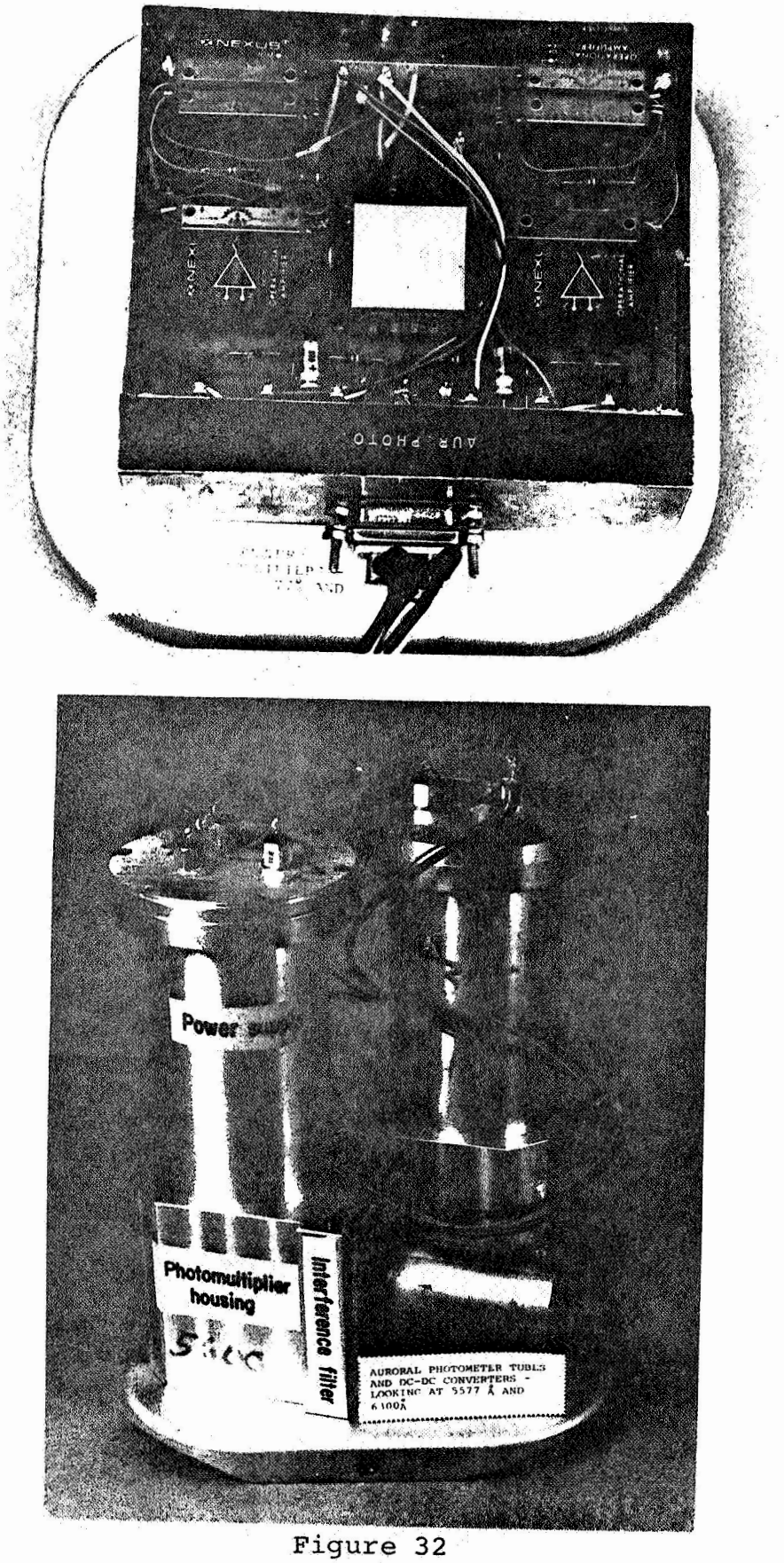
AUR PHOTO
Power supply
Photomultiplier housing
Interference filter
AURORAL PHOTOMETER TUBES AND DC-DC CONVERTERS - LOOKING AT 5577 Å AND 6100Å

Figure 32

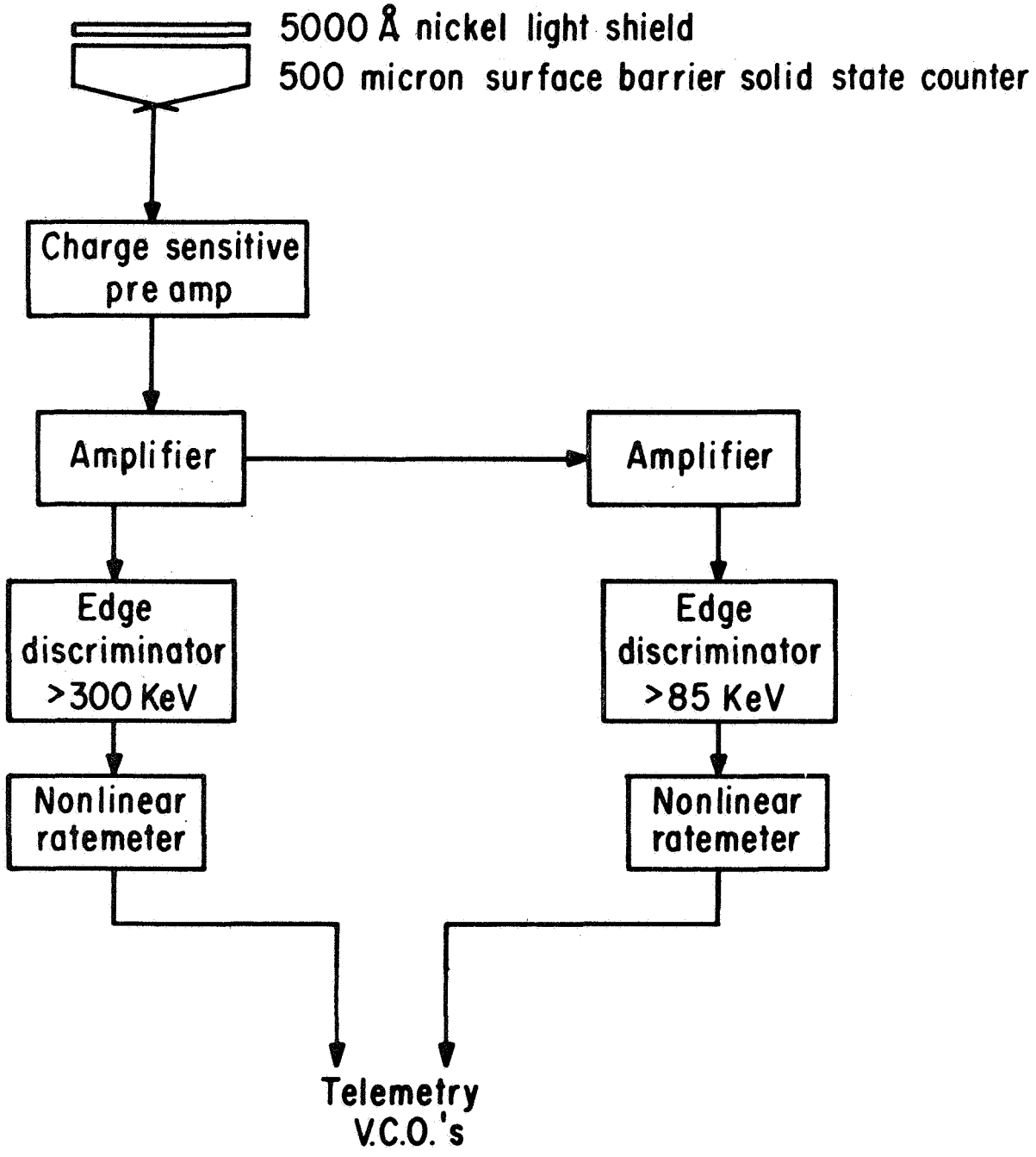

Solid state electron detector

Figure 33

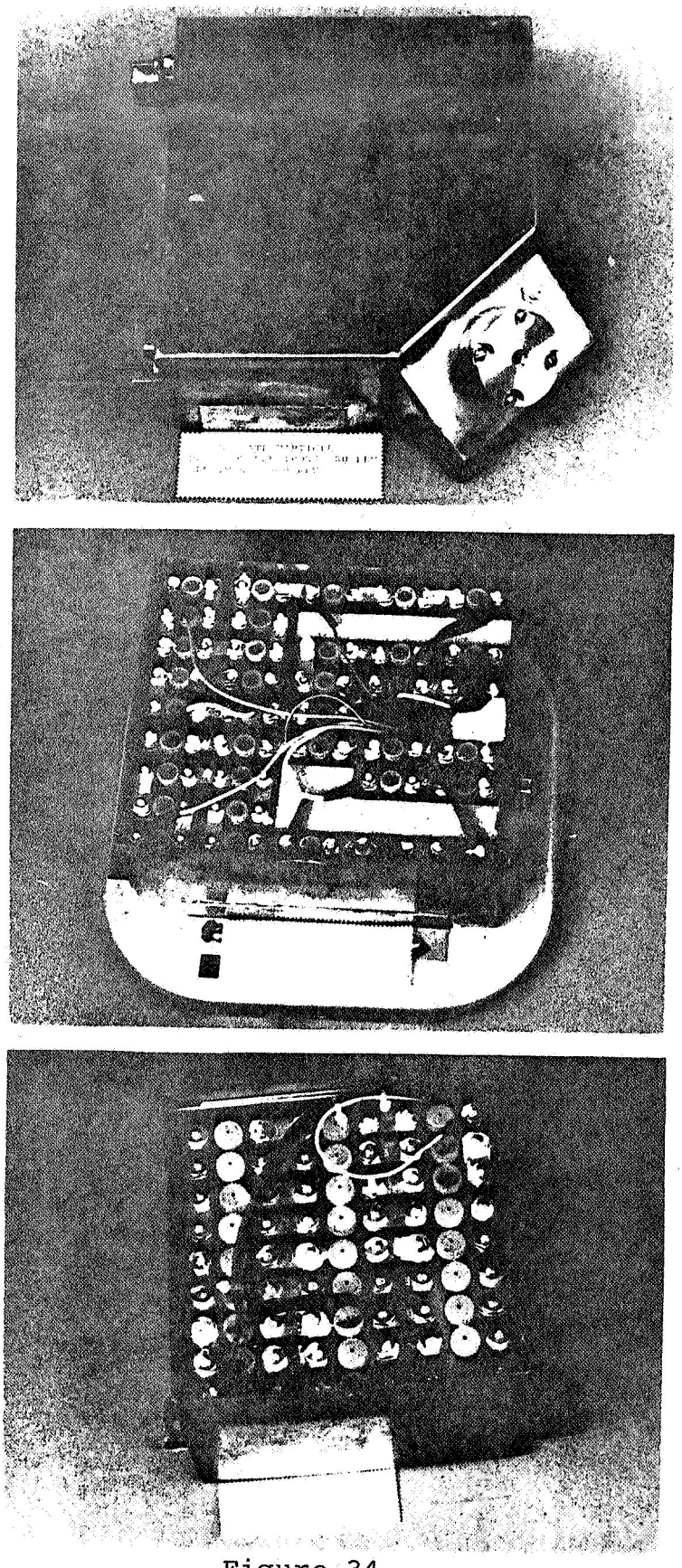

Figure 34

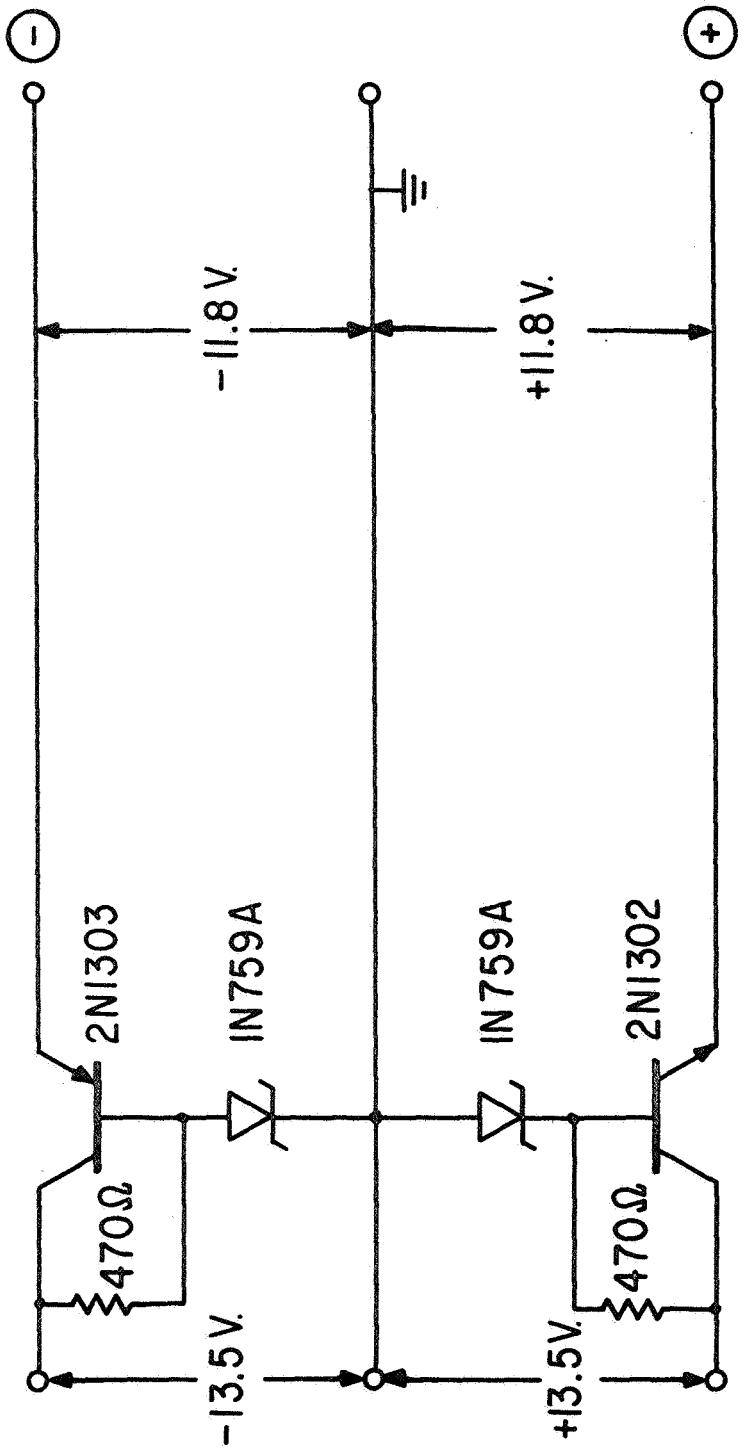

Simple D.C. voltage regulator

Figure 35

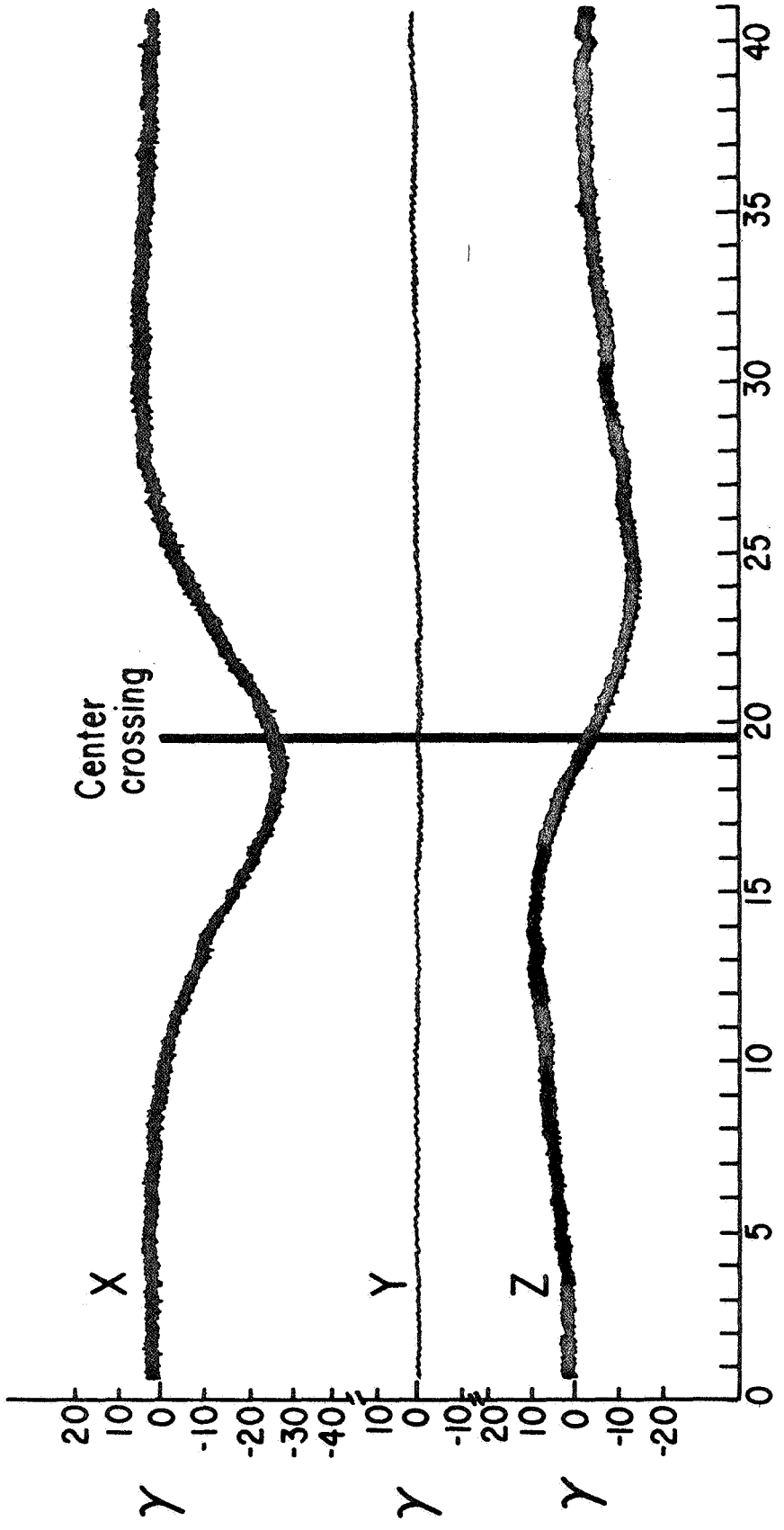
Center
crossing
X
Y
Z
γ
γ
γ
20
10
0
-10
-20
-30
-40
10
0
-10
-20
10
0
-10
-20
0
5
10
15
20
25
30
35
40
Seconds (from start of run)
Magnetic signature - Electric field meter

Figure 36

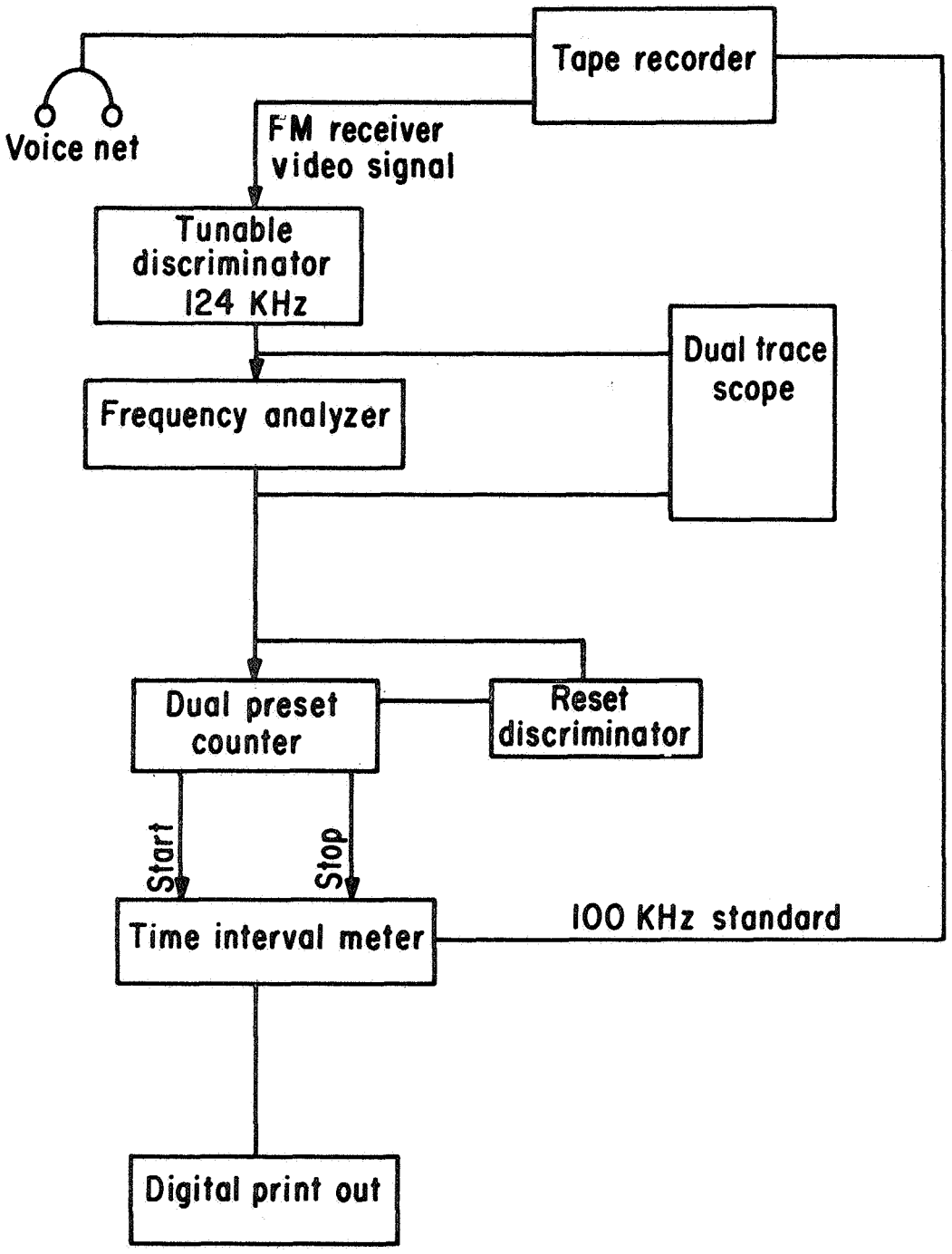

Proton magnetometer data reduction technique

Figure 37

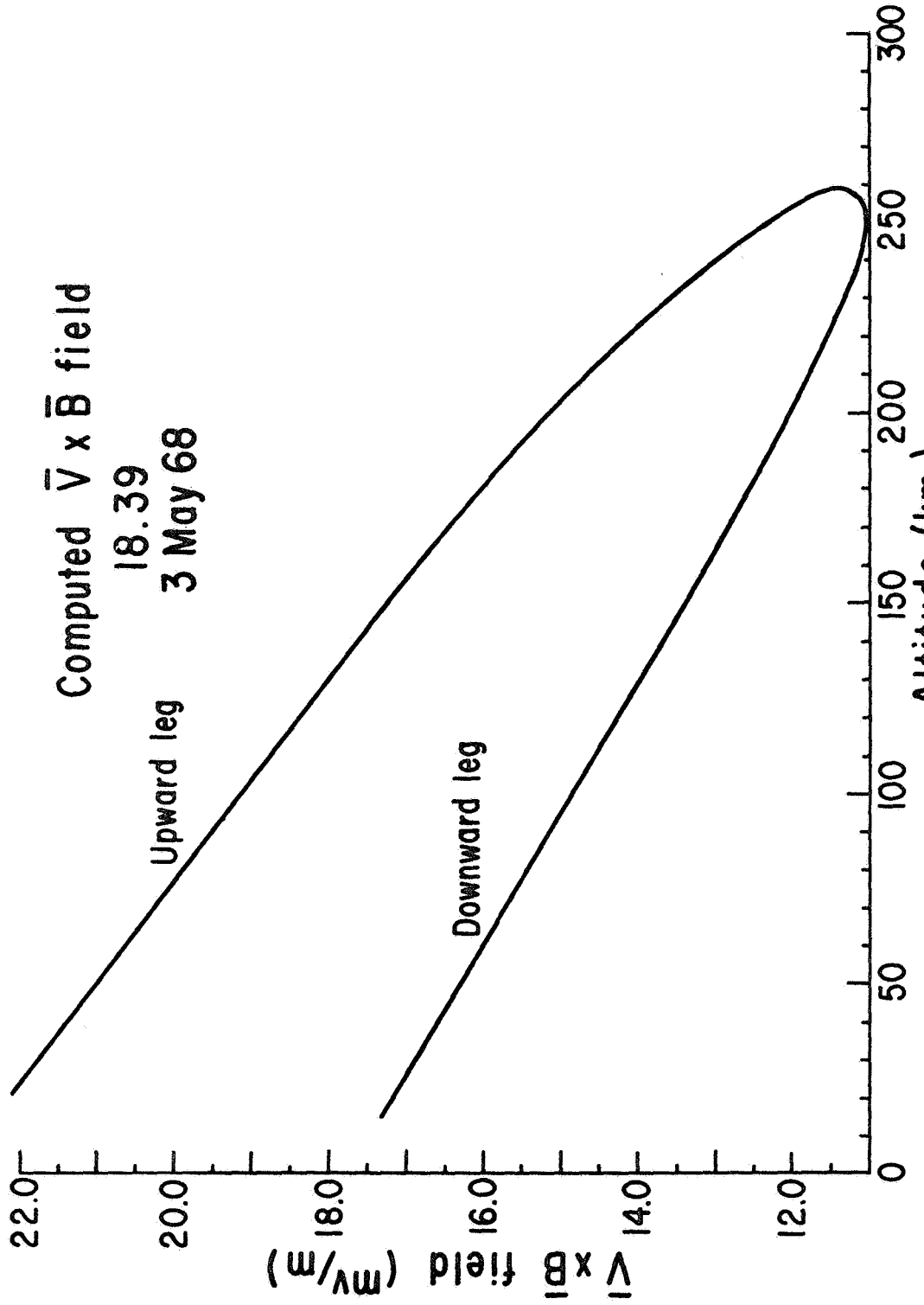
Computed $\bar{V} \times \bar{B}$ field
18.39
3 May 68
Upward leg
Downward leg
$\bar{V} \times \bar{B}$ field (mV/m)
22.0
20.0
18.0
16.0
14.0
12.0
0
50
100
150
200
250
300
Altitude (km.)

Figure 38

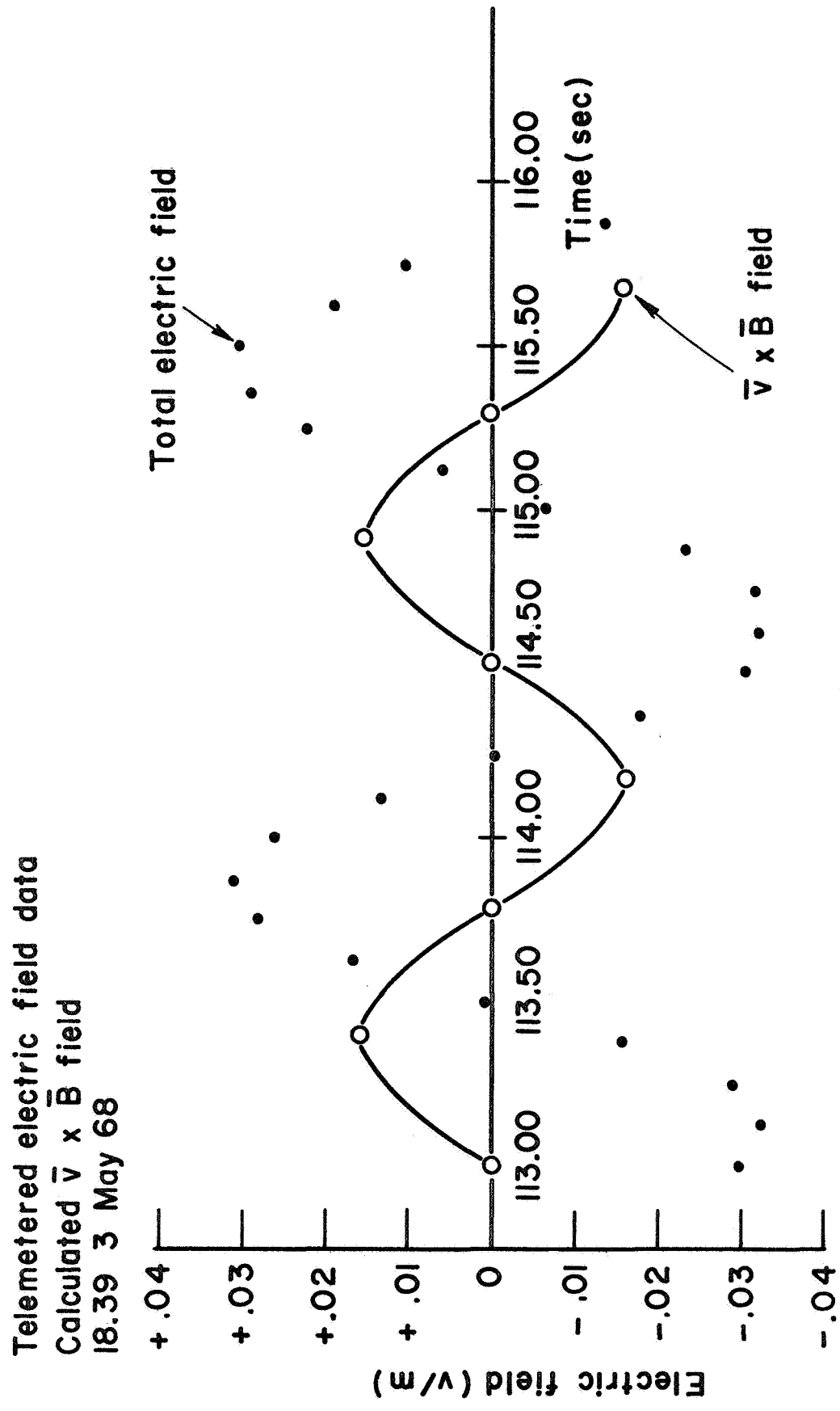
Telemetered electric field data
Calculated $\bar{v} \times \bar{B}$ field
18.39 3 May 68
Total electric field
$\bar{v} \times \bar{B}$ field
Time (sec)
Electric field (v/m)
+.04
+.03
+.02
+.01
0
-.01
-.02
-.03
-.04
113.00
113.50
114.00
114.50
115.00
115.50
116.00

Figure 39

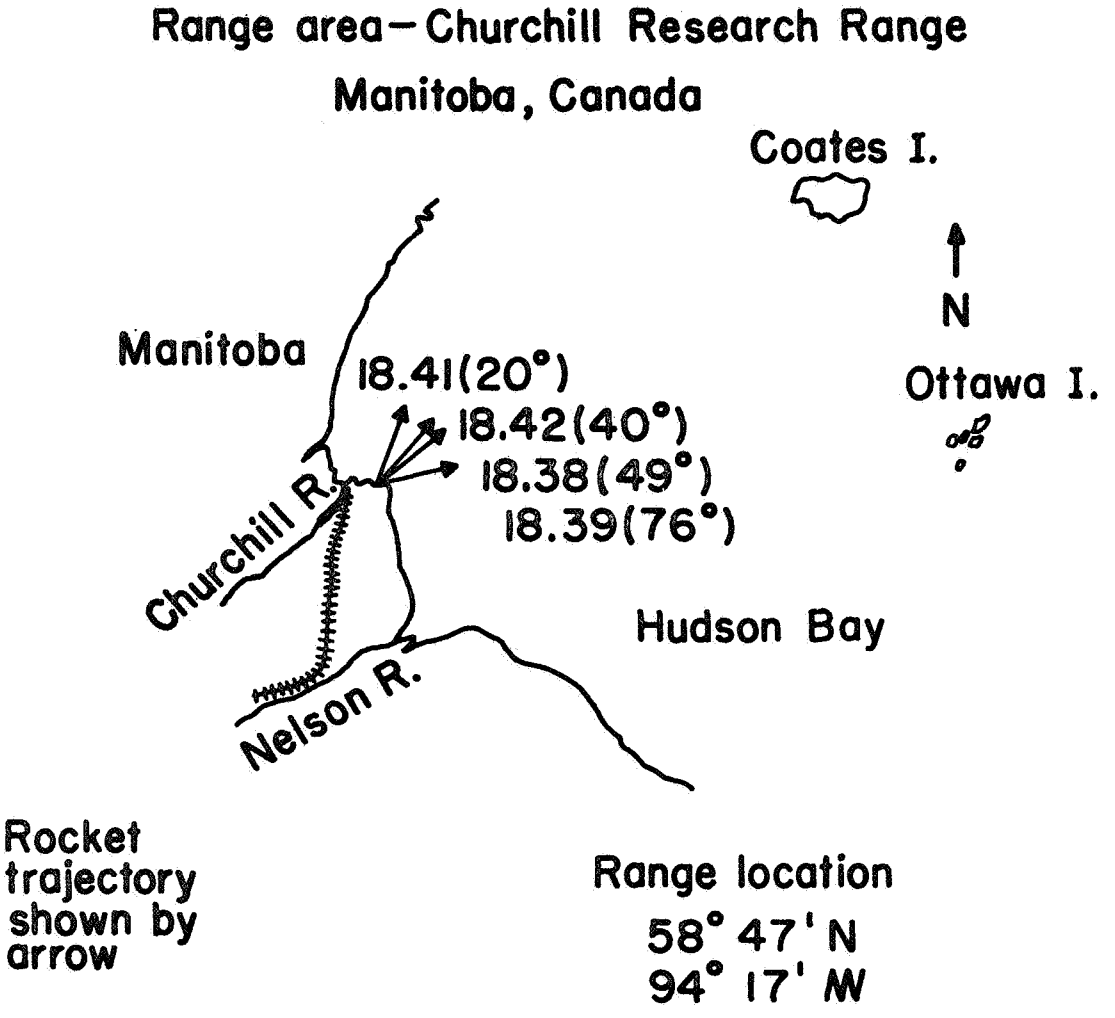
Range area—Churchill Research Range
Manitoba, Canada
Coates I.
N
Ottawa I.
Manitoba
18.41(20°)
18.42(40°)
18.38(49°)
18.39(76°)
Churchill R.
Hudson Bay
Nelson R.
Rocket trajectory shown by arrow
Range location
58° 47' N
94° 17' W

Figure 40

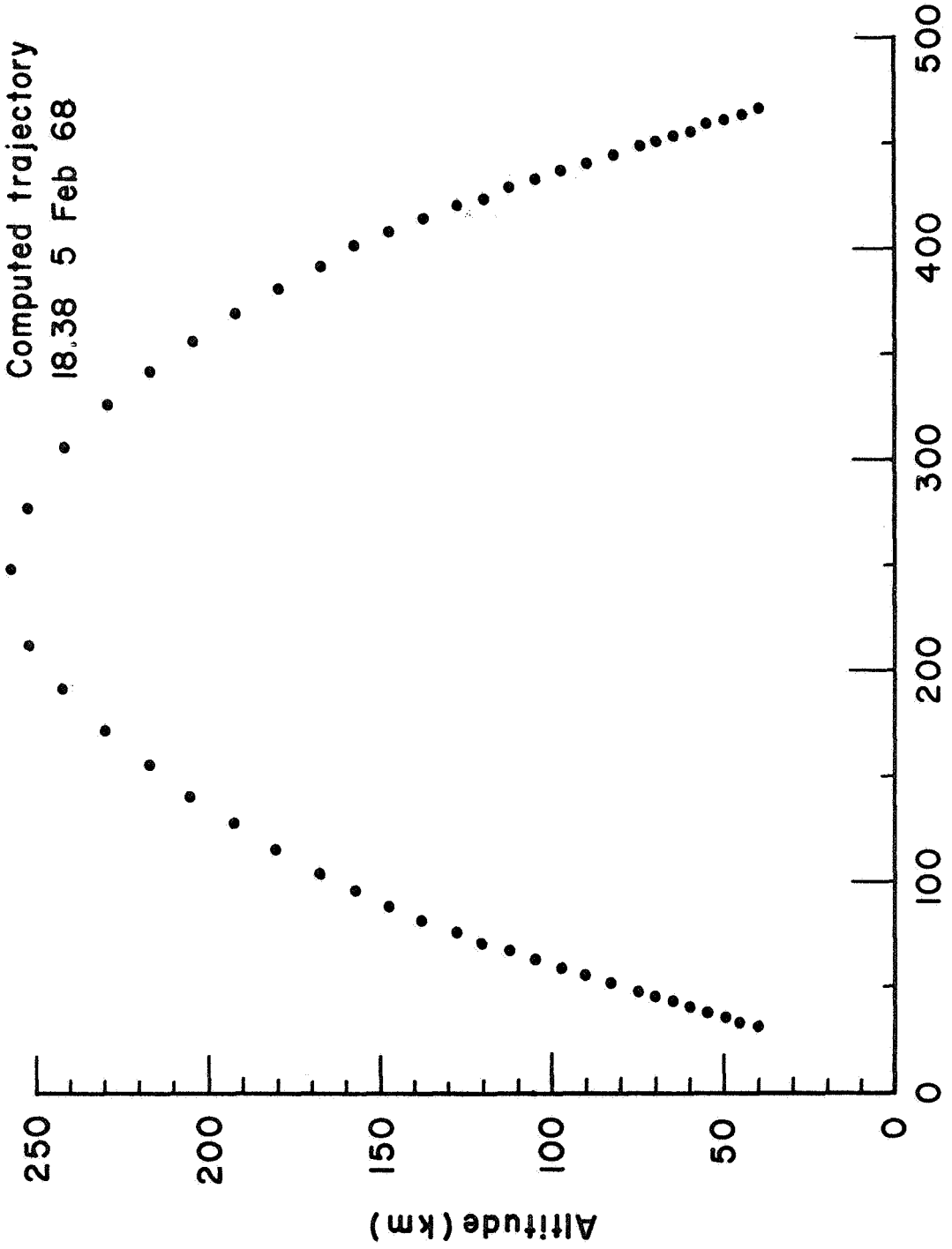
Computed trajectory
18.38 5 Feb 68
Altitude (km)
250
200
150
100
50
0
0
100
200
300
400
500
Time (sec)

Figure 41

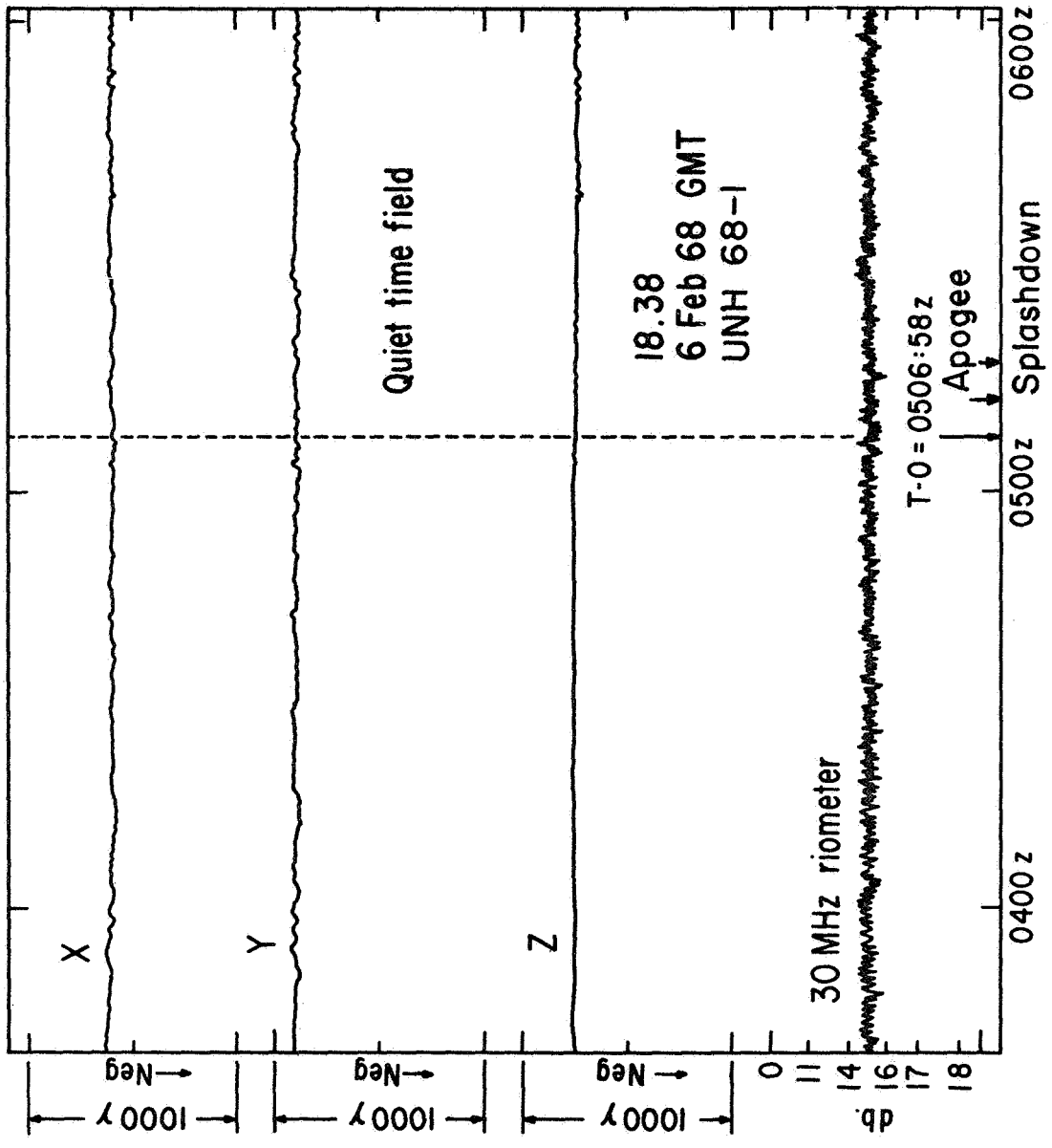
X
Y
Z
Quiet time field
18.38
6 Feb 68 GMT
UNH 68-I
30 MHz riometer
T-0 = 0506:58 z
Apogee
Splashdown
0400 z
0500z
0600z
1000 γ
Neg
db
0
11
14
16
17
18

Figure 42

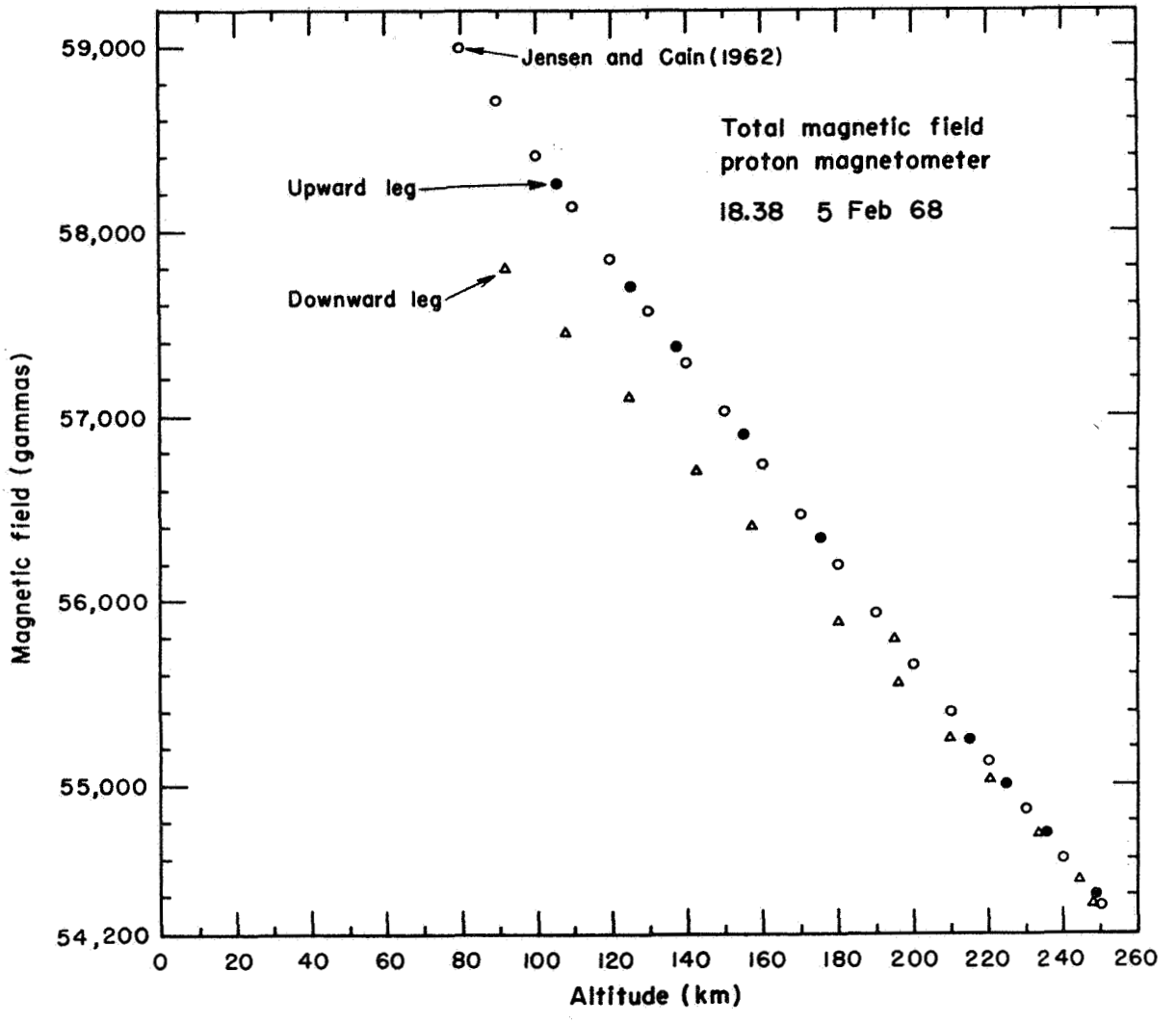
Jensen and Cain (1962)
Total magnetic field
proton magnetometer
18.38 5 Feb 68
Upward leg
Downward leg
59,000
58,000
57,000
56,000
55,000
54,200
Magnetic field (gammas)
0
20
40
60
80
100
120
140
160
180
200
220
240
260
Altitude (km)

Figure 43

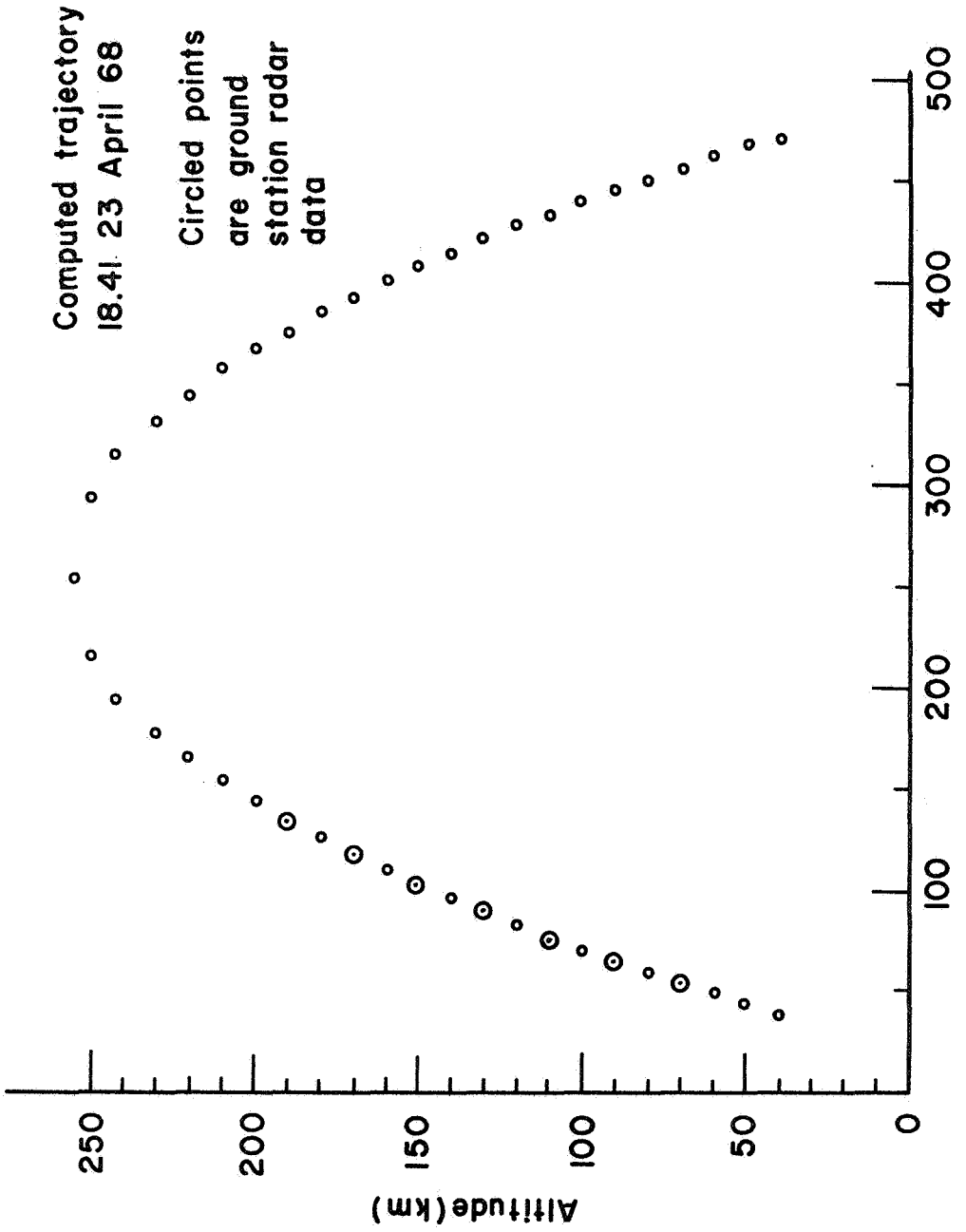
Computed trajectory
18.41 23 April 68
Circled points
are ground
station radar
data
Altitude(km)
250
200
150
100
50
0
100
200
300
400
500
Time(sec)

Figure 44

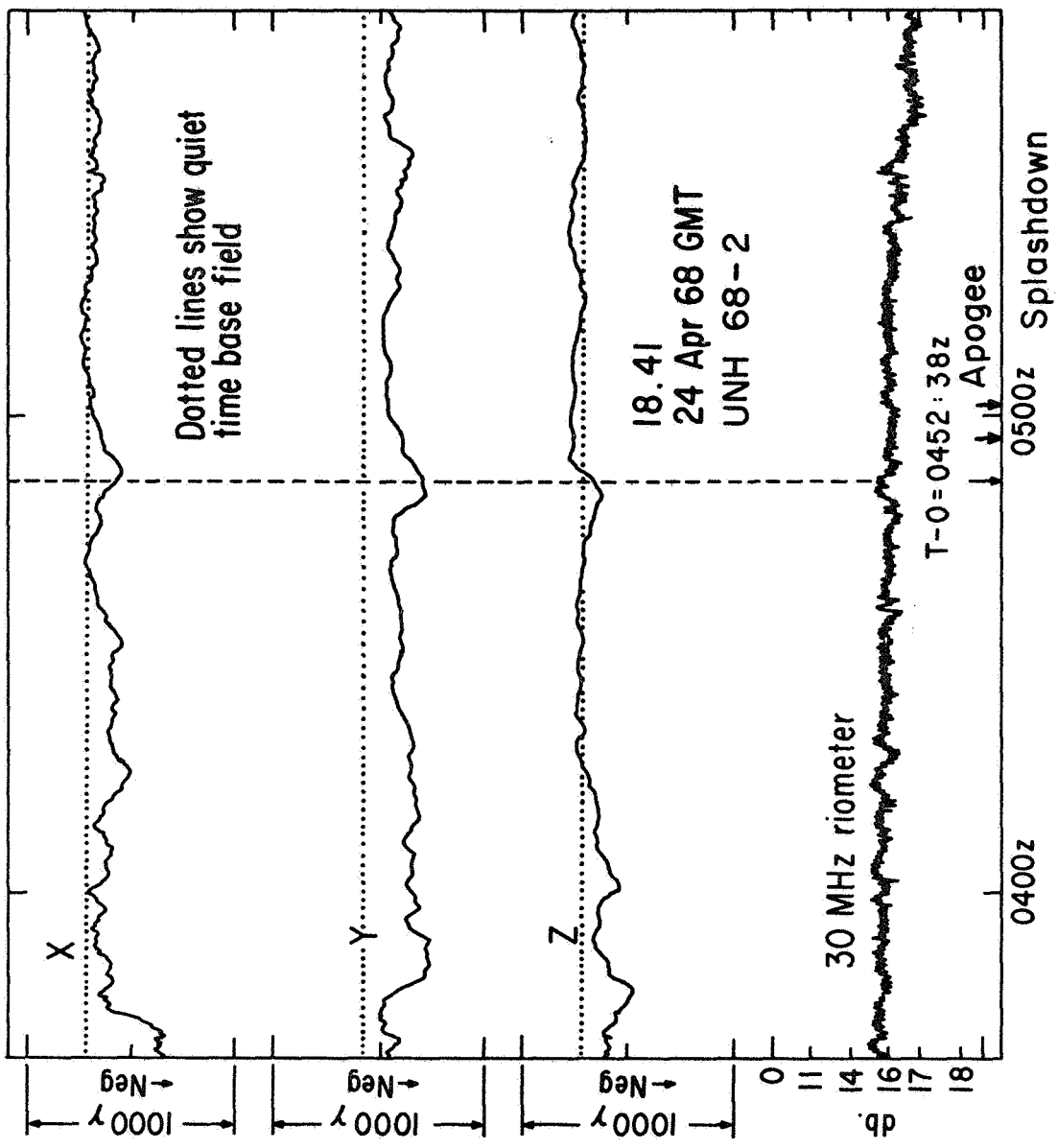
X
Y
Z
1000γ
Neg
Dotted lines show quiet time base field
18.41
24 Apr 68 GMT
UNH 68-2
30 MHz riometer
db
0
11
14
16
17
18
T-0=0452:38z
Apogee
0400z
0500z
Splashdown

Figure 4.

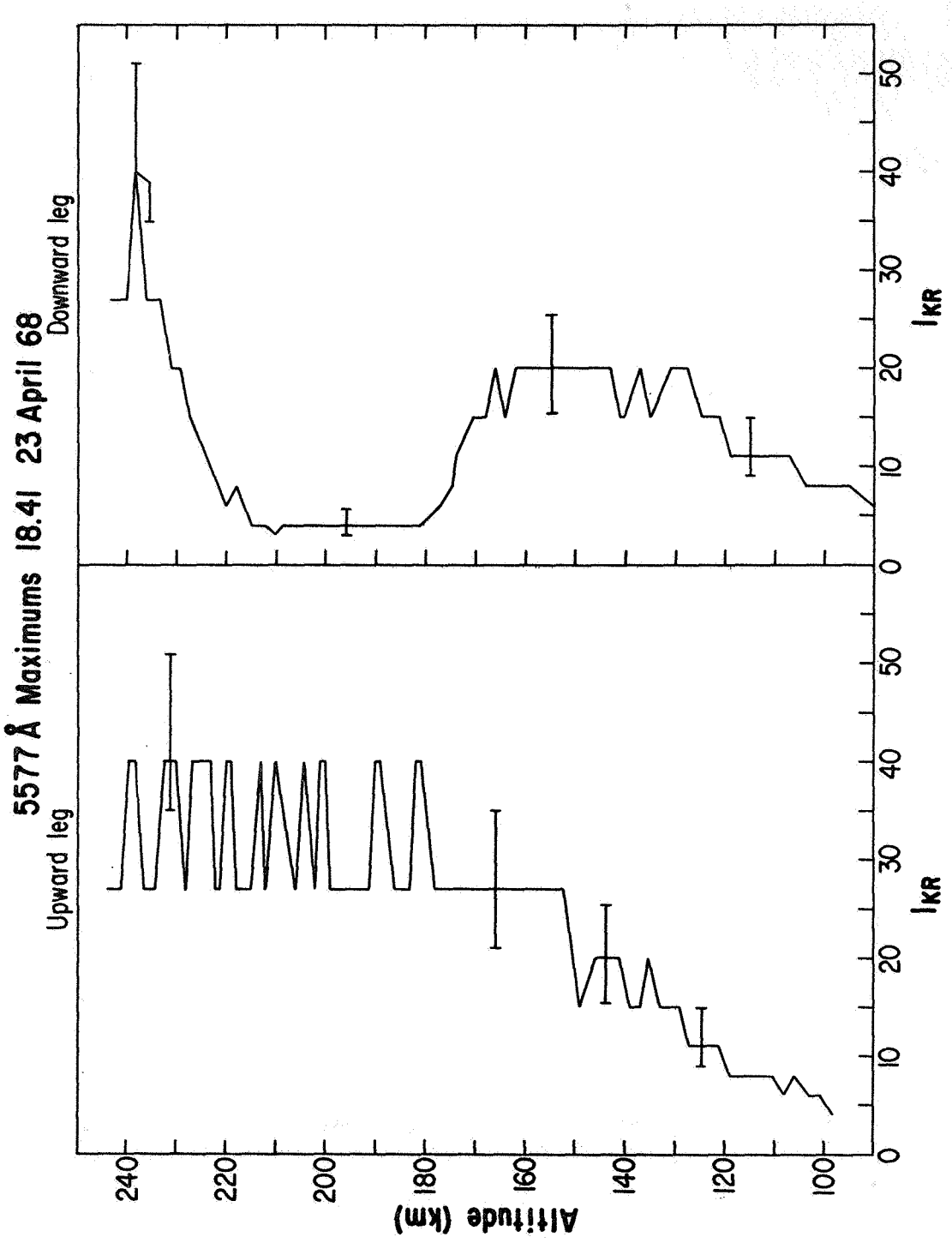
5577 Å Maximums 18.41 23 April 68
Upward leg
Downward leg
Altitude (km)
240
220
200
180
160
140
120
100
0
10
20
30
40
50
I_{KR}

Figure 46

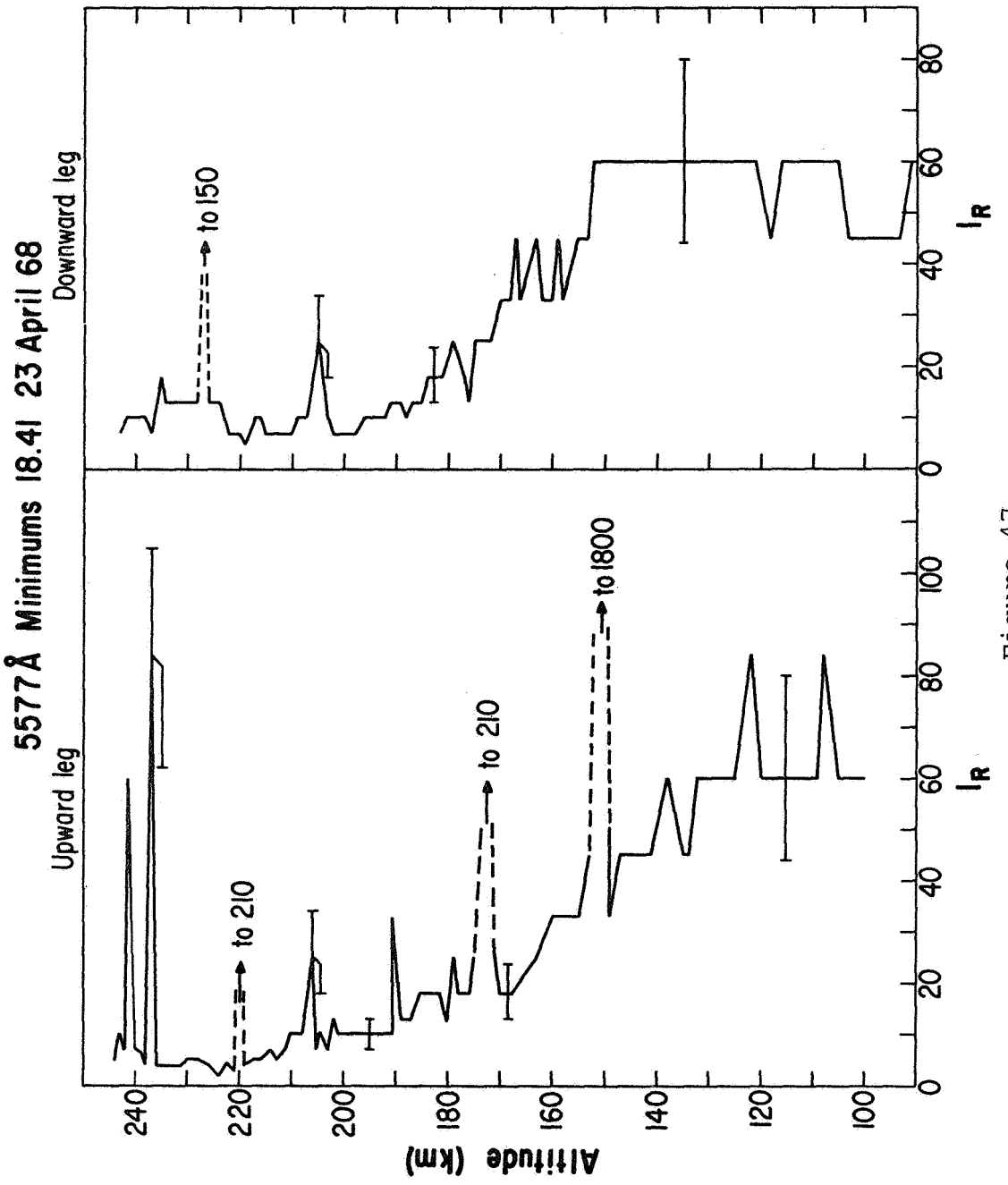
5577Å Minimums 18.41 23 April 68
Upward leg
Downward leg
to 210
to 210
to 1800
to 150
Altitude (km)
240
220
200
180
160
140
120
100
0
20
40
60
80
100
I_R

Figure 47

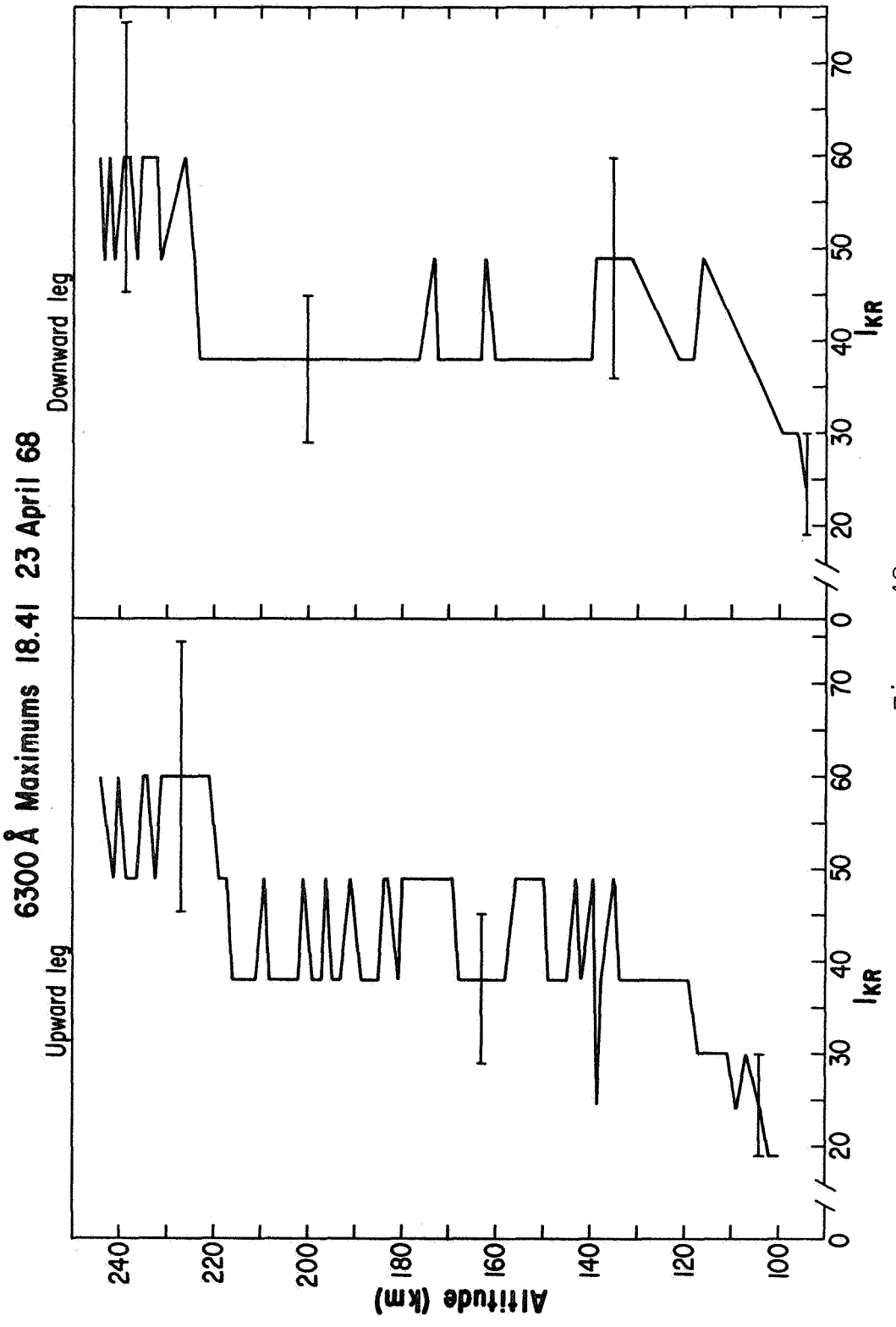
6300 Å Maximums 18.41 23 April 68
Upward leg
Downward leg
Altitude (km)
240
220
200
180
160
140
120
100
0
20
30
40
50
60
70
I_{KR}

Figure 48

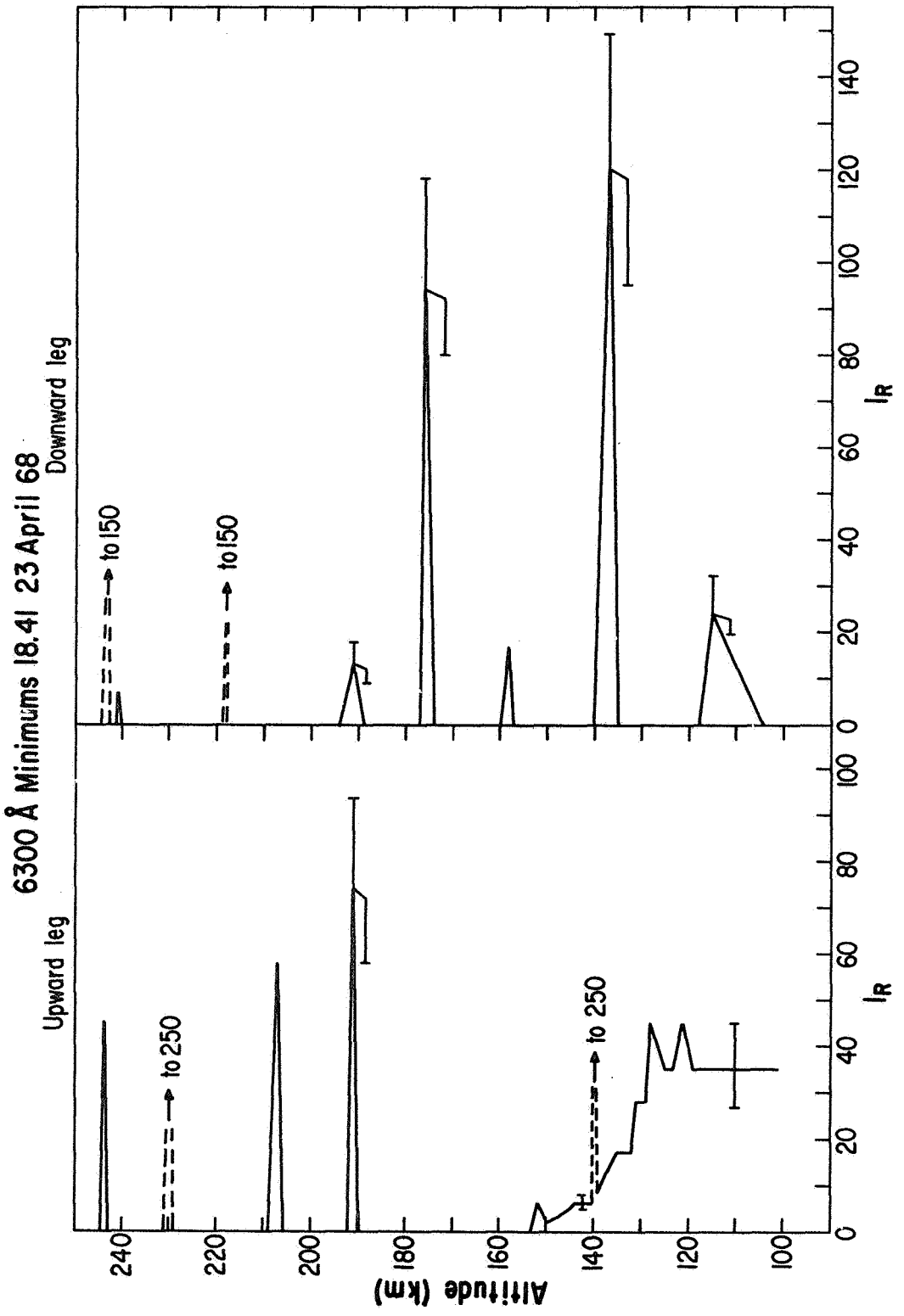
6300 Å Minimums 18.41 23 April 68
Upward leg
Downward leg
to 250
to 150
to 150
to 250
Altitude (km)
240
220
200
180
160
140
120
100
0
20
40
60
80
100
120
140
I_R
I_R

Figure 49

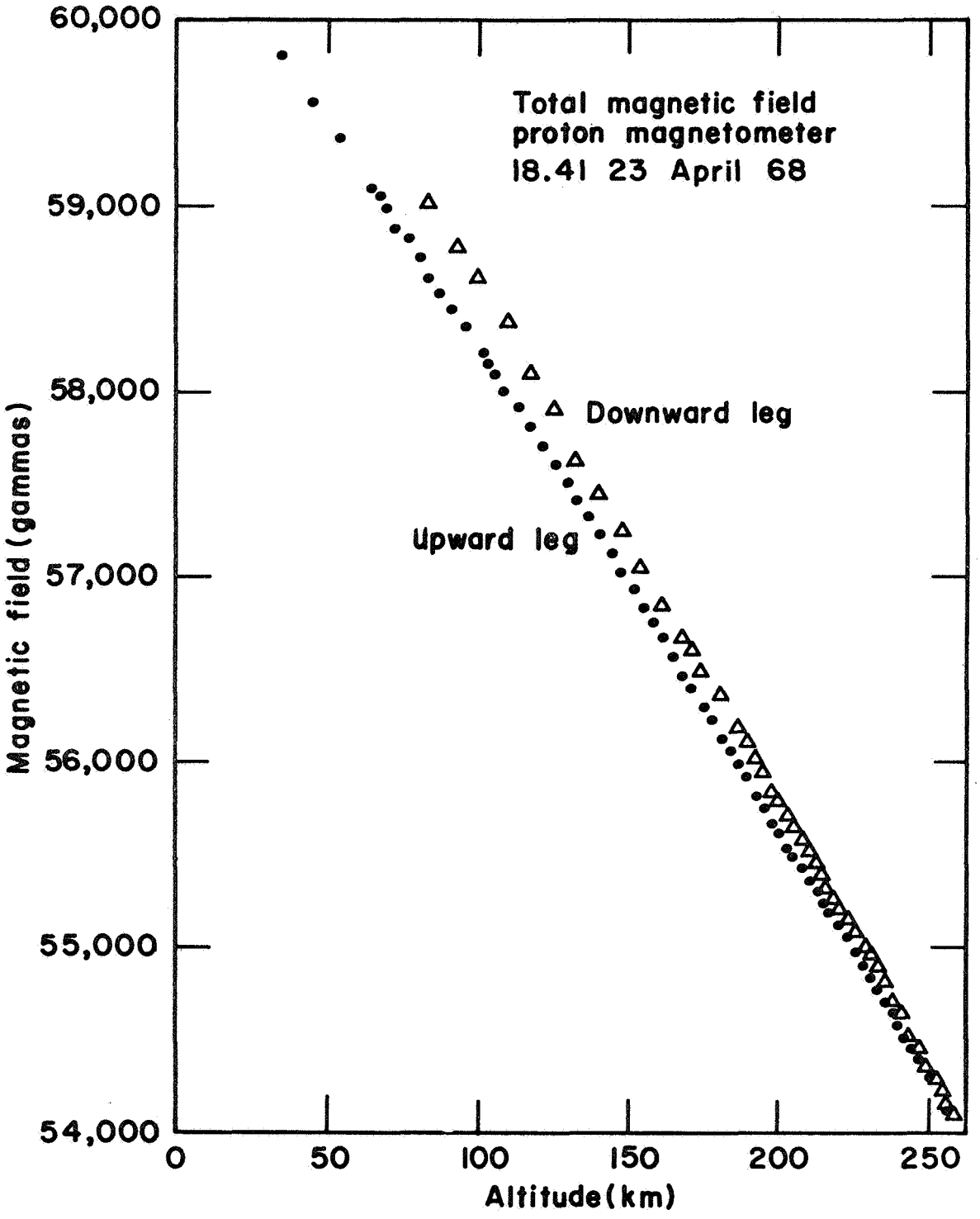
60,000
59,000
58,000
57,000
56,000
55,000
54,000
Magnetic field (gammas)
0
50
100
150
200
250
Altitude (km)
Total magnetic field
proton magnetometer
18.41 23 April 68
Downward leg
Upward leg

Figure 50

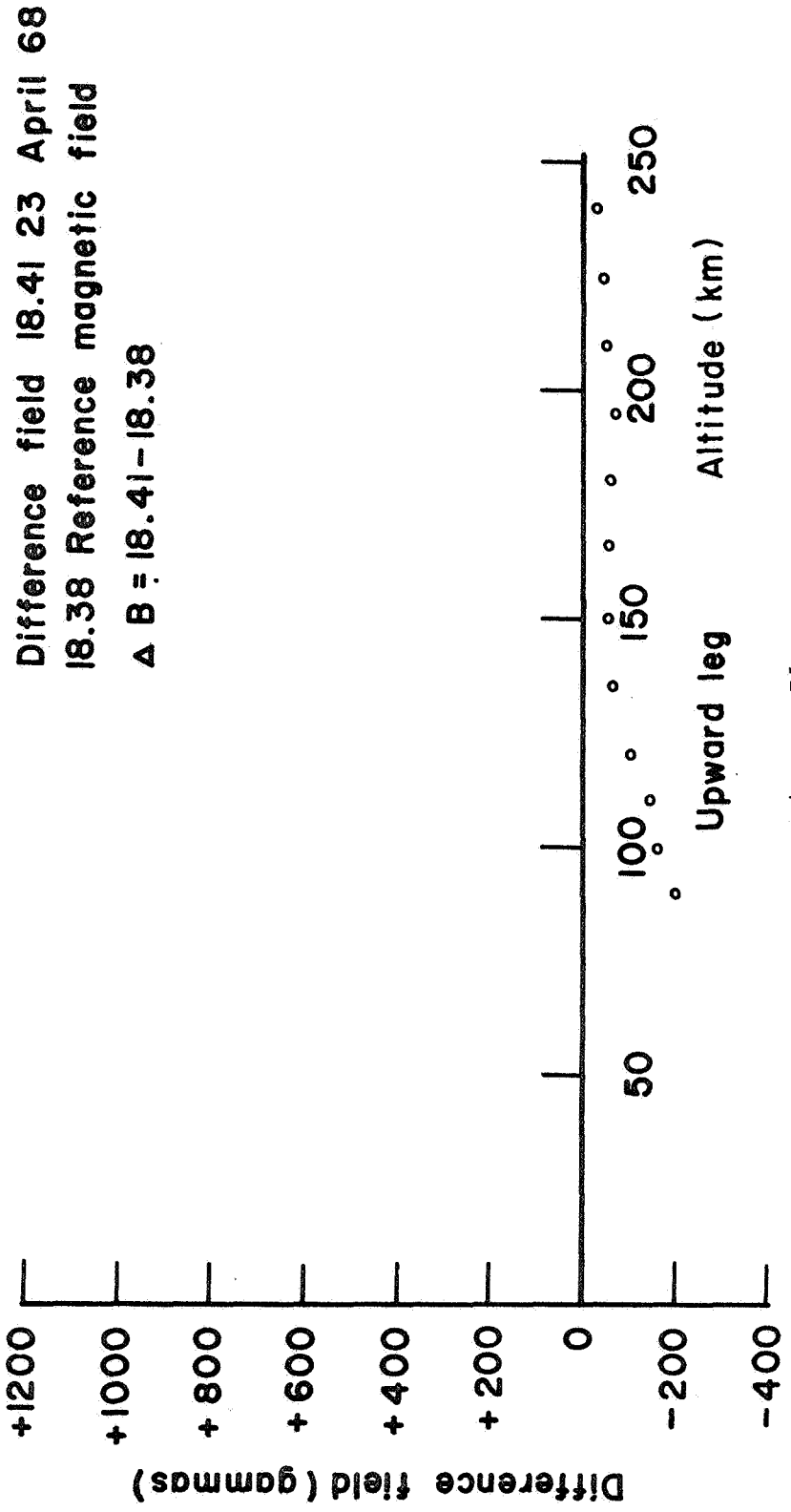
Difference field 18.41 23 April 68
18.38 Reference magnetic field
Δ B = 18.41 - 18.38
Difference field (gammas)
+1200
+1000
+800
+600
+400
+200
0
-200
-400
50
100
150
200
250
Upward leg
Altitude (km)

Figure 51

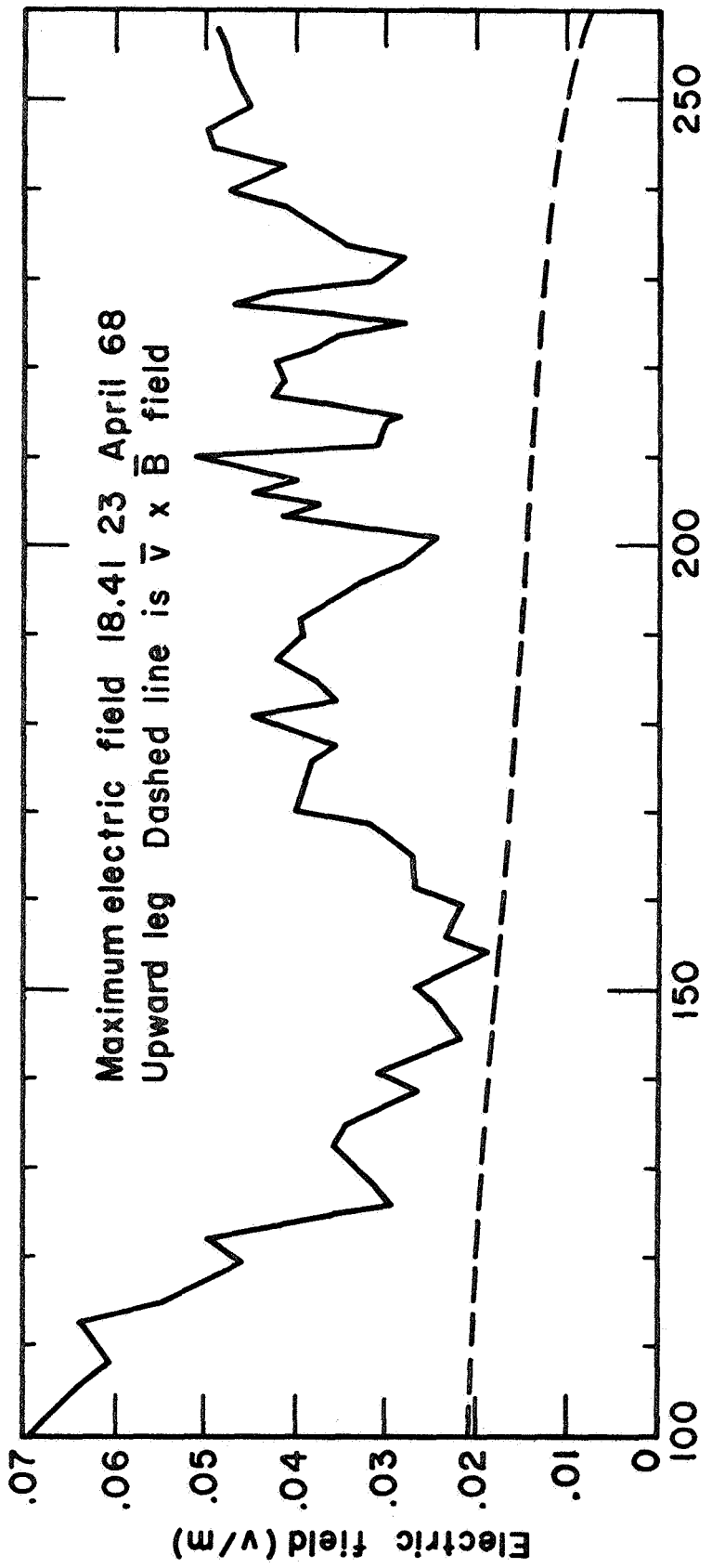
Maximum electric field 18.41 23 April 68
Upward leg Dashed line is $\bar{v} \times \bar{B}$ field
Electric field (v/m)
.07
.06
.05
.04
.03
.02
.01
0
100
150
200
250
Altitude (km)

Figure 52

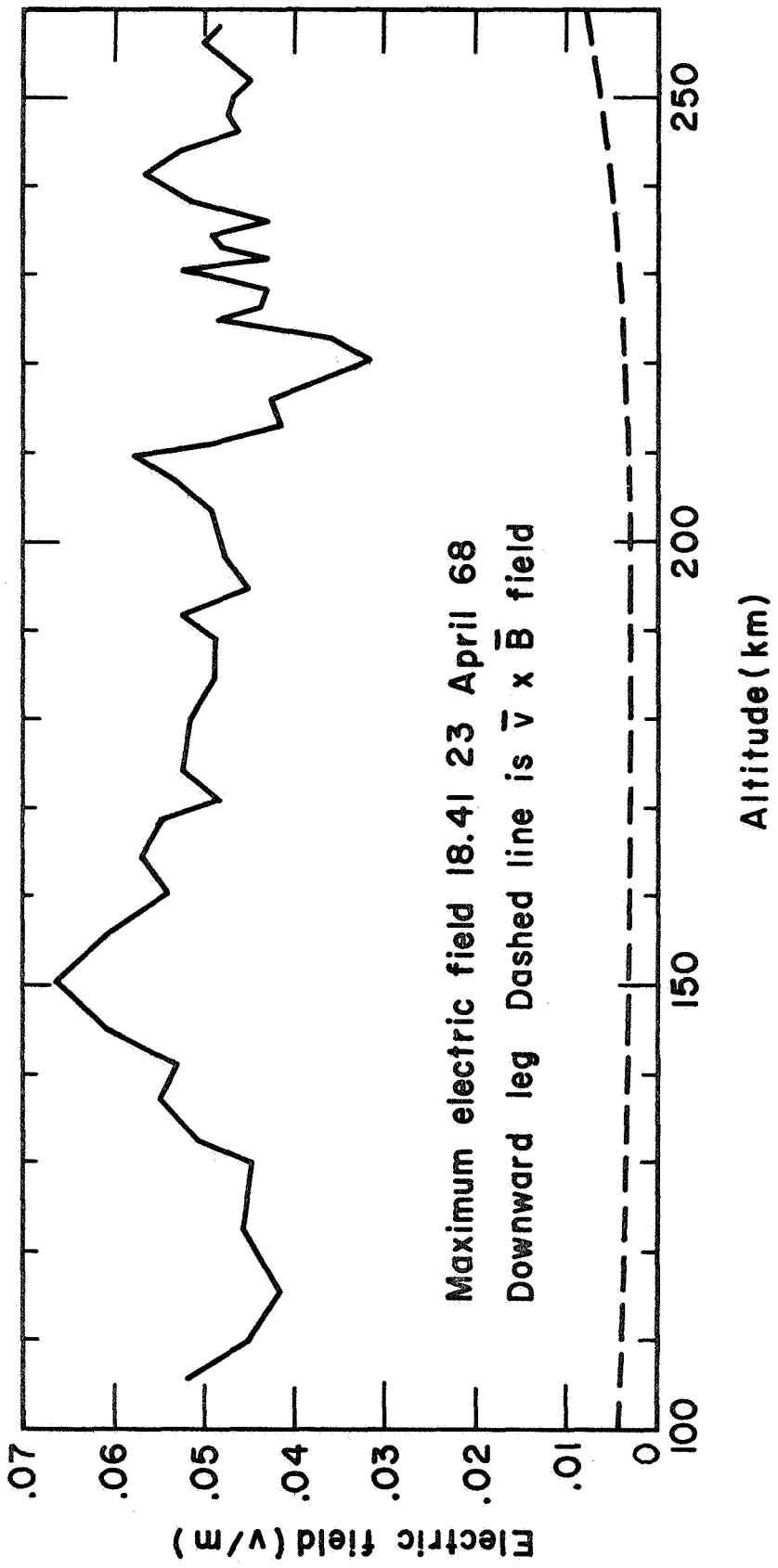
Maximum electric field 18.41 23 April 68
Downward leg Dashed line is $\bar{v} \times \bar{B}$ field
Electric field (v/m)
.07
.06
.05
.04
.03
.02
.01
0
100
150
200
250
Altitude (km)

Figure 53

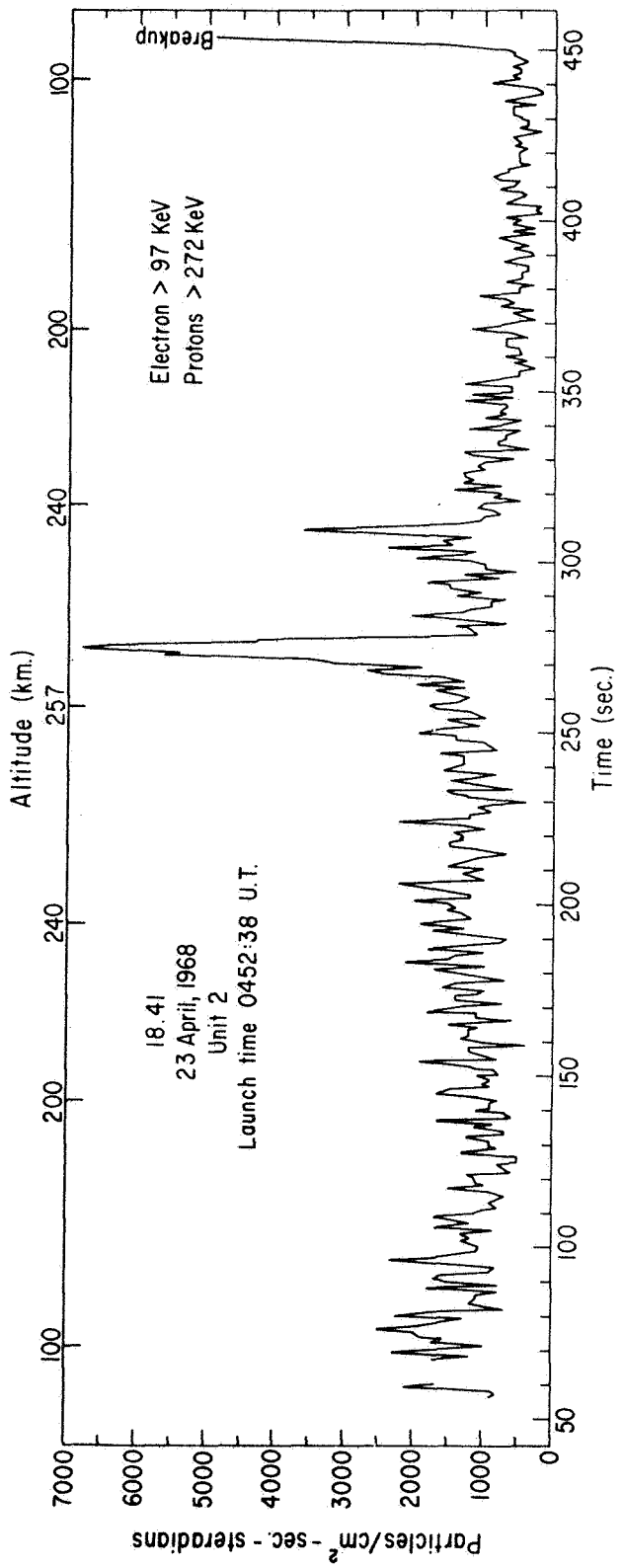
Breakup
Electron > 97 KeV
Protons > 272 KeV
18.41
23 April, 1968
Unit 2
Launch time 0452:38 U.T.
Altitude (km.)
Time (sec.)
Particles/cm² - sec. - steradians
100
200
240
257
50
100
150
200
250
300
350
400
450
1000
2000
3000
4000
5000
6000
7000
0

Figure 54

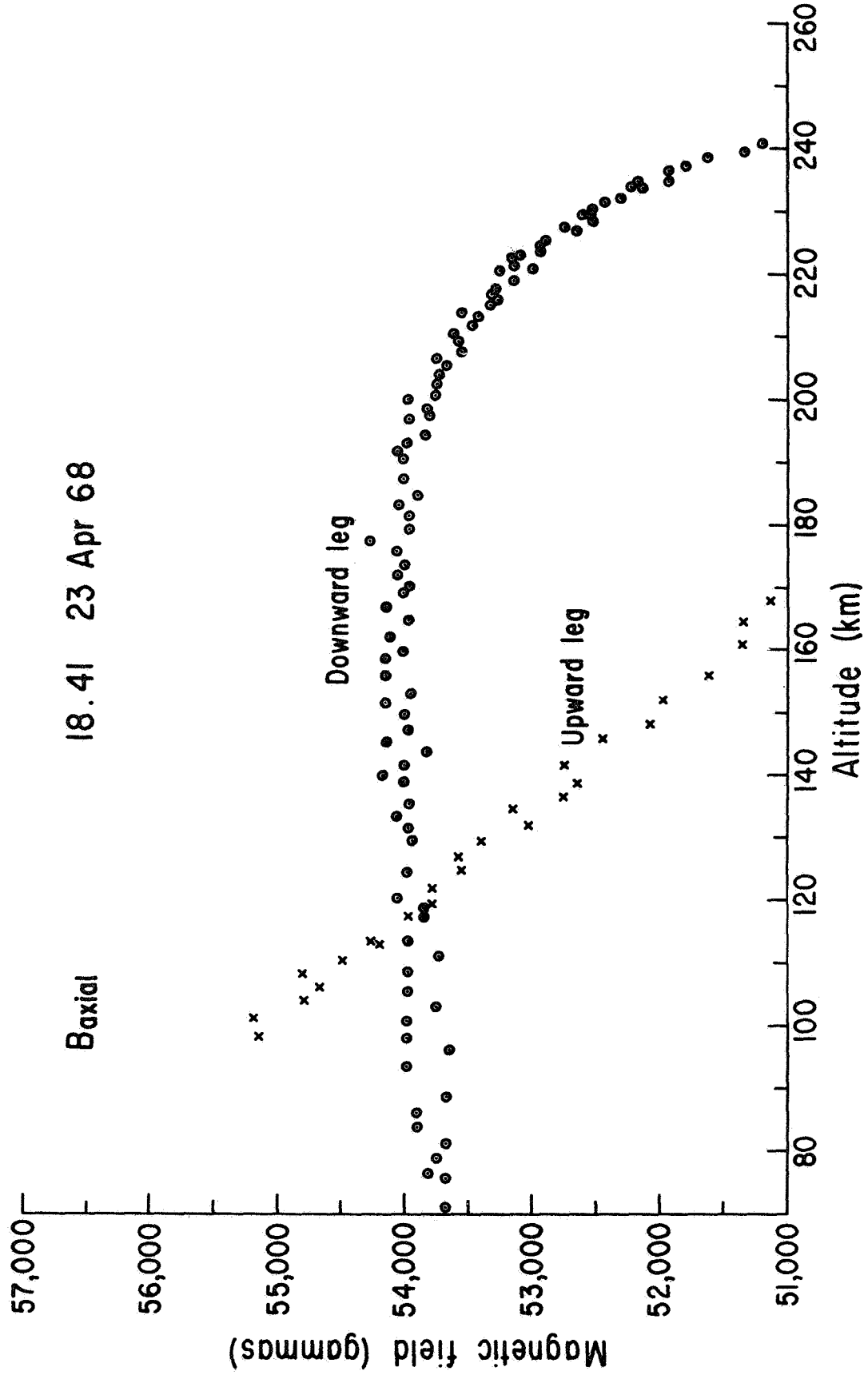
Baxial
18.41 23 Apr 68
Downward leg
Upward leg
Magnetic field (gammas)
Altitude (km)
57,000
56,000
55,000
54,000
53,000
52,000
51,000
80
100
120
140
160
180
200
220
240
260

Figure 55

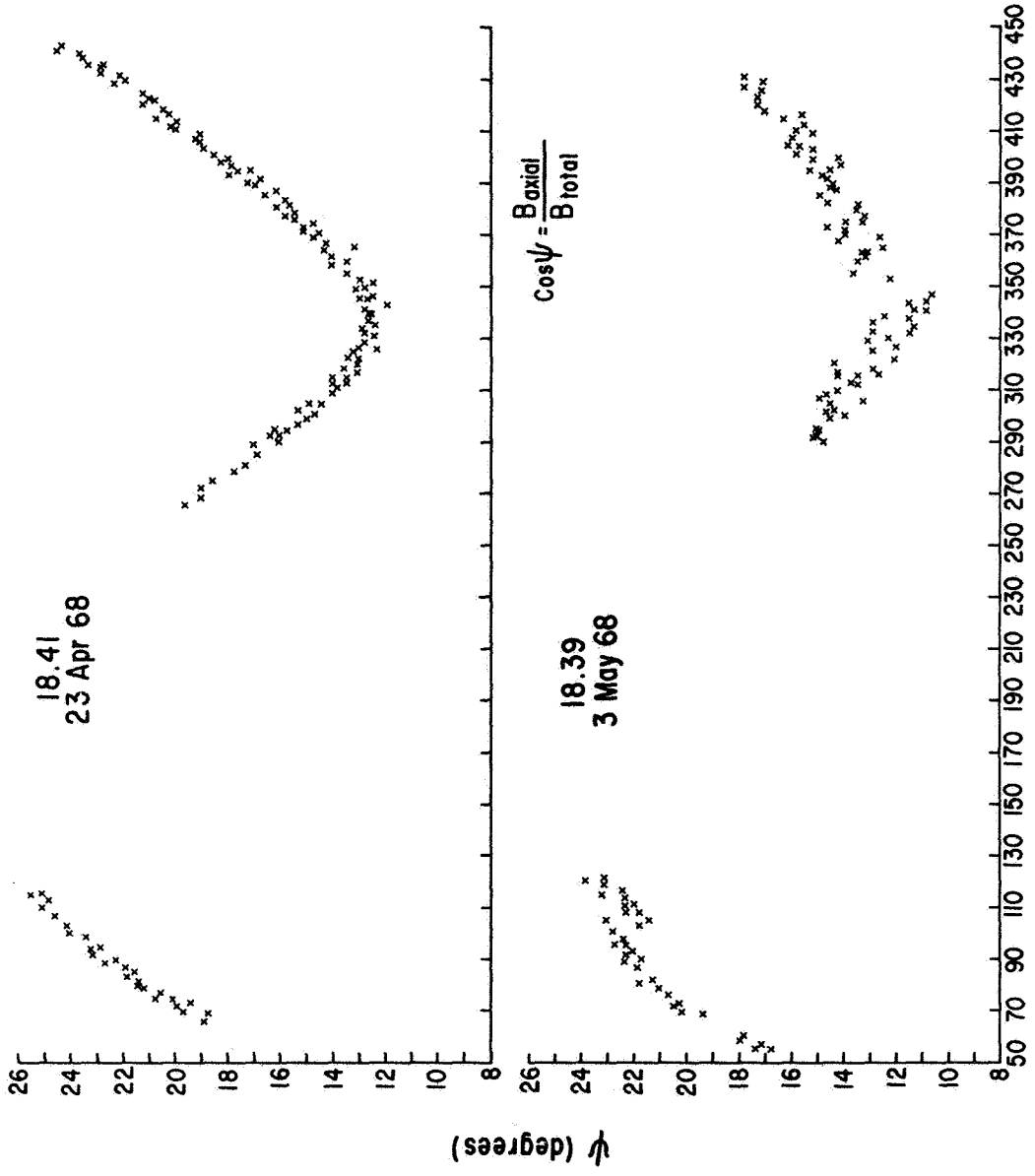
18.41
23 Apr 68
18.39
3 May 68
$\cos\psi = \frac{B_{axial}}{B_{total}}$
ψ (degrees)
Time (sec.)

Figure 56

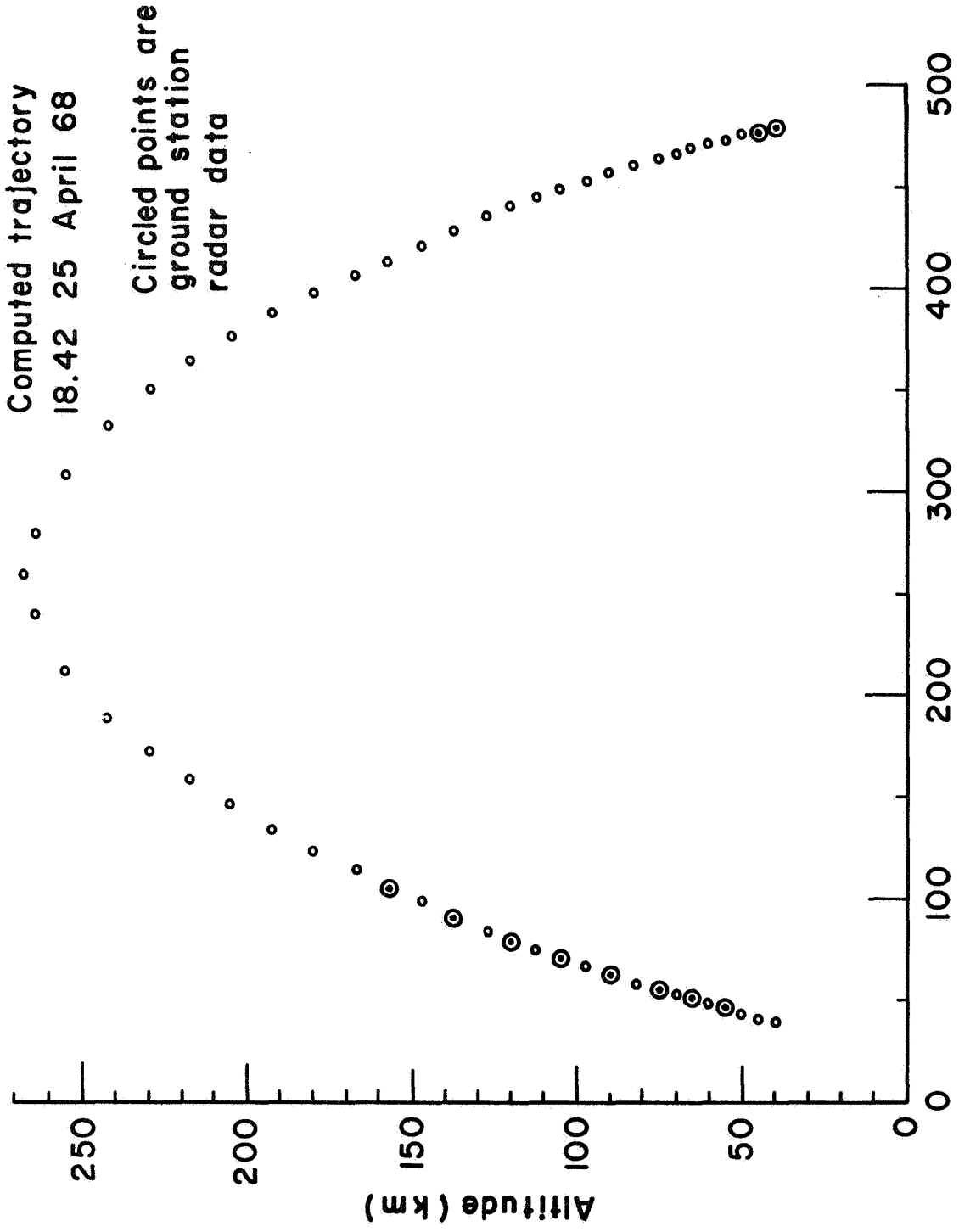
Computed trajectory
18.42 25 April 68
Circled points are
ground station
radar data
Altitude (km)
250
200
150
100
50
0
0
100
200
300
400
500
Time(sec)

Figure 57

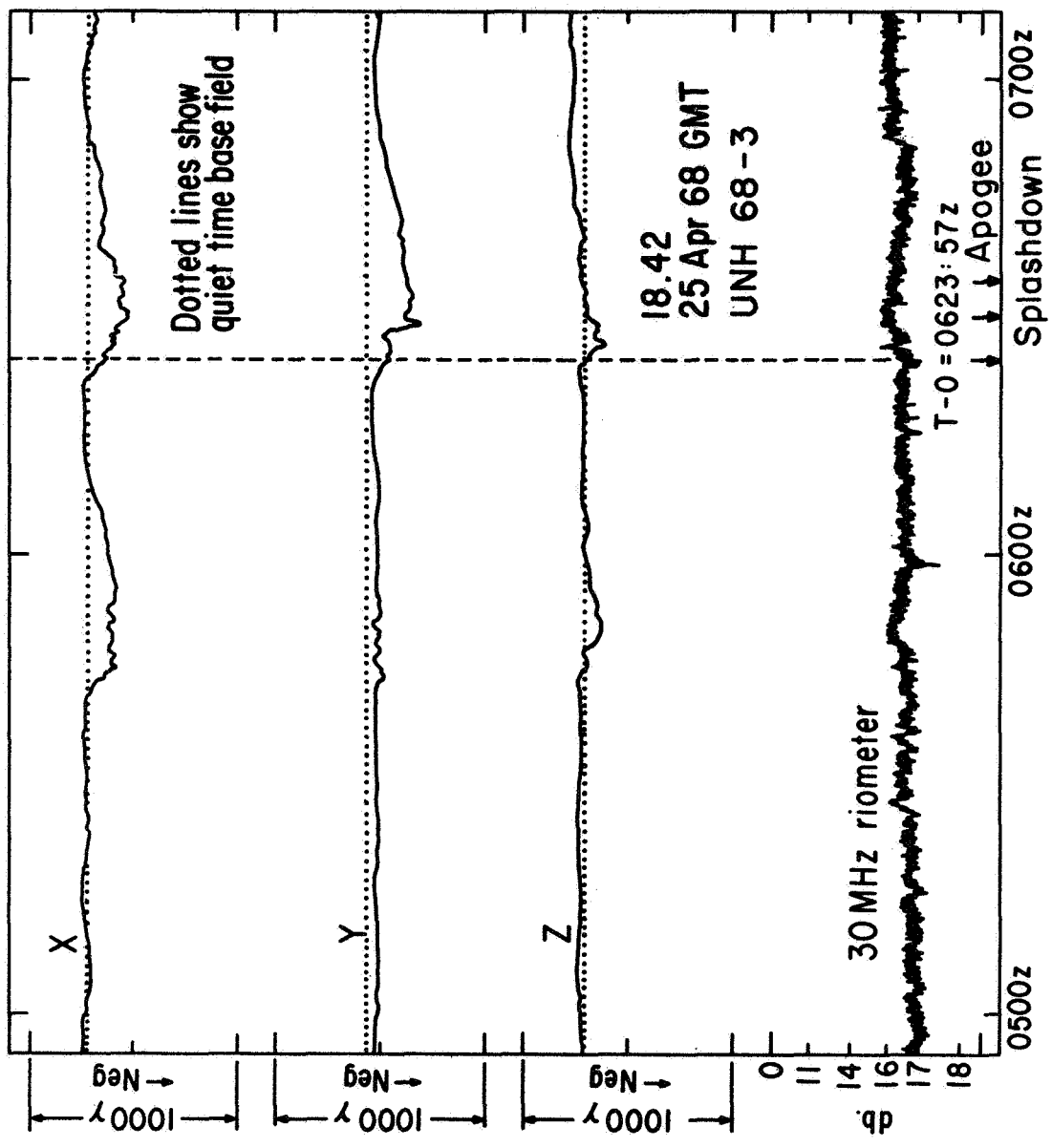
Dotted lines show
quiet time base field
X
Y
Z
18.42
25 Apr 68 GMT
UNH 68-3
30 MHz riometer
T-0 = 0623:57z
Apogee
Splashdown
0500z
0600z
0700z
1000γ
Neg
db
0
11
14
16
17
18

Figure 58

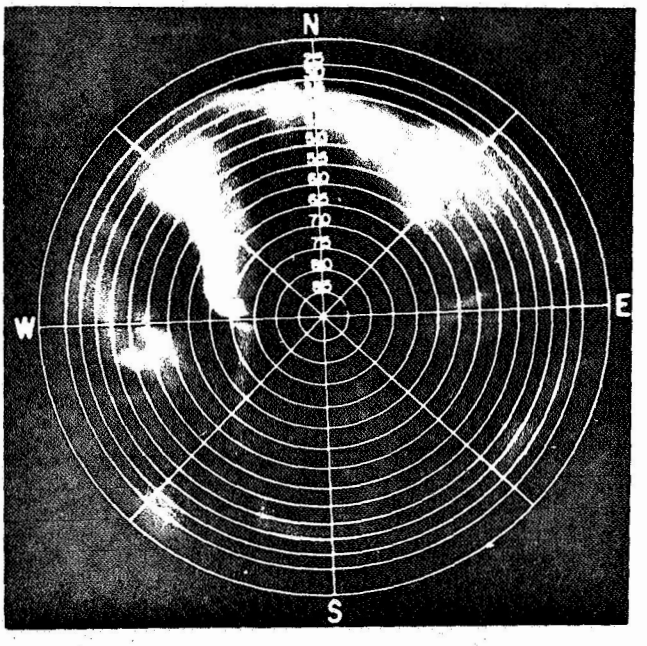

a

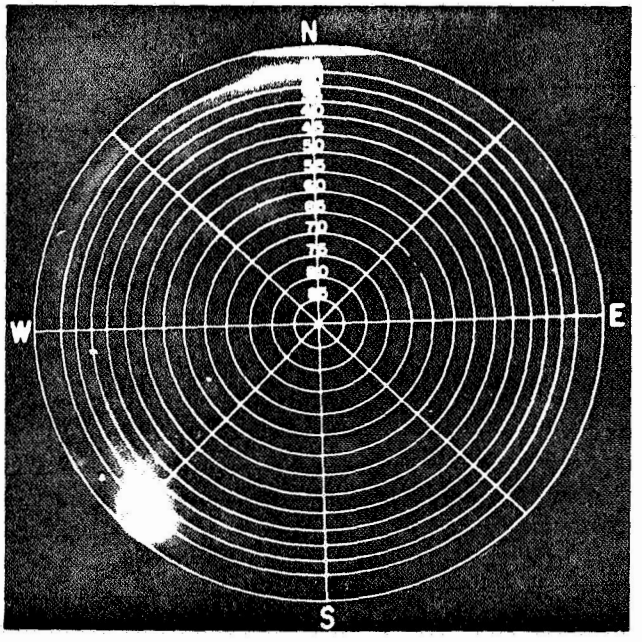

b

Figure 59

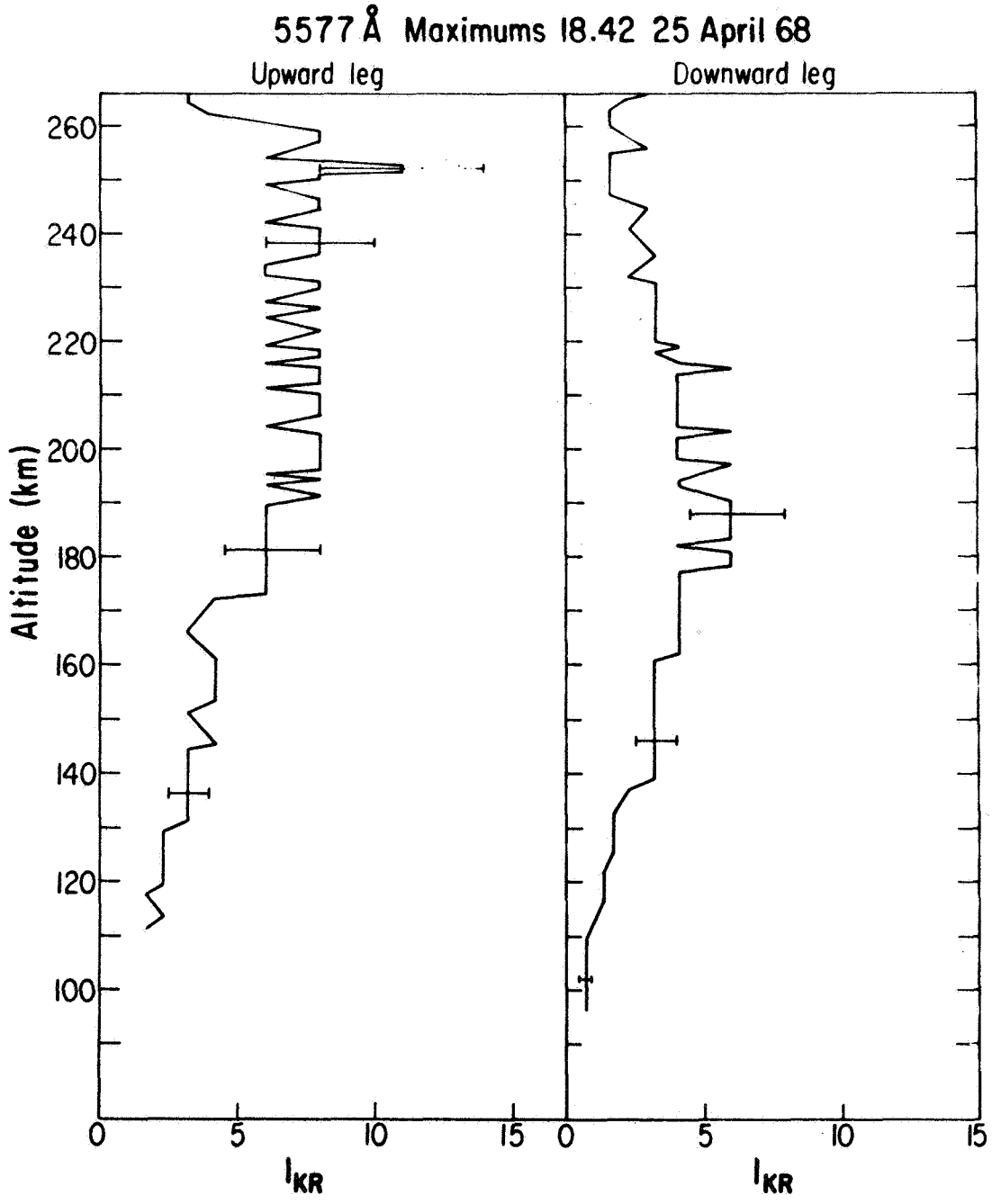
5577 Å Maximums 18.42 25 April 68
Upward leg
Downward leg
Altitude (km)
260
240
220
200
180
160
140
120
100
0
5
10
15
I_{KR}

Figure 60

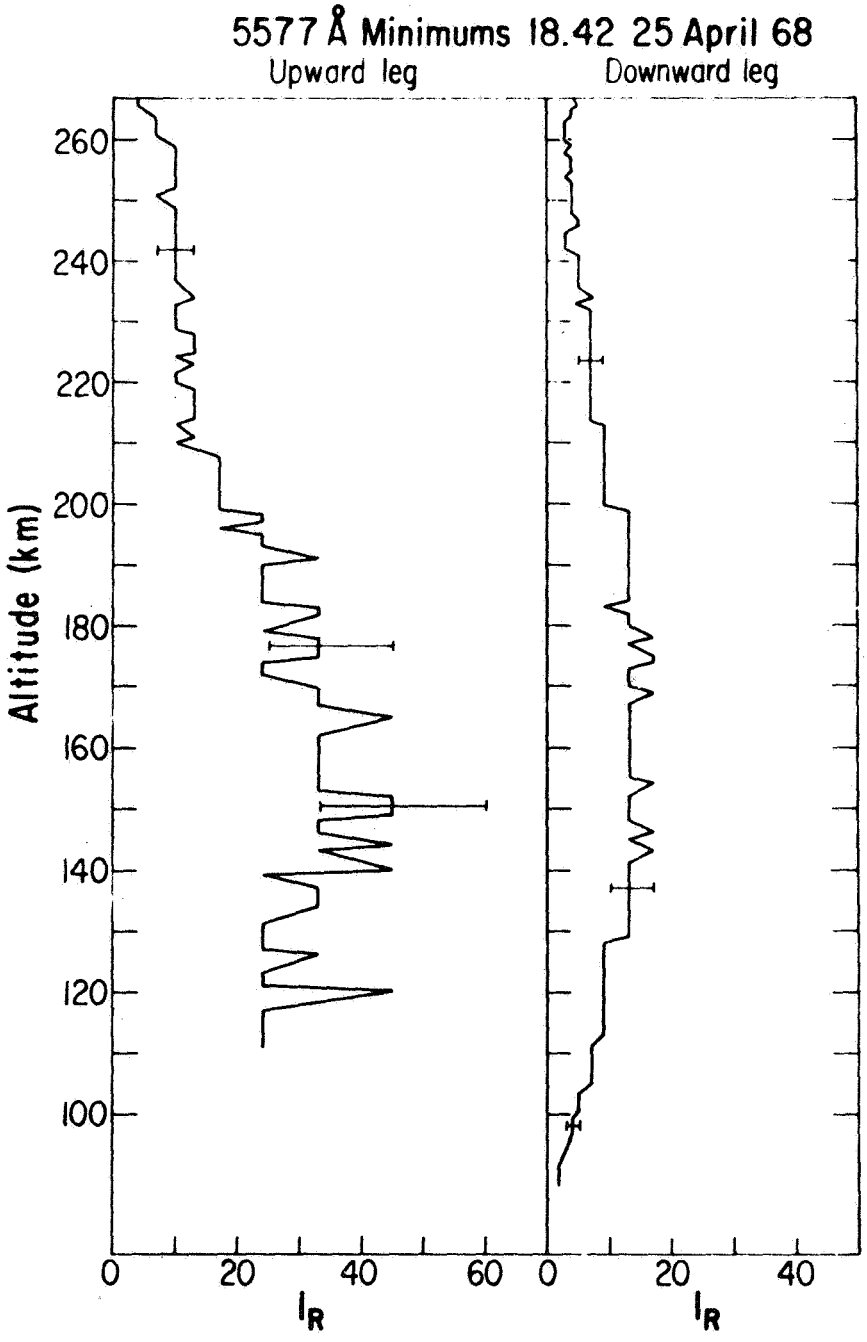
5577 Å Minimums 18.42 25 April 68
Upward leg
Downward leg
Altitude (km)
260
240
220
200
180
160
140
120
100
0
20
40
60
0
20
40
I_R
I_R

Figure 61

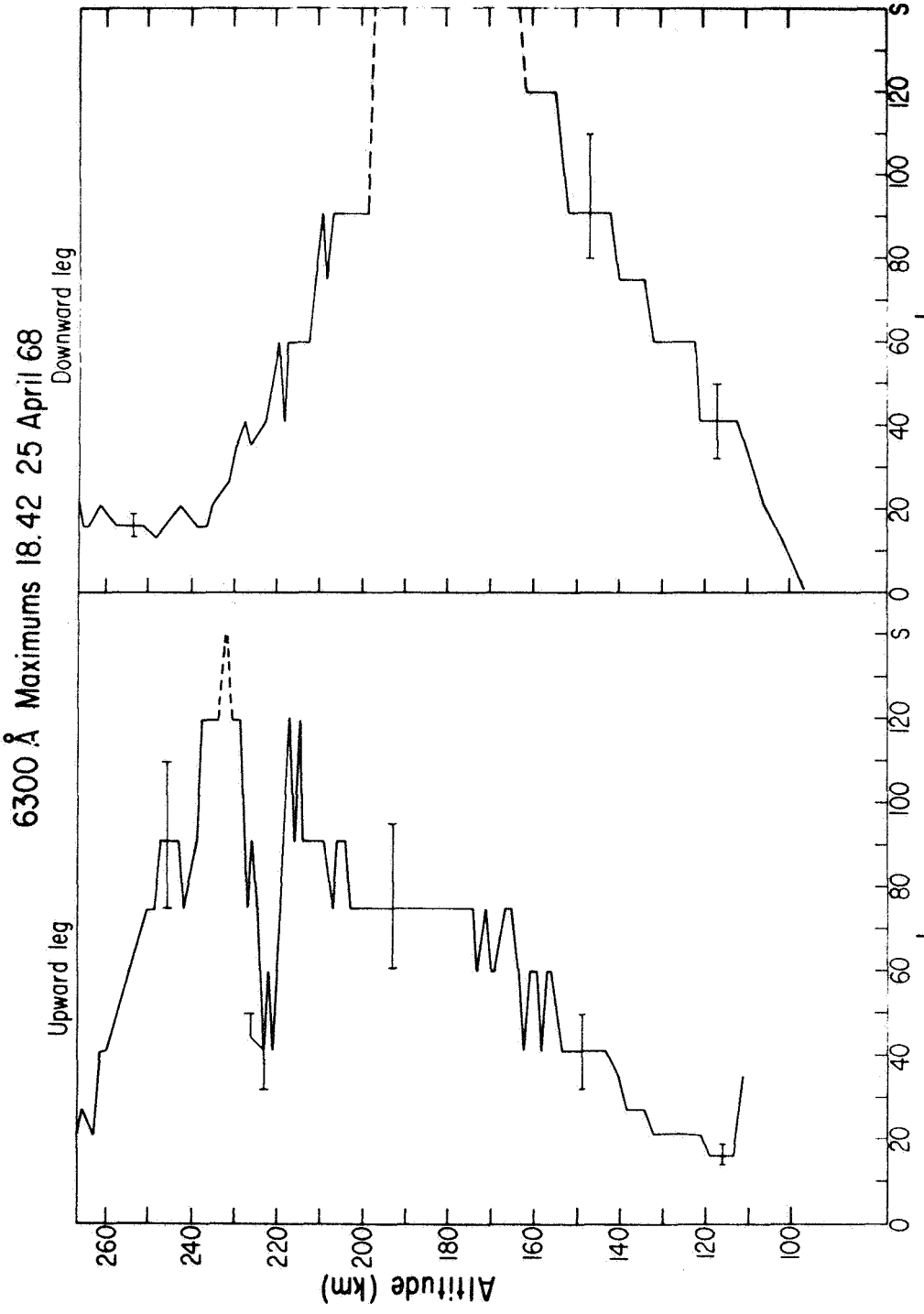
6300 Å Maximums 18.42 25 April 68
Upward leg
Downward leg
Altitude (km)
260
240
220
200
180
160
140
120
100
0
20
40
60
80
100
120
S
I_{KR}

Figure 62

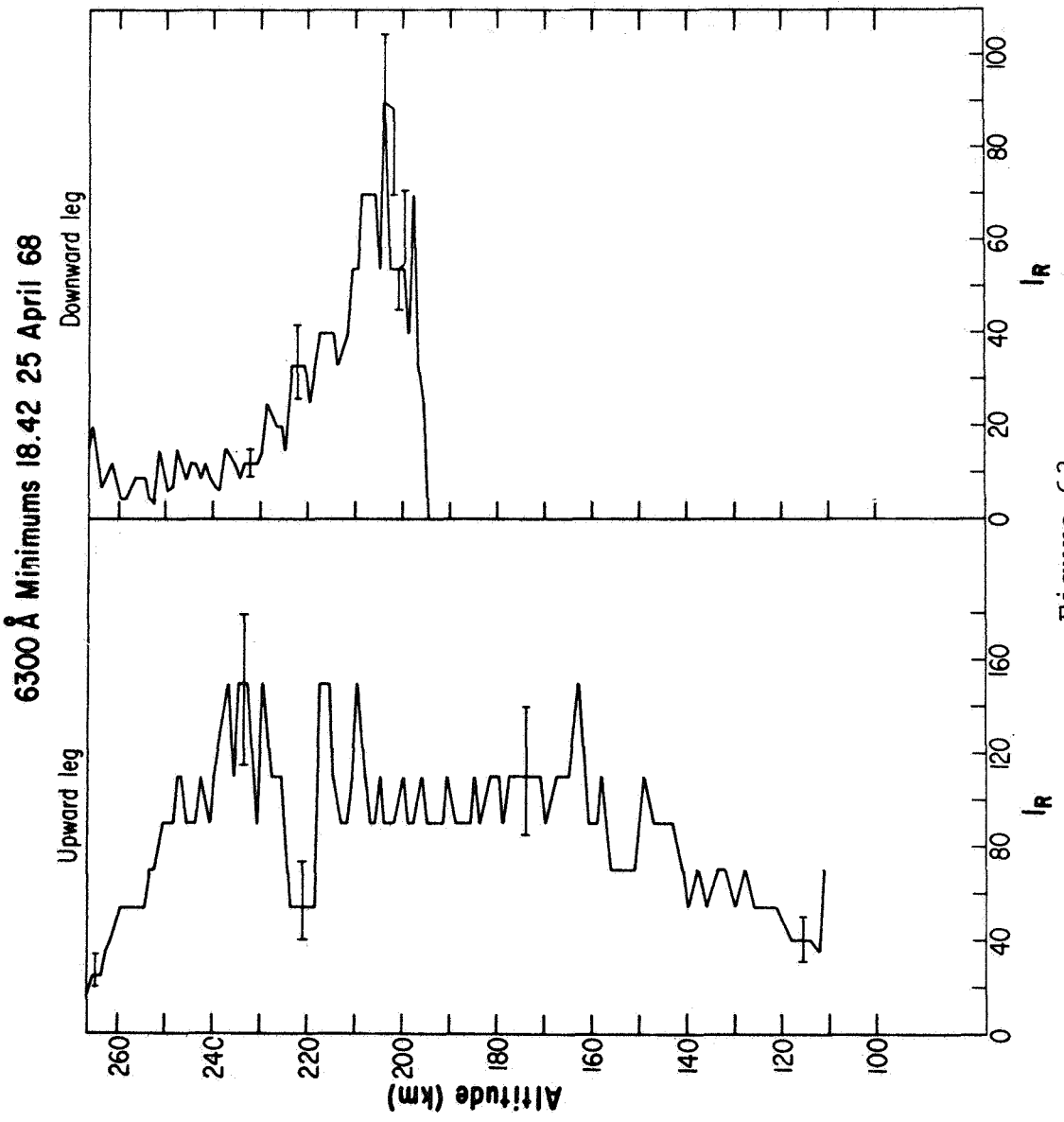
6300 Å Minimums 18.42 25 April 68
Downward leg
Upward leg
I_R
I_R
Altitude (km)
260
240
220
200
180
160
140
120
100
0
20
40
60
80
100
120
160

Figure 63

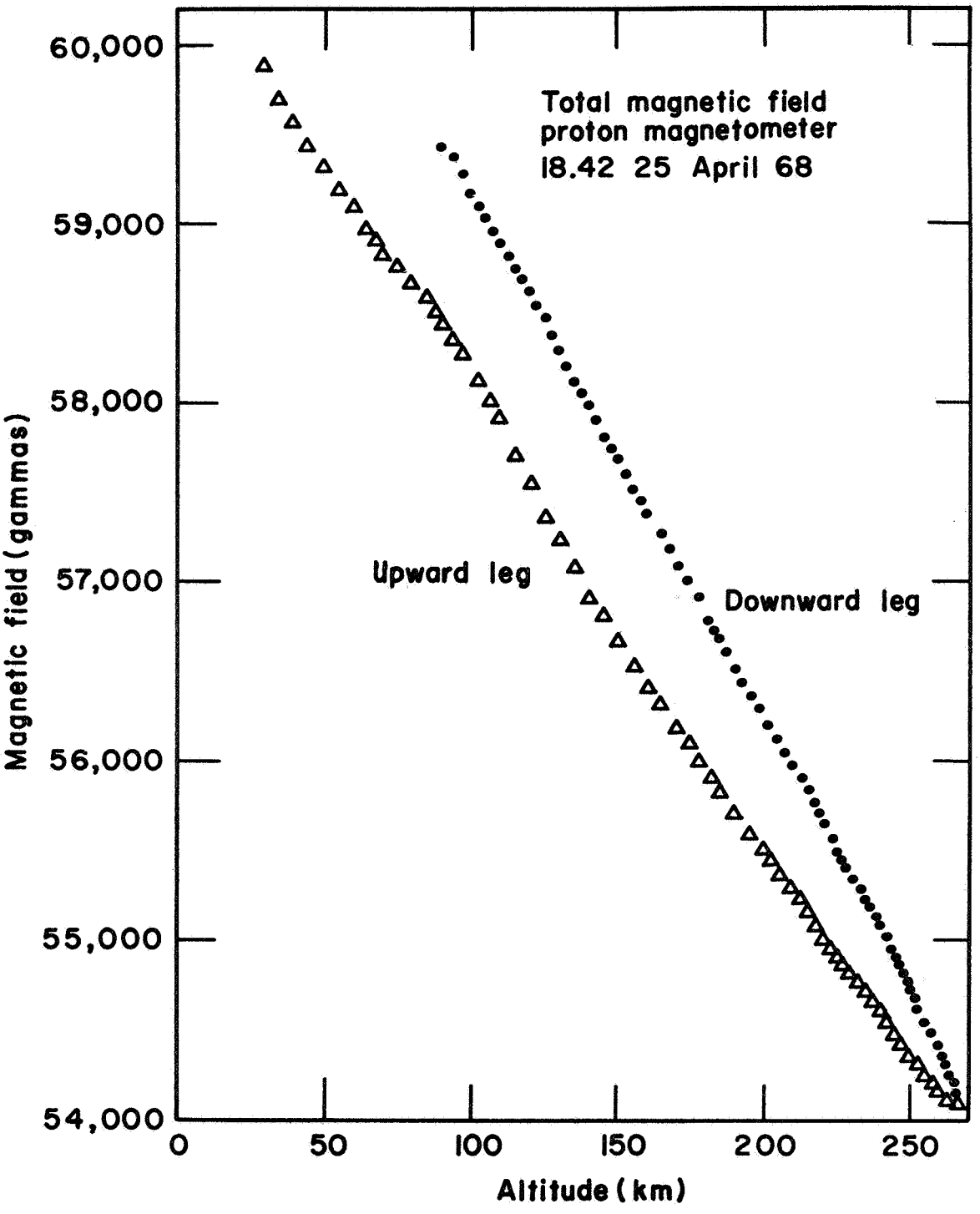
Total magnetic field
proton magnetometer
18.42 25 April 68
Upward leg
Downward leg
Magnetic field (gammas)
60,000
59,000
58,000
57,000
56,000
55,000
54,000
0
50
100
150
200
250
Altitude (km)

Figure 64

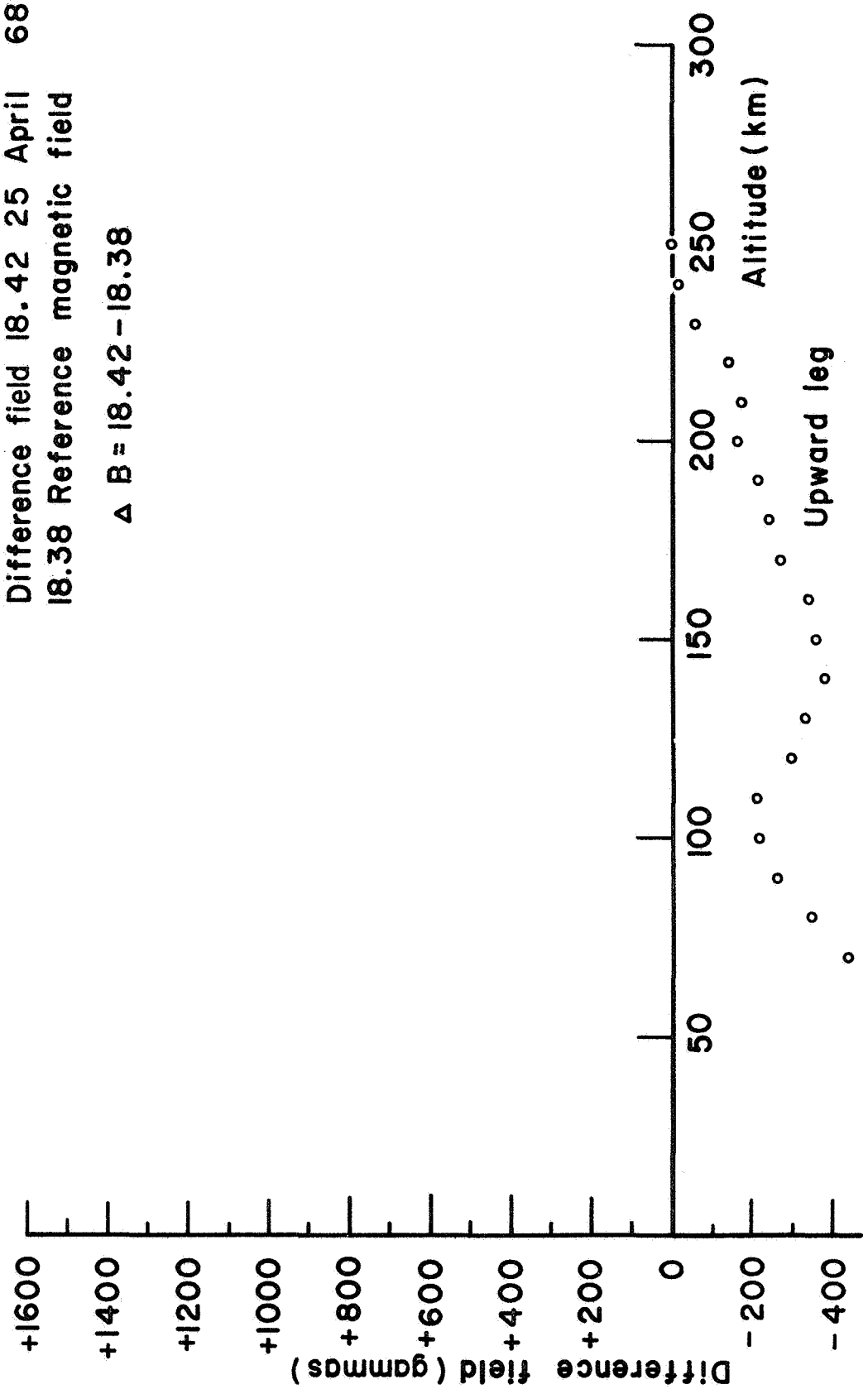
Difference field 18.42 25 April 68
18.38 Reference magnetic field
Δ B = 18.42 − 18.38
Difference field (gammas)
+1600
+1400
+1200
+1000
+800
+600
+400
+200
0
−200
−400
50
100
150
200
250
300
Altitude (km)
Upward leg

Figure 65

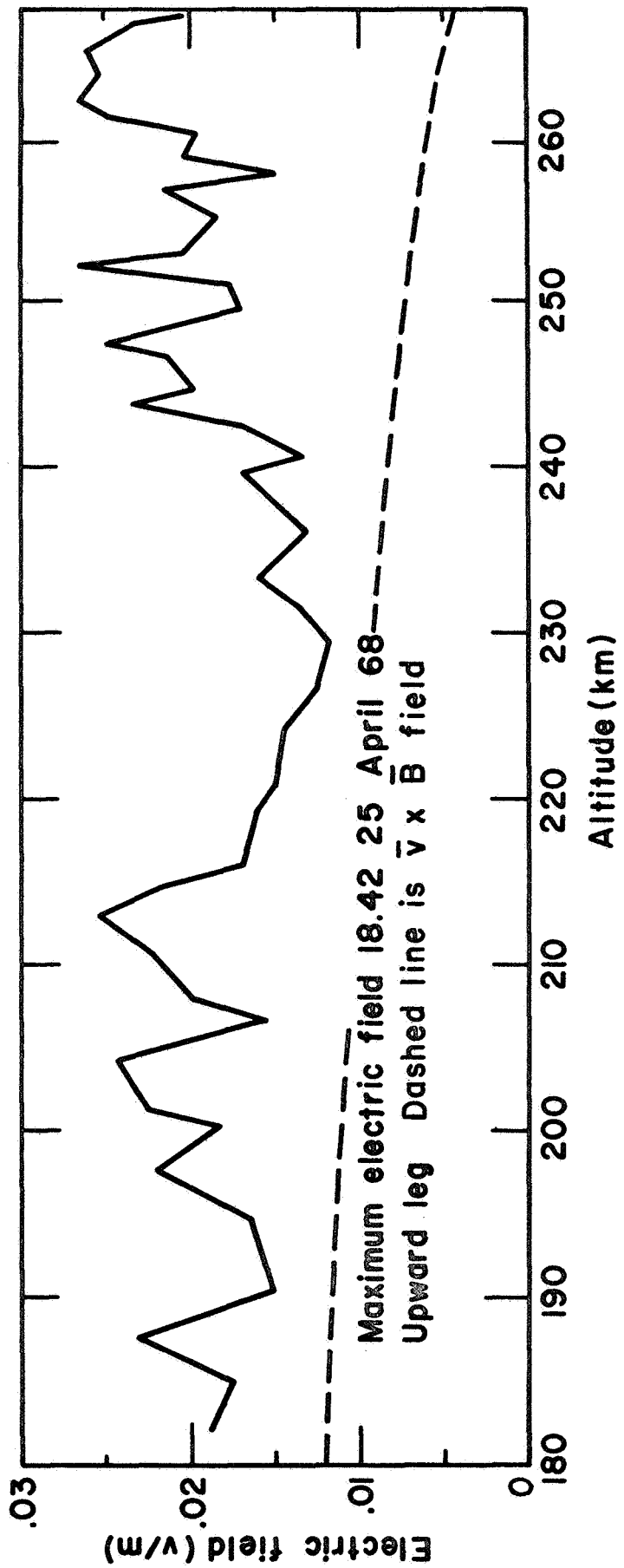
Electric field (v/m)
.03
.02
.01
0
180
190
200
210
220
230
240
250
260
Altitude (km)
Maximum electric field 18.42 25 April 68
Upward leg Dashed line is $\bar{v} \times \bar{B}$ field

Figure 66

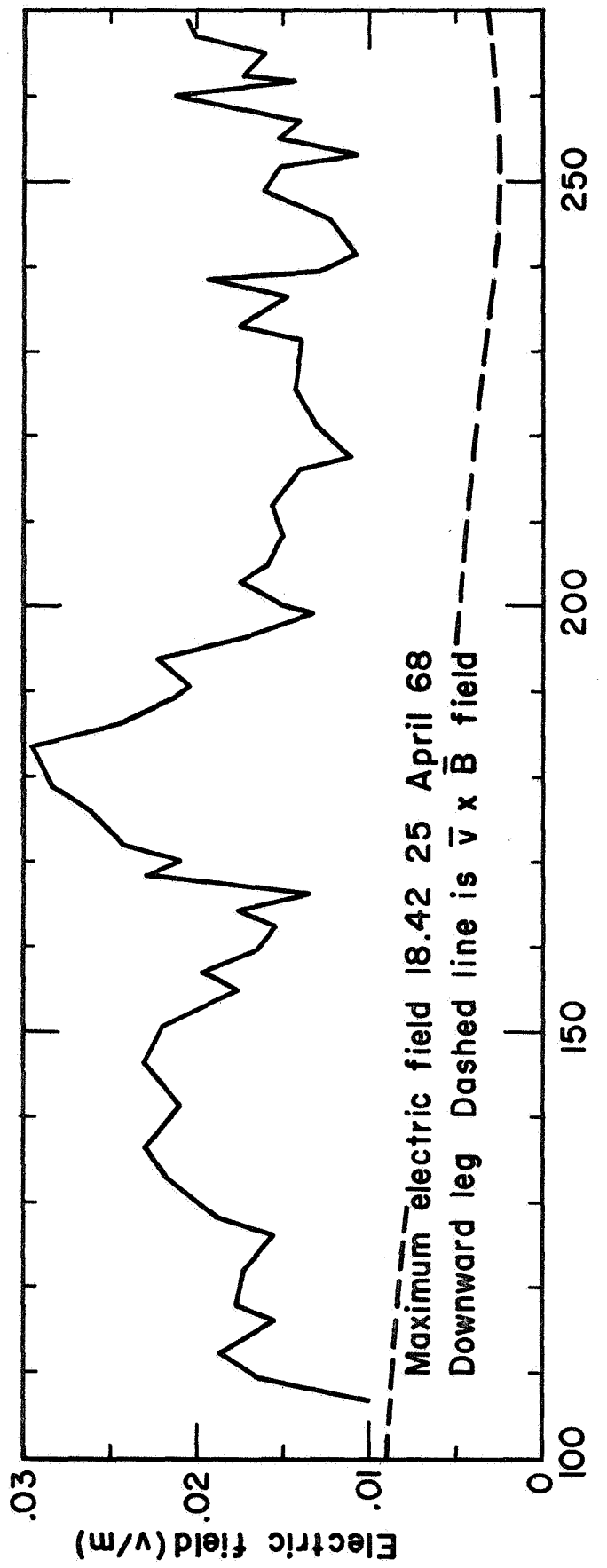
Maximum electric field 18.42 25 April 68
Downward leg Dashed line is $\bar{v} \times \bar{B}$ field
Electric field (v/m)
.03
.02
.01
0
100
150
200
250
Altitude (km)

Figure 57

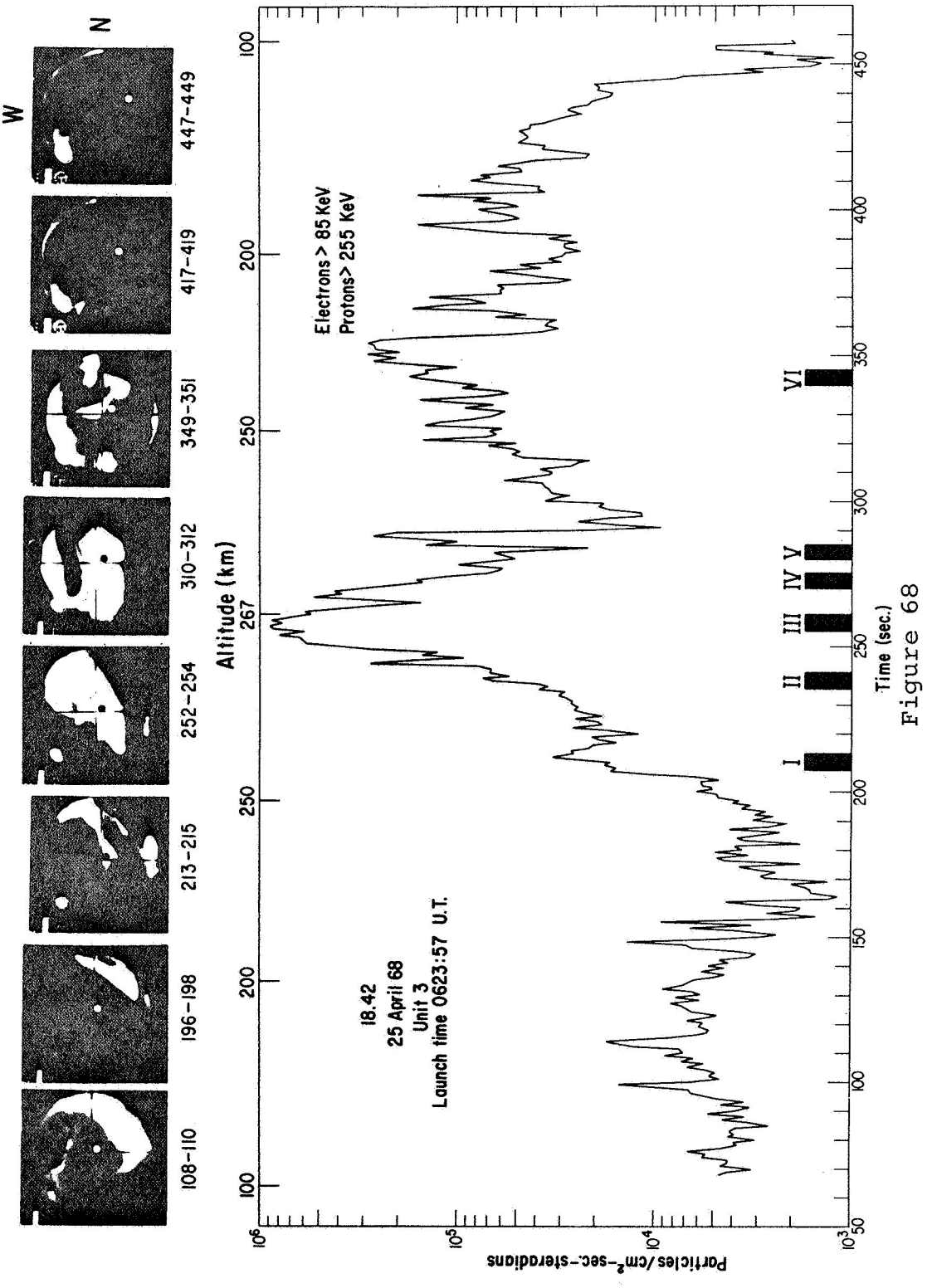
W
N
108-110
196-198
213-215
252-254
310-312
349-351
417-419
447-449
Altitude (km)
100
200
250
267
Electrons > 85 KeV
Protons > 255 KeV
18.42
25 April 68
Unit 3
Launch time 0623:57 U.T.
I
II
III
IV
V
VI
Particles/cm²-sec.-steradians
Time (sec.)

Figure 68

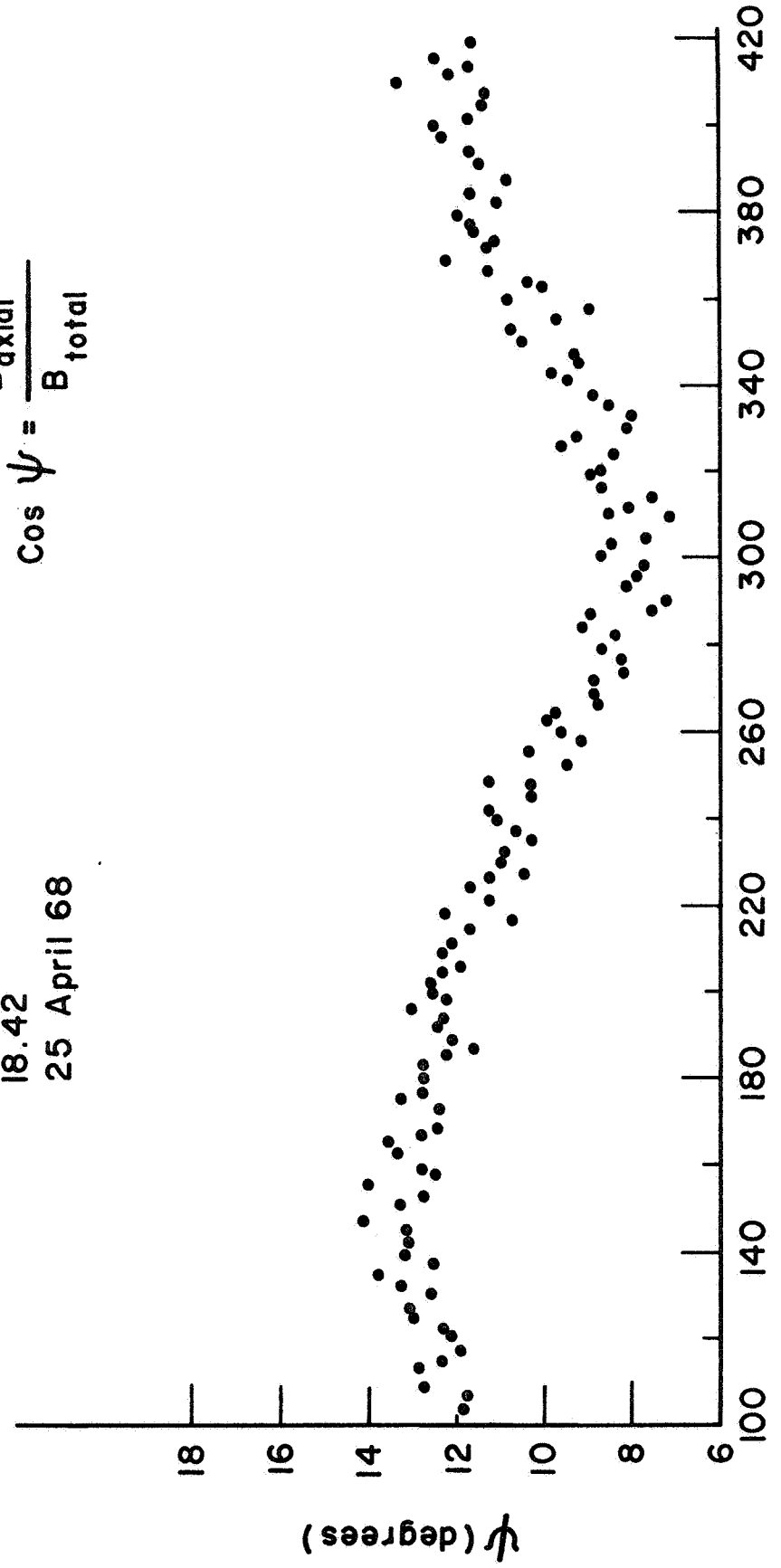
18.42
25 April 68
Cos ψ = B axial / B total
ψ (degrees)
18
16
14
12
10
8
6
100
140
180
220
260
300
340
380
420
Time(sec)

Figure 69

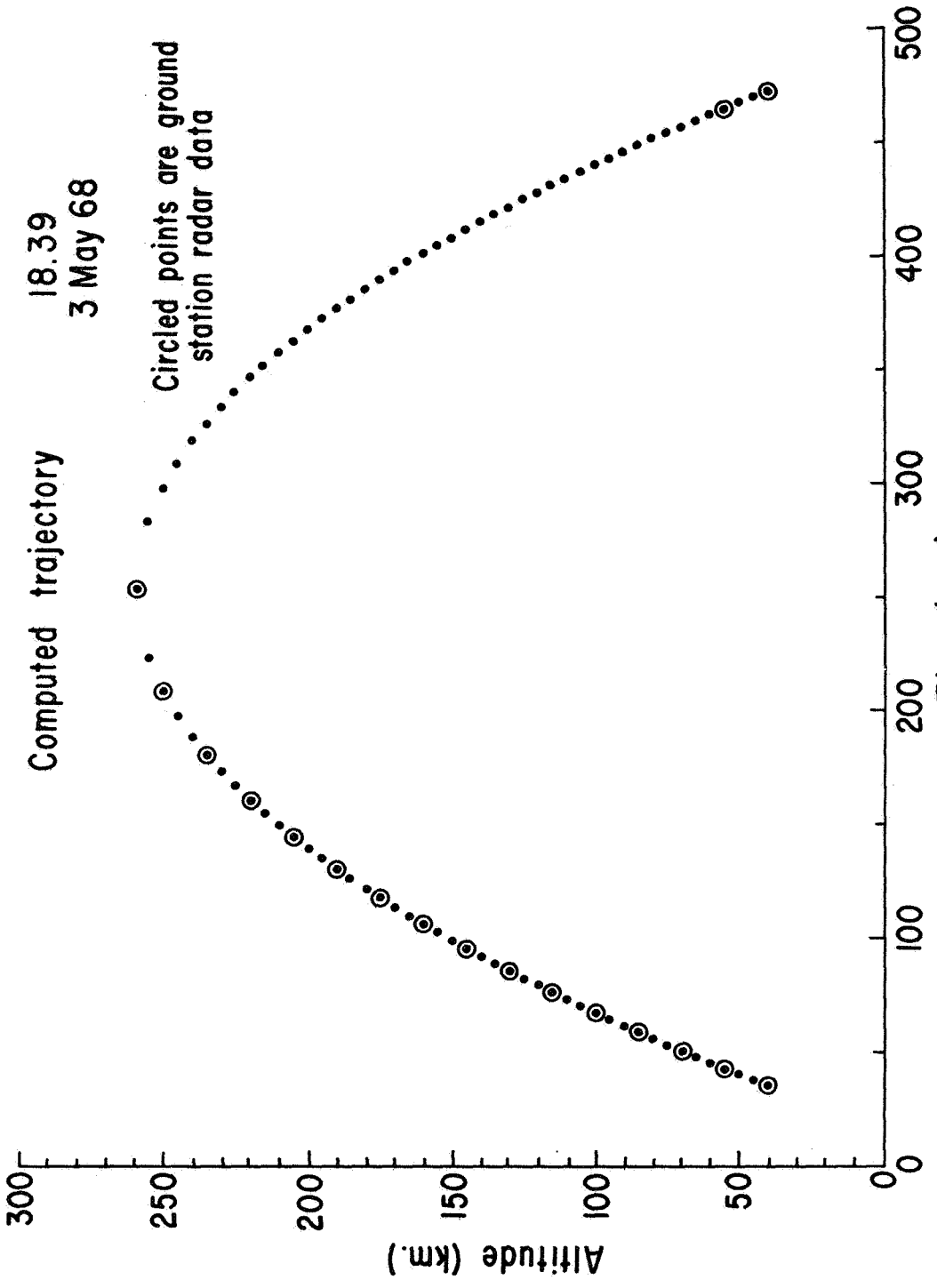
Computed trajectory
18.39
3 May 68
Circled points are ground station radar data
Altitude (km.)
Time (sec.)
300
250
200
150
100
50
0
0
100
200
300
400
500

Figure 70

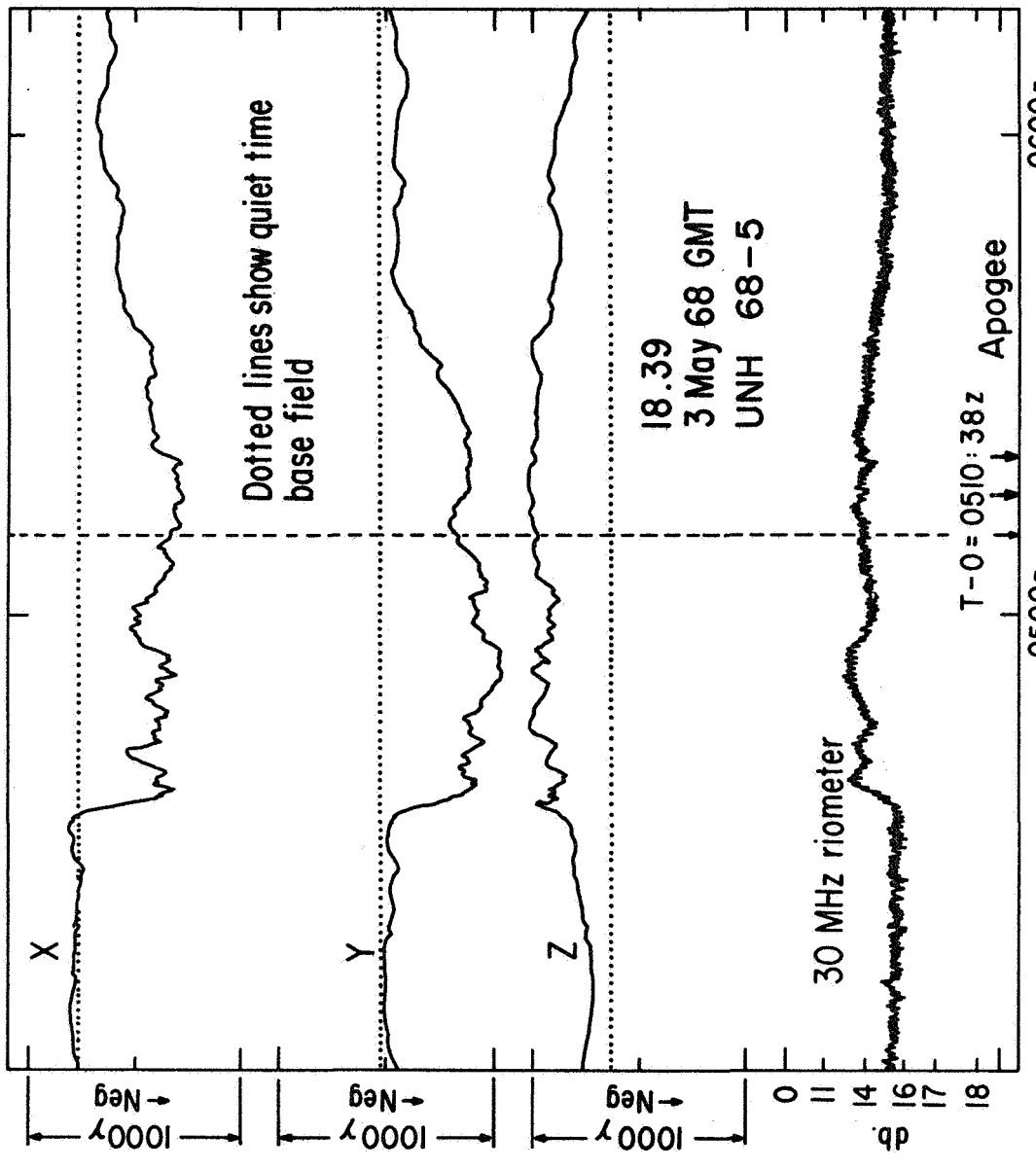
X
Y
Z
1000γ
Neg
Dotted lines show quiet time
base field
18.39
3 May 68 GMT
UNH 68-5
30 MHz riometer
db
0
11
14
16
17
18
T-0 = 0510:38z
Apogee
Splashdown
0500z
0600z

Figure 71

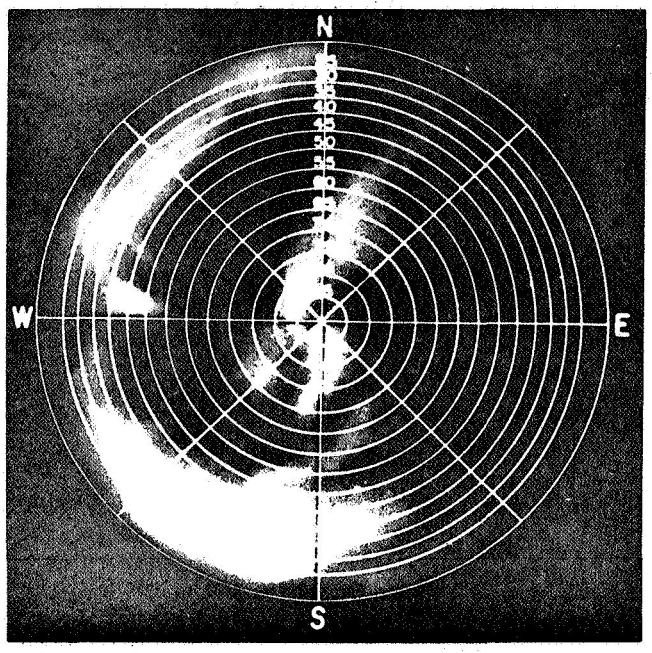

a

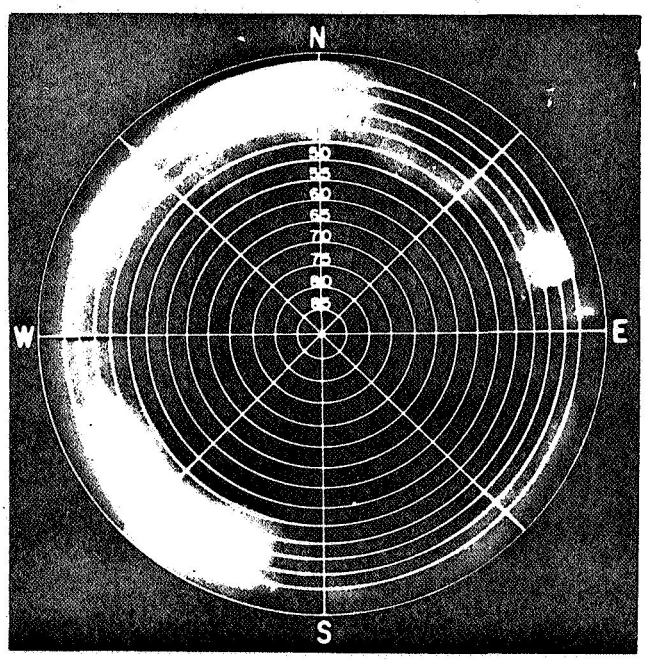

b

Figure 72

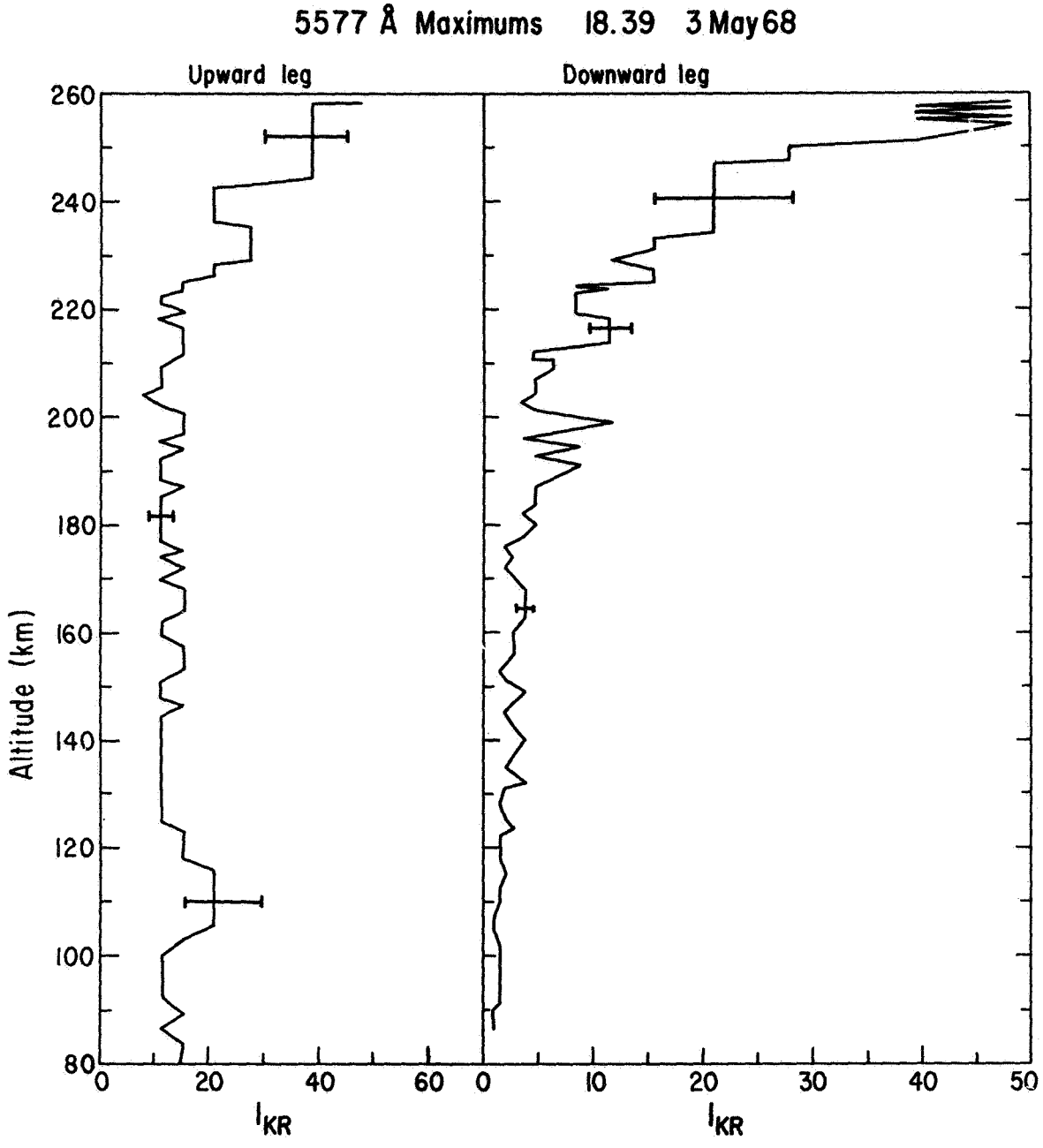
5577 Å Maximums 18.39 3 May 68
Upward leg
Downward leg
Altitude (km)
260
240
220
200
180
160
140
120
100
80
0
20
40
60
0
10
20
30
40
50
I_{KR}
I_{KR}

Figure 73

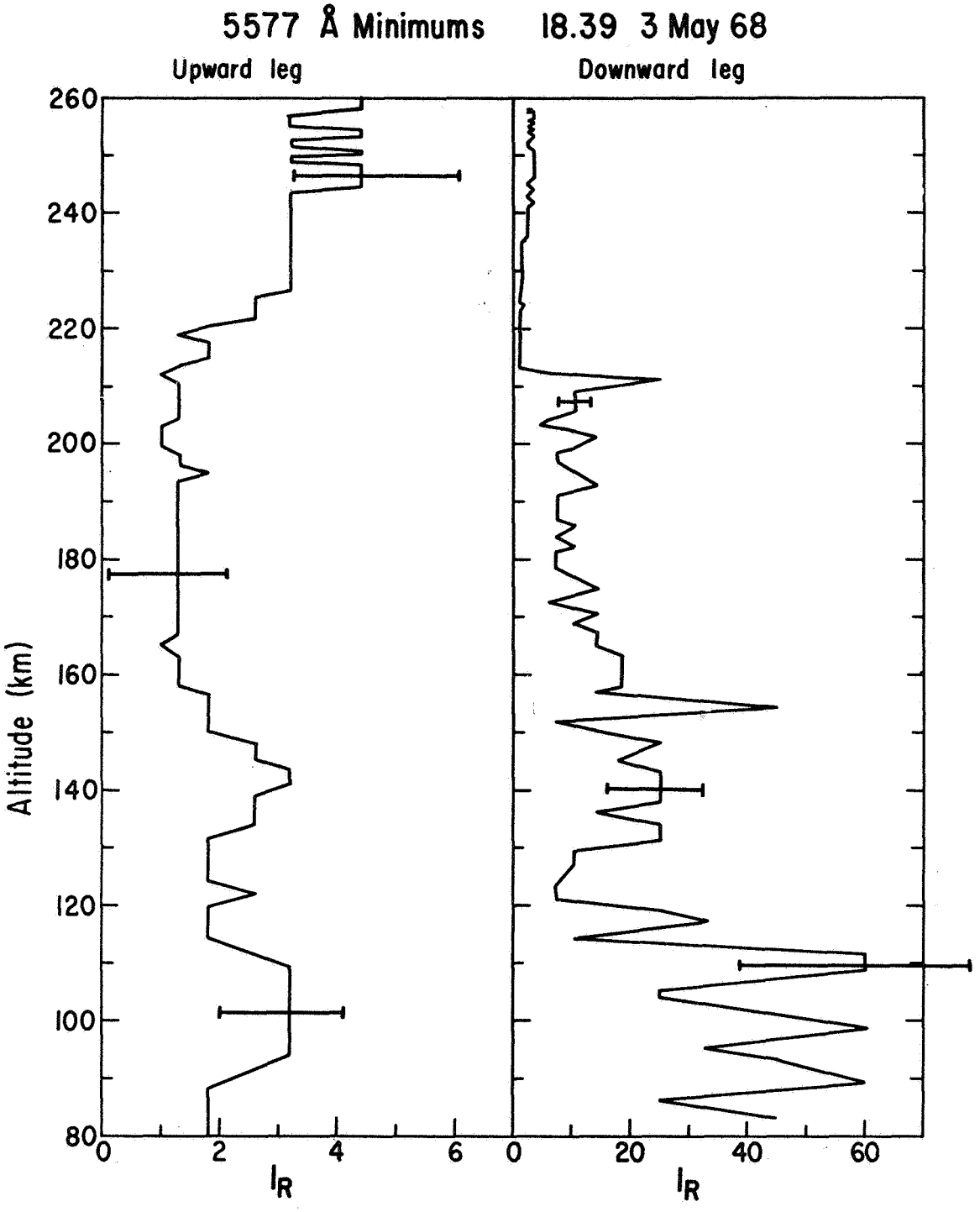
5577 Å Minimums 18.39 3 May 68
Upward leg
Downward leg
Altitude (km)
260
240
220
200
180
160
140
120
100
80
0
2
4
6
0
20
40
60
I_R
I_R

Figure 74

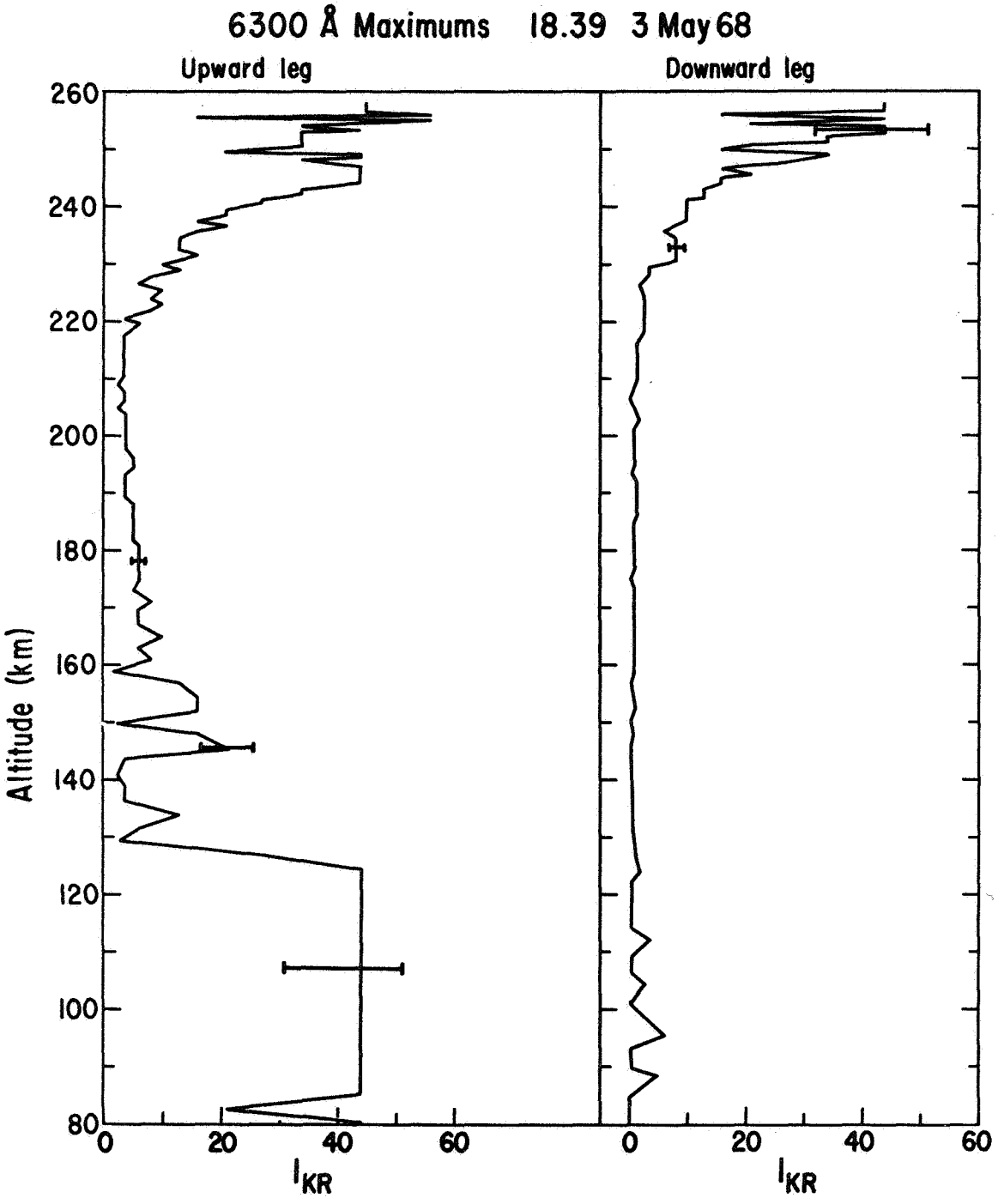
6300 Å Maximums 18.39 3 May 68
Upward leg
Downward leg
Altitude (km)
260
240
220
200
180
160
140
120
100
80
0
20
40
60
I_{KR}

Figure 75

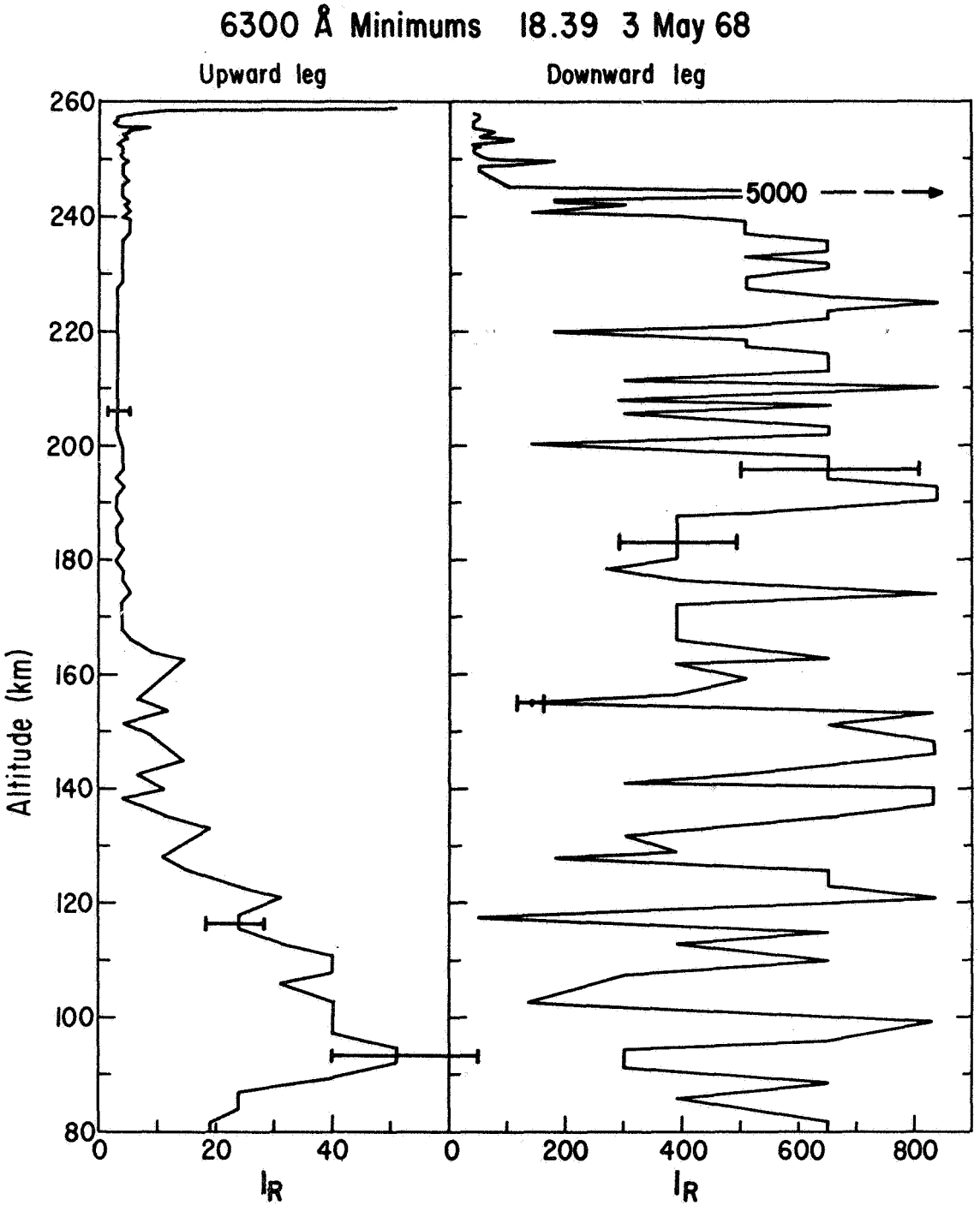
6300 Å Minimums 18.39 3 May 68
Upward leg
Downward leg
Altitude (km)
260
240
220
200
180
160
140
120
100
80
0
20
40
0
200
400
600
800
5000
I_R
I_R

Figure 76

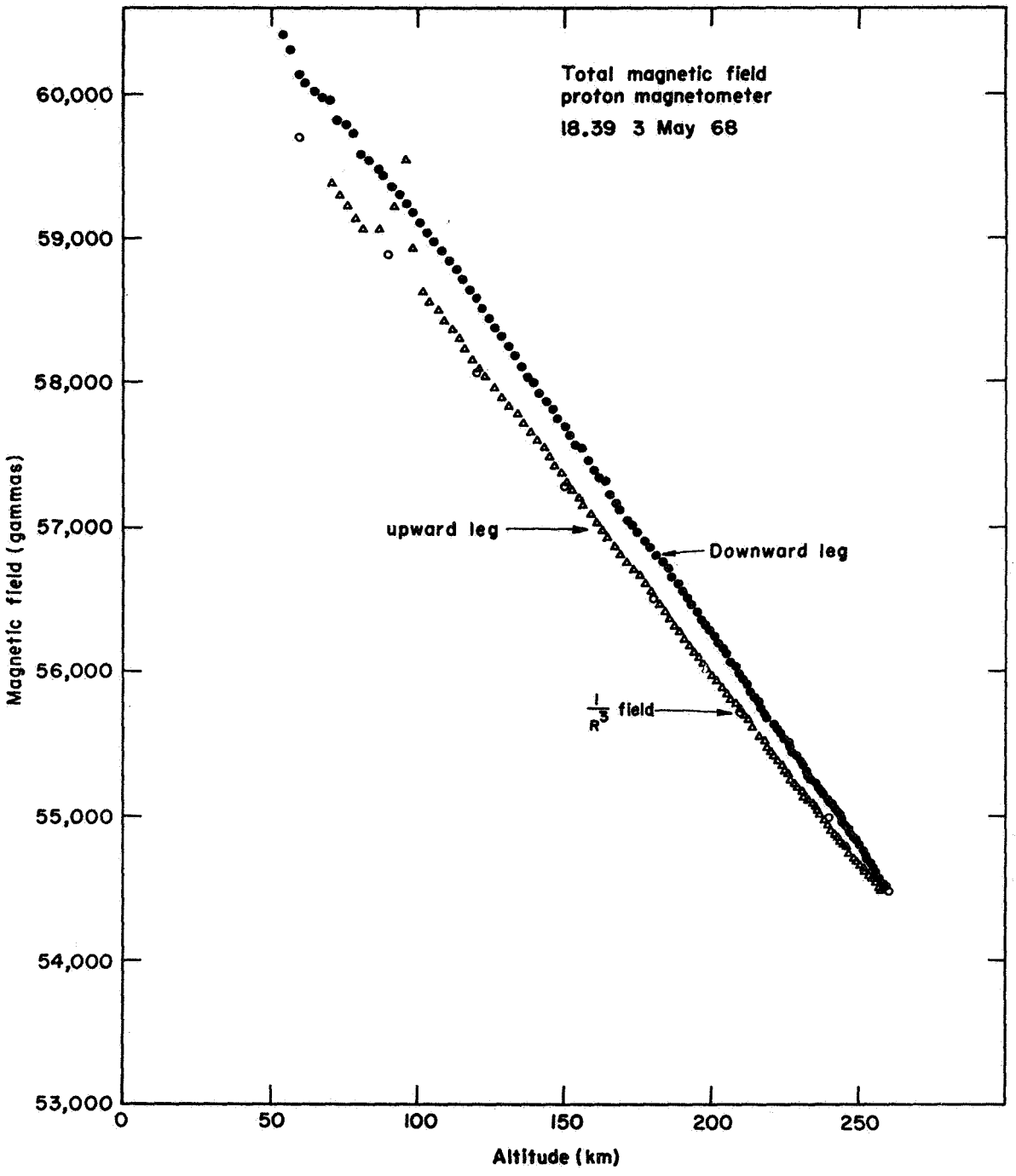
Total magnetic field
proton magnetometer
18.39 3 May 68
upward leg
Downward leg
1/R³ field
Magnetic field (gammas)
60,000
59,000
58,000
57,000
56,000
55,000
54,000
53,000
0
50
100
150
200
250
Altitude (km)

Figure 77

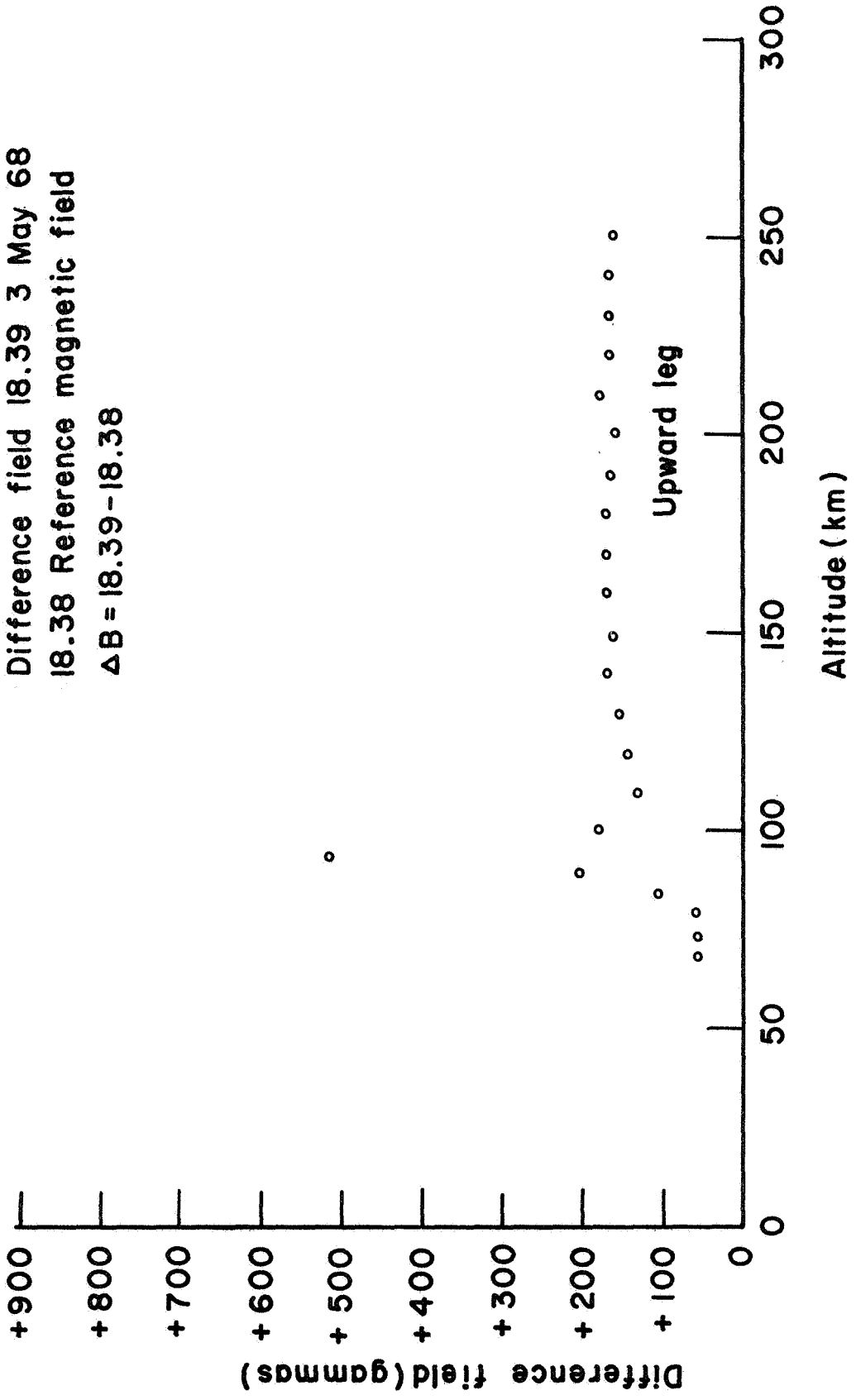
Difference field 18.39 3 May 68
18.38 Reference magnetic field
ΔB = 18.39 − 18.38
Upward leg
Difference field (gammas)
+900
+800
+700
+600
+500
+400
+300
+200
+100
0
0
50
100
150
200
250
300
Altitude (km)

Figure 78

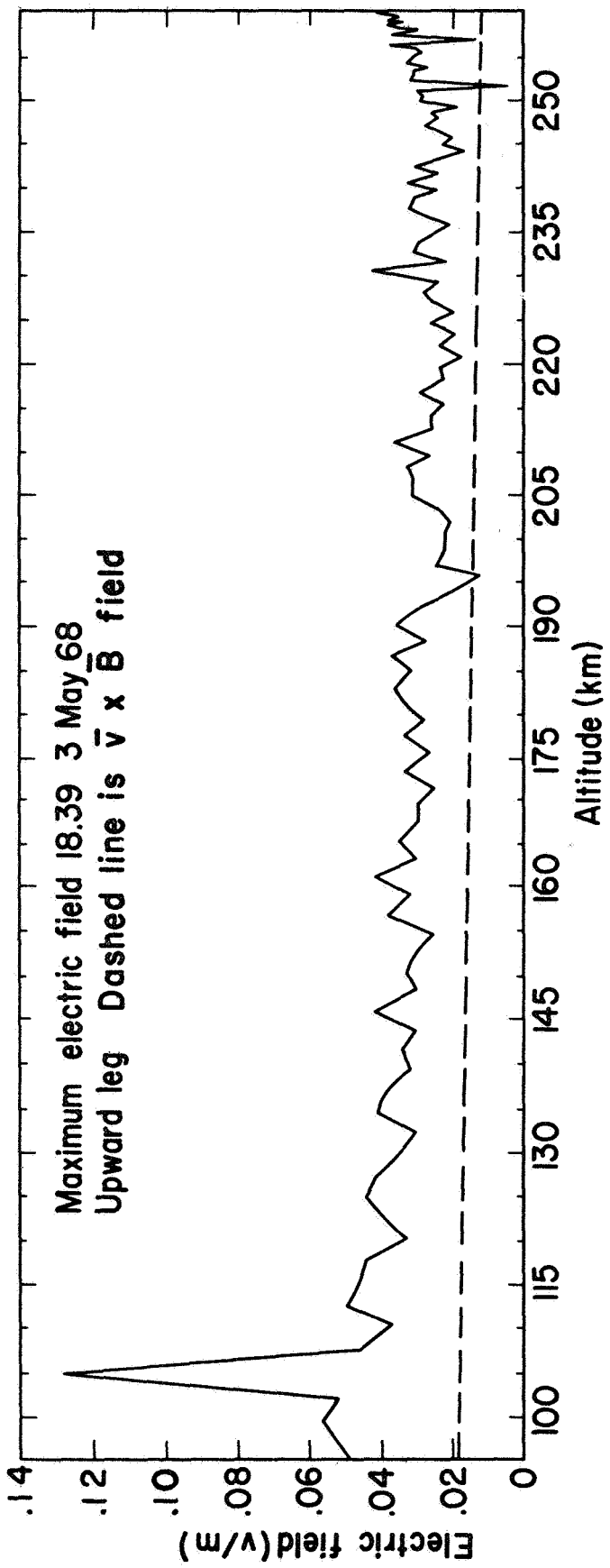
Maximum electric field 18.39 3 May 68
Upward leg Dashed line is $\bar{v} \times \bar{B}$ field
Electric field (v/m)
.14
.12
.10
.08
.06
.04
.02
0
100
115
130
145
160
175
190
205
220
235
250
Altitude (km)

Figure 79

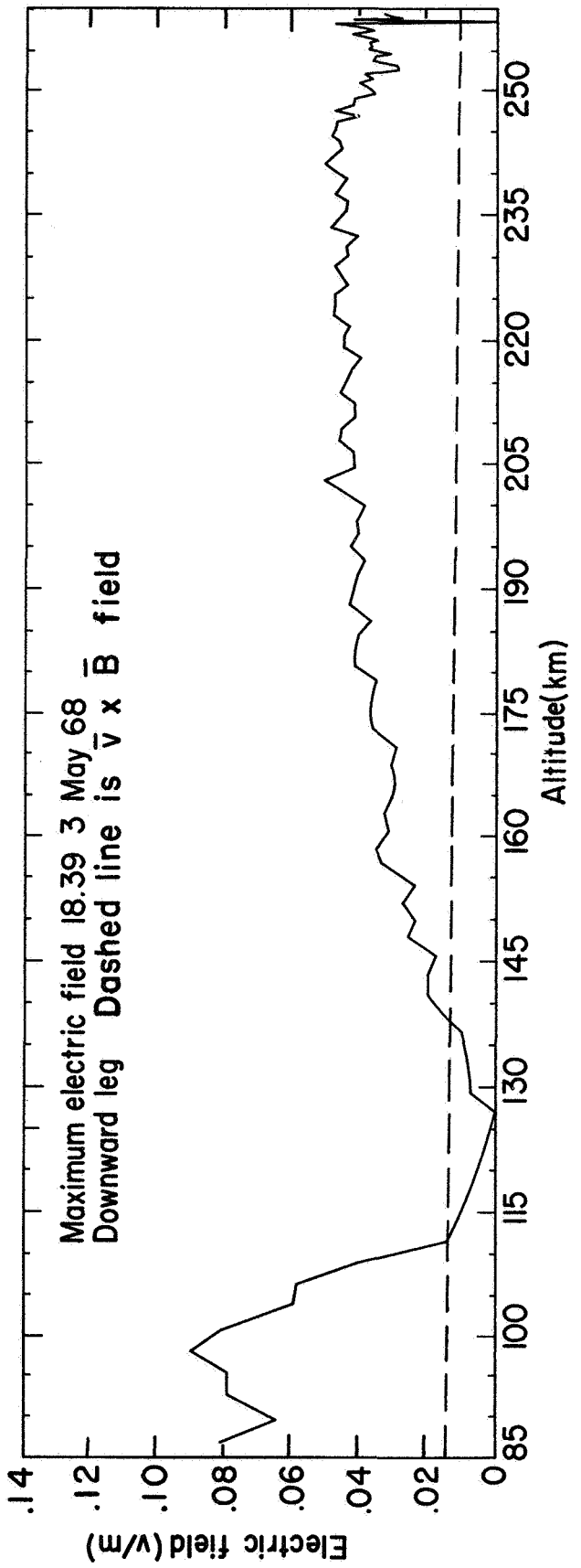
Maximum electric field 18.39 3 May 68
Downward leg Dashed line is $\bar{v} \times \bar{B}$ field
Electric field (v/m)
.14
.12
.10
.08
.06
.04
.02
0
85
100
115
130
145
160
175
190
205
220
235
250
Altitude(km)

Figure 80

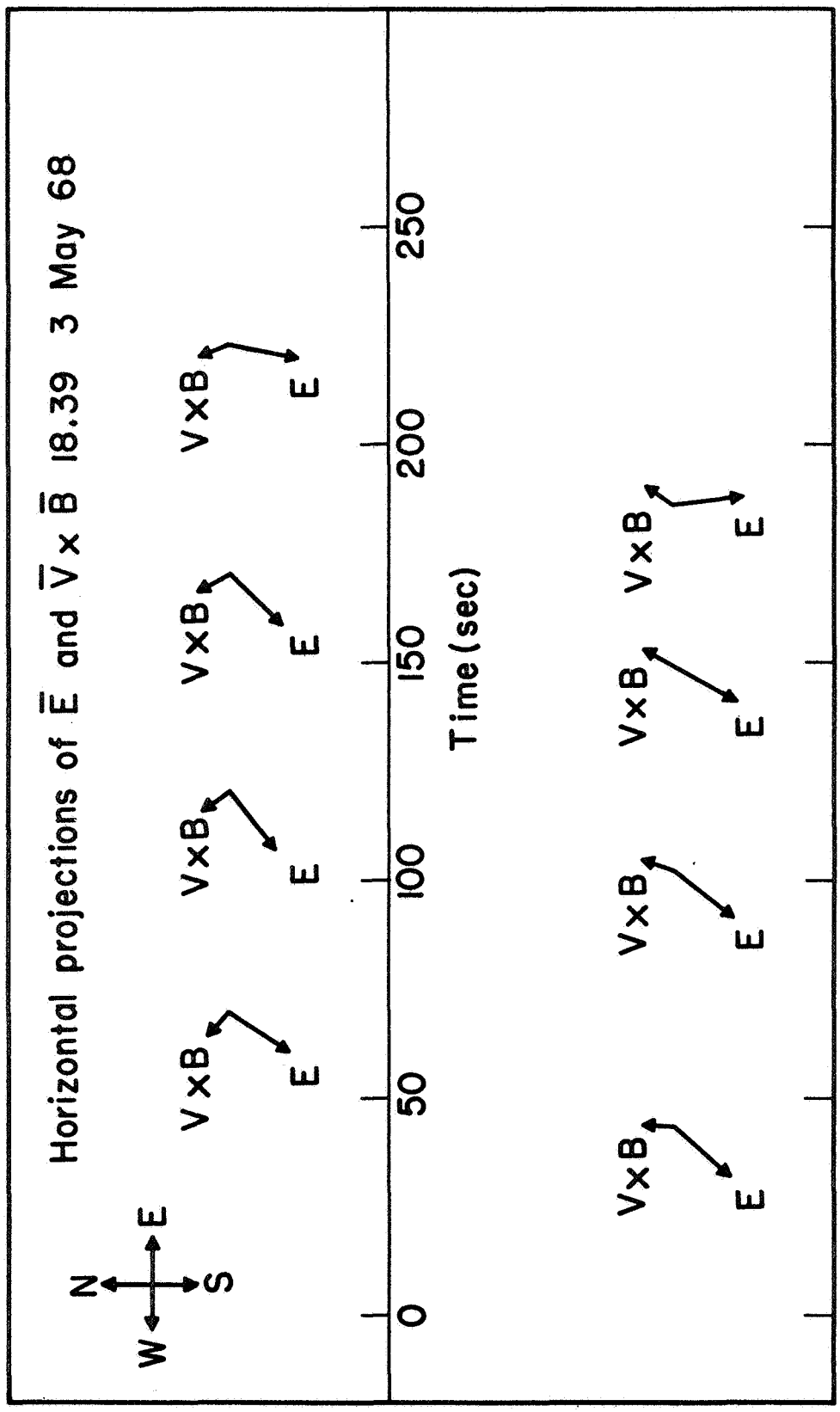
Horizontal projections of $\bar{E}$ and $\bar{V} \times \bar{B}$ 18.39 3 May 68
N
E
S
W
V×B
E
0
50
100
150
200
250
300
350
400
450
500
Time (sec)
Time (sec)

Figure 81

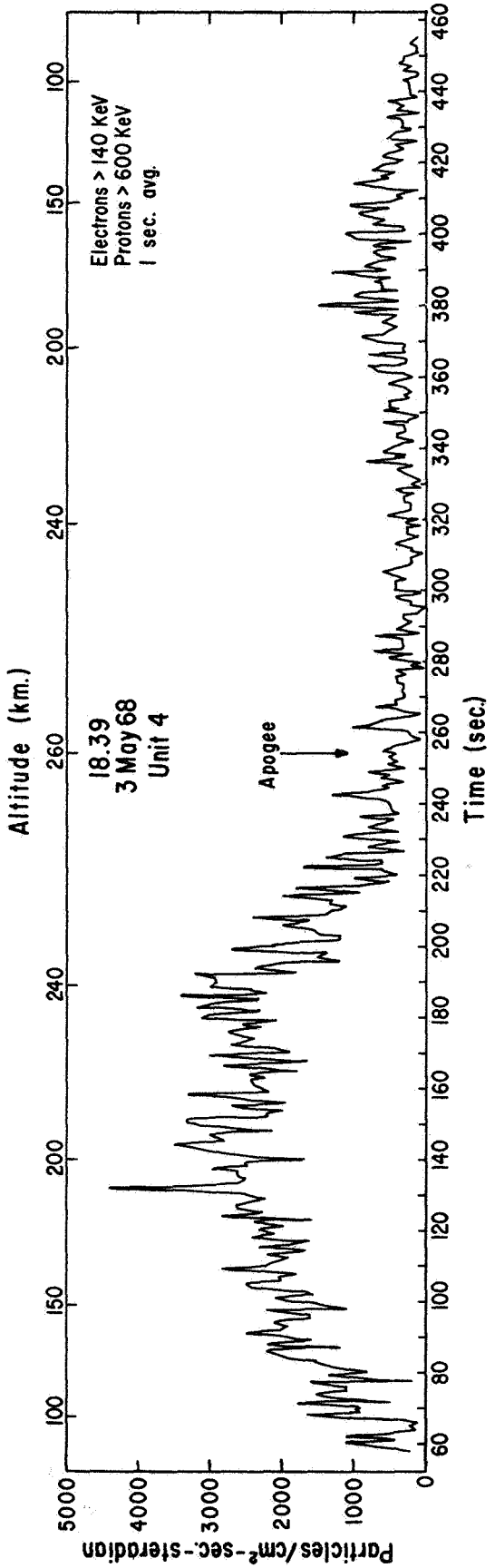
Electrons > 140 KeV
Protons > 600 KeV
1 sec. avg.
18.39
3 May 68
Unit 4
Apogee
Altitude (km.)
Time (sec.)
Particles/cm²-sec.-steradian

Figure 82

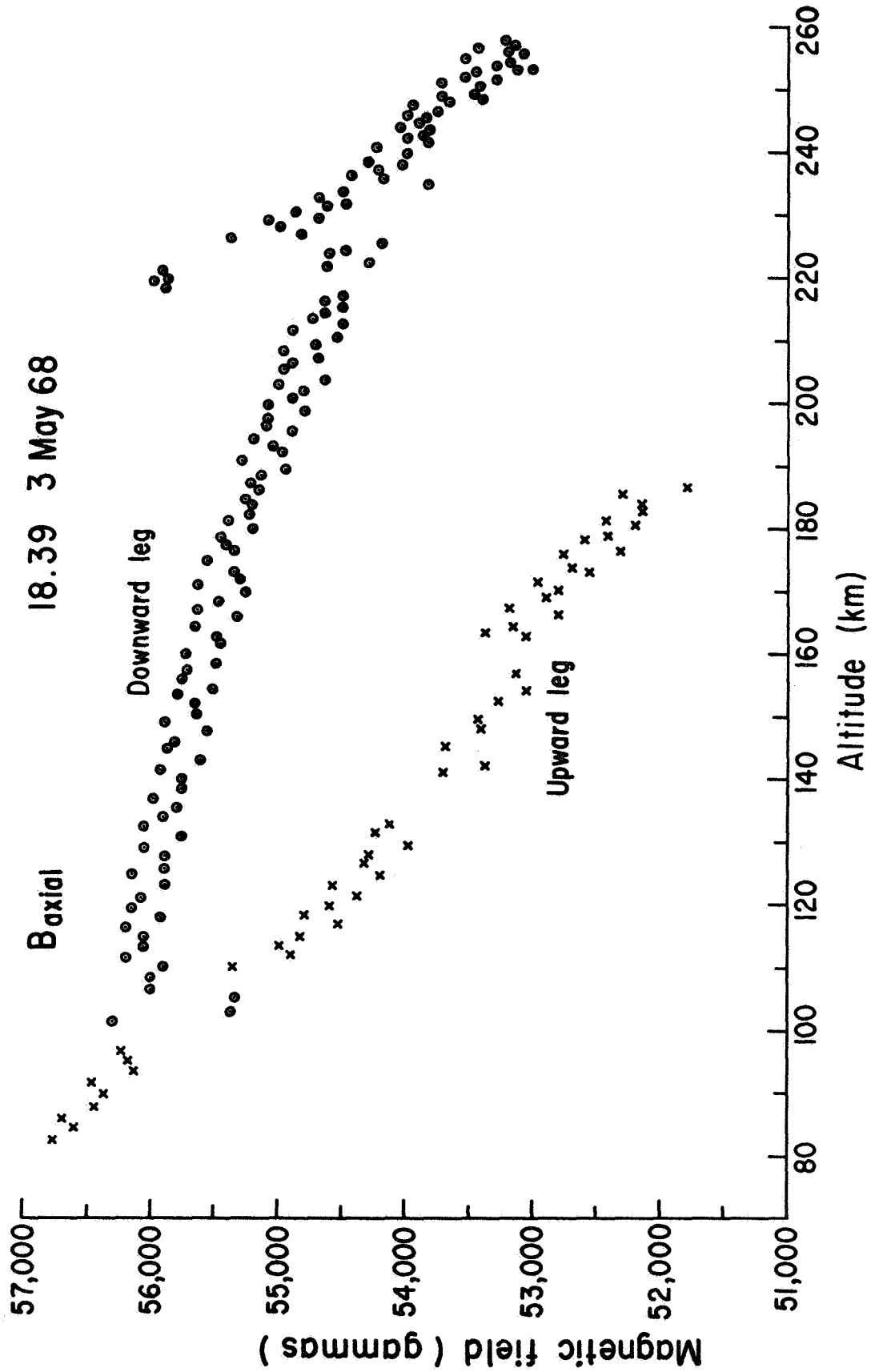
B axial
18.39 3 May 68
Downward leg
Upward leg
Magnetic field (gammas)
Altitude (km)
57,000
56,000
55,000
54,000
53,000
52,000
51,000
80
100
120
140
160
180
200
220
240
260

Figure 83